Fabrication, Characterization and Application of PZT-Silane Nano-Composite Thin-Film Sensors and Actuators

Weiwei Xu

A dissertation
submitted in partial fulfillment of the
requirements for the degree of

Doctor of Philosophy

University of Washington

2019

Reading Committee:

I. Y. (Steve) Shen, Chair

Guozhong Cao

J. Devin MacKenzie

Program Authorized to Offer Degree:
Mechanical Engineering

University of Washington

Abstract

Fabrication, Characterization and Application of PZT-Silane Nano-Composite Thin-Film Sensors and Actuators

Weiwei Xu

Chair of the Supervisory Committee:
Professor I. Y. (Steve) Shen
Mechanical Engineering

Structural health monitoring (SHM) plays a very important role in improving structural safety, preventing catastrophic failures and lowering maintenance costs. Current sensing methods have some limitations, such as being bulky, heavy, or brittle, making them unsuitable for SHM of composite structures. In response to the need for a flexible, printable sensor with low curing temperature, a nano-composite thin-film with additive manufacturing capability that consists of numerous lead-zirconate-titanate (PZT) nanoparticles embedded in a silane matrix is proposed and studied in this dissertation.

This dissertation includes fabrication, characterization, and applications of proposed thin-films with rigid or flexible substrates and parallel-plate or interdigitated electrodes as piezoelectric actuators and sensors. Fabrication includes the following steps: First, PZT nanoparticles with size distribution ranging from 300 to 800 nanometers, are fabricated via hydrothermal synthesis. The PZT nanoparticles are then suspended in a silane-based fluid to form a PZT ink that can be printed, sprayed, or drop-cast onto a substrate. The deposited PZT ink is subsequently cured at low temperature (e.g., 120 $^\circ C$) to form the PZT-silane thin-film sensor. A similar ink and thin-film sensor using crushed bulk PZT is also fabricated for comparison. The aerosol-jet printed results for both inks are provided and compared.

Characterizing the material properties of the PZT-silane thin films includes two parts:

dielectric and piezoelectric characterization. The dielectric constant and loss are measured through an impedance analyzer. Piezoelectric properties are estimated by applying a calibrated force directly onto the film while an accurate, double-end charge amplifier isolates and records the tiny induced charge from background electrical noise. A finite element model is created to simulate the experimental setup in order to estimate the piezoelectric coefficient d_{33} from the measurements.

A PZT-silane nano-composite thin film with parallel-plate electrodes, drop-cast near the fixed edge of a thin flexible cantilever beam made of kapton, has been successfully demonstrated as an actuator. Velocity measurements at the free end are found to be in synchronization with actuation signals when driving the PZT-silane thin film actuator near natural frequencies of the beam. To demonstrate its validity as a vibration sensor, a PZT-silane thin film is attached to a square aluminum plate supported by four pillars. The frequency response of the charge measured from the PZT thin-film sensor is in close agreement with the vibration measurements from a laser Doppler vibrometer.

PZT ink is drop-cast on a flexible substrate in two electrode formats for evaluation: parallel-plate and interdigitated electrodes (IDEs). The parallel-plate electrode format is difficult to implement, because silver electrodes cannot be properly printed onto the PZT film with high conductivity and dimension accuracy. In contrast, IDEs inkjet-printed onto a polyethylene terephthalate (PET) film demonstrate excellent resolution and conductivity. Sinusoidal voltage applied over the IDEs drives PZT thin-film with IDEs device into resonance serving as a resonator.

PZT thin films with printed IDEs are demonstrated as vibration and strain sensors. Vibration tests are carried out on wing and beam structures with small angle oscillations. PZT thin-film with IDEs are attached on one side of these test structures and commercially acquired foil strain gauges on the other side for comparison and characterization. Strain and charge frequency domain measurements are recorded and amplitude peaks correlate to struc-

tural vibration frequencies. PZT-IDE sensor outputs at wing/beam oscillation frequency are found to increase with vibration amplitude and charge responses are approximately proportional to strain gauge outputs. This validates PZT-silane thin films with printed IDEs as strain sensors. The directional dependence of their sensing capability is demonstrated in theory, finite element analysis and experimentation. Two PZT-silane thin film devices with printed IDEs oriented 90 degrees apart show different sensitivities towards single-axis strain and experimentation proves PZT thin films with IDEs can distinguish strains in two dimensions.

Keywords: Structural health monitoring (SHM) of composite structures, PZT nanoparticles, PZT-silane ink, printed PZT thin film, inkject printed interdigitated electrodes, nanocomposite sensor and actuator

TABLE OF CONTENTS

LIST OF FIGURES

LIST OF TABLES

Chapter 1

INTRODUCTION

1.1 Motivation

Monitoring the integrity of structures on a real-time basis while they are in service has always been important for manufacturers, users and maintenance crew in a wide variety of industries, such as aerospace and civil engineering. This area, known as structural health monitoring (SHM), has attracted vast technical and scientific interest for the last 30 years as it promises to improve safety, and assures the monitored structural components perform in a reliable and cost effective fashion. For example, in the case of aircraft safety, SHM can be used to detect impending damage by continuously monitoring the critical structures in service for variances that could indicate the onset of catastrophic failure. It also brings economic benefits, such as reduction in maintenance labor costs by replacing the regular scheduled inspection with condition-based maintenance and optimizing the lifetime of a component by indicating exactly when it should be replaced. SHM has been widely studied and has helped decrease maintenance costs and increase reliability for multiple applications, such as aircraft structures, engines, and bridges [1–7].

SHM systems can be installed noninvasively on aged structures to apprise users of any incipient damages in real time and estimate their remaining lifetime. SHM systems can also be built into a new structure for assessment of the structural performance during its life-span. By integrating sensors and actuators inside a new structure, its traditionally designed safety factor could be lower, thus making scaling down dimensions, weight and costs possible [8, 9].

The key component in a SHM system is the data acquisition unit, which contains an on-board network of transducers. One of the most commonly used types of transducers for

SHM process is piezoelectric transducers. They are manufactured from a special type of materials called “piezoelectric material” that utilizes *piezoelectricity*.

Piezoelectricity was introduced to the world by the Curie brothers, Jacques Curie and Pierre Curie in 1880. They discovered that certain crystalline materials such as quartz and Rochelle salt, would produce voltages that are proportional to the external force. Electric potential changes sign when that material is under tension or compression. This unusual phenomenon was called ‘the piezoelectric effect’ by W.G. Hankel. This direct effect is represented schematically in Fig. 1.8. The converse piezoelectric effect states that when a piezoelectric material is exposed in an electric field, its size will change in proportion to the electric field strength. Figure 1.9 shows that material would extend or shrink depending on the polarity of the applied electric field [10]. As a result, this type of material can produce an electrical charge utilized by as sensors when deformed and when driven electrically, it will deform and function as an actuator.

Piezoelectric sensors rely on the direct piezoelectric effect, which linearly converts mechanical stress or strain into an electric charge. Examples are pressure sensors and vibration sensors. Piezoelectric actuators (such as resonators), exploit the inverse piezoelectric effect, which linearly convert the electrical signal (electric field strength) to the mechanical strain in that material. Taking advantage of this piezoelectric effect, piezoelectric sensors and actuators can be used for non-destructive evaluation (NDE) by embedding them inside or bonding them onto the surface of a monitored structure [9]. In practice, piezoelectric actuators and several satellite piezoelectric sensors can be arranged near a high-stress, high-fatigue area (e.g., a joint [11–13]) for SHM process. The actuators periodically send out an interrogating signal to the sensors. When the structure is healthy, the sensor’s response will serve as a reference signature. When damage occurs (e.g., fatigue cracks or delamination), the sensors will deviate from the reference signature accordingly. Monitoring and analyzing the sensor signatures will thus allow users to evaluate the structural health [7, 14–16].

Moreover, knowledge of the strain state of a structure is vital for the prediction of its behavior or shape. Monitoring the mechanical strain distribution in real-time provides current physical status of a structure or change in its structural characteristics, which are important for the detection of damage and the diagnosis of structural health [17]. For example, strain sensors can be installed on wind turbine blades to remotely monitor their structural health and to detect damage in composites before failure occurs [18, 19]. This will greatly improve wind energy harvesting efficiency and safety, lower the possibility of sudden breakdowns and significant failures, and lower the maintenance, repair costs and down-time.

Strain sensors can easily be modified into force or shape sensors. For instance, strain sensors were attached directly on the wing spars of a micromechanical flying insect, a type of micro aerial vehicle (MAV), to measure real-time wing forces for commercial and military applications. This information is very important for characterizing forces generated during wing motion and provides feedback for the onboard flapping wing control system [20]. Furthermore, strain sensors are useful in the automotive industry for estimating the forces that act upon vehicles when direct measurements of the forces are difficult or expensive. For example, Pylypchuk et al. presented an effective methodology for tire force measurements by using strain sensors to measure elastic strains on different wheel-suspension parts [21]. Strain sensors have also been implemented into a micro cantilever force sensor [22] for microelectromechanical systems (MEMS).

Strain sensors can also become shape sensors and have been proven to enable numerous structural applications in aerospace and medical industries [23, 24]. With the help of strain measurements determined by embedding strain sensors within the monitored structures and proper utilization of strain-displacement relationships, dynamic structural deformations can be reconstructed. This usually is a two-step process. First, strain sensors, such as conventional metal strain gauges or fiber optic sensors [25, 26] are attached or embedded to measure in-plane strains of the structures. Second, a shape reconstruction algorithm, such as a modal transformation algorithm [27, 28] or a finite element (FE) model of the target structure [29] is applied to estimate out-of-plane displacements.

The advent of additive manufacturing technologies has revolutionized many fields and SHM is no exception. If piezoelectric thin films could be printed on flexible substrates, such as polyethylene terephthalate (PET) shown in Fig. 1.1 or Kapton shown in Fig. 1.2, numerous new opportunities and applications for SHM would become available. Since the substrate is polymeric, it has a much higher shock resistance than bulk PZT. Therefore, additively manufactured PZT thin films on flexible substrates may offer a different perspective to implementing sensing and actuation.

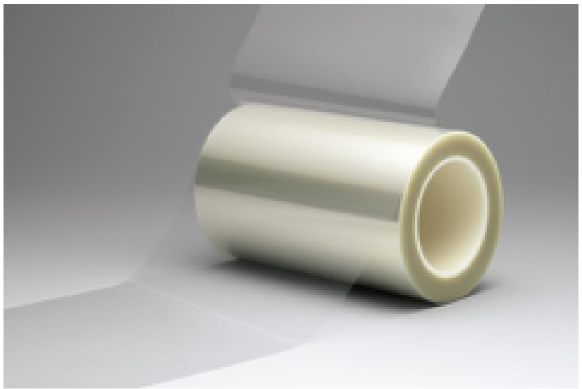

Figure 1.1: PET (polyethylene terephthalate) film https://www.tekra.com/

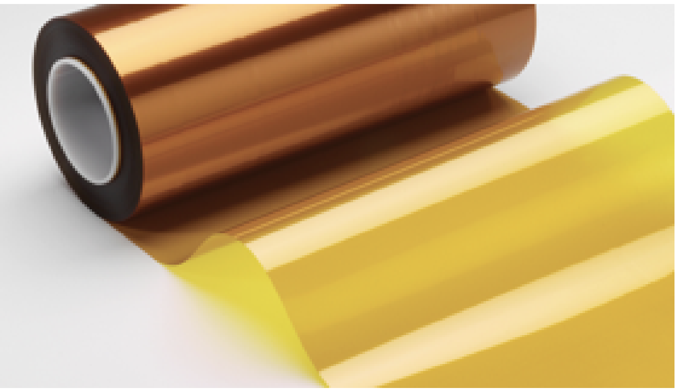

Figure 1.2: Kapton (polyimide) film http://www.dupont.com/

Use of additive manufacturing to fabricate piezoelectric thin-films with low-curing temperatures on flexible substrates for sensor and actuator applications have some unique advantages. Traditional manufacturing involving pure PZT thin films and rigid substrates requires very expensive equipment and semiconductor processes (e.g., sputtering and lithography). These semiconductor processes are not agile: they are financially suitable for mass production, but not for small production of a limited supply of highly customized products. These disadvantages become more evident when the sensors and actuators scale down in size, resulting in even shorter product cycles. In contrast, additive manufacturing benefits from scaling downs. Its equipment and processes are inexpensive. Its processes can be adjusted for mass production (e.g., via roll-to-roll printing in Fig. 1.3) or highly customized products with low volume.

Figure 1.3: UW Roll-to-Roll Printer

1.2 Common Types of Strain Sensors and Their Limitations

The most common types of strain sensors are strain gauges, which convert the elastic deformation of the target body to a change in resistance (Fig. 1.4). The resistance change is later transformed to a bridge (e.g., Wheatstone bridge) imbalance output signal. These strain gauges can be divided into several categories depending on the materials used in making the active sensing element. Two popular categories are the metallic foil strain gauges and the semiconductor (or piezoresistive) strain gauges.

Metallic foil strain gauges are the most conventional strain gauges , and have many advantages. They are inexpensive and easy to use. Furthermore, they can be used on either flat or rounded surfaces because they are flexible (e.g., on the inside or outside of a tube) and to measure both static and dynamic strains. However, in order to measure strain with a strain gauge, one needs to use an electric circuit capable of measuring the change in resistance, a DC or AC power supply, adhesives to attach the sensor to host structure and wiring, which make it too heavy and bulky to use on smaller host structures.

When compared to a metallic strain gauge, semiconductor (silicon) or piezoresistive strain sensors have some significant advantages, a much higher sensitivity and a smaller size. Nonetheless, piezoresistive strain sensors have several disadvantages. First, the rela-

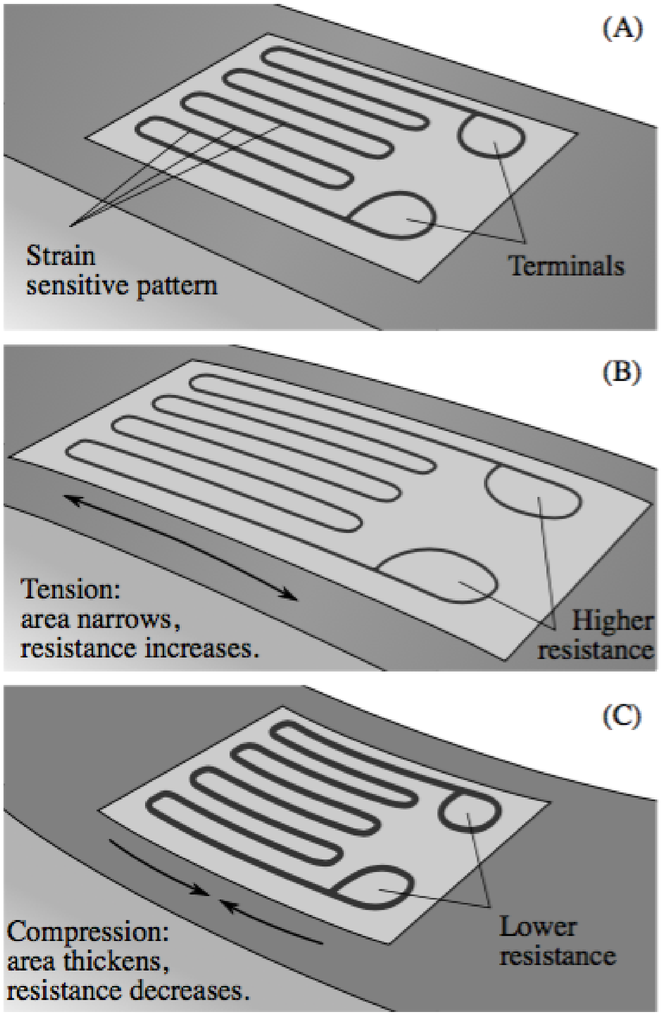

Figure 1.4: The working principle of strain gauges: (A) Unstressed (B) In tension (C) In compression [30]

tionship between voltage output and strain is non-linear. Second, they are expensive and difficult to use lithography and etching steps to pattern the sensing element when the silicon section is thin and small (smaller sensor). Third, the resulting measurement is very sensitive to temperature change because the current needs to pass through the silicon section during the measurement and will generate a lot of heat in their tiny volume, causing the sensor's temperature to raise. This will create thermal noise and diminish the accuracy of its reading greatly.

Recently optical fiber sensors (OFS) have received increasing attention in the field of SHM because they can measure many important physical parameters in a system, such as strain, vibration, temperature and pressure. One of the most popular types of optical fiber sensors for strain measurement is the fiber Bragg grating (FBG) sensor. These optic fibers consist of three main components: a very small inner core 4-9 μm in diameter, cladding made of pure silica glass (SiO_2) 125 μm in diameter and an outer buffer coating that protects the fiber from external conditions (Fig. 1.5). The inner core has a higher refraction index relative to the cladding and this difference of refraction indexes allows the light to propagate only through the small core [31, 32]. Figure 1.6 illustrates the working principle of a fiber Bragg grating sensor. When a broad incident spectrum is transmitted into a fiber Bragg grating sensor, the reflections from each segment of the fiber Bragg grating cause the sensor to reflect a specific frequency of light with wavelength λ_B. When the fiber Bragg grating sensor is under tension, the Bragg wavelength, λ_B, will shift toward a longer wavelength as shown in Fig. 1.7. On the other hand, when it is under compression, λ_B will shift toward a shorter wavelength. This shift in wavelength of the reflected spectrum is an function of strain and can be used for strain measurement [33].

Fiber Bragg grating sensors have many advantages. They are lightweight, small, and highly immune to electromagnetic interference. However, FBG sensors also have some weaknesses. First, FBG sensors are very sensitive to temperature changes. The temperature change of 1 °C will have the same change in wavelength over the Bragg wavelength ($\Delta\lambda/\lambda_B$) as a strain change of 8 $\mu m/m$. Thus, a temperature sensor is needed at the same location for temperature compensation purposes. Second, FBG sensors are very sensitive to lateral forces. A transverse stress will lead the fiber towards birefringence. In this case, the reflected spectrum will be split into several peaks, which makes it hard to determine λ_B [34, 35]. Thus a special sensor system is needed to solve this issue. Third, FBG sensors aren't as small as other strain gauges because the radius of the fiber is usually larger than 10 mm. The size of a FBG sensor system can be quite large if FBG sensors are arranged as rosettes for measuring

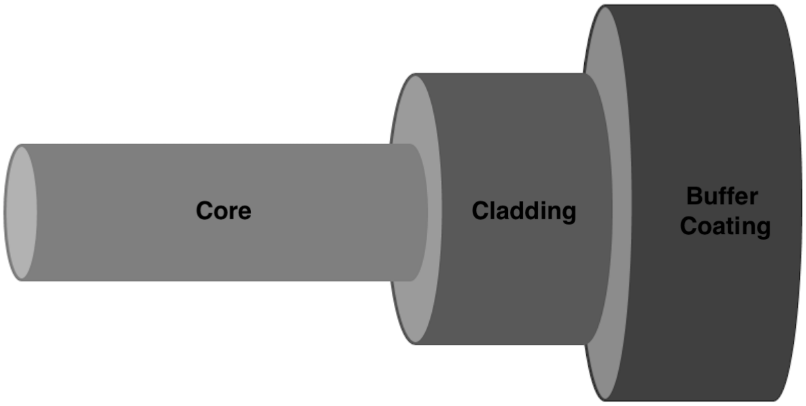

Figure 1.5: Cross section of a typical fiber-optic cable

the full strain state of the host structure [34]. Fourth, FBG sensors need ingress/egress points when embedded into the host structure [36]. Last but not least, FBG sensor require rather expensive interrogator instrument and signal processing hardware to receive and analyze signals [23].

1.3 Popular Choices for Piezoelectric Materials and Their Limitations

1.3.1 Review of Piezoelectric Materials

A material is classified as dielectric when its dimension changes in response to an applied external electric field. A dielectric crystal lattice can be modeled as cations and anions, while the chemical bonds that connect them can be modeled as springs. Cations have positive charges and anions have negative charges. When an external electric field is present, the cations will move in the direction of the applied electric field and the anions will move in the opposite direction, which causes deformation within the material. Depending on the centrosymmetricity of this dielectric crystal, deformation may be rather small or very large [37].

All dielectric crystals can be sorted into 32 crystal symmetry classes. 11 of these classes

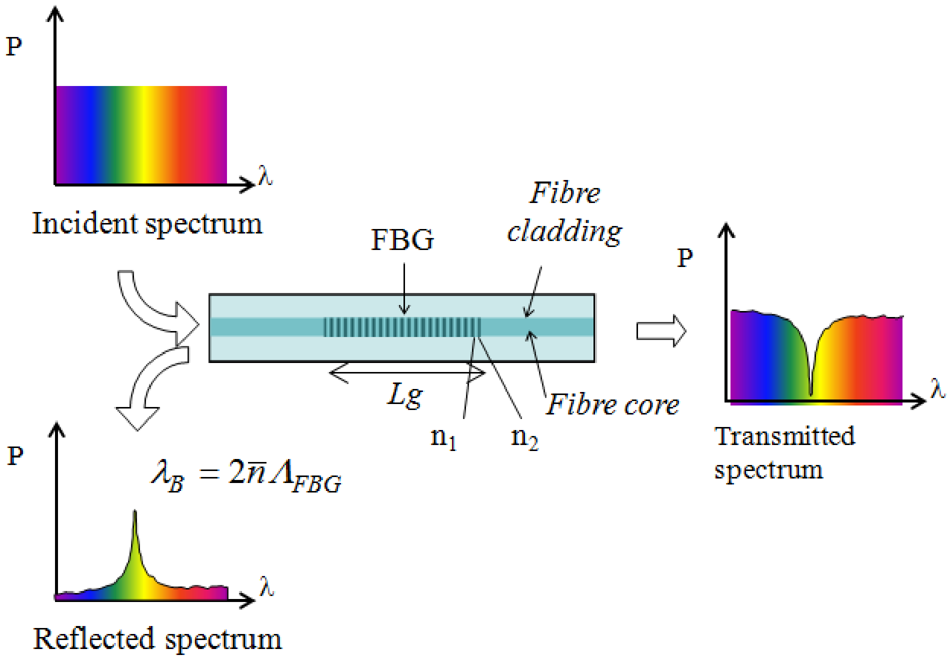

Figure 1.6: Working principle of fiber Bragg grating sensors [33]

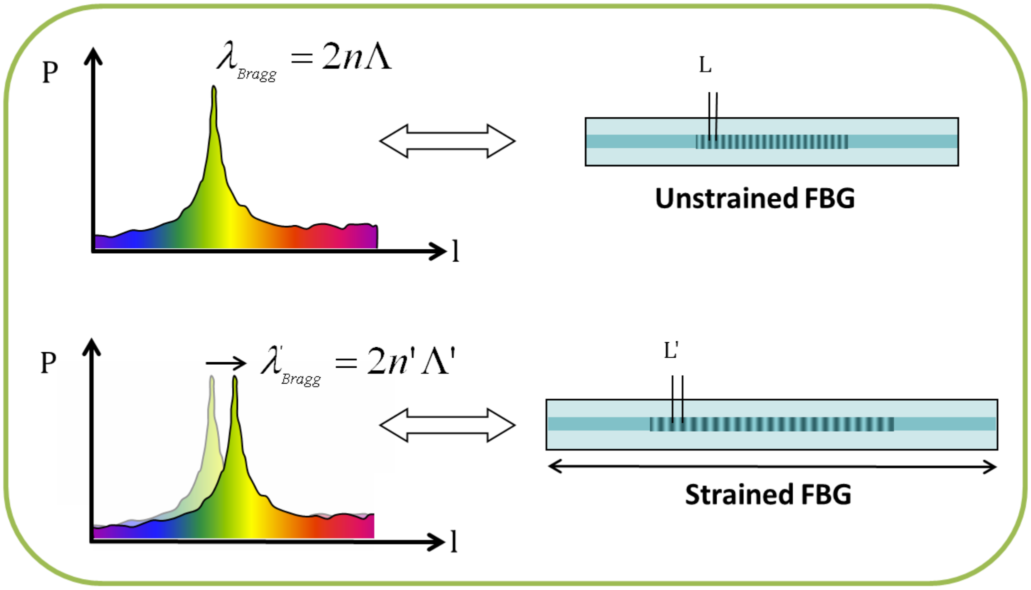

Figure 1.7: FBG sensors response as function of strain [33]

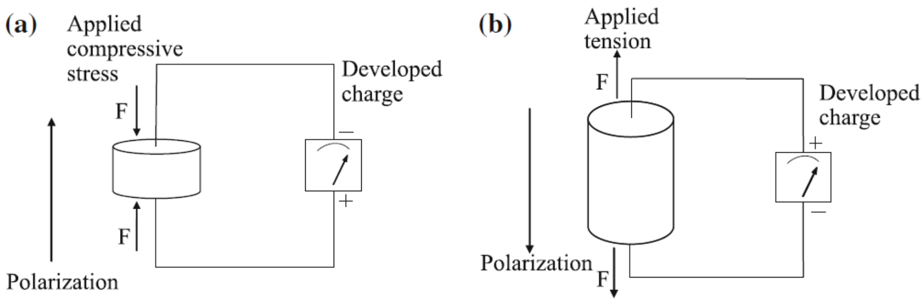

Figure 1.8: The direct piezoelectric effect: (a) in compression (b) in tension [10]

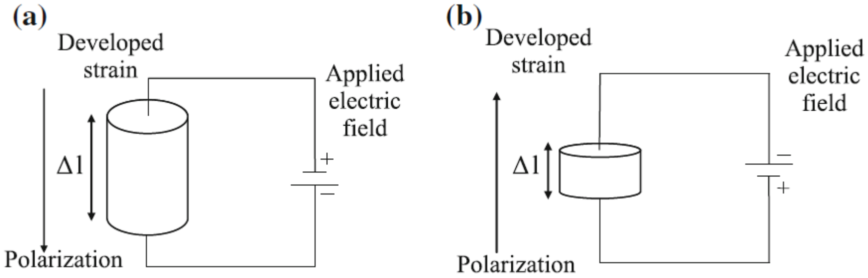

Figure 1.9: The inverse piezoelectric effect at different polarity of the electric field [10]

are centrosymmetric[1] and 21 of them are noncentrosymmetric[2]. Centrosymmetric dielectric materials are non-piezoelectric and non-centrosymmetric are piezoelectric materials. In short, piezoelectric materials are a special class within dielectric materials that lack a center of symmetry. They can create electricity when subjected to mechanical stress or generate strain by the application of an electric field [37–39].

There are three types of piezoelectric materials that are commonly used in manufacturing sensors and actuators: ceramics, polymers and composites.

---

[1] The class that contains a center of symmetry or an inversion center

[2] The class that lacks a center of symmetry or an inversion center

1.3.2 Piezoelectric Ceramics

Piezoelectric ceramics are an important group of piezoelectric materials. Examples are quartz, barium titanate, and lead zirconate titanate (PZT). They are popular because they are inexpensive and available in many shapes, such as discs, cylinders, plates and thin films.

1.3.2.1 Lead Zirconate Titanate (PZT)

Lead zirconate titanate is one of the best-known piezoelectric materials for sensor and actuator applications. It has significantly superior piezoelectric, excellent dielectric and mechanical properties. Lead zirconate titanate ceramic was discovered in the 1950s and is a solid solution of two oxides: lead zirconate oxide ($PbZrO_3$) and lead titanate oxide ($PbTiO_3$). The chemical formula is $Pb(Zr_x, Ti_{1-x})O_3$, with x ranging from 0 to 1. The PZT phase diagram is shown in Fig. 1.11. Its crystal structure depends on the temperature and the composition (mole ratio of zirconium to titanium in PZT).

PZT has a perovskite crystal structure (tetragonal/rhombohedral) and its unit cell is provided in Fig. 1.10. The lead atoms are situated at the corners ($8 \times \frac{1}{8} = 1$ atom per unit cell), oxygen atoms at the face centers ($6 \times \frac{1}{2} = 3$ atom per unit cell) and titanium or zirconium atoms at the body center (1 atom per unit cell). atom/unit cell

At temperatures above the Curie temperature (T_C), which is around 350 °C, PZT exhibits a simple cubic crystal structure with positive charges completely counteracting negative charges. In this case, the structure is centrosymmetric and the net dipole moment is zero. At temperatures below the Curie temperature (T_C), the crystal structure becomes tetragonal or rhombohedral, so the positive and negative charge sites do not coincide anymore. As shown in Fig. 1.11, the crystal structure of this solid solution is determined by the mole percent of $PbZrO_3$. In this case, there is a net dipole moment present in the material. This dipole moment can be reversed or switched to other orientations according to the direction of an applied electric field.

The process of developing a net polarization in piezoelectric ceramics is called “poling

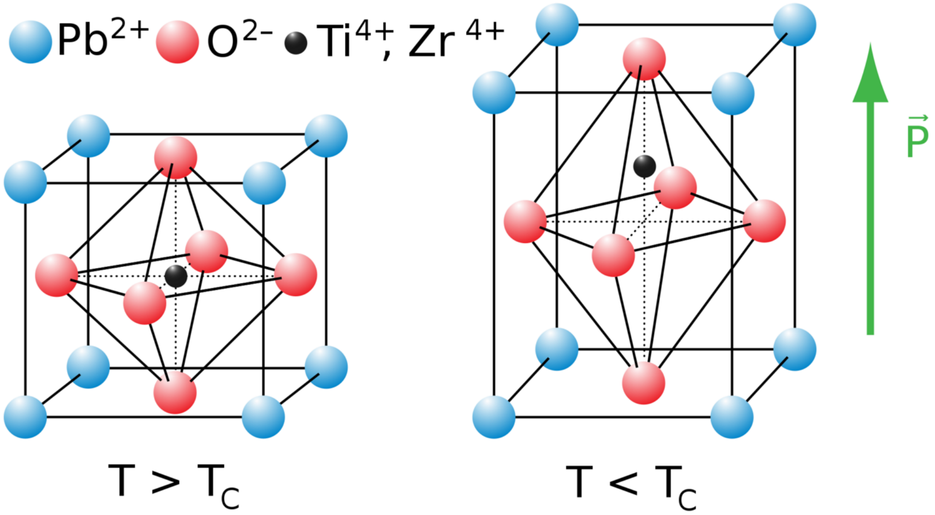

Figure 1.10: PZT unit cell [40]

treatment", and is usually done by applying a strong electric field to the material. Before poling, the random distribution of the dipole moments suppresses any piezoelectric effects as shown in Fig. 1.12 (a). Upon poling, all the dipole moments will align with the external electric field, and the material will be extended in the poling direction, see Fig. 1.12 (b). Even when the electric field is removed, the dipole moments will remain in the vicinity of the previous alignments, resulting in a remanent polarization (Fig. 1.12 (c)). This material will also have a permanent deformation along the poling direction, which makes it *anisotropic*, more specifically *transversely anisotropic*.

One commonly studied chemical composition for PZT is $Pb(Zr_{0.52}, Ti_{0.48})O_3$, which has 52% $PbZrO_3$ and 48% $PbTiO_3$. This particular composition lies near the *morphotropic phase boundary* (MPB) indicated in the phase diagram Fig. 1.11. $Pb(Zr_{0.52}, Ti_{0.48})O_3$ is considered to possess two coexisting phases: tetragonal and rhombohedral. This allows 14 possible polarization directions in the material. All of piezoelectric coefficients (d_{33}, d_{15} and d_{31}) peak at this composition, as shown in the dependence of piezoelectric coefficients on composition (in mole % of $PbZrO_3$) near MPB (Fig. 1.13) [38]. Figure 1.14 in another

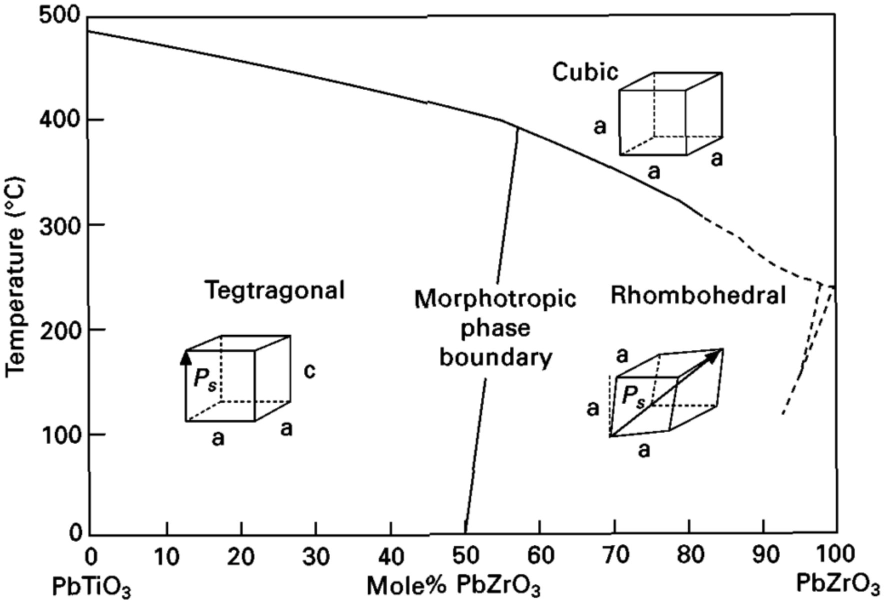

Figure 1.11: PZT phase diagram [38]

study [41] indicates that both the piezoelectric coefficient d_{33} and the dielectric constant of PZT reach their maximum at 52% of $PbZrO_3$ - 48% $PbTiO_3$ composition (mole % basis). As a result, most of the commercially available PZT ceramics have compositions close to $Pb(Zr_{0.52}, Ti_{0.48})O_3$.

The double subscripts of the piezoelectric coefficients (d_{33}, etc.) gives the directions of electrical and mechanical quantities. Subscripts 1, 2, and 3 represent X, Y, and Z of the three axes in a Cartesian coordinates system as shown in Fig. 1.15.

Doping various elements in PZT ceramics will have a dramatic effect on their properties. "*Soft*" PZTs, such as PZT-5H are doped with ions like Nb^{5+} or Ta^{5+} (also referred to as *donors*). Meanwhile, "*Hard*" PZTs, such as PZT-8, are doped with ions like Fe^{3+} or Sc^{3+} (also referred to as *acceptors*). The properties of some commercially available PZTs, such as soft PZT-5H, semi-hard PZT-4, and hard PZT-8, are presented in Tab. 1.1 [38].

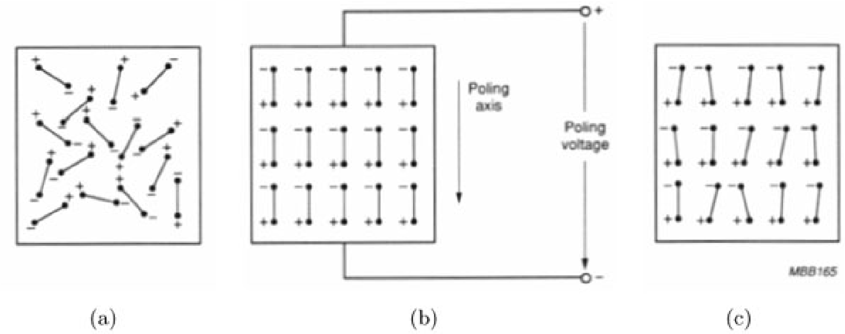

Figure 1.12: Electric dipole moments in Weiss domains (a) before poling (b) during poling (c) after poling [42]

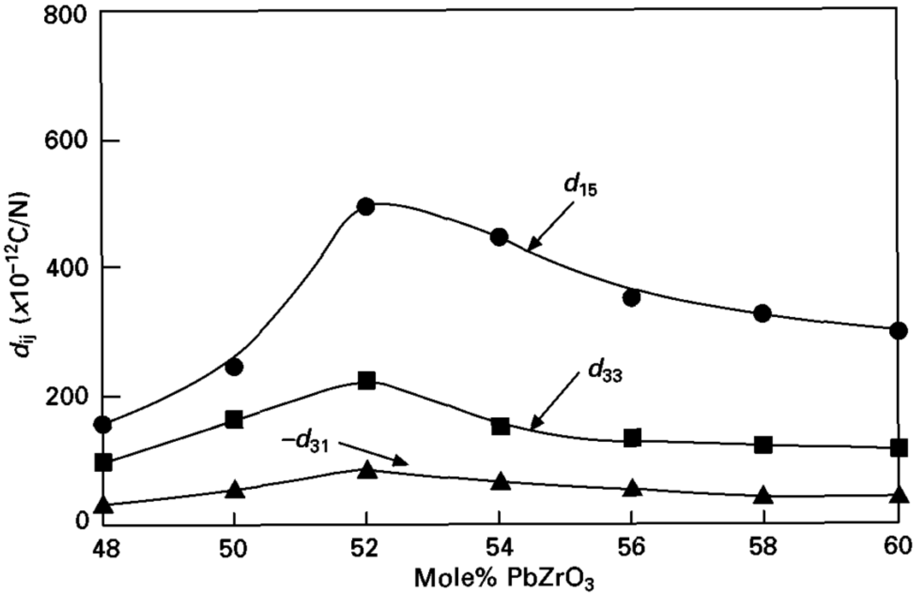

Figure 1.13: PZT piezoelectric constants as a function of composition near the morphotropic phase boundary (MPB) [38]

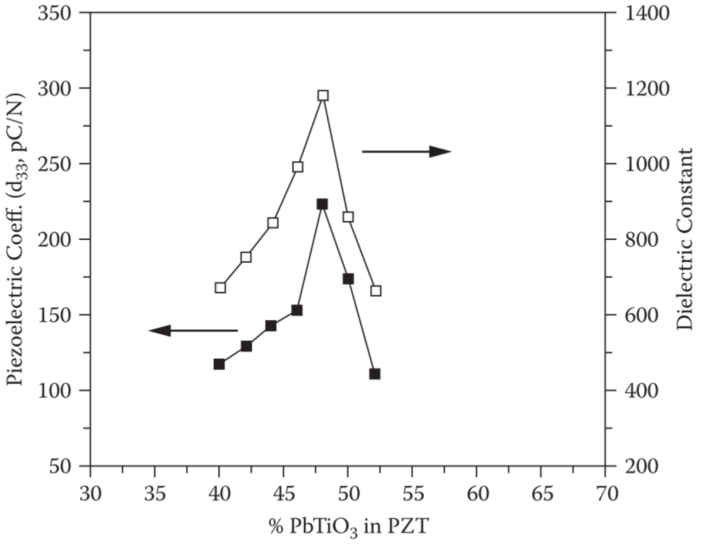

Figure 1.14: Composition dependence of piezoelectric coefficient d_{33} and dielectric constant [41]

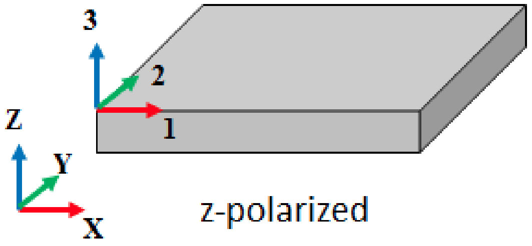

Figure 1.15: Reference axes [43]

Table 1.1: Piezoelectric, dielectric and mechanical properties of some typical PZTs [38]

	Soft **PZT-5H**	**Semi-hard** **PZT-4**	**Hard** **PZT-8**
Piezoelectric coefficient $(10^{-12}\, m/V\, or\, pC/N)$			
d_{31}	-274	-122	-97
d_{33}	593	285	225
d_{15}	741	495	330
Relative Permittivity			
ε_{33}^{T}	3400	1300	1000
ε_{11}^{T}	3130	1475	1290
Dielectric loss $(tan\delta)$ (%)	2.00	0.40	0.40
Elastic compliance $(10^{-12}m^2/N)$			
s_{11}^{E}	16.40	12.20	11.50
s_{12}^{E}	-4.70	-4.10	-3.70
s_{13}^{E}	-7.20	-5.30	-4.80
s_{33}^{E}	20.80	15.20	13.50
s_{44}^{E}	43.50	38.50	32.30
Density $\rho\, (10^3 kg/mm^3)$	7.5	7.5	7.6
Curie temperature (°C)	193	325	300

1.3.3 Piezoelectric Polymers

Piezoelectric polymers generally have much lower piezoelectric properties compared to piezoelectric ceramics, such as PZTs. However, they have certain advantages over bulk PZTs that make them attractive for piezoelectric sensor applications. First, they are flexible, lightweight, and can be easily formed into different curvatures. Second, they can be manufactured at much lower temperatures than bulk PZTs. Last but not least is their low acoustic impedance, for it matches well with water and human tissue. This has proven extremely useful for medical applications.

1.3.3.1 Polyvinylidene Fluoride (PVDF)

Poly(vinylidene fluoride) is among the most widely researched and used piezoelectric polymers because it demonstrates excellent piezoelectric properties amongst other polymers and has a variety of applications. Its piezoelectricity was first discovered in 1969 by Kawai [44] after following two treatments.

1. At temperatures of 100 - 150 °C, stretch PVDF film to several times its original length.
2. Polarize the film by applying an electric field of about 300 kV/cm along the thickness direction. Meanwhile ramp the temperature from 25 °C to 90 °C and cool down slowly.

PVDF films are now commercially available in thicknesses from 9 to 50 μm. Their density is 1.78 g/cm^3, dielectric constant is 12 at 1 kHz, piezoelectric coefficient d_{33} is around 16-30 pC/N (about 7% of that of PZT) [45]. PVDF has a low elastic modulus of 2-4 GPa that is poorly suited for actuator applications, but favorable for sensors such as pressure and shock wave sensors.

The chemical formula for PVDF is $[CH_2 - CF_2]_n$, as shown in Fig. 1.16. PVDF polymers generally exist in three different phases: α, β and γ, depending on the fabrication conditions. α phase is non-polar, as shown in Fig. 1.17 (a), and β and γ phases are polar. The α phase is formed from the melt when temperatures exceed 167 °C, and is considered to be the most

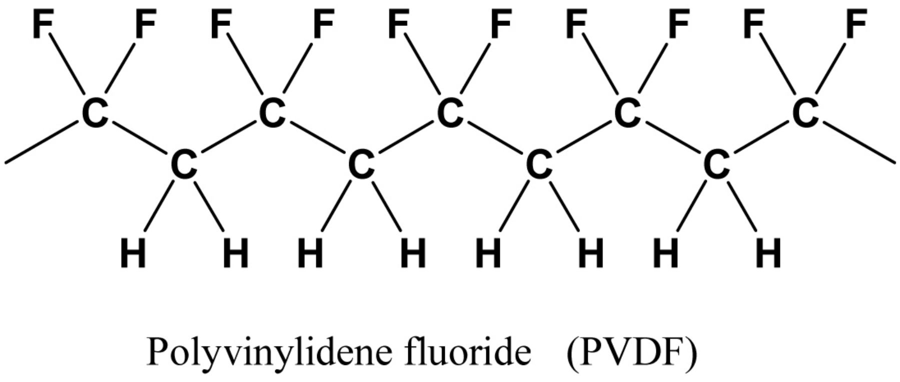

Figure 1.16: Poly(vinylidene fluoride) chemical formula (β phase)

chemically stable phase of PVDF. The fluorine atoms with negative charges are coupled with the hydrogen atoms with positive charges and since they appear on both side of the polymer chain, no net dipole moments result in this phase. The fluorine and hydrogen atoms in β phase, one the other hand, are aligned in a highly polar manner with positive charges on one side of the polymer chain and negative charges on the other as shown in Fig. 1.17 (b), which make this phase produce a lot of net dipole moments [37, 46].

The β phase of polyvinylidene fluoride is used for piezoelectric applications, because it is the most responsive phase of all. However, production of piezoelectric β phase PVDF is challenging. There are two methods of producing the piezoelectric β phase, both of which involve mechanical stretching the α phase until transition occurs. The first method is formed from the melt. After melting, PVDF polymer film is quenched to 80 °C, and then stretched to 3-5 times its original length, or at least 300% strain to transform into the highly polar β phase. The second method is fabrication from solution. PVDF can be synthesized from solvents like dimethyl formamide or dimethyl acetamide. PVDF polymer is then poled under a rather high electric field on the order of 200kV/cm in the stretched state [37, 46].

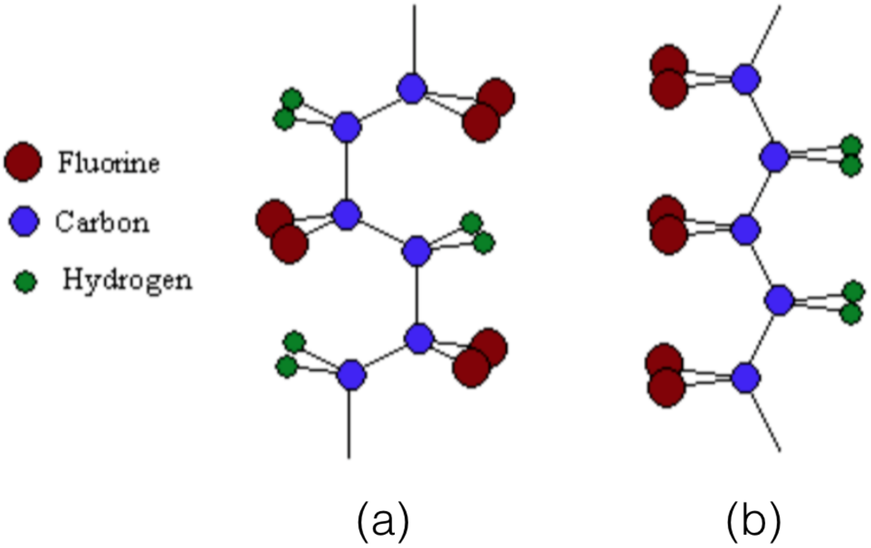

Figure 1.17: Molecular and crystal structures of PVDF (a) α phase (b) β phase [46]

1.3.4 Limitations of the Popular Choices in Piezoelectric Materials

Bulk ceramic PZTs are heavily used to manufacture piezoelectric sensors and actuators because they are inexpensive and demonstrate excellent piezoelectric performance. One common practice is to embed PZT sensors and actuators into the structures of interest. This idea has been proved extensively in labs, for example, through use of bulk PZTs on simple structures (e.g., beams and plates) [47, 48]. Extension of this concept to real aircraft structures, however, proves to be extremely difficult for the following reasons.

1. Bulk PZT is brittle and difficult to machine. Hence, it is difficult and expensive to incorporate bulk PZT in aircraft structures that have complex surface topology and geometry.

2. Bulk PZT cannot be fabricated directly onto composite aircraft structures because PZT requires high temperatures (e.g., 650 °C) to crystallize. Such high processing

temperature would damage the composite structure hosting the PZT, because the curing temperature of most composite host structure is approximately 130 °C-150 °C.

3. Embedded PZT requires electrodes, wiring, interconnects, and packaging to form a working unit. These components are not only difficult to integrate into aircraft manufacturing processes, but also very expensive to maintain in subsequent aircraft operations.

Piezoelectric polymers like PVDF can overcome the material limitation of bulk PZT. Due to their flexibility, they can be incorporated into curved surfaces. However, PVDF has its restrictions too. First, untreated PVDF (α phase) needs special mechanical stretching and high electric field poling processes for transformation into the piezoelectric β phase. Additionally, PVDF has a thermal limitation in that its maximum functional temperature is 90 °C [49]. PVDF's piezoelectric β phase is not stable above 80 °C. This is because the β phase will anneal[3] to the non-piezoelectric α phase at temperature above 80 °C [46].

1.4 A New Promising Piezoelectric Material

1.4.1 Composite Piezoelectric Materials

In order to overcome the limitations of both piezoelectric ceramics (e.g., bulk PZT) and polymers (e.g.,PVDF) in Section 1.3.4, a new type of piezoelectric materials is developed by combining ceramic PZT with a polymer matrix. This type of material is called "composite piezoelectric material", and has been found to possess several improved features. Table 1.2 reports the strengths and weaknesses of piezoelectric ceramic, polymer and composites, where (+) means a favorable property and (−) means an unfavorable property.

PZT ceramics have excellent electromechanical coupling factors and high dielectric constants (around 1000-3500 for bulk PZTs). They are cheaper and easier to fabricate than piezoelectric polymers, yet brittle and cannot be formed onto curved or complex surfaces. In

---

[3] Heat and allow to cool slowly

Table 1.2: Comparison of properties pertinent to transducer applications of piezoelectric ceramic, polymer and composites, where (+) means a favorable property and (−) means an unfavorable property [50, 51]

Parameter	**Ceramic**	**Polymer**	**Composite**
Acoustic impedance	High (−)	Low (+)	Low (+)
Coupling factor	High (+)	Low (−)	High (+)
Dielectric constant	High (+)	Low (−)	Medium (+)
Flexibility	Stiff (−)	Flexible (+)	Flexible (+)
Cost	Cheap (+)	Expensive (−)	Medium (+)

addition, due to their high acoustic impedance, PZT ceramics have a poor acoustic match to water. Piezoelectric polymers, on the other hand, are very flexible and have a good acoustic match to water. However, their electromechanical coupling factors and dielectric constants (around 12 for PVDF) are very low and they are rather expensive to fabricate. Piezoelectric ceramic-polymer composites combine the favorable properties of ceramic and polymer as shown in Tab. 1.2. They have low acoustic impedance, moderate electromechanical coupling factors and dielectric constants, high flexibility to accommodate complex geometry and moderate cost of fabrication [50, 51].

Composite piezoelectric materials are promising because they can be tailored to specific design requirements. In certain applications such as sensors in aircraft structures, materials with low processing temperatures that conform to complex geometry are required. To meet these new challenges, composite piezoelectric materials were chosen for this study.

1.4.2 PZT Nanoparticle-Silane Ink

The proposed technology in this study is printed PZT ink on composite aircraft structures with curing temperatures around or below 120 °C (in order to protect the host structure[4]). The required electrodes, wiring, interconnects and packaging are integrated using 3-D printing [52]. The use of 3-D printing has many advantages. First, it will accommodate complex surface topology and geometry, such as in aircraft structures. Second, it can print all elements layer by layer, including PZT films, electrodes, interconnects, wiring, and packaging. This will significantly simplify the manufacturing processes. Third, the thickness of the resulting PZT films can be controlled to be as thin as 10 μm or even less. They are not only lightweight, but also very easy to pole with low voltage. To enable this new technology, a major challenge is the development of PZT ink that is 3-D printable (i.e., jettable) and can be cured at a low temperature.

PZT ink and PZT printing techniques have been available for many years [53–56]. However, the printed PZT ink needs to be crystallized and sintered at a high temperature (e.g., 650 °C to 1250 °C [55, 57, 58]). In order for the PZT ink to have a low curing temperature (i.e., less than 120 °C), the PZT component in the ink must be prefabricated. The residual component of the PZT ink could be a polymer-based solvent that has a low curing temperature. When such PZT ink is deposited and cured, it will form a piezoelectric thin film with numerous prefabricated PZT particles embedded in a polymeric matrix(see Fig. 1.18). For sensor applications, the thin film could employ a soft matrix material, such as silane. For actuator applications, it is more preferable to have a stiffer matrix material, such as silica.

Study of PZT ink with prefabricated PZT particles and a low curing temperature is still at its infant stage. For example, Hale and Tuck [59] fabricated a dynamic strain sensor using a suspension of milled PZT ceramics with particle sizes ranging from 1-2 μm in a colorless painting lacquer. The resulting PZT paint was sprayed or brushed on the substrate, cured at room temperature, poled at 600V for an hour and tested for dynamic properties. Later,

---

[4] The curing temperature of 120 °C is low enough that it will not damage the composite host structure.

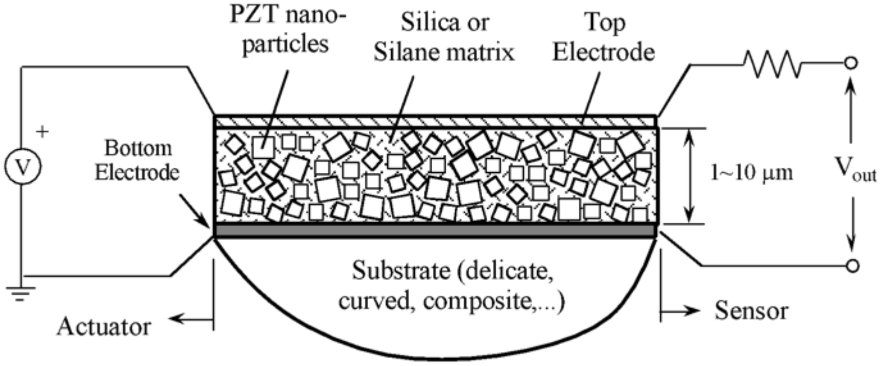

Figure 1.18: PZT-silane nano-composite thin film

Hale et al. improved this design with a water-based paint containing 70 wt% of PZT powder [60]. The film thickness was 50 - 100 μm and the piezoelectric sensitivity d_{33} was estimated between 10 to 30 pC/N. Egusa and Iwasawa developed an epoxy-based PZT paint using PZT powder that is commercially available [61] . The curing temperature of their film can be between room temperature and 150 °C. The film thickness ranges from 25 μm to 300 μm. The resulting PZT-epoxy films were tested as sensors and actuators, respectively. Zhang demonstrated dynamic strain sensing capability of PZT paint for measuring unidirectional strain [62]. The paint used commercial PZT powder, embedded into a liquid epoxy resin and was cured at room temperature for two days. The paint film thickness was 170 μm and was poled at 80 °C. The feasibility of using this PZT paint sensor for acoustic emission-based sensing was also demonstrated [63]. The wet paint was cured at room temperature for three days with a thickness of 740 μm for this application. Similarly, Hsueh and Wu developed a silica-based PZT ink using crushed PZT particles that are commercially available [64]. The curing temperature of the fabricated PZT nano-composite films was 150 °C and thickness of the film was 7 μm. Also, the PZT-silica film was deposited on polyimide with electrodes to demonstrate its feasibility as an actuator.

The PZT ink formulas summarized above all employ PZT particles that are commercially available by milling and crushing bulk PZT. Therefore, these PZT particles possess a wide range of size distribution and a fairly high level of aggregation, from hundreds of nanometers to tenths of microns [65]. The large size of PZT particles creates many problems for 3-D printing.

- First, PZT particles could clog nozzles or print heads due to their large particle size. The rule of thumb is that the particles should not be larger than 1/50 of the nozzle diameter [66]. For instance, if the nozzle diameter is 0.5 mm, then the allowable size of PZT is 10 μm. A larger nozzle diameter, of course, means a lower precision and resolution of the printed films.

- Second, the PZT particles in the ink precipitate easily due to their large size because the precipitation rate is proportional to the particle size [55]. When the PZT ink is pumped from its reservoir to the print heads via a feed catheter, these PZT particles could precipitate and clog the catheter. Therefore, the resulting PZT ink often has a low solid content of PZT particles (e.g., 10 wt%) in order to maintain its stability.

- Third, the PZT ink needs to have high viscosity to avoid precipitation because of the large particle size. For example, PZT ink formulas in [61–63] employ epoxy, which has a much higher viscosity than organic solvents, such as ethanol. The jettability then becomes very poor, since it is inversely proportional to the viscosity [66]. Moreover, high viscosity limits applications of the PZT ink greatly. This is especially true when a thinner film is desired (e.g., 3 μ m).

There are generally two ways to address the problems stated above. One is to filter out PZT particles that are larger than 10 μm through sieves. There are, however, two major challenges to this approach. The first one is a practical difficulty encountered in the filtration processes. The large amount of aggregates in the crushed PZT particles could easily block the apertures and clog the sieves. Another challenge is the significant material loss associated with sieving. Even if the clogging issue is resolved, the large amount of aggregates could mean a material loss of more than 50% by volume. It is entirely possible that future developments in membrane technologies, centrifugal separation methods, or filtration processes may completely solve these challenges.

The other approach is to employ PZT particles in the nanoscale in lieu of the crushed PZT particles. As an example, we have developed a hydrothermal process to fabricate PZT nanoparticles [67]. Compared to crushed PZT particles, this alternative approach produces a narrower size distribution, good morphology, adequate crystallinity, and low degree of agglomeration. Therefore, the technology of dispersing PZT nanoparticles produced by hydrothermal synthesis into silane ink was adopted in this research.

There are two unique features in this technology. The first unique feature is use of PZT nanoparticles in the ink. The PZT nanoparticles are fabricated via an expedited hydrothermal process (EHP) with fast ramping and cooling [67]. As a result, the size distribution of the PZT nanoparticles is in the range of 300 nm to 800 nm as shown in Fig. 1.19. The small particle size allows us to use a low-viscosity solvent, such as ethanol, thus making the ink considerably more 3-D printable. The small particle size also significantly reduces precipitation. The PZT ink remains relatively stable without immediate and severe precipitation, even when the PZT nanoparticle solid content reaches 20 wt% of the PZT ink. Field uses of this PZT ink in 3-D printing facilities exhibit no clogging of print heads and feed catheters. The 3-D printed PZT film is shown in Fig. 1.20.

The second unique feature is low curing temperature. Often, lowered curing temperature will more or less jeopardize the reliability of fabricated films. Also, a lower curing temperature often accompanies long curing time (e.g., 150 °C for 45 minutes verses room temperature for 3 days [62]). To solve this dilemma, a silane binder that is UV-sensitive is selected in making the ink to enhance the curing quality with UV light. Thereby, curing of the PZT ink does not rely on temperature and heat entirely. With a UV-sensitive binder, the curing temperature can be lowered to 120 °C or less without prolonged curing time while maintaining excellent film quality.

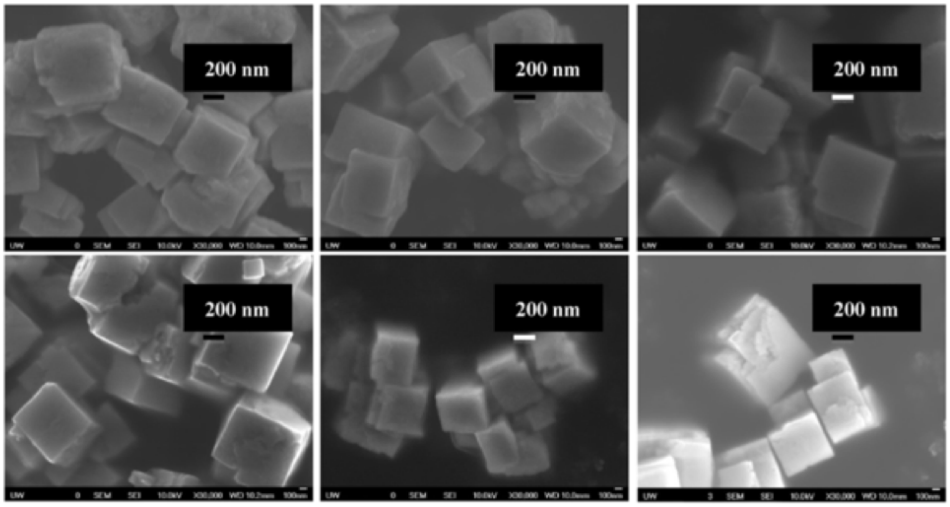

Figure 1.19: SEM image of PZT nanoparticles from EHP [67]

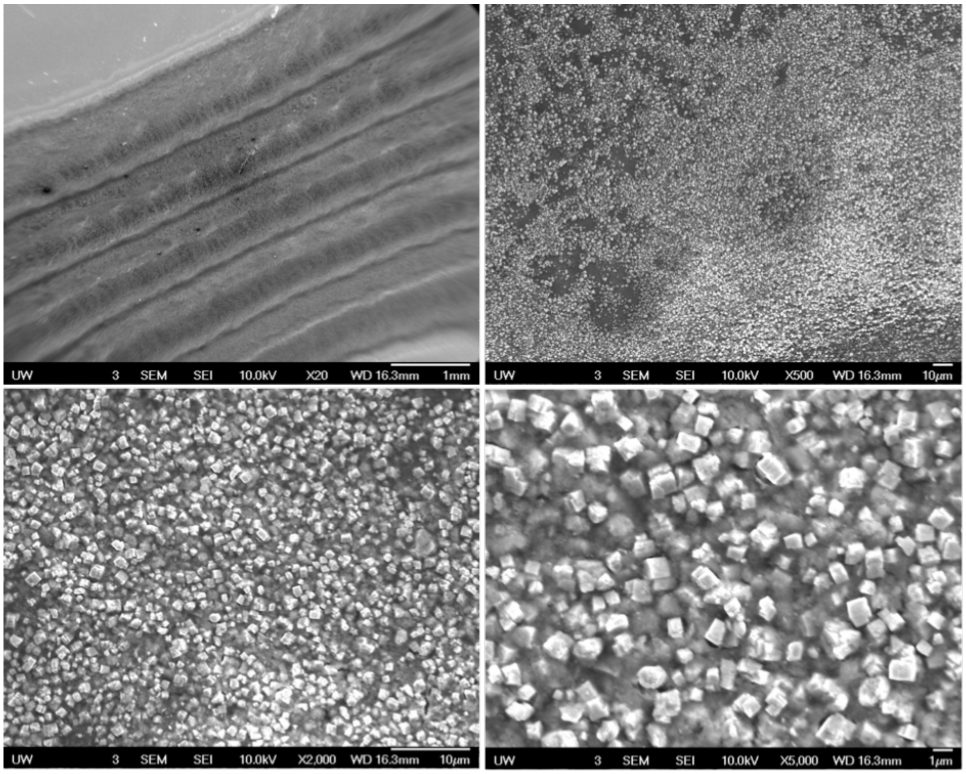

Figure 1.20: 3-D printed PZT film

1.5 Research Goal and Objectives

The goal of this research is to develop novel PZT-silane thin film sensors and actuators that are extremely lightweight and thin with 5-10 μm in thickness. Their whole manufacturing process, including electrodes, wiring and packaging, can be integrated via printing. In addition, the proposed thin film sensors and actuators can accommodate any complex or flexible surfaces, preserve the surface's structural integrity and can be printed and cured directly on the host structure without imposing any physical damage due to the manufacturing procedures. To achieve this goal, several milestones needed to be achieved. Thus, the objectives for this research are defined as follows:

1. To fabricate PZT nanoparticles, PZT-silane ink and thin films based on the proposed technology presented in Section 1.4.2.

2. To characterize the material properties of the fabricated PZT nanoparticles and PZT-silane thin films through X-Ray Diffraction (XRD) analysis and Scanning Electron Microscopy (SEM).

3. To measure the dielectric properties of the deposited PZT thin films through complex impedance analysis.

4. To design the test setup and perform experiments for characterization of the fabricated PZT-silane thin films and their piezoelectric performance.

5. To estimate the piezoelectric coefficient of the fabricated PZT-silane thin films by mean of finite element simulation of the experimental setup.

6. To demonstrate the applications of PZT-silane thin films with parallel-plate electrodes as an actuator and an accurate vibration sensor.

7. To transition the manufacturing platform from a rigid substrate to a flexible substrate with additive manufacturing capability and print interdigitated electrodes on PET/Kapton films.

8. To demonstrate PZT-silane thin films with interdigitated electrodes as an actuator, vibration and strain sensors on wing structures with small angle oscillations.

9. To demonstrate PZT-silane thin film strain sensors with printed interdigitated electrodes can distinguish strain directions in theory, finite element simulation and experimentation.

Chapter 2

FABRICATION AND MATERIAL CHARACTERIZATION OF PZT NANOPARTICLES AND PZT-SILANE THIN FILMS

This chapter describes the fabrication and material characterization aspects in the research, including fabricating PZT nanoparticles, PZT-silane ink and thin films based on the new technology proposed in Section 1.4.2. In the material characterization section, these hydrothermally grown PZT nanoparticles, ink and thin films were analyzed and compared with the commercially available crushed particles, ink and thin films through X-ray diffraction (XRD) analysis and scanning electron microscope (SEM).

2.1 Fabrication

2.1.1 Fabrication of PZT Nanoparticles

PZT nanoparticles used in this work for preparing the ink are obtained by 'expedited hydrothermal process' (EHP), as previously reported [67]. The main fabrication parameters adopted are as follows: (a) the furnace temperature is maintained at 200°C (no ramping) for two-hour hydrothermal growth of PZT nanoparticles; (b) 2.5 M KOH mineralizer and 50 wt.% excess lead are added during feedstock preparation; (c) the autoclave, which contains PZT nanoparticles, is cooled down naturally at room temperature after the hydrothermal growth. Full recipe for this process is documented in Appendix A.

2.1.2 Fabrication of PZT-Silane Ink

PZT-silane ink is prepared using the recipe developed by Hsien-Lin Huang, a former graduate student in Professor Shen's lab at University of Washington. The full recipe is shown in the list below.

1. 0.1 M Polyethylene Glycol (PEG) is added to PZT fine powder at a 1:2 ratio by weight inside a glass vial. The compound is then stirred with a stir bar at room temperature for at least 30 minutes.

2. (Optional) Lubricating additive (e.g., Ethylene Glycol or Thioglycolic acid) is added and the compound is stirred for 20 minutes. The amount of additive can be up to 10 wt.% of the PZT powder used in Step 1.

3. MPTS[1] (i.e., 3-Methacryloxypropyl-tirmethoxysilane) is used as a polymer binder in making PZT-silane ink. It is prepared by stirring a mixture of 3-(Trimethoxysilyl)propyl Methacrylate and 0.1 M HCl at the weight ratio of 100:11 at room temperature for 24 hours. Binder MPTS is then added in the amount of 5 wt.% with respect to the PZT powder in the compound.

4. PZT-silane ink uses ethanol as solvent. The final PZT colloid can have two different PZT solid contents, 10 or 20 wt.% of PZT powder, depending on which type of PZT particles is used. For the 10 wt.% PZT ink, the amount of ethanol added is 8.45 times the weight of the prescribed amount of PZT particles and for the 20 wt.% PZT ink, the amount of ethanol added is 3.45 times the amount of PZT particles. PZT-silane ink needs to be stirred continuously until film deposition.

2.1.3 Fabrication of PZT-Silane Thin-Films

PZT-silane nano-composite thin films were manufactured in the following steps.

1. Prepare silicon wafers with layers of silicon oxide, silicon nitride, titanium, and platinum to form the substrate and bottom electrode.

---

[1] Note that MPTS is UV-sensitive, which will allow the film to be cured under UV light.

2. Drop-cast the PZT ink onto the silicon substrate to form a thin fluid layer. Cure the newly deposited layer under UV light for 5 minutes to form a PZT-silane film. Thickness of the newly deposited film may vary.

3. Repeat the drop-casting procedure in Step 2 to reach the desired film thickness. After the final layer is deposited, cure the PZT-silane film under UV light for 2.5 hours.

4. Cure the PZT-silane film in a furnace with 5°C/min ramping rate until the temperature reaches 120°C and dwell at 120°C for 12 hours.

5. Deposit a topcoat layer of MPTS onto the PZT-silane film. Cure the topcoat in a furnace using the same process parameters described in Step 4.

6. Deposit top electrode (gold on chromium) on the PZT-silane film via e-beam evaporation.

The fabrication procedure above is illustrated in Fig. 2.1. This process is highly flexible and allows for many variations. For example, the substrate in Step 1 does not have to be silicon. Silicon wafers were used here for convenience and demonstration purposes. Another type of substrate was used in Chapter 5 and has been proven to be successful. The deposition method in Step 2 can be changed to screen-printing, 3-D printing, spraying, or ink-jet printing. The curing procedure in Steps 4 and 5 depends on the binder used in the PZT ink. A lower curing temperature is certainly possible if a different binder is used. The MPTS topcoat layer in Step 5 is optional and its thickness is usually around 0.5-3 μm. The purpose for applying a topcoat is to provide additional protection from electrical short-circuiting, since the film may be porous. The chance for top electrode to short-circuit the bottom electrode could be eliminated with the protection of MPTS topcoat.

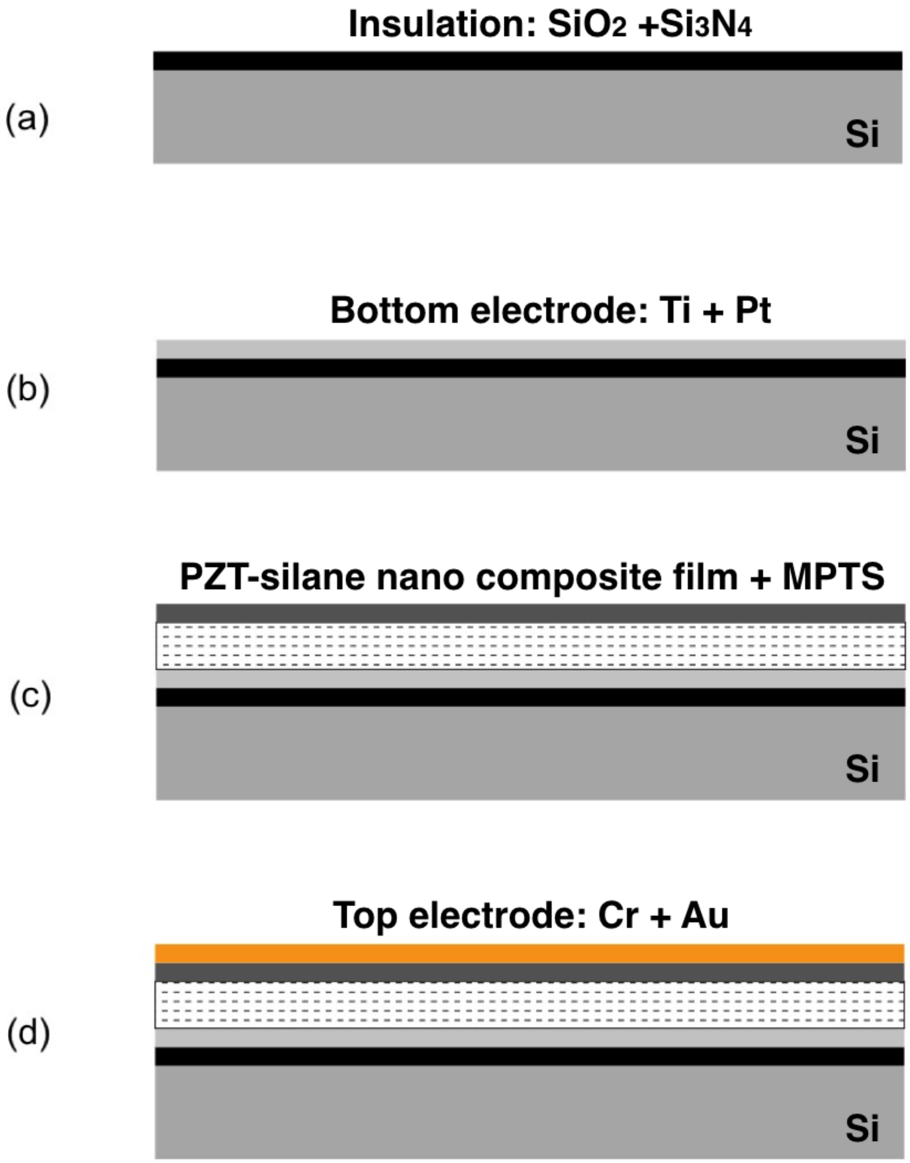

Figure 2.1: Fabrication process for PZT thin film sensor with top and bottom electrodes

2.2 Material Characterization Using XRD and SEM

2.2.1 PZT Particles

2.2.1.1 Hydrothermal Grown PZT Nanoparticles

After the hydrothermal process, the PZT powder were oven-dried and ground with mortar and pestle until turning into a fine powder. X-ray diffraction pattern of the obtained PZT powder was then measured at room temperature by X-ray diffraction (Bruker F8 Focus Powder XRD) using Cu K-alpha radiation (1.54Å) X-ray source. Figure 2.2 shows XRD pattern of one obtained powder, which is found to be consistent with the peak patterns of Lead Zirconium Titanium Oxide ($Pb(Zr_{0.52}, Ti_{0.48})O_3$) in the standards database. The XRD patterns of all hydrothermally grown PZT nanoparticles were taken and their phase compositions were verified to be PZT before dispersing them into ink. The sample variation observed from batch-to-batch for the hydrothermally grown PZT nanoparticles was insignificant according to XRD analysis, as seen in Fig. 2.3.

Microstructural characterization of PZT nanoparticles based on scanning electron microscopy (SEM) is also performed. Figure 2.4 shows SEM images of hydrothermally grown PZT nanoparticles at six different magnifications ranging from 1250x to 40,000x. The size distribution of the particles is primarily from 300 nm to 2 μm in particle size with low degree of agglomeration (about 1-3 μm in aggregate size).

2.2.1.2 Commercially Available Crushed PZT Particles

Commercially available crushed particles made by milling and crushing bulk PZT are also analyzed here as a comparison. They will be referred to as “crushed PZT particles” hereafter. X-ray diffraction analysis was performed on crushed PZT particles as well. Figure 2.5 shows the comparison of XRD patterns for hydrothermally grown PZT nanoparticles and crushed PZT particles. It is found that there are some extra phases presented in the expedited hydrothermally grown PZT, so there might be other compound or compounds other than

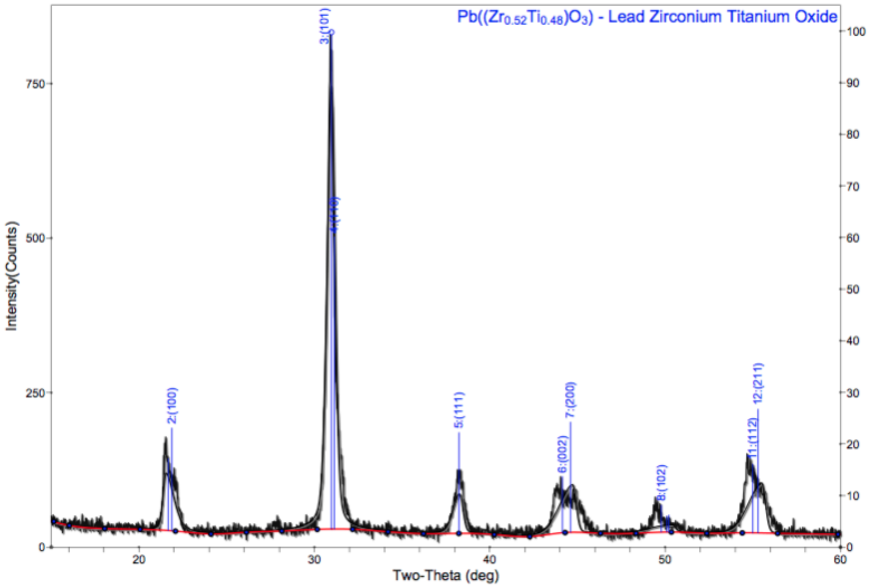

Figure 2.2: Peak identification for the obtained hydrothermally grown PZT nanoparticles

$Pb(Zr_{0.52}, Ti_{0.48})O_3$ in the obtained powder.

SEM images of crushed PZT particles in four different magnifications ranging from 500x to 40,000x are shown in Fig. 2.6. There appears to be a large amount of aggregates present in the PZT crushed particles, and most of the aggregates have spherical form with radius of 5-50 μm (see Fig. 2.6 (a) to (c)). Figure 2.6 (d) is a highly magnified SEM image on the surface of one aggregate sphere and it shows that the aggregate consists of many small irregularly shaped PZT fragments with size distribution ranging from 100 to 500 nm.

2.2.2 PZT-Silane Thin Films

Two different types of PZT particles, which are described in Section 2.2.1, are used here to make PZT-silane inks and thin films. Accordingly the two types of inks and thin films made from those particles will be referred to as "*hydrothermally grown PZT nanoparticles ink and thin film*" and "*crushed PZT particles ink and thin film*".

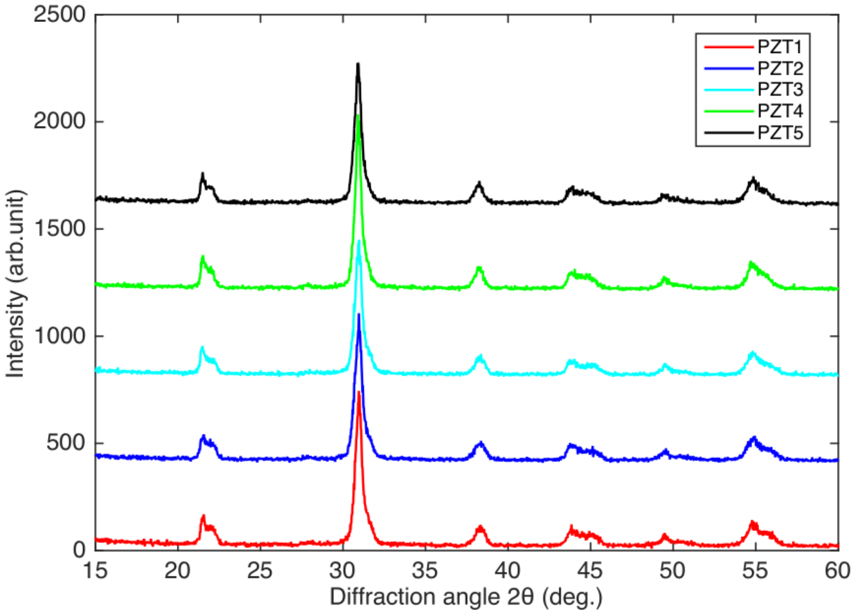

Figure 2.3: XRD patterns of various batches in the ink

Hydrothermal grown PZT nanoparticles is fabricated using the “expedited hydrothermal process” presented in Section 2.1.1. The PZT nanoparticles obtained have good morphology and crystallinity, as indicated by SEM and XRD, respectively, in Section 2.2. The resulting PZT colloid can be stable up to 20 wt.% of PZT solid content. Figure 2.7 shows the fabricated 20 wt.% PZT-silane ink made from PZT nanoparticles that are hydrothermally grown at the University of Washington. PZT-silane ink composition for hydrothermally grown PZT nanoparticles is given in Tab. 2.1.

The commercially available crushed PZT particles is made by crushing bulk PZT and the resulting PZT colloid contains 10 wt.% of PZT solid content. The dispersion is unstable, and precipitation occurs in roughly 5-10 seconds. Also, size distribution of the PZT particles is not uniform within the colloid. Larger PZT particles or particle aggregates tend to suspend near the bottom of the vial storing the PZT colloid, and in the meantime, smaller PZT particles suspend near the top or the center of the vial. Therefore, the size of PZT particles

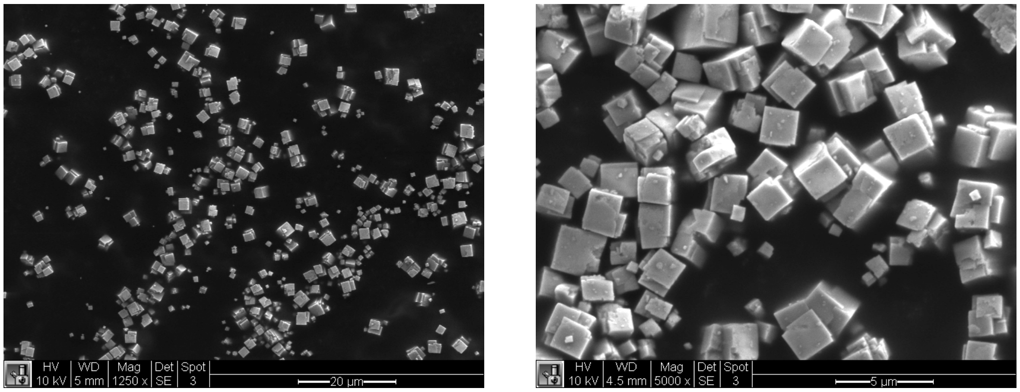

(a) Magnification: 1,250X

(b) Magnification: 5,000X

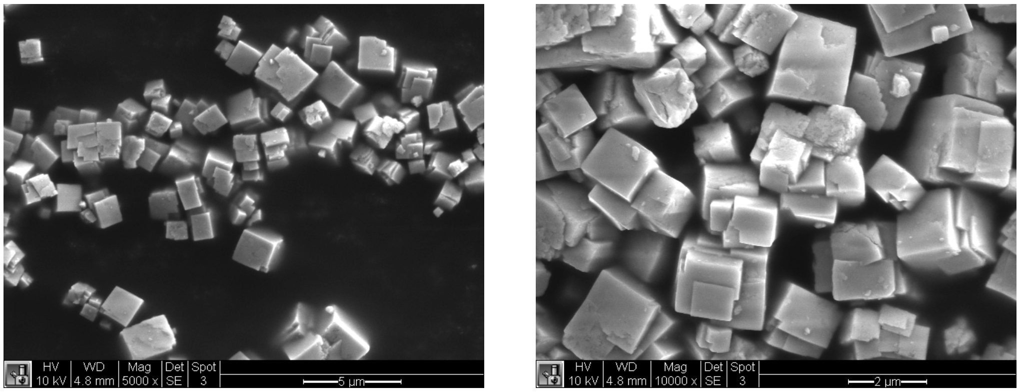

(c) Magnification: 5,000X

(d) Magnification: 10,000X

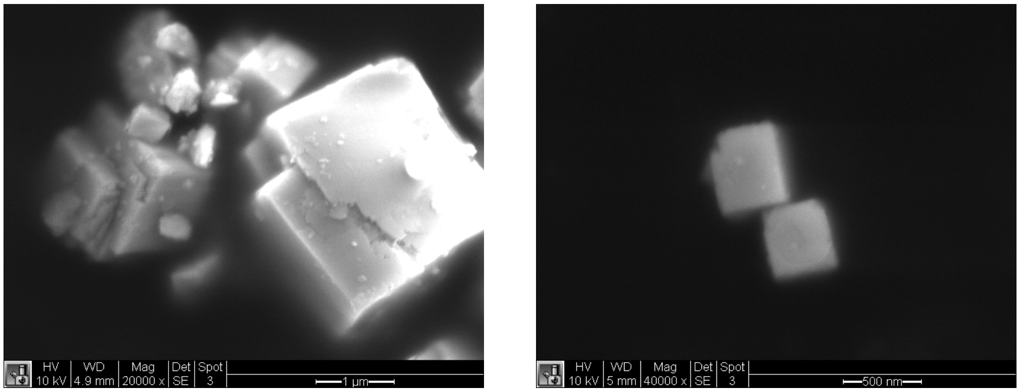

(e) Magnification: 20,000X

(f) Magnification: 40,000X

Figure 2.4: SEM of hydrothermally grown PZT nanoparticles in different magnifications

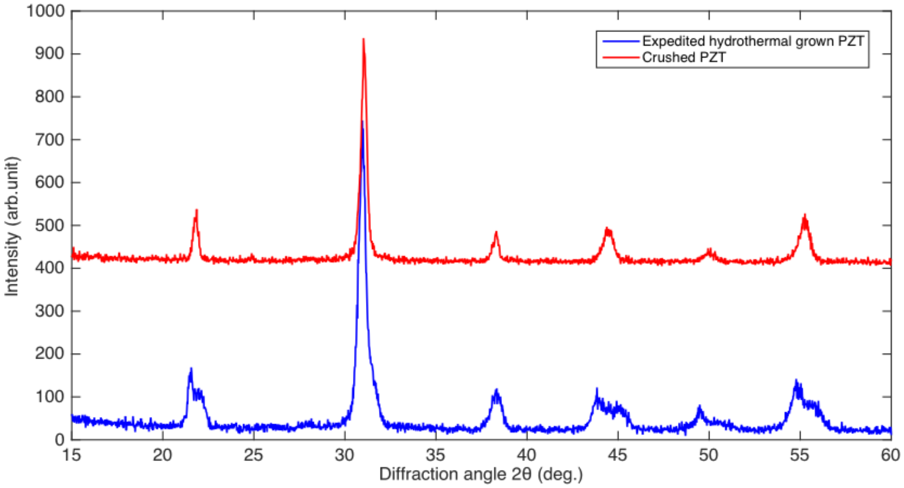

Figure 2.5: XRD patterns of (a) hydrothermally grown PZT nanoparticles and (b) crushed PZT particles

that eventually appear in the PZT-silane nano-composite thin films depends heavily on where the PZT ink is drawn from the vial. Table 2.2 shows the PZT-silane ink composition for crushed PZT particles.

Table 2.1: PZT-silane ink composition for hydrothermally grown PZT nanoparticles

Ingredient	**wt.%**
PZT nanoparticles	20
PEG 600	10
MPTS	1
Ethanol	69

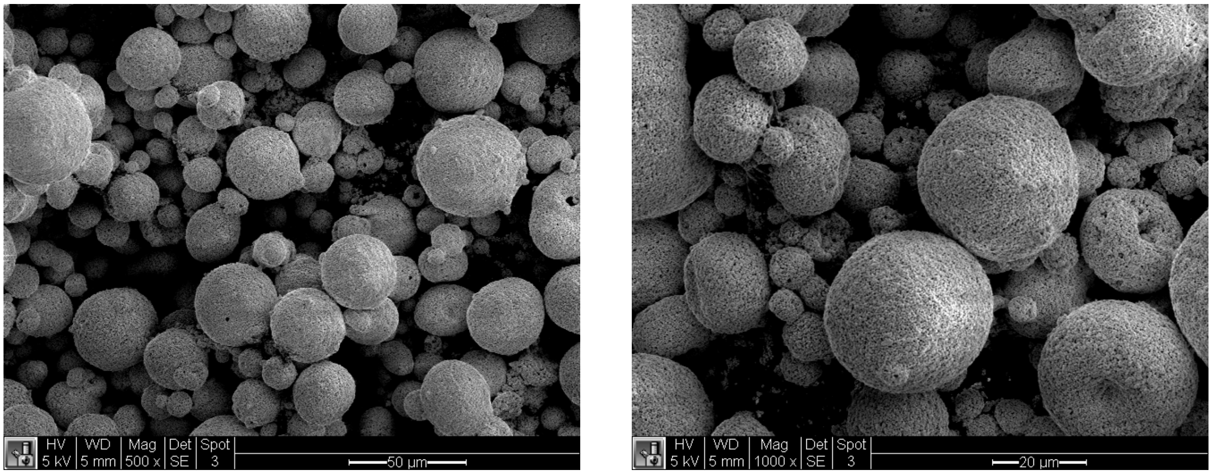

(a) Magnification: 500X (b) Magnification: 1,000X

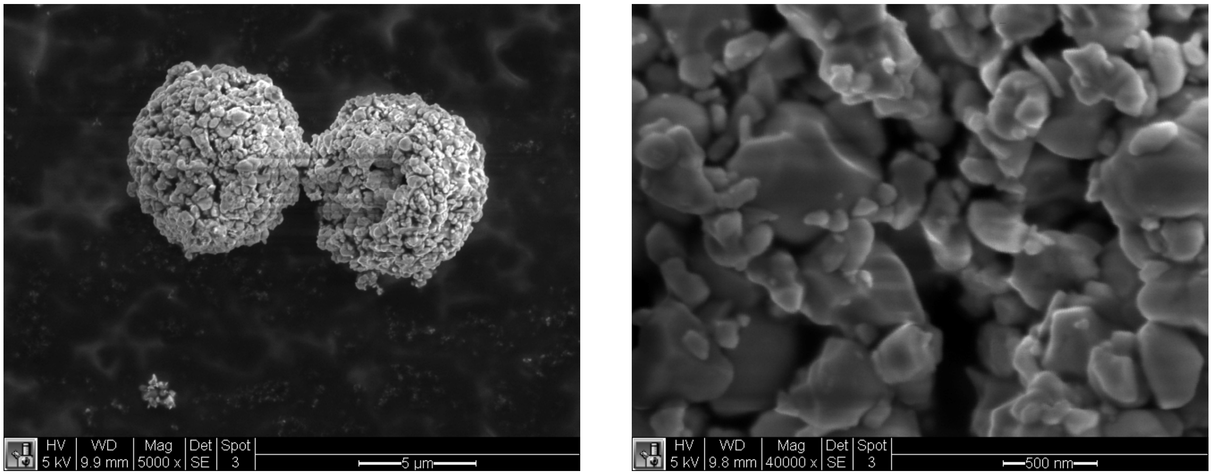

(c) Magnification: 5,000X (d) Magnification: 40,000X

Figure 2.6: Crushed PZT particles

2.2.2.1 Hydrothermal Grown PZT Nanoparticles Thin Film

Figure 2.8 shows the top view of a hydrothermally grown PZT nanoparticles thin film without the binder layer in various magnifications. There are voids appeared on the surface of the thin film with radius around 1-3 μm. That's why the topcoat layer is sometimes necessary for avoiding the short-circuit situation with the top and bottom electrodes. Another benefit

Figure 2.7: PZT colloidal ink

of using topcoat is to reduce the surface roughness of the thin films. Figure 2.9 is the cross sectional view of hydrothermally grown PZT nanoparticles thin film with binder on top, and it shows the thickness of the film is 11 μm, with binder thickness varies from 0.6-2 μm. The thickness of the film can be controlled to 5 μm or less by reducing the number of drop-casted nanoparticles ink layers.

2.2.2.2 Crushed PZT Particles Thin Film

The size distribution of crushed PZT particles found in the PZT-silane thin film is from 150 nm to 2 μm as shown in Fig. 2.10, the top view of crushed PZT particles thin film without binder. Although crushed PZT particles form a large amount of aggregates with size of 5-35 μm, they were not deposited on the film. Crushed PZT particles are not well dispersed in ink as indicated previously, so in order to form a thinner and more uniform film, only the top third of PZT colloid was used for drop casting crushed PZT particles thin films.

Figure 2.11 is the cross sectional view of crushed PZT nanoparticles thin film with binder on top, and the overall thickness is measured to be 7.5 μm with 5 μm thick PZT layer and

Table 2.2: PZT-silane ink composition for crushed PZT particles

Ingredient	wt.%
PZT crushed particles	10
PEG 600	5
MPTS	0.5
Ethanol	84.5

2.5 μm thick binder layer. Cross sectional view of another crushed PZT nanoparticles thin film with binder and gold on top is shown in Fig. 2.12. The top layer is Au, and it is about 0.6 μm thick; the second layer is MPTS, 0.7 μm thick; and the bottom layer is PZT particles, 5 μm thick.

2.2.3 Discussion

The hydrothermally grown PZT nanoparticles are not expected to outperform the crushed PZT particles in piezoelectric properties for several reasons. First, the PZT nanoparticles contain a certain level of lead oxide, because excess lead is used to prevent lead vacancy when making the PZT nanoparticles. Second, the hydrothermal process used to make the PZT nanoparticles is a solution-based, low-temperature processing method, in which atoms have lower mobility. Moreover, the hydrothermal process for PZT nanoparticles is newly developed and there is a lot of room for improvement, such as more precise control of the chemical composition of $Pb(Zr_{0.52}, Ti_{0.48})O_3$ or better process control to obtain higher crystallinity.

The comparison of SEM images shows many distinctions. For example, the hydrothermally grown PZT nanoparticles present clear cubic structures with size ranging from 300 nm to 2 μm. In contrast, the crushed PZT particles present irregular shapes with size ranging from 100 to 500 nm. The hydrothermally grown PZT nanoparticles present little aggregation, whereas crushed PZT particles show a high level of aggregation with size ranging from

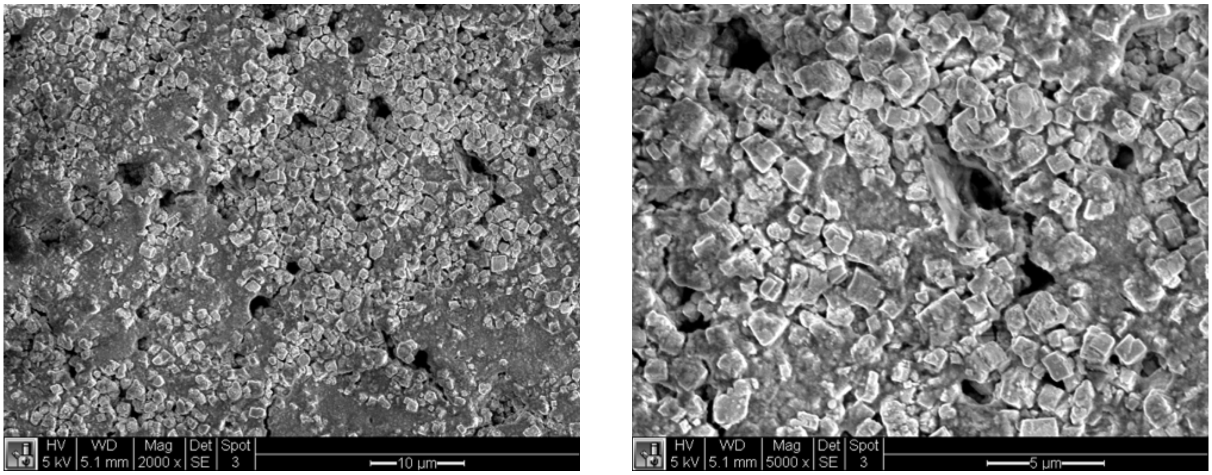

(a) Magnification: 2,000X

(b) Magnification: 5,000X

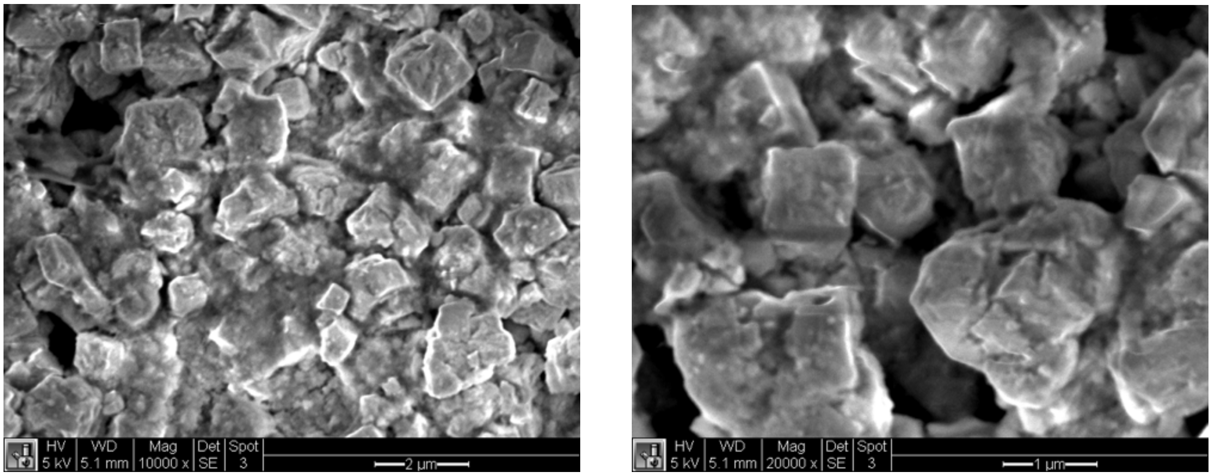

(c) Magnification: 10,000X

(d) Magnification: 20,000X

Figure 2.8: Top view SEM images of hydrothermally grown PZT nanoparticles thin film without binder

5 to 35 μm in spherical forms.

2.3 Printing Results of PZT-Silane Inks

A major goal in this research is to print PZT-silane inks developed thus far and evaluate the quality of the resulting thin films. Printing of PZT-silane inks was carried out by Md Taibur

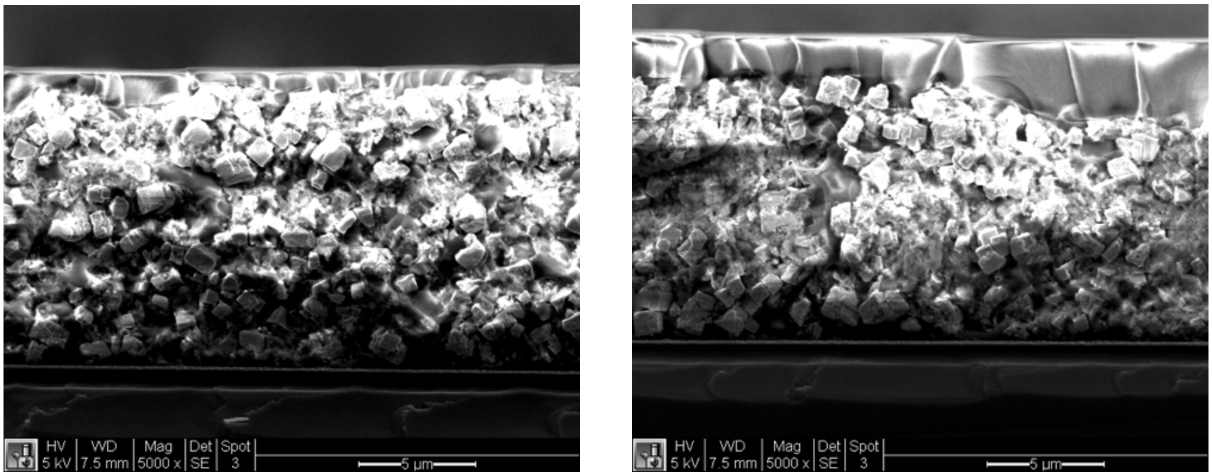

(a) Thickness: PZT 11μm, Binder 0.6μm

(b) Thickness: PZT 11μm, Binder 2μm

Figure 2.9: Cross sectional view SEM images of hydrothermally grown PZT nanoparticles thin film with binder on top

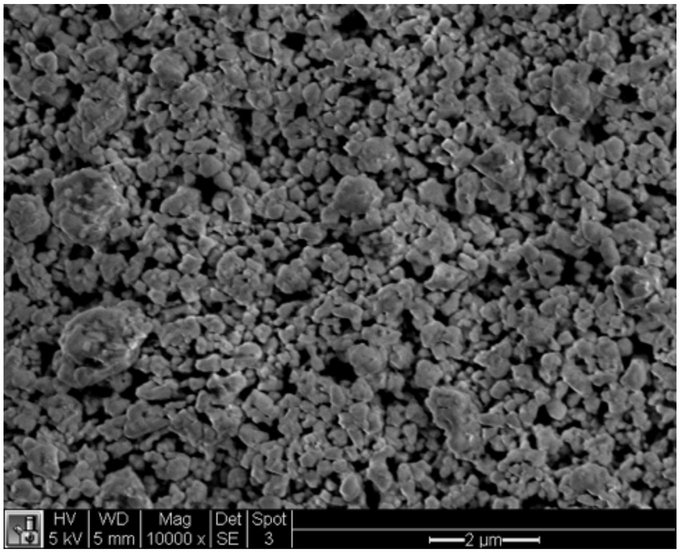

Figure 2.10: Top view SEM image of crushed PZT nanoparticles thin film without binder

Rahman and Professor Rahul Panat at Washington State University with the aerosol-jet micro-additive manufacturing equipment (shown in Fig. 2.13) in Professor Rahul Panat's

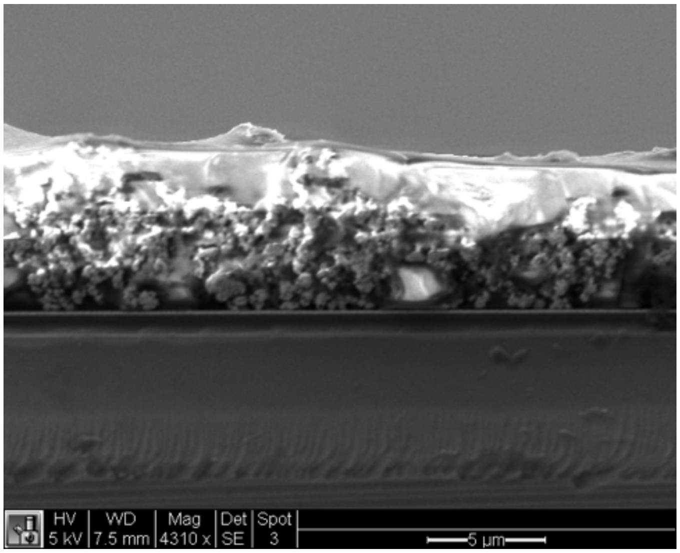

Figure 2.11: Cross sectional view SEM image of crushed PZT nanoparticles thin film with binder on top

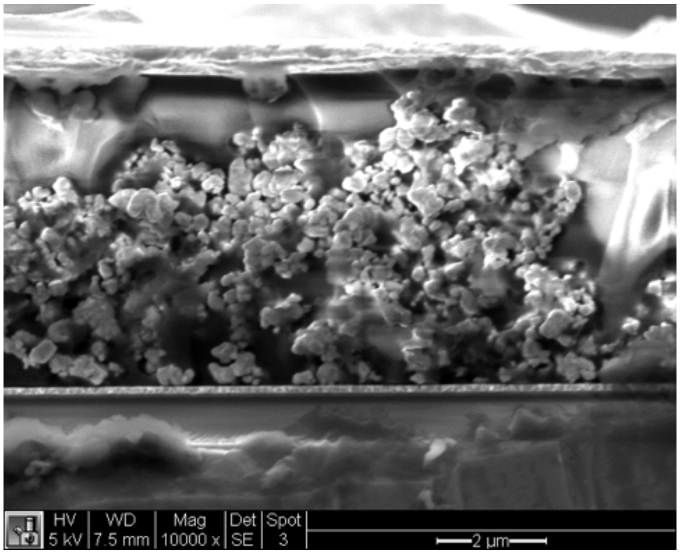

Figure 2.12: Cross sectional view SEM image of crushed PZT nanoparticles thin film with binder and gold on top

lab. After PZT thin films have been successfully printed on the substrate, they were sent back to our lab and subsequently cured and characterized at University of Washington.

Two different types of inks were printed via aerosol-jet micro-additive manufacturing, which are (a) PZT-silane ink with hydrothermally grown PZT nanoparticles (composition see Table 2.1) and (b) PZT-silane ink with crushed PZT particles (composition see Table 2.2), and their printing results will be presented in this section. All the film samples discussed have three printed layers on $0.2 \times 18 \times 18$ (mm) glass slides by the aerosol-jet.

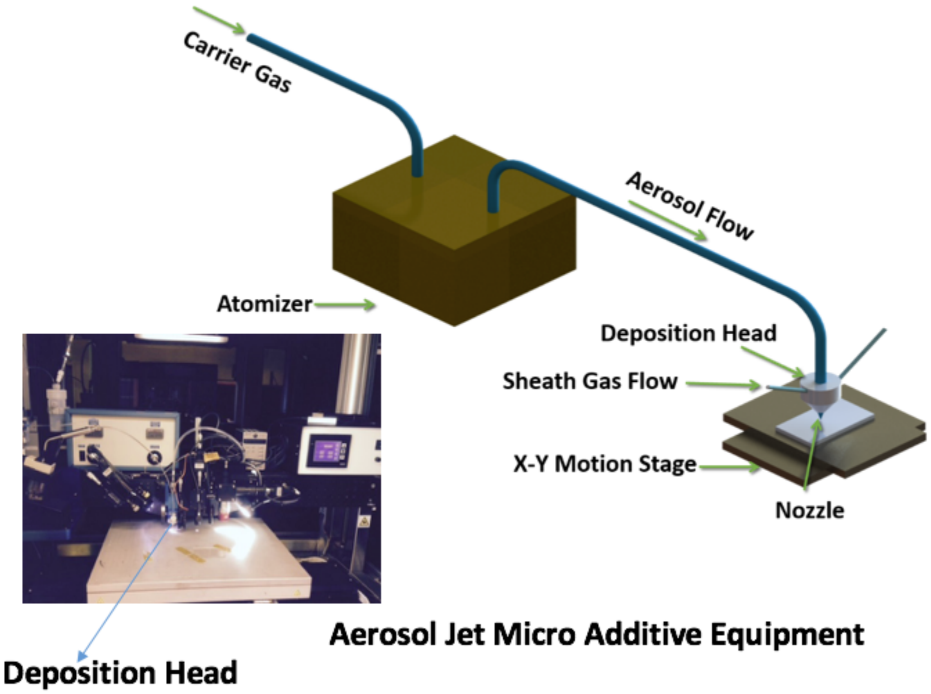

Figure 2.13: Aerosol-jet micro-additive manufacturing equipment. Courtesy of Md Taibur Rahman and Rahul Panat at Washington State University.

Surface profilometry of the printed films was performed on a *Tencor P15 stylus based profilometer* and six measurements along the directions indicated by Fig. 2.14 were taken per sample. The area of PZT films are all 3 mm by 3 mm and the film thickness can be estimated from the six surface's profile measurements.

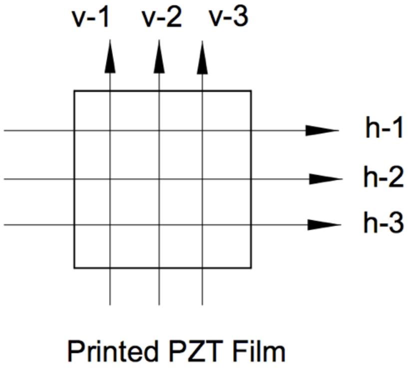

Figure 2.14: Profilometer measurement directions

2.3.1 Printed PZT-silane ink with hydrothermally grown PZT nanoparticles

Figure 2.15 shows the surface profile of one printed PZT-silane thin film with hydrothermally grown PZT nanoparticles. The film thickness was estimated to be 7.33 μm by taking the average of the thickness data measured in six different locations. Table 2.3 presents these six measurements of the printed film thickness with hydrothermally grown PZT nanoparticles taken along the direcitons shown in Fig. 2.14. It can be observed from Fig. 2.15 that the printed PZT-silane thin film with hydrothermally grown PZT nanoparticles had a rather smooth surface, except for the profile presented in Fig. 2.15 (f). This is due to the fact that Fig. 2.15 (f) was taken at the edge of the film where discontinuities inevitably occur.

Figure 2.16 shows the optical microscope images[2] of the printed PZT thin films with three layers before curing. Figure 2.16 (a) was taken immediately after printing of PZT inks, (b) was taken after the ethanol (solvent) was fully evaporated, (c) displays a magnified image of the edge of the printed film and (d) displays the magnified image of its corner. Figure 2.16

---

[2] Images were taken by stereo-microscopy and compound microscopy. Those images are provided by Md Taibur Rahman and Professor Rahul Panat at the Washington State University.

(b)-(d) show that both the edge and the corner of the printed film were ragged.

Figure 2.17 shows the SEM images of the printed thin film with hydrothermally grown PZT nanoparticles and it has a magnification of $11,336\times$. The reason why the images appeared blurry is that the PZT nanoparticles were embedded in the non-conductive polymer matrix and the film surface is uneven, making it difficult to resolve all of the features. It can be observed that all PZT nanoparticles are within 1 μm ranging from 150 nm to 980 nm as shown in Fig. 2.17 (d).

Table 2.3: Printed film thickness with hydrothermally grown PZT nanoparticles

Thickness (μm)	h-1	h-2	h-3	v-1	v-2	v-3
Sample	8.15	8.5	5.83	7.14	9.2	5.16

2.3.2 Printing PZT-silane ink with crushed PZT particles

Figure 2.18 shows the surface profile of a printed PZT-silane thin film with crushed PZT particles. The film thickness was estimated to be 6.33 μm following the same average method described prior. Table 2.4 presents the six measurements of the printed film thickness with crushed PZT particles taken along the direcitons shown in Fig. 2.14. It appears that the printed film with crushed PZT particles had a rather rough surface.

Figure 2.19 shows the SEM images of the printed thin film with crushed PZT particles in various magnifications ranging from $500\times$ to $8,000\times$. It can be observed from the figure that there were quite a few PZT particles or aggregates with 2-3 μm in diameter rest on the surface or inside the film.

2.3.3 Conclusions

- Printed PZT films using UW made hydrothermally grown PZT nanoparticles have a smoother surface profile than the crushed PZT particle thin films. According to the

Table 2.4: Printed film thickness with crushed PZT particles

Thickness (μm)	h-1	h-2	h-3	v-1	v-2	v-3
Sample	5.58	7.65	7.05	5.93	6	5.78

SEM images, it appears that all (or most) of the particles in the film are smaller than 1 μm.

- Printed PZT films using crushed PZT particles have a rather rough surface profile. During this printing process, four (out of six) samples have multiple holes (see Fig. 2.20 (a) and (b)). And it can be observed from Fig. 2.20 (b) that some of the particles or aggregates in the film are 2-3 μm in diameter.

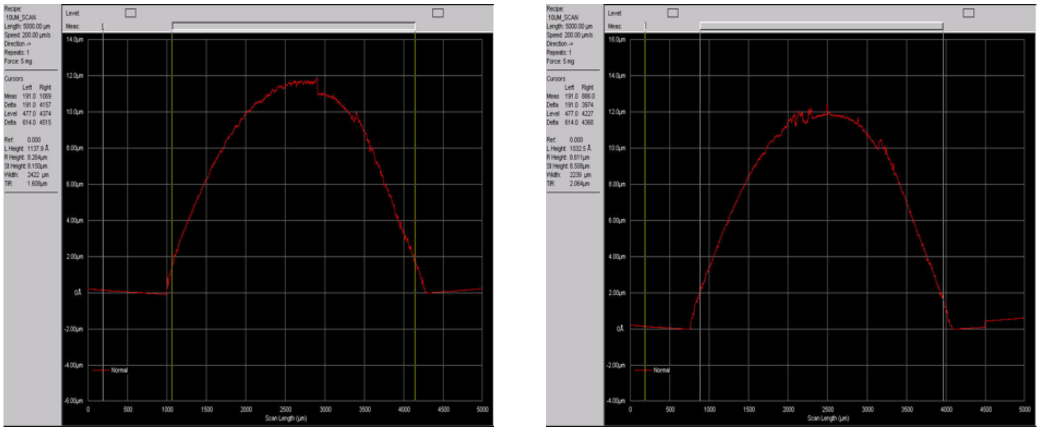

(a) H-1 (b) H-2

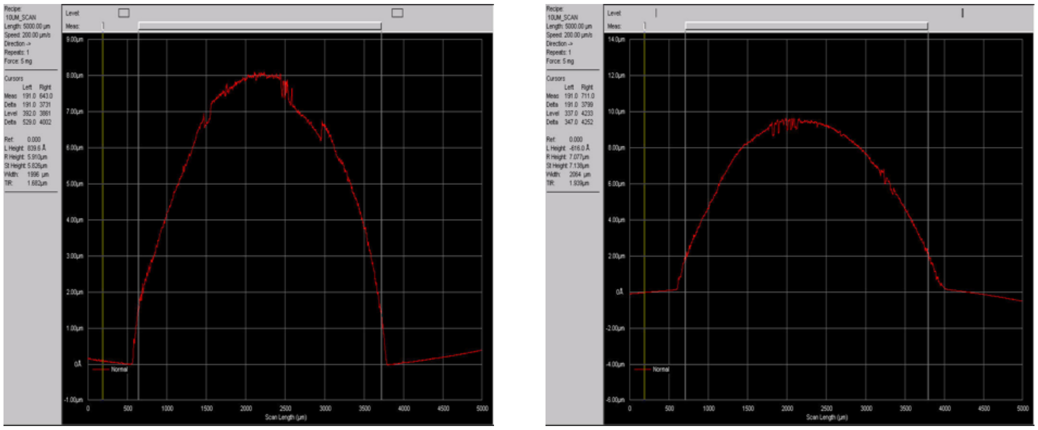

(c) H-3 (d) V-1

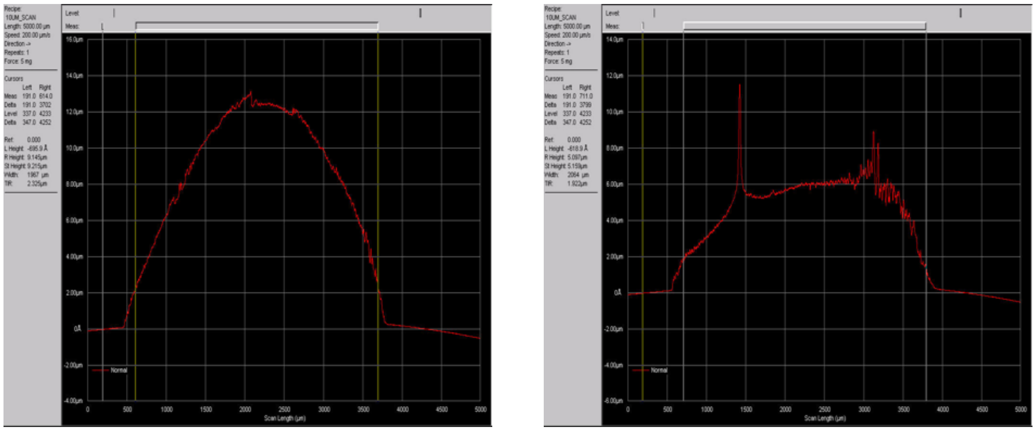

(e) V-2 (f) V-3

Figure 2.15: Surface profilometry of printed UW PZT nanoparticles ink

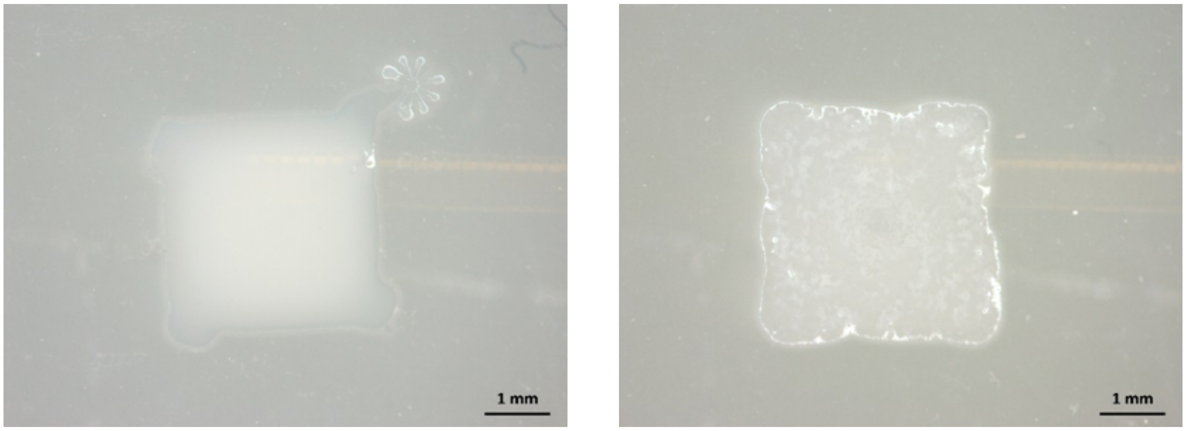

(a) Right after printing
(b) After the solvent was evaporated

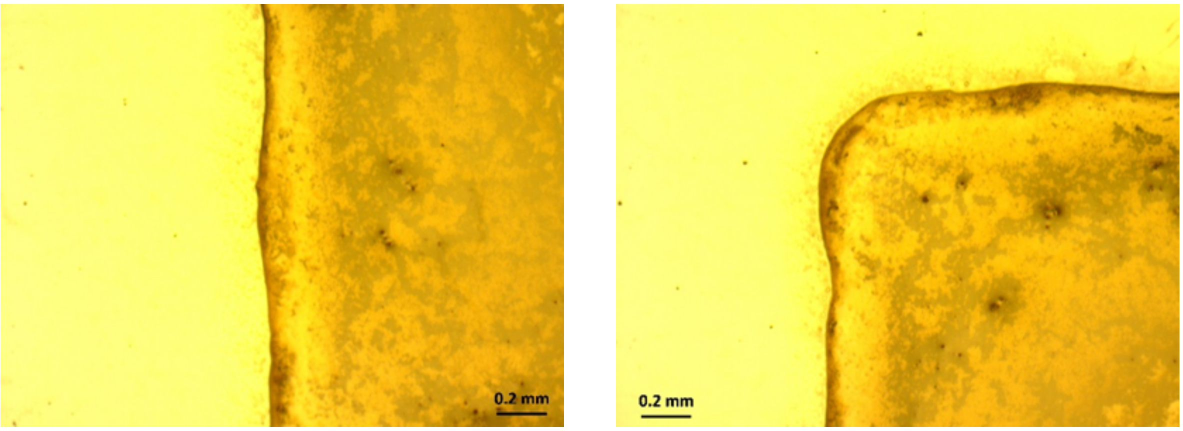

(c) Edge of the printed film
(d) Corner of the printed film

Figure 2.16: Printed PZT thin films with three layers before curing. Images were taken by stereo-microscope and compound microscope. Those images were provided by Md Taibur Rahman and Professor Rahul Panat at Washington State University.

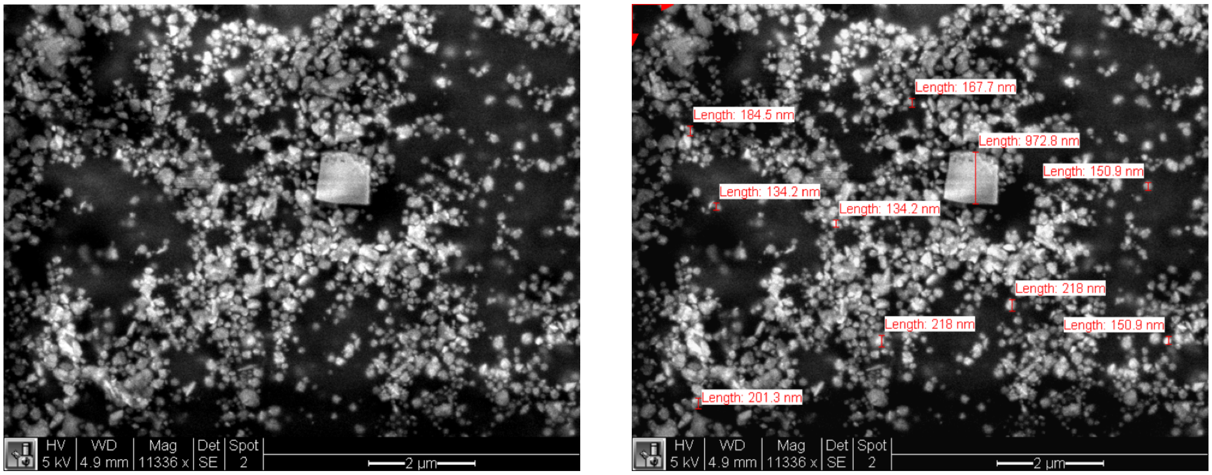

(a) (b)

Figure 2.17: SEM image of a printed thin film with hydrothermally grown PZT nanoparticles

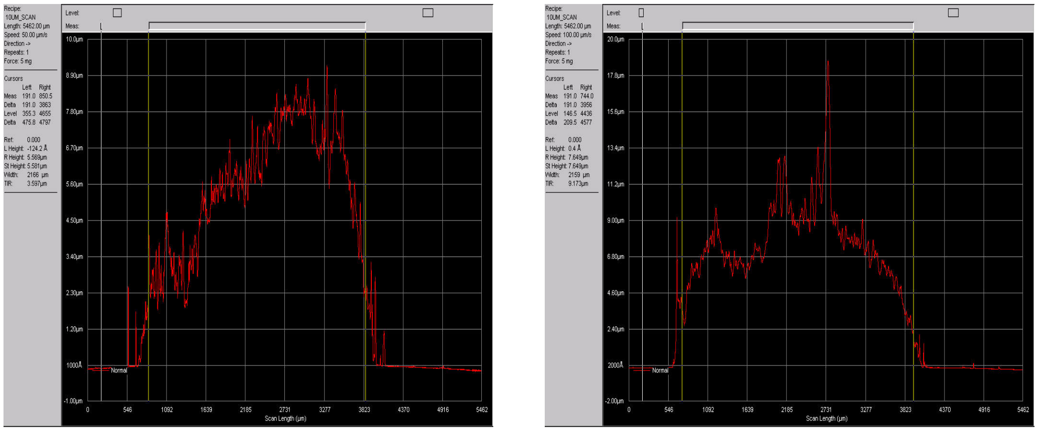

```
Recipe:
 10UM_SCAN
Length: 5462.00 µm
Speed: 50.00 µm/s
Direction ->
Repeats: 1
Force: 5 mg

Cursors
         Left   Right
Meas     191.0  850.5
Delta    191.0  3863
Level    355.3  4655
Delta    475.8  4797

Ref:        0.000
L Height:   -124.2 Å
R Height:   5.569µm
St Height:  5.581µm
Width:      2166  µm
TIR:        3.597µm
```

```
Recipe:
 10UM_SCAN
Length: 5462.00 µm
Speed: 100.00 µm/s
Direction ->
Repeats: 1
Force: 5 mg

Cursors
         Left   Right
Meas     191.0  744.0
Delta    191.0  3956
Level    146.5  4436
Delta    209.5  4577

Ref:        0.000
L Height:   0.4 Å
R Height:   7.649µm
St Height:  7.649µm
Width:      2159  µm
TIR:        9.173µm
```

(a) H-1 (b) H-2

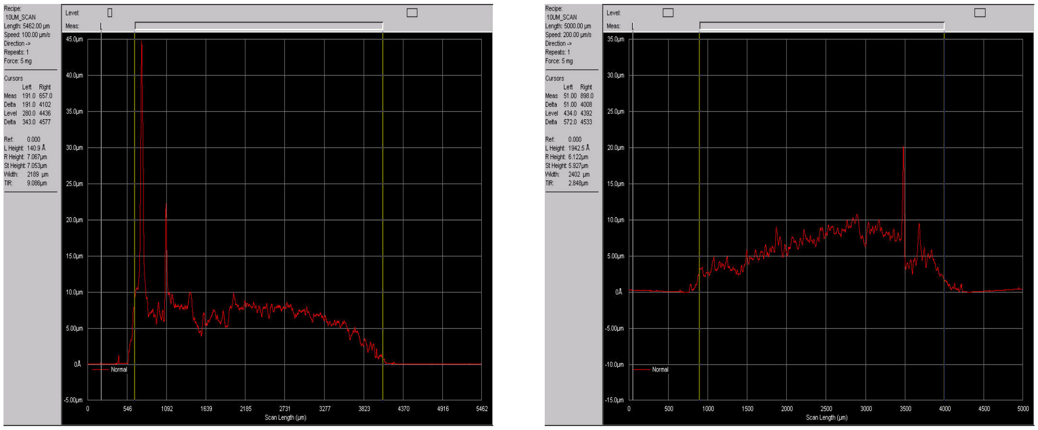

```
Recipe:
 10UM_SCAN
Length: 5462.00 µm
Speed: 100.00 µm/s
Direction ->
Repeats: 1
Force: 5 mg

Cursors
         Left   Right
Meas     191.0  657.0
Delta    191.0  4102
Level    280.0  4436
Delta    343.0  4577

Ref:        0.000
L Height:   140.9 Å
R Height:   7.067µm
St Height:  7.053µm
Width:      2189  µm
TIR:        9.086µm
```

```
Recipe:
 10UM_SCAN
Length: 5000.00 µm
Speed: 200.00 µm/s
Direction ->
Repeats: 1
Force: 5 mg

Cursors
         Left   Right
Meas     51.00  898.0
Delta    51.00  4008
Level    434.0  4392
Delta    572.0  4533

Ref:        0.000
L Height:   1942.5 Å
R Height:   6.122µm
St Height:  5.927µm
Width:      2402  µm
TIR:        2.848µm
```

(c) H-3 (d) V-1

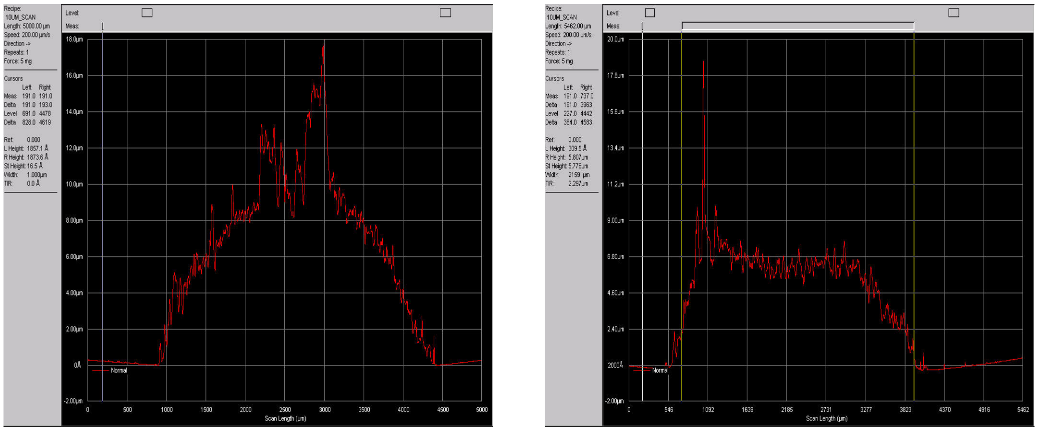

```
Recipe:
 10UM_SCAN
Length: 5000.00 µm
Speed: 200.00 µm/s
Direction ->
Repeats: 1
Force: 5 mg

Cursors
         Left   Right
Meas     191.0  191.0
Delta    191.0  193.0
Level    691.0  4478
Delta    828.0  4619

Ref:        0.000
L Height:   1857.1 Å
R Height:   1873.6 Å
St Height:  16.5 Å
Width:      1.000µm
TIR:        0.0 Å
```

```
Recipe:
 10UM_SCAN
Length: 5462.00 µm
Speed: 200.00 µm/s
Direction ->
Repeats: 1
Force: 5 mg

Cursors
         Left   Right
Meas     191.0  737.0
Delta    191.0  3963
Level    227.0  4442
Delta    364.0  4583

Ref:        0.000
L Height:   309.5 Å
R Height:   5.807µm
St Height:  5.776µm
Width:      2159  µm
TIR:        2.297µm
```

(e) V-2 (f) V-3

Figure 2.18: Surface profilometry of printed crushed PZT particles ink

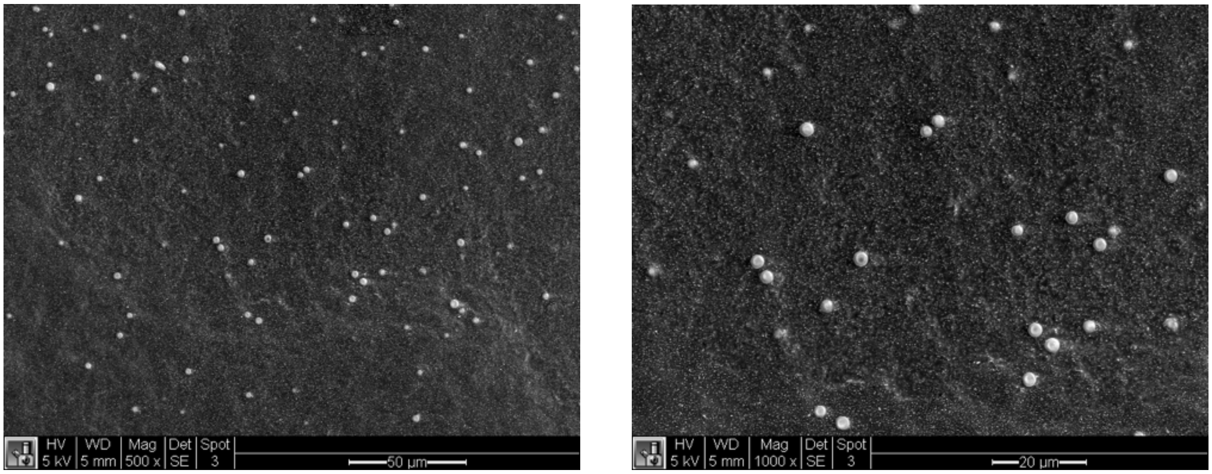

(a) Magnification: 500X

(b) Magnification: 1000X

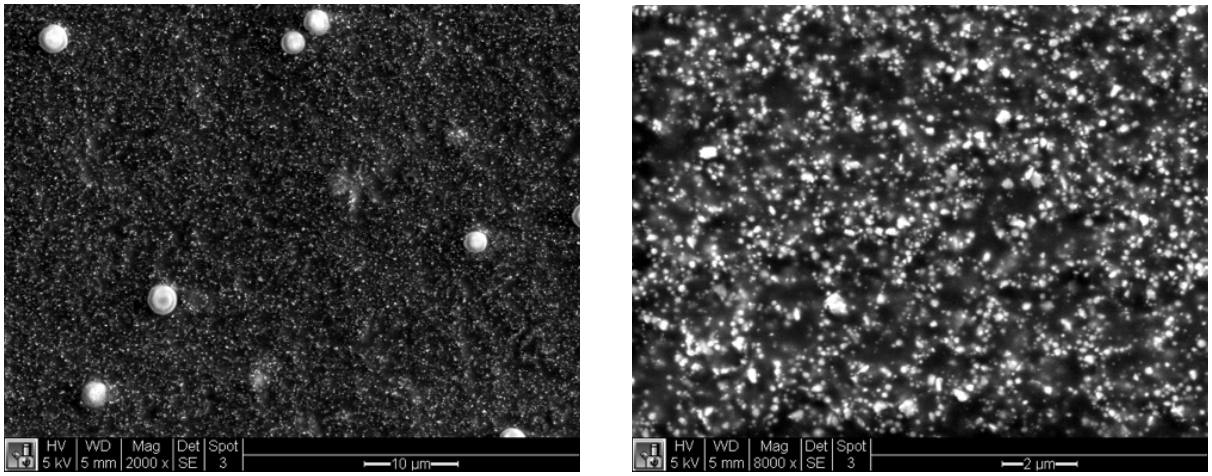

(c) Magnification: 2000X

(d) Magnification: 8000X

Figure 2.19: Printed films from crushed PZT particles ink

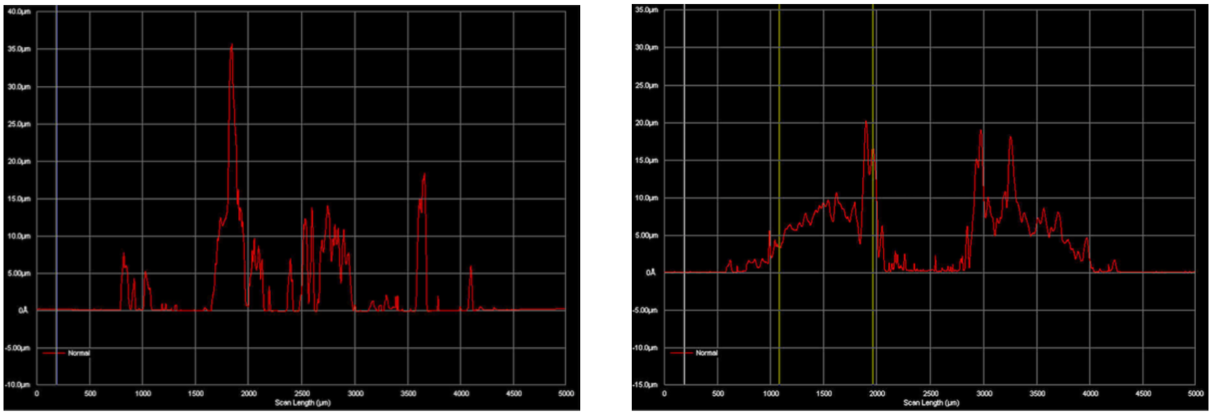

(a) Surface profilometry of sample with mutiple holes

(b) Surface profilometry of sample with one hole in the middle

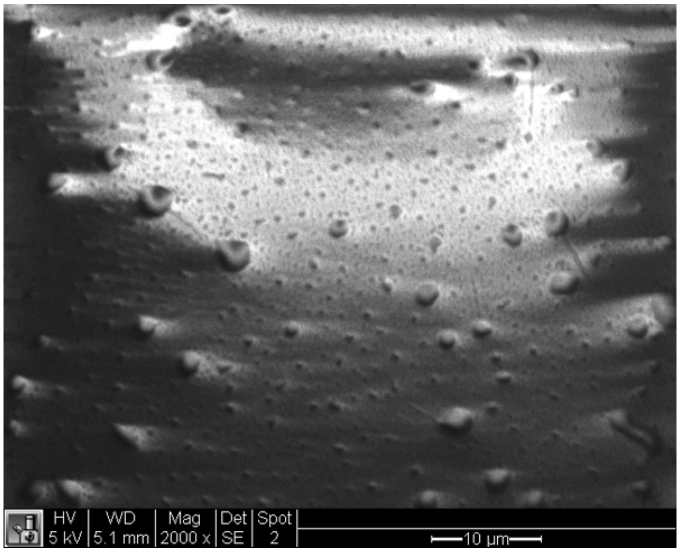

(c) SEM

Figure 2.20: Printed crushed PZT particle films with holes

Chapter 3

DIELECTRIC CHARACTERIZATION OF PZT-SILANE FILMS

Characterization of the PZT-silane thin films sensors consists of three parts: material characterization through XRD and SEM in the previous chapter, dielectric characterization through impedance measurements and piezoelectric characterization through impact tests and finite element simulations. In this chapter, characterization of the PZT-silane nanocomposite thin films' dielectric properties will be presented. Characterization of piezoelectric properties is more complicated and will be explained in great detail in the next chapter.

3.1 Dielectric Basics

3.1.1 Impedance Measurement Basics

Impedance is an important parameter in characterizing electronic circuits and materials. This parameter is typically denoted as Z and defined as a total generalized resistance in a circuit or material at given frequencies. It is a complex quantity that generalize the affects of resistors, inductors and capacitors in the circuits and follows the relation (3.1), where V is the voltage, I is the current and ω is the input frequency in radians per second. The input frequency ω is related to frequency in hertz (Hz) by 2π (see Eqn. (3.2)).

$$V(\omega) = I(\omega)Z(\omega) \tag{3.1}$$

$$\omega = 2\pi f \tag{3.2}$$

Since impedance is complex, it can be graphically shown as a vector in an complex plane with real axis (denoted as Re) and imaginary axis (denoted as Im) in Fig. 3.1. Impedance

Z consists of a real part (resistance R) and an imaginary part (reactance X) and can be expressed in Cartesian coordinate as Eqn. (3.3), where i is the imaginary unit. And it can also be represented in Polar coordinate, where $|Z|$ is the magnitude (ratio between voltage amplitude and current amplitude) and θ is the phase angle (phase difference between voltage and current). The conversion from Polar to Cartesian can be found in Eqn. (3.4) and Eqn. (3.5).

$$Z = R + iX = |Z|\angle\theta \tag{3.3}$$

$$R = |Z|cos\theta \tag{3.4}$$

$$X = |Z|sin\theta \tag{3.5}$$

The admittance Y is often used for mathematical convenience, and $Y = 1/Z = 1/(R + iX)$. Impedance has the unit of Ohms (Ω) and admittance has the unit of Siemens (S) [68, 69].

$$Z_{resistor} = R \tag{3.6}$$

$$Z_{capacitor} = \frac{1}{(i\omega C)} \tag{3.7}$$

3.1.2 Parallel Plate Capacitor

As mentioned before, a dielectric material can deform and store energy when an external electric field is existed. In order to apply the electric field, two electrode plates should be placed on the top and bottom surfaces of the measured material. This parallel plate capacitor model is represented graphically in Fig. 3.2, where A is the smaller area among the two plates (the effective area), and t is the thickness of that material. The dielectric material can be modeled as a generalized capacitor that has a complex capacitance, thus a capacitor with capacitance C_p and a resistor with resistance R_p in parallel [68, 69].

The capacitance C_p is related to the dielectric constant of the material and the resistance R_p is related to the dielectric loss. Dielectric loss is the absorption of the electrical energy by the material and dissipation of that energy through the movement of charges into heat. When measuring the dielectric properties of a material, an AC sinusoidal voltage V is applied, and the current flows through the source will be measured. This current has two streams, one stream flows through the capacitor (charging, I_c) and the other flows through the resistor (loss, I_l).

The amount of charge a capacitor stores is proportional to the voltage drop between the plates and the capacitance, see Eqn. (3.8). The capacitance C is determined by the area A, material thickness t and the dielectric constant of the material. Consider the parallel plate capacitor without a dielectric material (vacuum), the capacitance is given by Eqn. (3.9) and for a parallel plate capacitor with dielectric material, the capacitance is given by Eqn. (3.10), where ε_o is the permittivity of vacuum and ε_r is the relative permittivity of the dielectric material to the vacuum.

$$Q = CV \tag{3.8}$$

$$C_o = \frac{\varepsilon_o A}{t}, \ \ \varepsilon_o = 8.854 \times 10^{-12} \ \ F/m \tag{3.9}$$

$$C_{dielectric} = \frac{\varepsilon_r \varepsilon_o A}{t} = \varepsilon_r \, C_o \tag{3.10}$$

3.1.3 Dielectric Constant and Dielectric Loss

According to Eqn. (3.1) and Eqn. (3.7), the relative permittivity ε_r can be estimated by Eqn. (3.11), where Y is the admittance of the material, and ω is the frequency in rad/s. Since the measured impedance Z is a complex number, the relative permittivity ε_r extracted

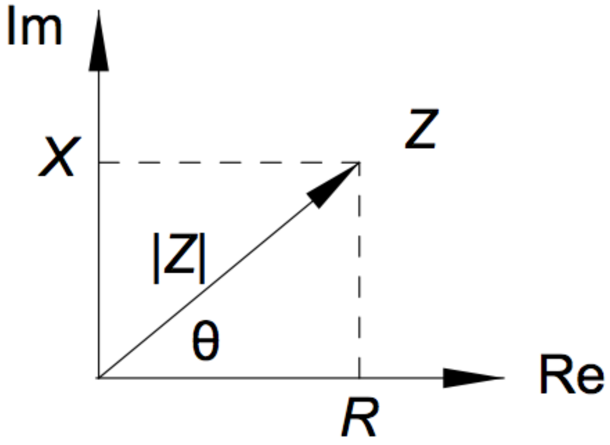

Figure 3.1: Impedance (Z) in the complex plane

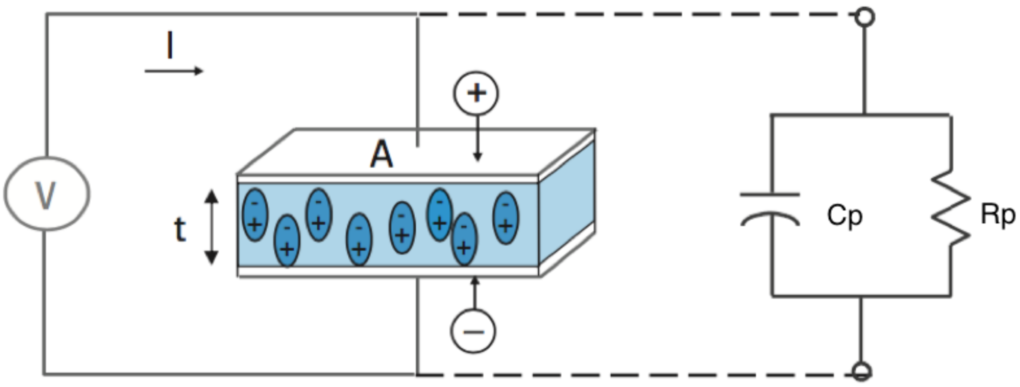

Figure 3.2: Parallel plate capacitor model [70]

is also a complex number given by Eqn. (3.12). The real part $\varepsilon_r^{'}$ represents the ability of a dielectric material to store charge and will be referred to as " estimated dielectric constant" hereafter. Meanwhile, the imaginary part $\varepsilon_r^{''}$ represents dielectric loss, i.e., the amount of electric energy dissipated into heat. The absolute permittivity of the material can be obtained by Eqn. (3.13). A loss tangent ($tan\delta$) is generally used to describe dielectric loss and is defined in Eqn. (3.14).

$$Y = \frac{1}{Z} = (i\omega C_{dielectric}) = (i\omega \frac{\varepsilon_r \varepsilon_o A}{t}) \tag{3.11}$$

$$\varepsilon_r = \varepsilon_r^{'} - i\varepsilon_r^{''} \tag{3.12}$$

$$\varepsilon = (\varepsilon_r^{'} - i\varepsilon_r^{''})\, \varepsilon_o \tag{3.13}$$

$$tan\delta = \frac{\varepsilon_r^{''}}{\varepsilon_r^{'}} \tag{3.14}$$

$$\begin{aligned} Y &= \frac{i\omega(\varepsilon_r^{'} - i\varepsilon_r^{''})\varepsilon_o A}{t} \\ &= \frac{i\omega\varepsilon_o\varepsilon_r^{'}A}{t} + \frac{\omega\varepsilon_o\varepsilon_r^{''}A}{t} \\ &= i\omega C_p + \frac{1}{R_p} \end{aligned} \tag{3.15}$$

3.2 Dielectric Properties of PZT-silane Nano-composite Sensors

3.2.1 Impedance Measurements

Impedance Z, phase angle $\angle\theta$, capacitance C_p and resistance R_p of the PZT-silane films were measured through use of an impedance analyzer (Model: Agilent 4294A Precision Impedance Analyzer). Experimentally this instrument can map out impedance Z as a function of frequency, so $Z(\omega)$ can be obtained.

Impedance data for sensors made with crushed PZT particles thin films and hydrothermally grown PZT nanoparticles thin films were measured from 40 Hz to 100 kHz at room temperature (25°C). Table B.1 in Appendix B represents one set of such data for hydrothermally grown PZT nanoparticles thin-film sensor NS1 after poling and is used here as an example for deriving the dielectric properties. Sensor NS1's phase angle θ, capacitance C_p and resistance R_p were plotted as a function of frequency in Hz and impedance Z was plotted by taking the logs on $|Z|$ and $frequency$ for better illustration, see Fig. 3.3. Figure 3.3 (a) shows that impedance magnitude plot in logarithmic form is a straight-line graph, similar to an ideal lossless capacitor ($Log(|Z|) = Log(1/\omega C) = Log(1/C) - Log(\omega)$). In the same manner, impedance plots for sensor NB1 made with crushed PZT particles thin films were produced in Fig. 3.4.

$$C_p = \frac{\varepsilon_o \varepsilon_r^{'} A}{t} \tag{3.16}$$

$$R_p = \frac{t}{\omega \varepsilon_o \varepsilon_r^{''} A} \tag{3.17}$$

3.2.2 Estimated Dielectric Properties

According to Eqn. (3.14), (3.16) and (3.17), the dielectric constant $\varepsilon_r^{'}$ and the loss tangent $tan\delta$ can be derived from the impedance measurement. Table 3.1 lists magnitude and phase of the measured impedance at 3 kHz and also the estimated dielectric constants and losses for samples made with crushed PZT particles thin films ($\mathrm{NB1} - \mathrm{NB4}$) and hydrothermally grown PZT nanoparticles thin films ($\mathrm{NS1} - \mathrm{NS4}$). As shown in the table, estimated dielectric constants of thin films with PZT nanoparticles is about twice of that with crushed PZT particles. The loss tangents are all very small for both types of PZT-silane thin films. Similarly, the estimated dielectric constant and loss tangent can be calculated for impedance measured over the entire frequency range. Figure 3.5 and Fig. 3.6 are two examples of estimated dielectric constants and loss plots over frequency range of $40\mathrm{Hz} - 100\mathrm{kHz}$ for

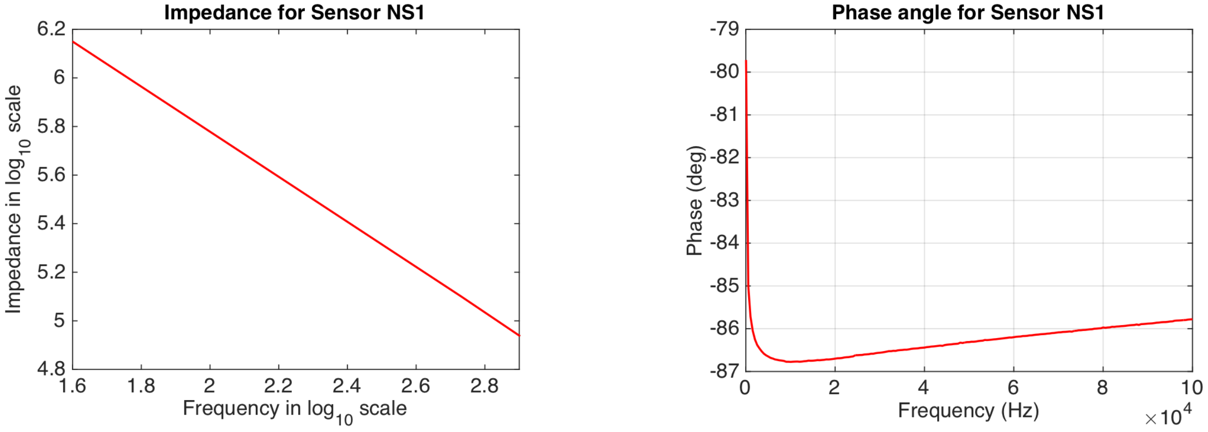

(a) NS1 impedance measurement

(b) NS1 phase measurement

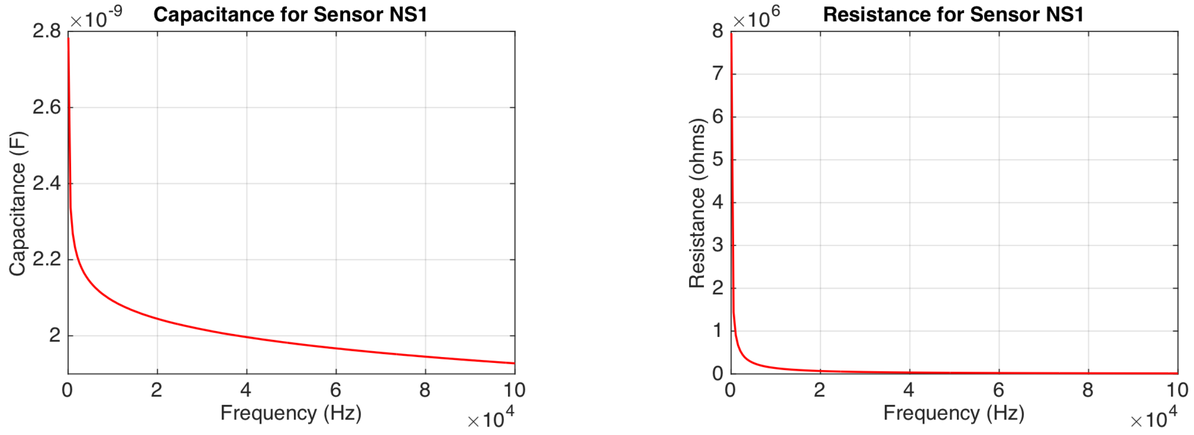

(c) NS1 capacitance measurement

(d) NS1 resistance measurement

Figure 3.3: Sensor NS1 impedance measurement data

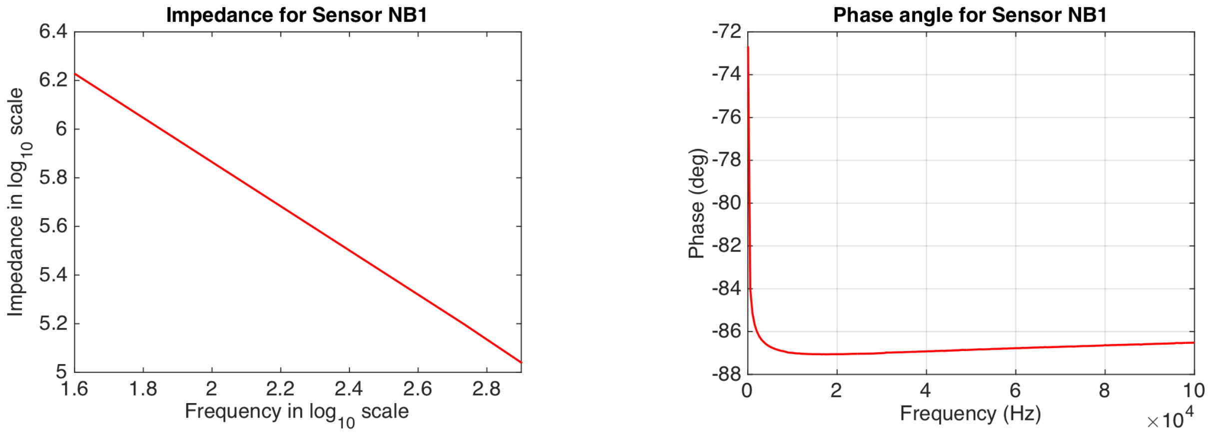

(a) NB1 impedance measurement

(b) NB1 phase measurement

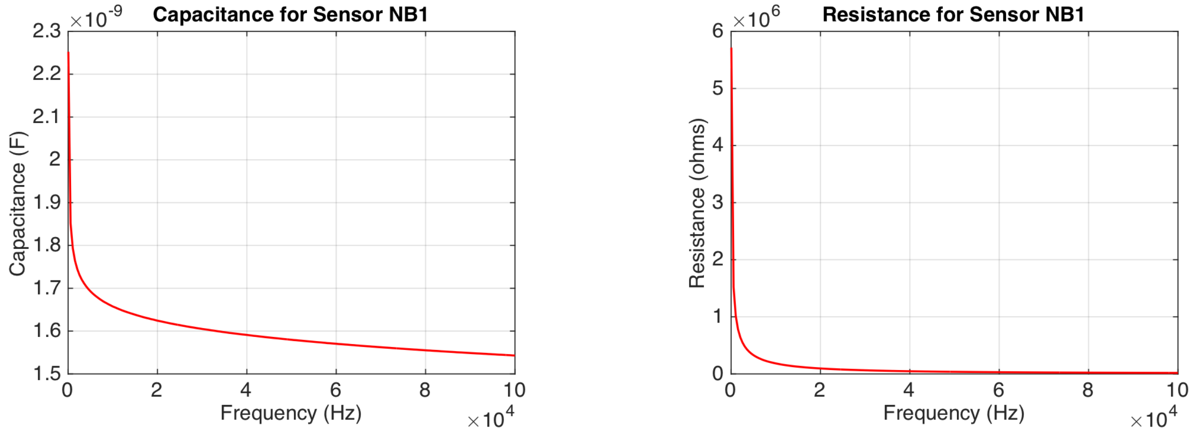

(c) NB1 capacitance measurement

(d) NB1 resistance measurement

Figure 3.4: Sensor NB1 impedance measurement data

Table 3.1: Measured and estimated dielectric properties of all specimens at 3 kHz

Specimens at 3 kHz	Impedance Magnitude (kΩ)	Impedance Phase Angle (degree)	Estimated dielectric constant	Estimated loss tangent
Crushed PZT Particles Thin Films				
NB1	30.4	-86.4	12.68	6.3E-2
NB6	36.2	-86.4	10.66	6.2E-2
NB3	28.7	-86	15.28	7.0E-2
NB4	42	-82	13.2	0.14
Expedited Hydrothermal Grown PZT Nanoparticles Thin Films				
NS1	24	-86.5	26.61	6.2E-2
NS2	29.4	-87	25.85	5.3E-2
NS3	23.8	-85.4	24.42	8.1E-2
NS4	43	-86	26.41	7.0E-2

sensors made with hydrothermally grown PZT nanoparticles thin films and crushed PZT particles thin films, respectively.

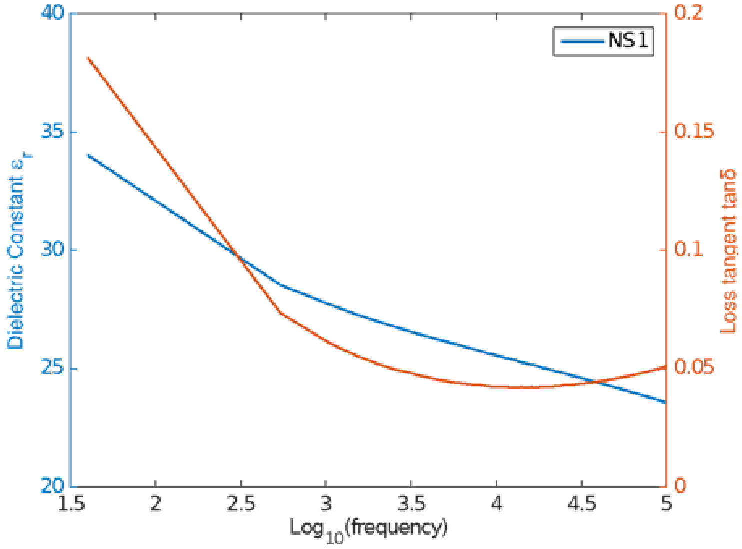

Figure 3.5: Estimated dielectric constant and loss tangent for PZT-silane thin film sensor NS1 with PZT nanoparticles in the frequency range of 40Hz-100kHz

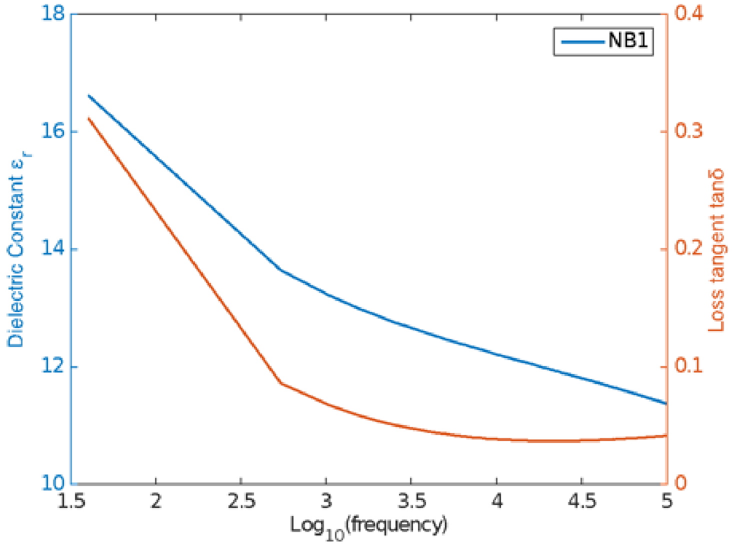

Figure 3.6: Estimated dielectric constant and loss tangent for PZT-silane thin film sensor NB1 with crushed PZT particles in the frequency range of 40Hz-100kHz

Chapter 4

PIEZOELECTRIC CHARACTERIZATION OF PZT-SILANE FILMS

4.1 Overview

Another key goal of this research is to provide some understanding of the piezoelectric performance of the formed PZT-silane thin films after depositing the PZT nanoparticles ink onto an electrode or a substrate. Characterization of the fabricated PZT-silane films for their piezoelectric performance faces many challenges and will be discussed here.

In general, it is relatively easy to demonstrate existence of piezoelectricity in the films. For actuator applications, one can drive a light and flexible structure (e.g., a beam) by supplying a high voltage (e.g., 50 V) across the PZT nano-composite films and measuring motion of the structure. For sensor applications, one can measure voltage output when the light and flexible structure is in resonance [65]. It is, however, more difficult to quantify piezoelectric properties of the fabricated PZT thin films. For actuator applications, the measured motion needs to be compared with a theoretical model to extract piezoelectric constants. For sensor applications, the measured voltage needs to be compared with a theoretical model or a separate strain measurement to extract piezoelectric constants [62].

These characterization processes are difficult to conduct for several reasons. First, response of the PZT thin films are coupled to the host structure. Therefore, an accurate theoretical model of the PZT thin film and the host structure are needed to extract piezoelectric coefficients. Second, response of the thin films might be very susceptible to environmental noise and uncertainties from the specimen (e.g., boundary conditions). This is especially true when the charge generated from the PZT films is tiny. Finally, many thin-film measurements primarily characterize piezoelectric coefficient d_{31}. Very few studies characterize piezoelectric coefficient d_{33}[1] of a PZT thin film.

In order to overcome these challenges, the approach here for characterization of piezoelectric coefficient d_{33} has two steps. First, a mini impact hammer is used to excite the PZT-silane thin films. In the meantime, an accurate, double-end charge amplifier isolates tiny induced charge from background electrical noise and measure the PZT-silane thin films' charge responses. Second, a finite element model is created to estimate the piezoelectric coefficient from the measurements. The specimen preparation, experimental setup, measured results, and finite element modeling are explained in detail as follows [71].

4.2 Piezoelectric Constitutive Equations

Piezoelectric ceramics (such as PZT-4) are transversely isotropic materials with physical properties that are symmetric about their poled direction. The poling axis is labeled as z-axis or 3-axis, and the plane of isotropy is xy-plane or 12-plane according to the IEEE Standard on Piezoelectricity [72] and are shown in Fig. 4.1.

The linear piezoelectric constitutive equations describe the relations between the four state variables in a piezoelectric material: the stress components T_{ij}, strain components S_{ij}, electric field components E_k, and the electric displacement components D_k. The symbols used in the equations and their units can be found in Tab. 4.1. Superscripts of T, S, E and D are used in several piezoelectric or dielectric constants that signifying a particular mechanical or electrical boundary condition. T and S are for mechanical boundary conditions and E and D are for electrical boundary conditions. The superscript t stands for the matrix transpose. They are listed in Tab. 4.2.

The piezoelectric constitutive equations have four different standard forms by taking two state variables as dependent and the other two as independent. The four standard forms are strain-charge, stress-charge, strain-voltage, and stress-voltage forms and can be transformed from one form to another. For example, the *stress-charge* form (Eqn. (4.1)) is

---

[1] 3 is the poling and thickness direction of the film.

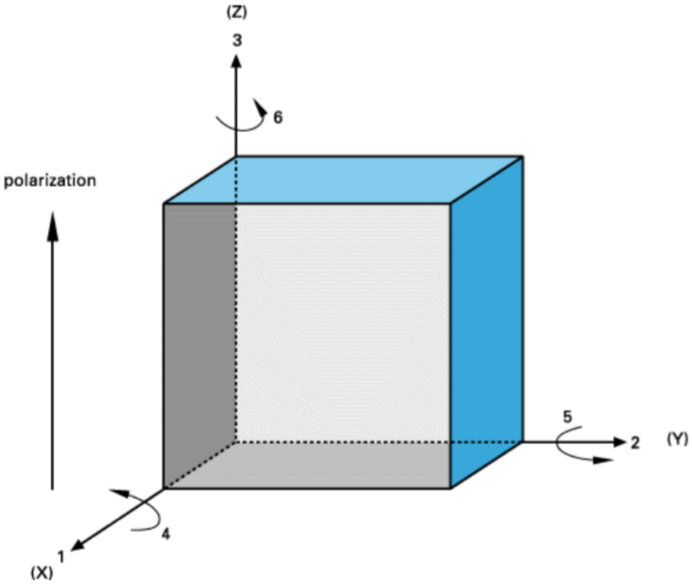

Figure 4.1: Designation of the axes and piezoelectric directions [73]

Table 4.1: List of symbols and units [72]

Symbol	**Definition**	**SI Unit**
T_{ij}, T_p	Stress component	N/m^2
S_{ij}, S_p	Strain component	
E_k	Electric field component	V/m
D_k	Electric displacement component	C/m^2
C_{ijkl}, C_{pq}	Elastic stiffness constant	N/m^2
s_{ijkl}, s_{pq}	Elastic compliance constant	m^2/N
d_{ijk}, d_{ip}	Piezoelectric constant	m/V or C/N
e_{ijk}, e_{ip}	Piezoelectric constant	C/m^2
ε_o	Permittivity of free space	F/m
ε_{ij}	Permittivity component	F/m

Table 4.2: Mechanical or electrical boundary condition symbols [72]

Superscript symbol	**Definition**	**Boundary condition**
T	At constant stress	Mechanically free
S	At constant strain	Mechanically clamped
E	At constant electric field	Short circuit
D	At constant electric displacement	Open circuit

$$\begin{bmatrix} \{\mathbf{T}\}_{\mathbf{6\times 1}} \\ \{\mathbf{D}\}_{\mathbf{3\times 1}} \end{bmatrix} = \begin{bmatrix} [\mathbf{C}^E]_{6\times 6} & -[\mathbf{e}]_{6\times 3} \\ [\mathbf{e}^t]_{3\times 6} & [\varepsilon^S]_{3\times 3} \end{bmatrix} \begin{bmatrix} \{\mathbf{S}\}_{6\times 1} \\ \{\mathbf{E}\}_{3\times 1} \end{bmatrix}, \tag{4.1}$$

where [**e**] are the piezoelectric stress constants with the unit of C/m^2 and $[\varepsilon^S]$ are the dielectric constants at constant strain.

Another useful form of piezoelectric constitutive equation is the *strain-charge* form, see Eqn. (D.3):

$$\begin{bmatrix} \{\mathbf{S}\}_{\mathbf{6\times 1}} \\ \{\mathbf{D}\}_{\mathbf{3\times 1}} \end{bmatrix} = \begin{bmatrix} [\mathbf{s}^E]_{6\times 6} & [\mathbf{d}]_{6\times 3} \\ [\mathbf{d}^t]_{3\times 6} & [\varepsilon^T]_{3\times 3} \end{bmatrix} \begin{bmatrix} \{\mathbf{T}\}_{6\times 1} \\ \{\mathbf{E}\}_{3\times 1} \end{bmatrix}, \tag{4.2}$$

where [**d**] are piezoelectric strain constants with the unit of m/V or C/N and $[\varepsilon^T]$ are dielectric constants at constant stress.

For piezoelectric transversely isotropic materials, the compliance matrix $[s^E]$, the piezoelectric constants $[d]$, and the dielectric constants $[\varepsilon^T]$ are shown in Eqn. (D.6), Eqn. (D.7) and Eqn. (D.8), respectively. Voigt's notation is used for presenting symmetric tensors here. Therefore the double subscripts can be replaced with a single notation following: 11 → 1, 22 → 2, 33 → 3, 23/32 → 4, 13/31 → 5, 12/21 → 6, such as in Eqn. (4.6).

$$\mathbf{s^E} = \begin{bmatrix} \mathbf{s}_{11}^E & \mathbf{s}_{12}^E & \mathbf{s}_{13}^E & 0 & 0 & 0 \\ \mathbf{s}_{12}^E & \mathbf{s}_{11}^E & \mathbf{s}_{13}^E & 0 & 0 & 0 \\ \mathbf{s}_{13}^E & \mathbf{s}_{13}^E & \mathbf{s}_{33}^E & 0 & 0 & 0 \\ 0 & 0 & 0 & \mathbf{s}_{55}^E & 0 & 0 \\ 0 & 0 & 0 & 0 & \mathbf{s}_{55}^E & 0 \\ 0 & 0 & 0 & 0 & 0 & \mathbf{s}_{66}^E \end{bmatrix} \tag{4.3}$$

$$\mathbf{d} = \begin{bmatrix} 0 & 0 & d_{31} \\ 0 & 0 & d_{31} \\ 0 & 0 & d_{33} \\ 0 & d_{15} & 0 \\ d_{15} & 0 & 0 \\ 0 & 0 & 0 \end{bmatrix} \tag{4.4}$$

$$\varepsilon^{\mathbf{T}} = \begin{bmatrix} \varepsilon_{11}^T & 0 & 0 \\ 0 & \varepsilon_{11}^T & 0 \\ 0 & 0 & \varepsilon_{33}^T \end{bmatrix} \tag{4.5}$$

$$\mathbf{C_{ijkl}} = \begin{bmatrix} C_{1111} & C_{1122} & C_{1133} & C_{1123} & C_{1113} & C_{1112} \\ C_{1122} & C_{2222} & C_{2233} & C_{2223} & C_{2213} & C_{2212} \\ C_{1133} & C_{2233} & C_{3333} & C_{3323} & C_{3313} & C_{3312} \\ C_{1123} & C_{2223} & C_{3323} & C_{2323} & C_{2313} & C_{2312} \\ C_{1113} & C_{2213} & C_{3313} & C_{2313} & C_{1313} & C_{1312} \\ C_{1112} & C_{2212} & C_{3312} & C_{2312} & C_{1312} & C_{1212} \end{bmatrix} =$$

$$\mathbf{C_{pq}} = \begin{bmatrix} C_{11} & C_{12} & C_{13} & C_{14} & C_{15} & C_{16} \\ C_{21} & C_{22} & C_{23} & C_{24} & C_{25} & C_{26} \\ C_{31} & C_{32} & C_{33} & C_{34} & C_{35} & C_{36} \\ C_{41} & C_{42} & C_{43} & C_{44} & C_{45} & C_{46} \\ C_{51} & C_{52} & C_{53} & C_{54} & C_{55} & C_{56} \\ C_{61} & C_{62} & C_{63} & C_{64} & C_{65} & C_{66} \end{bmatrix} \tag{4.6}$$

Eqn. (D.3) can also be expressed as two equations (D.4) and (D.5). Among them, Eqn. (D.5) is used for calculating the piezoelectric coefficient d_{33} of the PZT-silane nanocomposite thin films. This equation shows the accumulated charge density D_i has two sources, one part is from the mechanical strain $d_{ikl}T_{kl}$ and the other part is from the capacitance $\varepsilon^T_{ik}E_k$.

$$S_{ij} = s^E_{ijkl}T_{kl} + d_{kij}E_k \tag{4.7}$$

$$D_i = d_{ikl}T_{kl} + \varepsilon^T_{ik}E_k \tag{4.8}$$

The electric displacement (or charge density) D is related to the charge Q generated by Eqn. (4.9), where A_i is the area of the plane that is normal to the i-axis. In the experiment, only the planes that are normal to the poling axis (3-axis) have electrodes for the charges to gather. Hence $D_1 = 0$, $D_2 = 0$ and the charge Q is linked to D_3 directly by Eqn. (4.10). When characterizing d_{33} using a impact force and recording its charge response Q via a charge amplifier, an open-circuit condition is created, so that there is no net charge going in or out of the electrodes, thus $D_3 = d_{33}T_3 + \varepsilon_{33}^T E_3 = 0$. As a result, the piezoelectric coefficient d_{33} can be estimated by Eqn. (4.11). For a parallel plate capacitor mentioned in Section 3.1.2, the charge Q can also be expressed as Eqn. (3.8) and (3.9). The electric filed in the 3 direction E_3 can then be derived as Eqn. (4.12). In addition the stress in the 3 direction can be linked to the applied force F_3 using Eqn. (4.13). Substituting Eqn. (4.12) and (4.13) into (4.11), piezoelectric coefficient d_{33} is found to be proportional to the ratio of Q/F_3, as shown in (4.14). This is the theoretical foundation for the subsequent experiments and analysis.

$$Q = \int\int \begin{bmatrix} D_1 & D_2 & D_3 \end{bmatrix} \begin{bmatrix} dA_1 \\ dA_2 \\ dA_3 \end{bmatrix} \tag{4.9}$$

$$Q = D_3 \times A_3 \tag{4.10}$$

$$d_{33} = -\frac{\varepsilon_{33}^T E_3}{T_3} \tag{4.11}$$

$$E_3 = \frac{V_3}{t} = \frac{Q}{\varepsilon_{33}^T A_3} \tag{4.12}$$

$$T_3 = \frac{F_3}{A_3} \tag{4.13}$$

$$d_{33} = -\frac{Q}{F_3} \tag{4.14}$$

4.3 Specimen Preparation

To evaluate piezoelectric performance in the 33[2]-direction, a force F_3 (downward) is applied on the top surface of the PZT-silane films and the generated charge Q is measured. Therefore, the PZT-silane films made with the recipe in Section 2.1.3 needs to be slightly modified in order to withstand the force and export the charge.

To protect the top electrode and withstand the applied force, a droplet of epoxy is added on the top electrode. Silver paster is applied between the top and bottom electrodes with external lead wires for interconnects, so that the produced charge can be exported. The silver paste needs to be cured at 120°C for 30 minutes and reinforced with epoxy after curing.

After all the preparations have been made, the specimens are glued onto an aluminum block via epoxy and poled at room temperature for 18 hours at 24V (DC voltage) across the PZT-silane film between the top and bottom electrodes.

4.4 Experimental Setup

A simple and cost-effective experimental approach, which was developed by a former Ph.D student Q. Guo [74], is adopted here for characterization of the new PZT-silane thin film's piezoelectric coefficient d_{33}. The method uses an electric motor driving a mini impact hammer to excite bulk PZT thin film. The impact force is recorded through the load cell that is on the hammer tip, and simultaneously the corresponding charge produced by the thin film is measured through a charge amplifier. The experimental setup for measuring bulk PZT thin film's piezoelectric properties is presented in Fig. 4.2. This method was repeated on bulk PZT thin films and obtained successful results. Figure 4.3 is one of the results showing the charge generated across bulk PZT thin film in Channel 2 in response of the applied force in Channel 1.

However, a few adjustments need to be made in instrumentation before applying this

---

[2] The double subscript in the piezoelectric coefficients indicate the link between the electrical and mechanical directions. The first subscript is the direction of electric field or charge and the second is the direction of mechanical stress or strain.

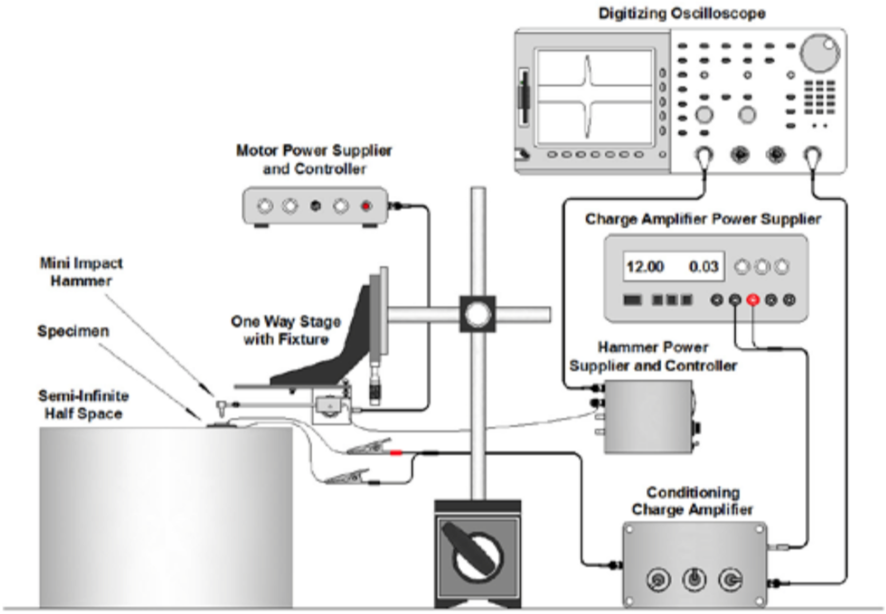

Figure 4.2: Experimental setup for bulk PZT thin films' piezoelectric measurements [75]

method to measuring the charge response of PZT-silane thin films, since the charge to be measured is tiny. First, a double-end charge amplifier is used to float the measured charge. Second, the use of electric motor is no longer possible, because the electrical noise it produced will compromise the signal significantly. Figure 4.4 shows the noise level with the plug-in electric motor is 216 mV and without is 33.6 mV. Therefore, by removing the plug-in electric motor, the noise level can be reduced by 500%. Third, all parts are properly grounded to avoid ground loops. Unfortunately no matter how well all units are grounded, the housing of impact hammer still carries a tiny amount of electric charge forming a parallel capacitor with the PZT-silane film as the hammer approaches the film. Therefore last but not least, a wooden or bamboo stick (Fig. 4.5 (b)) is introduced between the hammer and the PZT-silane film to remove the parallel capacitor effect while maintaining the transmitted force as much as possible as shown in Fig. 4.5.

Figure 4.6 shows the schematic diagram of experimental setup for evaluating PZT-silane

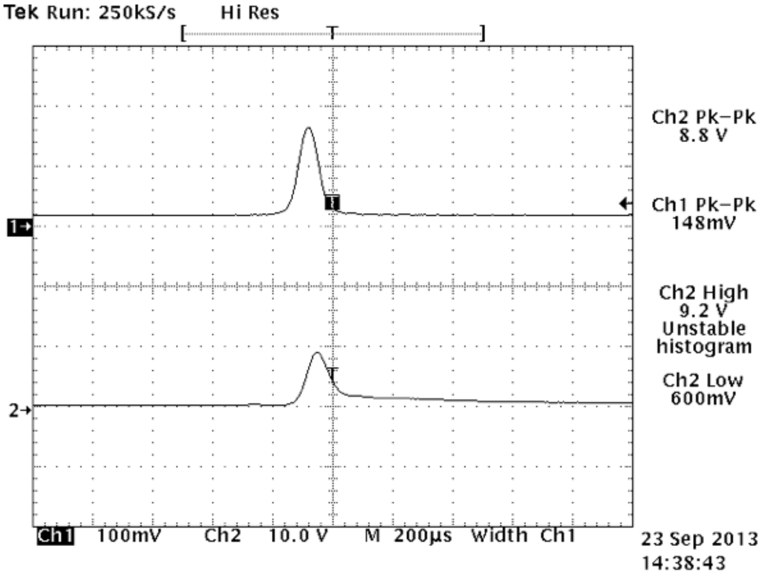

Figure 4.3: Charge-force measurement in time domain of a bulk PZT thin film under impact test: top trace (Channel 1) from impact force F_3 and bottom trace (Channel 2) from produced charge Q

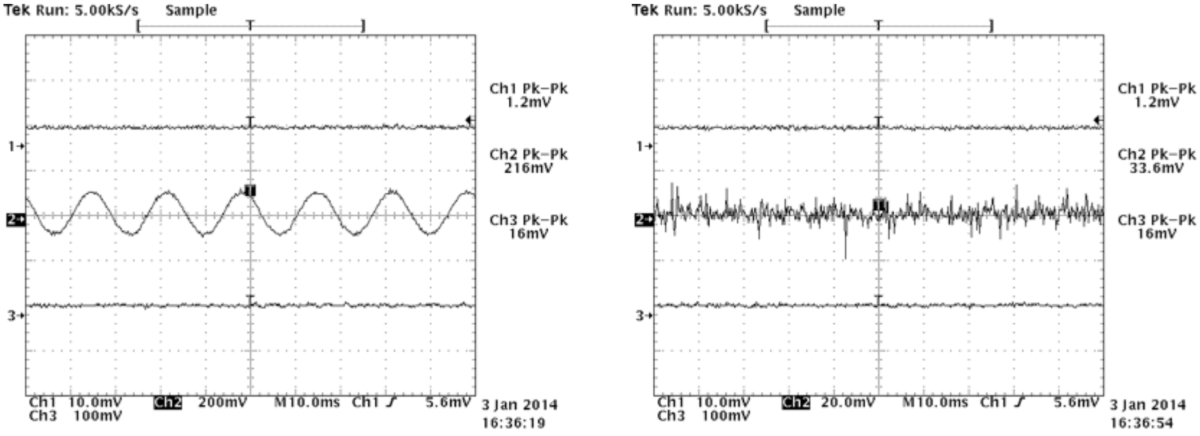

(a) With plug-in electric motor

(b) Without plug-in electric motor

Figure 4.4: Noise level with or without plug-in electric motor

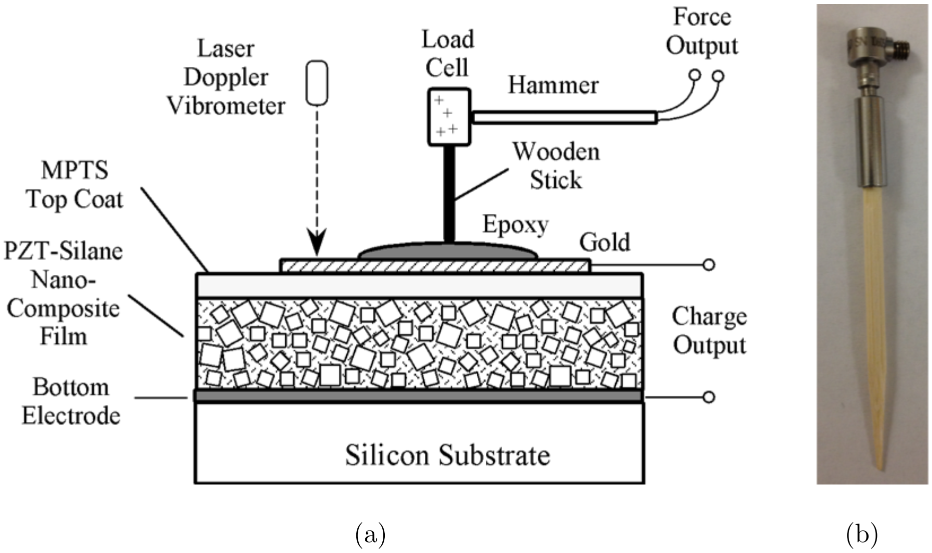

Figure 4.5: Schematic diagram of special adjustments in experimental setup (not to scale): (a) Experimental setup (b) Hammer tip with bamboo stick

thin films' piezoelectric performance. An impact hammer taps on the epoxy that protects the top electrode to generate an impact force to the PZT-silane film. The load cell at the tip of impact hammer measures the applied force F[3] under the conversion of 22 mV/N. In the meantime, electric charge generated by the PZT-silane film is recorded via a charge amplifier between the top and bottom electrodes. The working frequency range of the charge amplifier is from 10 Hz to 10.6 kHz, and the sensitivity is 100 mV/pC. A laser Doppler vibrometer monitors the velocity of top electrode for reference with a sensitivity of 25 $mm/s/V$. Finally, the impact force F, electric charge Q, and the velocity V are measured in the time domain via a digital oscilloscope. Table 4.3 lists the equipment and their sensitivities used during the measurements.

---

[3] F_3 is labeled as F for simplicity for the rest of the chapter.

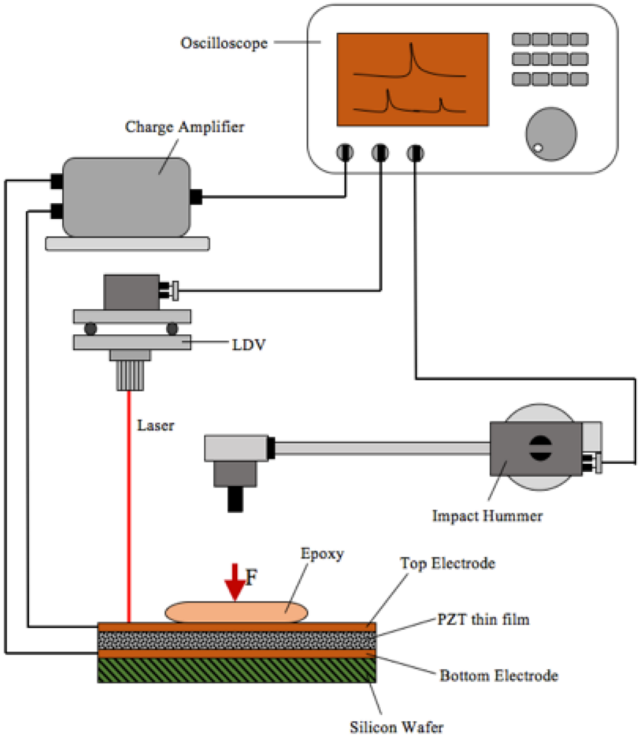

Figure 4.6: Schematic diagram of experimental setup to evaluate piezoelectric performance of PZT-silane films

Table 4.3: List of equipment and their sensitivities used during experiments

Instrument	Model	Sensitivity
Impact Hammer	PCB Piezotronics, Model No. 086E80	22 mV/N
Charge Amplifier	*Brüel* & Kjær, Preamplifier Type 2663	100 mV/pC
Laser Doppler Vibrometer	Polytec, OFV-3001	25 $mm/s/V$
Digital Oscilloscope	Tektronix, TDS540A	N/A

4.5 Experimental Results and Discussion

By varying the impact force F and measuring the corresponding electric charge Q, a force-charge relationship can be obtained and used to evaluate piezoelectric performance of the fabricated PZT-silane films. There are, however, two things worth noting. First, the force-charge relationship is not quite the piezoelectric constant d_{33} of the PZT-silane films. Because the force-charge relationship depends on the substrate material's properties, thickness of the films, and many other factors [74]. Second, the impact force recorded, technically speaking, is not exactly the same as force transmitted to the PZT-silane film because the epoxy has some inertia. Part of the impact force is used to accelerate the epoxy, and the rest is transmitted to the PZT-silane film. As long as the inertia of the epoxy is small enough, the force-charge relationship should be reasonably accurate.

Four specimens with PZT nanoparticles (specimen label starting with NS) and four specimens with crushed PZT particles (specimen label starting with NB) were tested. Measurements for one specimen are presented and explained in detail as follows.

Then measurements of all specimens are presented, compared and discussed.

Figure 4.7 shows one of the time-domain measurements for specimen NS1 from the oscilloscope. The top trace (Ch 1) is from the impact force F, the middle trace (Ch 2) is from the electric charge generated Q, and the bottom trace (Ch 3) is from the velocity V. The impact force F appears in a form of a major impulse, followed by a couple of very small residual ripples. These residual ripples might be caused by the elasticity of epoxy. The measured electric charge Q appears only in one major impulse and is in sync with the measured impact force F. The measured velocity V shows significant oscillations, because it captures the vibration of the entire experimental setup (i.e., specimens, substrate, and supporting fixture).

The maximum amplitudes of the impact force F and the electric charge Q from measurements such as Fig. 4.7 are then plotted in Fig. 4.8 to reveal a force-charge relationship by varying the impact force and repeating the test. Figure 4.8 shows that the force-charge

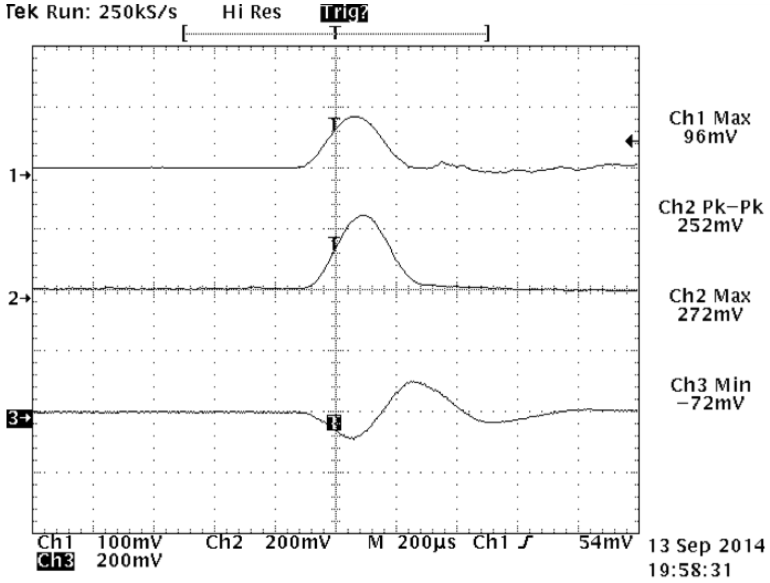

Figure 4.7: Specimen NS1 time-domain measurement; top trace (Ch 1) from impact force F, middle trace (Ch 2) from electric charge Q, and bottom trace (Ch 3) from velocity V

response is very linear with a slope of 0.65 pC/N. This non-zero slope indicates the amount of charge generated per unit force (termed charge-to-force ratio hereafter), and it is a representation of piezoelectric performance of the PZT-silane film. This test protocol is repeated to all test specimens.

Table 4.4 presents specimens' top electrode areas, thicknesses and the measurement results of Q/F ratio for expedited hydrothermally grown PZT nanoparticles thin films. The charge-to-force ratios of 4 specimens (NS1, NS2, NS3, NS4) containing PZT nanoparticles are very close, ranging from 0.38 to 0.67 pC/N. Since all samples are poled under a DC voltage of 24V, the one with a smaller thickness will get a larger poling electric field magnitude. NS1 and NS3 have higher charge-to-force ratios, this is probably due to the fact that they are thinner.

Table 4.5 shows crushed PZT particles thin films' top electrode areas, thicknesses and the measured Q/F ratios. The four specimens (NB1, NB6, NB3, NB4) with crushed PZT

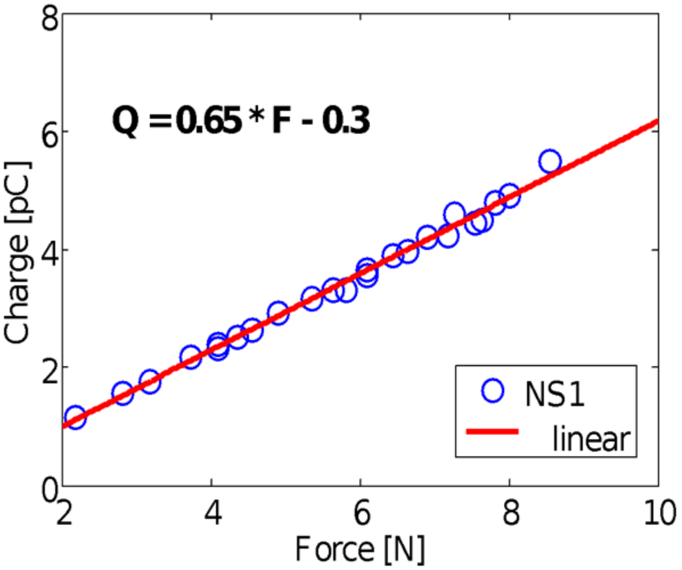

Figure 4.8: NS1 measured force-charge relationship in the time domain

particles have charge-to-force ratios from 1.91 to 8.41 pC/N, which are higher than expedited hydrothermally grown PZT nanoparticles thin films. Hence in terms of charge-to-force ratios, the crushed PZT particles outperform the hydrothermally grown PZT nanoparticles approximately by a factor of 5 to 10. In view of the higher crystallinity of the crushed PZT particles as compared with the crystallinity of the hydrothermal PZT particles, this might be expected.

Table 4.4: Measured Q/F ratios for expedited hydrothermally grown PZT nanoparticles thin films

Specimen	**Top Electrode Area** (mm^2)	**Thickness** (μm)	**Poling Electric Field** ($V/\mu m$)	**Charge/Force Ratio** (pC/N)
NS1	72	7.79	3.08	0.65
NS2	64	8.23	2.92	0.43
NS3	80	7.9	3.04	0.67
NS4	50	9.62	2.5	0.38

Table 4.5: Measured Q/F ratios for crushed PZT particles thin films

Specimen	**Top Electrode Area** (mm^2)	**Thickness** (μm)	**Poling Electric Field** ($V/\mu m$)	**Charge/Force Ratio** (pC/N)
NB1	63	4.11	5.84	2.91
NB6	77	5.03	4.77	1.91
NB3	64	4.76	5.04	4.72
NB4	36	3.41	7.04	8.41

4.6 Finite Element Analysis for d_{33} Estimation

The linear force-charge relation in Fig. 4.8 proves the existence of piezoelectricity in PZT-silane thin films. However, the piezoelectric coefficient d_{33} has not yet been estimated. As explained earlier, the charge response of PZT-silane thin films is always coupled to their host structure. Therefore, the charge-to-force ratio is not simply the piezoelectric coefficient d_{33}.

One simple way to estimate d_{33} of piezoelectric thin films is to use finite element analyses [74]. The approach is listed as follows.

1. Create a finite element model of the experimental setup, including the piezoelectric thin film and the substrate with appropriate boundary conditions and material properties.
2. Assume tentatively that the piezoelectric thin film is made from a bulk PZT material whose piezoelectric coefficients are well known (e.g, PZT-5A).
3. Predict the charge-to-force ratio using the finite element model under the assumption made in the previous step.
4. Compare the experimentally measured charge-to-force ratio and the predicted ratio to estimate d_{33}. For example, if the measured charge-to-force ratio is 10% of that predicted by a finite element model employing PZT-5A as a reference, the piezoelectric coefficients of PZT-silane films are 10% of those of PZT-5A. In principle, it is the same approach as in [62] but more elaborate.

Based on the approach outlined above, an finite element analysis was conducted to extract d_{33}. Figure 4.9 shows a finite element model of the specimen NS1 with the experimental setup shown Fig. 4.6. The model consists of a host structure (a thick aluminum block) and a PZT-silane specimen as presented in Fig. 4.9 (a). The specimen is located at the center of the host structure. Figure 4.9 (b) shows a close up image of the PZT-silane sensor and the applied force location (at the center of the top epoxy). The PZT-silane sensor itself consists of a silicon substrate, a bottom electrode layer, a PZT-silane nano-composite layer, an MPTS topcoat, a top electrode layer, and a piece of protective epoxy on top; see Fig. 4.9 (b) and Fig. 4.9 (c). Note that the epoxy layer gluing the PZT sample to the host structure is also modelled (cf. bottom epoxy in Fig. 4.9 (b)). Figure 4.9 (d) shows the boundary condition of the model, which is a fixed support at the bottom of the Al block.

The PZT-silane layer was modelled using piezoelectric element, and the rest of the model was created via solid element. For the electrical boundary conditions, voltage of the nodes on the bottom surface of the PZT-silane layer was set to zero (grounded). All the nodes on the top surface of the PZT-silane layer was set to be identical but as an unknown variable to be calculated from the finite element analysis.

Table 4.6 shows the dimensions, density, Young's modulus, and Poissons ratio for each layer (except for the PZT-silane film) used in the finite element model. As explained earlier, a reference PZT material would be chosen for the PZT-silane film layer as a baseline. In this simulation, PZT-4 was used. The material properties of PZT-4 used are provided below.

- Density: $\rho = 7500 \quad kg/m^3$

- Compliance matrix:

$$\mathbf{s^E} = \begin{bmatrix} 12.3 & -4.05 & -5.31 & 0 & 0 & 0 \\ -4.05 & 12.3 & -5.31 & 0 & 0 & 0 \\ -5.31 & -5.31 & 15.5 & 0 & 0 & 0 \\ 0 & 0 & 0 & 39 & 0 & 0 \\ 0 & 0 & 0 & 0 & 39 & 0 \\ 0 & 0 & 0 & 0 & 0 & 32.7 \end{bmatrix} \times 10^{-12} \, \frac{m^2}{N} \qquad (4.15)$$

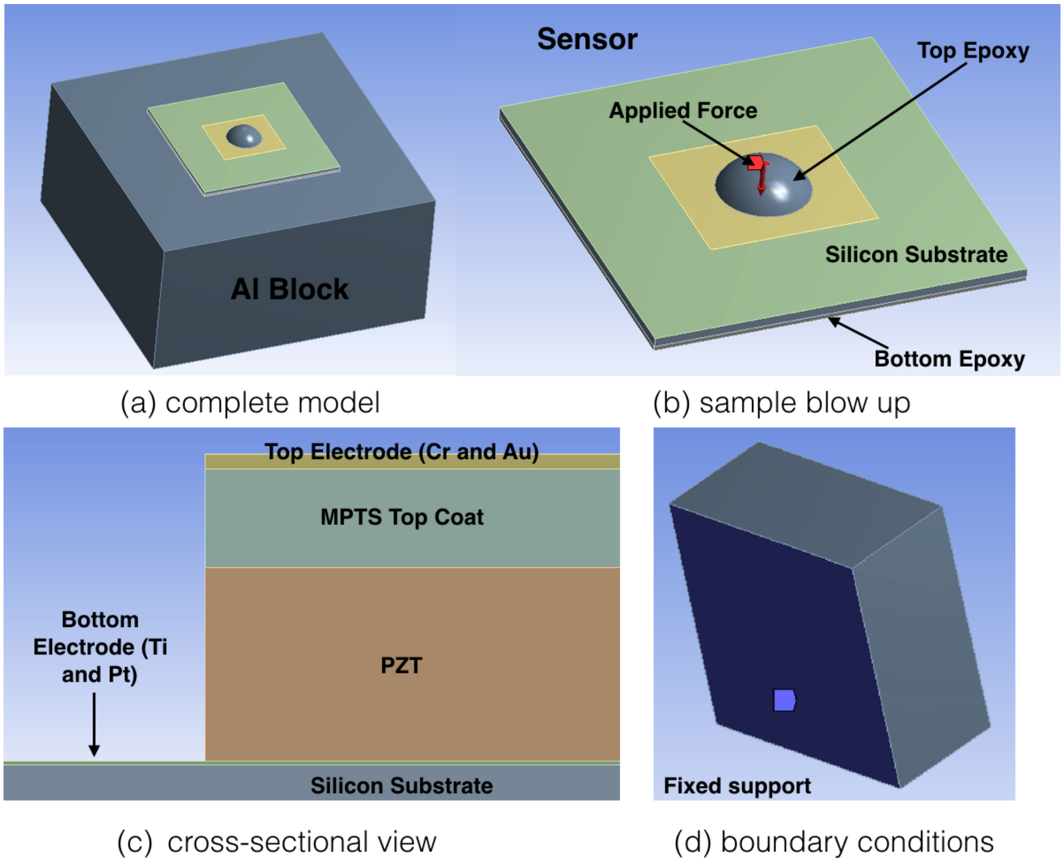

(a) complete model (b) sample blow up (c) cross-sectional view (d) boundary conditions

Figure 4.9: Finite element model to extract d_{33}: (a) the complete model (upper left), (b) view of the sample (upper right), (c) cross-sectional view (lower left) and (d) boundary conditions (lower right)

- Piezoelectric matrix:

$$\mathbf{d} = \begin{bmatrix} 0 & 0 & -123 \\ 0 & 0 & -123 \\ 0 & 0 & 289 \\ 0 & 496 & 0 \\ 496 & 0 & 0 \\ 0 & 0 & 0 \end{bmatrix} \times 10^{-12}\ \frac{C}{N} \tag{4.16}$$

Table 4.6: Dimensions and material properties of the finite element model

	Block Al	**Epoxy glue**	**Si**	**Pt**	**MPTS**	**Au**	**Epoxy top**
Length (mm)	40	20	20	20	Same as film size		
Width (mm)	40	20	20	20	Same as film size		
Radius (mm)							2.4
Thickness (μm)	2×10^4	250	500	0.15	4	0.6	1500
Density (kg/m^3)	2770	1250	2330	21450	1250	19280	1250
Young's Modulus (GPa)	71	3.5	202	168	2	80	3.5
Poisson's Ratio	0.33	0.33	0.33	0.38	0.33	0.42	0.33

- Dielectric matrix:

$$\frac{\varepsilon^{\mathbf{T}}}{\varepsilon_{\mathbf{o}}} = \begin{bmatrix} 1475 & 0 & 0 \\ 0 & 1475 & 0 \\ 0 & 0 & 1300 \end{bmatrix}, \ \varepsilon_{\mathbf{o}} = 8.854 \times 10^{-12} \, \frac{F}{m} \tag{4.17}$$

Under these conditions, a static analysis was performed to find out the strain distribution and the charge-to-force ratio of the PZT thin film layer. Although an impact force is applied in the experiment, the inertia of the PZT-silane film is so small compared with the structure that the deformation of the PZT-silane is indeed quasi-static. In the simulation, a unit static force is applied to the center of the protective epoxy. Deformation of the test setup (i.e., the hosting structure and the specimen) and the resulting voltage of the PZT-silane layer are calculated. The charge generated by the PZT-silane film is then calculated via $q = CV$, where C is the theoretical capacitance of the film and V is the calculated voltage across the PZT-silane film.

Figure 4.10 shows the strain distribution of the PZT-silane layer under the concentrated load. The strain is localized at the specimen, in particular, within a circle of $2 - mm$ radius around the concentrated load. Outside this circle, the strain is virtually zero and consequently the four corners of the PZT-silane film do not experience any deformation.

Table 4.7 and Table 4.8 lists the calculated charge-to-force ratios from the finite element analysis based on PZT-4 for all 8 specimens (dimensions and thicknesses were varied). There are several things worth noting here. First, PZT-silane films from crushed PZT particles (Tab. 4.8) do not behave like bulk PZT. The films have an estimated ranging from 1.85% to 9.8% of bulk PZT-4. There may be multiple reasons causing the low values. For example, the PZT-silane films have much smaller compliance and dielectric matrices, and the PZT-silane film may have been poled at a too low electric field. Nevertheless, the results indicate that the PZT-silane films are piezoelectric and their could be roughly estimated.

In comparison, the PZT-silane films with PZT nanoparticles have an estimated d_{33} ranging from 0.4% to 0.6% of bulk PZT-4 as shown in Tab. 4.7. Obviously, the PZT-silane films with crushed PZT particles have a higher d_{33}. There might be several factors contributing to the difference in d_{33}. For example, the thin films made from crushed PZT particles have smaller thickness and thus a larger poling electric field resulting in better piezoelectric performance. As explained earlier, PZT nanoparticles are not expected to outperform the crushed PZT particles due to the presence of lead oxide and room for better process control. The crushed PZT particles that are commercially available are stoichiometrically optimized and have accurate composition to maximize its piezoelectric performance.

Since the stiffness property of PZT-silane film is unknown, the effect of assumed Young's modulus was also studied to see how sensitive the simulated charge-to-force ratio depends on the stiffness property. For the PZT-silane films, numerous hard PZT particles are embedded in a soft silane matrix. The lower bound of the film stiffness should be the stiffness of the silane matrix. Therefore a series of finite element analyses were conducted with assumed Young's modulus of the thin films as 0.1%, 1%, 10% and 100% of that of bulk PZT-4, where the film stiffness of 0.1% is roughly in the range of a soft polymer. Table 4.9 shows the effect of

Young's modulus of PZT nanoparticles thin films and Tab. 4.10 shows the Effect of Young's modulus of PZT crushed particles thin films. Under these conditions, the charge-to-force ratio changes roughly 20% and does not significantly affect the extracted d_{33}.

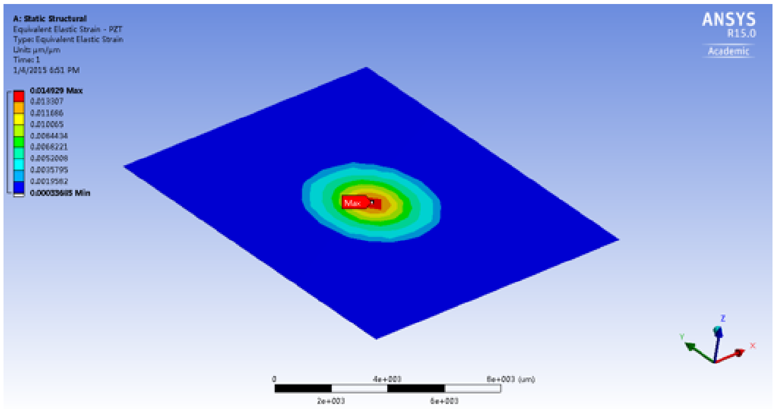

Figure 4.10: Strain distribution under a concentrated load

Table 4.7: Piezoelectric coefficient d_{33} of NS specimens estimated from the finite element analysis

Used 100% PZT-4 Properties in FE	NS1	NS2	NS3	NS4
Length (mm)	8	8	8	10
Width (mm)	9	8	10	5
Area (mm^2)	72	64	80	50
Thickness (μm)	7.79	8.227	7.899	9.616
$\frac{\varepsilon^{\mathbf{S}}}{\varepsilon_{\mathbf{o}}}$	663	663	663	663
$\varepsilon_o \quad (pF/m)$	8.854	8.854	8.854	8.854
Simulated Voltage (mV)	1.98	2.34	1.8	2.87
Calculated Q/F ratio (pC/N)	107.6	106.7	107.1	87.53
Experimental result (pC/N)	0.65	0.43	0.67	0.38
Estimated d_{33} (in percentage of PZT-4)	0.60%	0.40%	0.63%	0.43%

Table 4.8: Piezoelectric coefficient d_{33} of NB specimens estimated from the finite element analysis

Used 100% PZT-4 Properties in FE	NB1	NB6	NB3	NB4
Length (mm)	7	7	8	6
Width (mm)	9	11	8	6
Area (mm^2)	63	77	64	36
Thickness (μm)	4.109	5.029	4.758	3.414
$\frac{\varepsilon^{\mathbf{S}}}{\varepsilon_{\mathbf{o}}}$	663	663	663	663
$\varepsilon_o \quad (pF/m)$	8.854	8.854	8.854	8.854
Simulated Voltage (mV)	1.16	1.15	1.36	1.39
Calculated Q/F ratio (pC/N)	104.4	103.2	107	85.78
Experimental result (pC/N)	2.91	1.91	4.72	8.41
Estimated d_{33} (in percentage of PZT-4)	2.79%	1.85%	4.41%	9.80%

Table 4.9: Effect of Young's modulus of PZT nanoparticles thin films

Assuming Young's Modulus of the thin film as x% of that of PZT-4		**NS1**	**NS2**	**NS3**	**NS4**
x = 0.1%	ε_r^s	1299	1299	1299	1299
	Simulated voltage (V)	1.23E-3	1.46E-3	1.12E-3	2.19E-3
	Q/F ratio (pC/N)	130.86	130.86	130.86	130.98
	d_{33} (% of PZT-4)	0.50%	0.33%	0.51%	0.29%
x = 1%	ε_r^s	1294	1294	1294	1294
	Simulated voltage (V)	1.23E-3	1.46E-3	1.13E-3	2.19E-3
	Q/F ratio (pC/N)	130.52	130.52	130.52	130.3
	d_{33} (% of PZT-4)	0.50%	0.33%	0.51%	0.29%
x = 10%	ε_r^s	1236	1236	1236	1236
	Simulated voltage (V)	1.28E-3	1.52E-3	1.17E-3	2.23E-3
	Q/F ratio (pC/N)	129.7	129.6	129.63	127.1
	d_{33} (% of PZT-4)	0.50%	0.33%	0.52%	0.30%
x = 100%	ε_r^s	663	663	663	663
	Simulated voltage (V)	1.98E-3	2.34E-3	1.8E-3	2.87E-3
	Q/F ratio (pC/N)	107.56	106.74	107.12	87.53
	d_{33} (% of PZT-4)	0.60%	0.40%	0.63%	0.43%

Table 4.10: Effect of Young's modulus of PZT crushed particles thin films

Assuming Young's Modulus of the thin film as x% of that of PZT-4		**NB1**	**NB2**	**NB3**	**NB4**
x = 0.1%	ε_r^s	1299	1299	1299	1299
	Simulated voltage (V)	7.42E-04	7.43E-04	8.46E-04	1.08E-03
	Q/F ratio (pC/N)	130.87	130.88	130.87	130.85
	d_{33} (% of PZT-4)	2.22%	1.46%	3.61%	6.43%
x = 1%	ε_r^s	1294	1294	1294	1294
	Simulated voltage (V)	7.43E-04	7.44E-04	8.47E-04	1.08E-03
	Q/F ratio (pC/N)	130.49	130.48	130.52	130.26
	d_{33} (% of PZT-4)	2.23%	1.46%	3.62%	6.46%
x = 10%	ε_r^s	1236	1236	1236	1236
	Simulated voltage (V)	7.70E-04	7.70E-04	8.80E-04	1.10E-03
	Q/F ratio (pC/N)	129.27	129.12	129.62	126.86
	d_{33} (% of PZT-4)	2.25%	1.48%	3.64%	6.63%
x = 100%	ε_r^s	663	663	663	663
	Simulated voltage (V)	1.98E-3	2.34E-3	1.8E-3	2.87E-3
	Q/F ratio (pC/N)	107.56	106.74	107.12	87.53
	d_{33} (% of PZT-4)	2.79%	1.85%	4.41%	9.80%

Chapter 5

THIN FILM DEMONSTRATION AS AN ACTUATOR AND A VIBRATION SENSOR

Piezoelectric sensors and actuators used in this chapter are manufactured from PZT nanoparticles ink. When deformed, the fabricated PZT-silane thin films produce electrical charges serving as sensors. When driven electrically, these thin films deform acting as actuators.

5.1 Actuator Application

The objective of in this section is the applications of PZT-silane thin films. They have been successfully demonstrated as a actuator and a vibration sensor. This section will mainly focus on fabrication and demonstration a new PZT-silane nano-composite actuator that is bonded on a flexible kapton tape cantilever beam.

5.1.1 Fabrication of PZT Thin Film Actuator

A prototype PZT-silane thin film actuator is fabricated using the following procedures. The PZT-silane thin film is drop-cast and surface bonded near the clamped edge of the flexible kapton tape cantilever beam for maximum strain.

1. Print a silver layer (Ag) on the kapton substrate to form bottom electrode on a flexible substrate.

2. Cut the kapton tape into a 30 mm by 5 mm rectangle (dimensions may vary), as shown in Fig. 5.1.

3. Drop-cast PZT ink (2012 UW PZT Ink) into a 10 mm by 4 mm rectangle thin film (dimensions may vary) and cure the film under UV light for 5 min. This procedure can be repeated for several times in order to form a desired film thickness. In this experiment, the current step was repeated 1 time. Thus there are two ink drop-cast layers in the final deposited ink.

4. Cure the final deposited ink under UV light for 1.5 hours and then in furnace at 120°C for 12 hours.

5. Deposit a topcoat with diluted MPTS on top of the film. Cure the topcoat layer in furnace at 120°C for 12 hours.

6. A gold on chromium layer is then deposited by e-beam evaporation as top electrode.

7. Connect the top and bottom electrodes through lead wires and use epoxy to secure the wires. The fabricated PZT-silane thin film actuator is shown in Fig. 5.2.

The challenges associated with using this substrate are (a) the kapton tape is uneven, (b) the silver bottom electrode surface is rough and porous, which make it difficult to drop cast thin films with small surface roughness and (c) the wettability of the printed silver bottom electrode was poor. As a result, PZT ink droplets on the bottom electrode surface had spherical form rather than spread out as a sheet of thin film, causing the formation of a thick PZT layer. The thickness of the PZT layer could be reduced, if proper surface treatment is perform before the deposition, such plasma surface treatment.

The actuator specimen fabricated using the procedures listed in Section 5.1.1 will be referred to as "E3" for the rest of the thesis. The last step in the fabrication of a PZT-silane thin film actuator is the poling process. PZT thin film actuator E3 was poled under 24V for 12 hours. E3 before the poling process will be referred to as "Pre-pole E3", whereas E3 after the poling process will be referred to as "Poled E3". The impedance measurement and results for 'Pre-pole E3" and "Poled E3" can be found in Fig. B.1 of Appendix B.

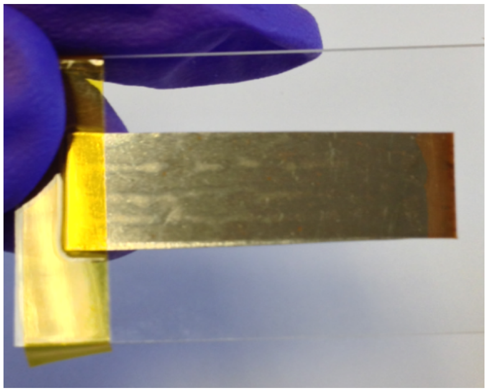

Figure 5.1: Kapton tape with deposited Ag layer

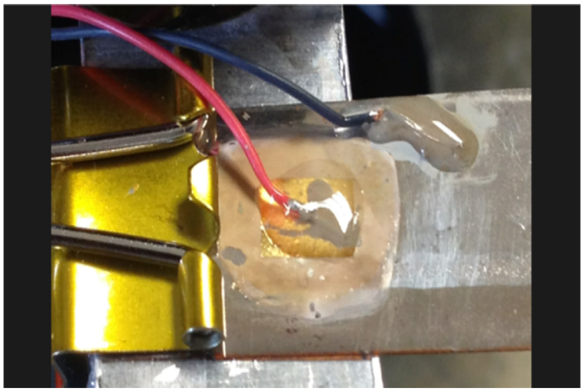

Figure 5.2: PZT-silane nano-composite actuator

5.1.2 Experiment Setup

Figure 5.3 shows the setup for the actuator test on a cantilever beam. The PZT thin film was attached to the beam, which is made from a kapton tape, close to the clamped/fixed edge for maximum constraint. The fixed boundary condition was first created by using a binder clip, and the experiment setup for this configuration and all the test data generated are provided in Appendix E. Later a C-clamp was used to fix the kapton tape beam and similar results have been obtained for the new boundary condition setup. Thus only one set of data will be explained here, which is the experimental setup for PZT-silane thin film actuator E3 with C-clamp shown in Fig. 5.4.

The test setup includes a dynamic signal analyzer (referred to as spectrum analyzer in Fig. 5.3), an oscilloscope, a power amplifier and a laser Doppler vibrometer (LDV). Their models and sensitivity information can be found in Tab. 7.3. The built-in function generator in the dynamic signal analyzer was used to generate the desired sinusoidal wave input in varies frequencies. However, the amplitude of the input voltage/current is not big enough to drive the beam to any notable vibration. Hence a power amplifier was utilized to boost the input signal.

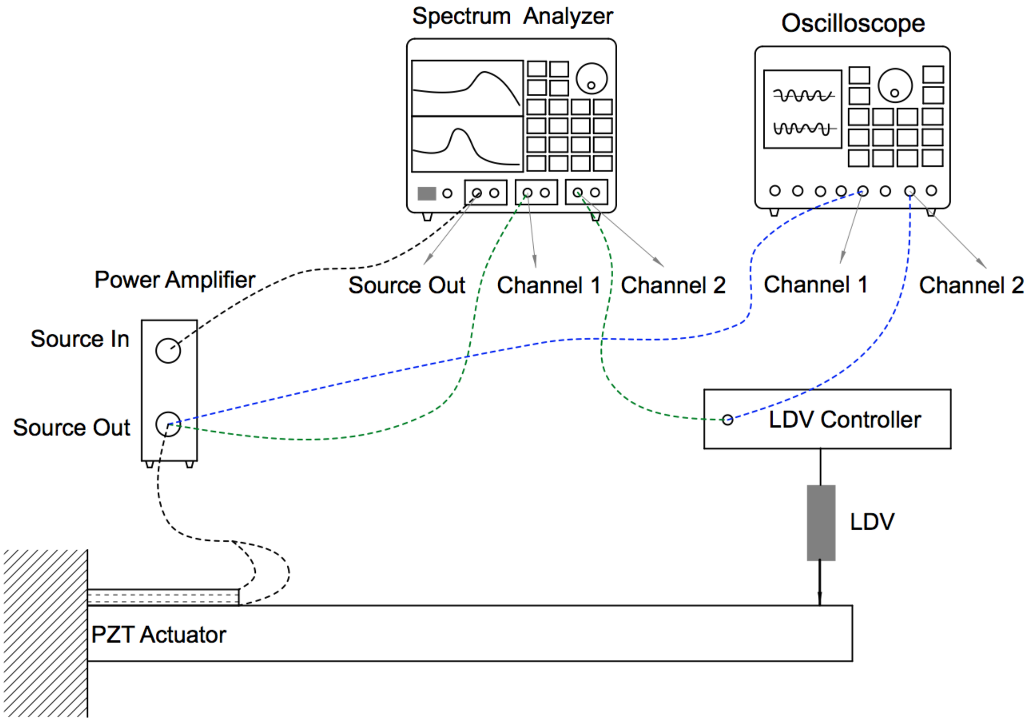

Figure 5.3: Schematic diagram of the experimental setup for PZT actuator demonstration

5.1.3 Test Plan and Results

The test plan for PZT-silane thin film actuator E3 consists of two steps.

1. Identify the resonance frequencies of the cantilever beam under test.

2. Demonstrate that the PZT-silane thin film actuator can excite the cantilever beam into vibration at the same frequency as the driving frequency of the input signal.

5.1.3.1 Swept Sine Frequency Response

In the first part of the experiments, a spectrum analyzer and a power amplifier were used to drive the PZT-silane thin film actuator E3 with swept sine from 40 Hz to 5 kHz. Vibration of the PZT-silane thin film actuator E3 produced deflection in the cantilever beam, which

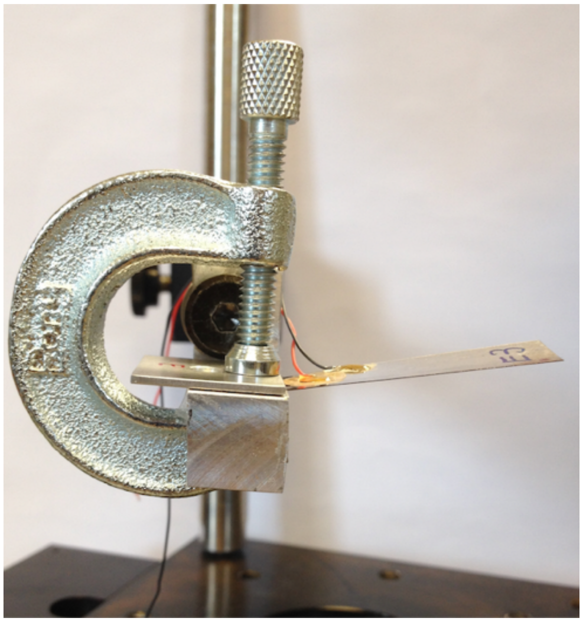

Figure 5.4: Experimental setup for PZT-silane thin film actuator E3 with C-clamp

was maximum at the free end. Thus a laser Doppler vibrometer (LDV) was used to capture this vibration of the beam at the corner of its free end, which was marked with a red dot as shown in the photo of the test specimen (Fig. 5.5).

The spectrum analyzer was then used to produce frequency response functions (FRF) of the vibration of the cantilever beam via LDV measurements (Channel 2 in Fig. 5.3) and PZT actuation voltage via power amplifier (Channel 1 in Fig. 5.3). Figure 5.3 shows the connection of those two channels for swept sine frequency response in green dashed line.

Figure 5.6 shows the measured swept sine FRF of beam tip velocity over driving voltage for the poled PZT thin film actuator E3. Channel A in the graph represents the linear spectrum of the driving voltage for the actuator E3 and Channel B displays the FRF of the beam velocity over the actuating voltage. It can be observed from the bottom graph (Channel B) that the first three resonance frequencies of the test structure were (1) 244 Hz, (2) 613 Hz and (3) 1.05 kHz.

Table 5.1: List of equipment and their sensitivities used in the setup

Instrument	Model	Sensitivity
Dynamic Signal Analyzer (spectrum analyzer)	Model SR785	N/A
Laser Doppler Vibrometer	Polytec, OFV-3001	25 $mm/s/V$
Digital Oscilloscope	Tektronix, TDS540A	N/A
Power Amplifier	AVC 790 Series	N/A

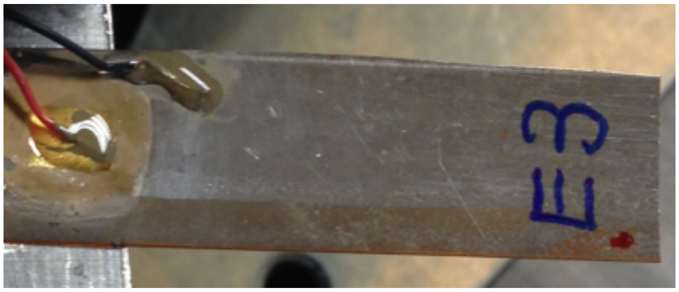

Figure 5.5: The photo of the laser location at the corner of the free end

5.1.3.2 Demonstration of the PZT-silane thin film actuator

The second part of the experiments was to demonstrate the feasibility of using PZT-silane thin film actuator to excite the cantilever beam at the same frequency as the driving frequency of the input signal. The actuator E3 was driven at the following three resonance frequencies found in the previous section:

1. 244 Hz
2. 613 Hz
3. 1.05 kHz

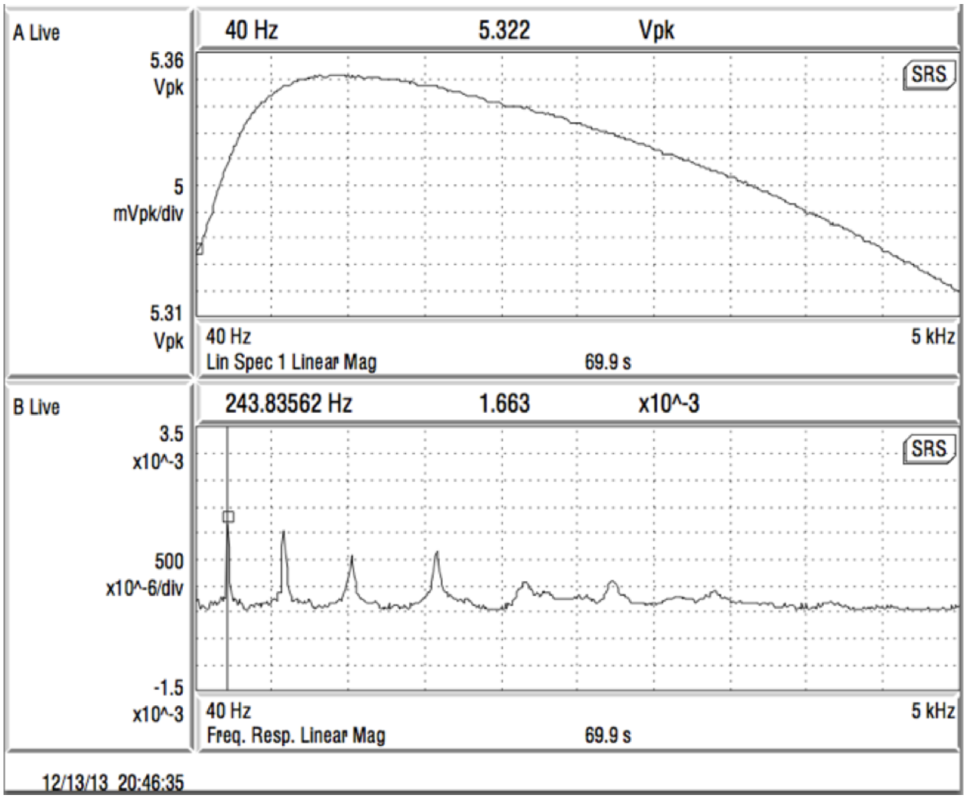

Figure 5.6: Measured swept sine frequency response function of the beam. Channel A is the linear spectrum of the driving voltage for the actuator E3 (top) and channel B is the FRF of the beam tip velocity over the driving voltage (bottom).

The digital oscilloscope was used to measure (1) the driving voltage output from the power amplifier (Channel 1 in Fig. 5.3) and (2) the velocity profile at the free end of the beam in the time domain (Channel 2 in Fig. 5.3). Figure 5.3 shows the connection of those two channels for the actuation test in blue dashed lines.

Figure 5.7, Figure 5.8 and Figure 5.9 show the LDV responses at 244 Hz, 613 Hz and 1.05 kHz, respectively. The results reveal that the vibration of the beam was synchronized with the actuation signals when driving PZT-silane thin film actuator at frequencies near the natural frequencies of the beam. This indicates that the PZT-silane thin film can serve as an actuator.

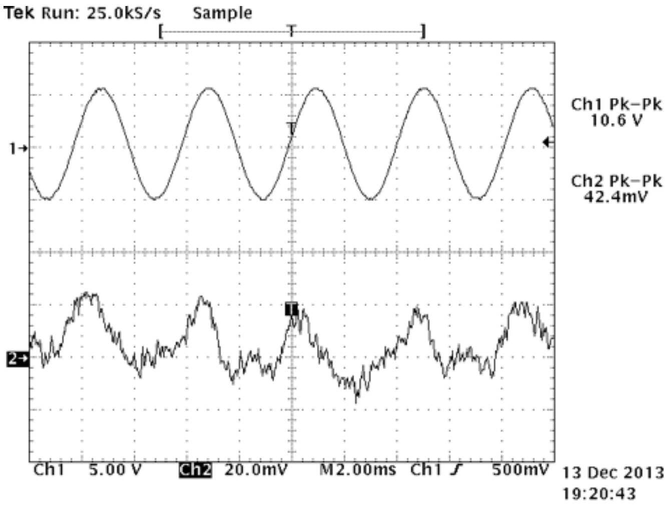

Figure 5.7: Response of PZT thin film actuator E3 to a sinusoidal voltage of 244 Hz across the electrodes. Top trace (channel 1) is the driving voltage output of the power amplifier and bottom trace (channel 2) is the velocity at the free end of the beam.

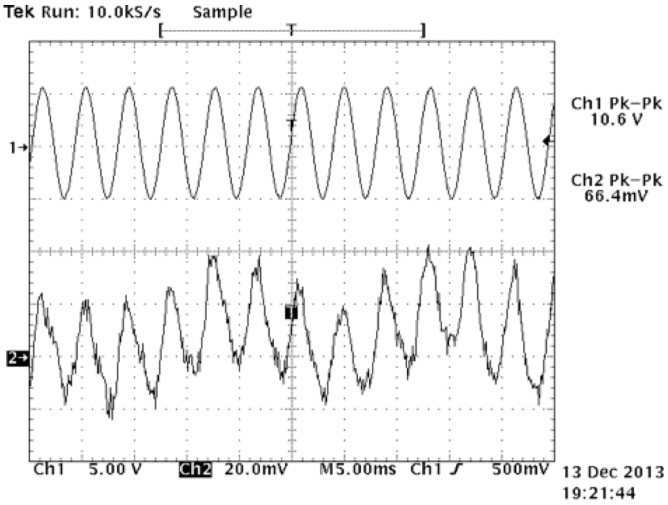

Figure 5.8: Response of PZT thin film actuator E3 to a sinusoidal voltage of 613 Hz across the electrodes. Top trace (channel 1) is the driving voltage output of the power amplifier and bottom trace (channel 2) is the velocity at the free end of the beam.

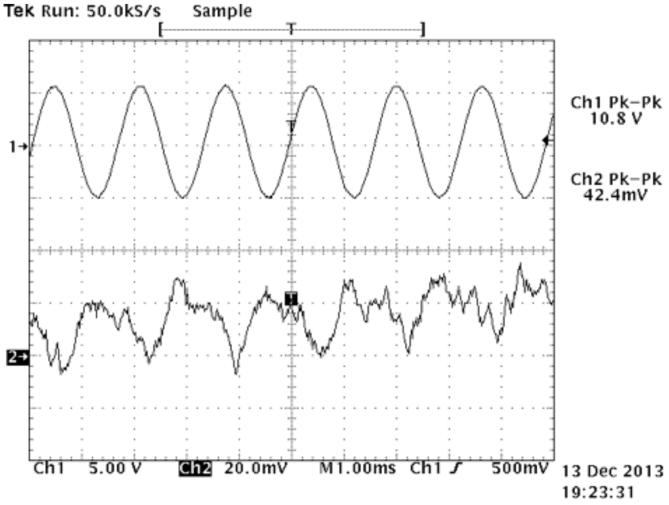

Figure 5.9: Response of PZT thin film actuator E3 to a sinusoidal voltage of 1.05 kHz across the electrodes. Top trace (channel 1) is the driving voltage output of the power amplifier and bottom trace (channel 2) is the velocity at the free end of the beam.

5.2 Sensor Application

In this section, another test structure was built and its vibrations was measured via a PZT-silane thin film and a laser Doppler vibrometer (LDV) simultaneously. The purpose is to demonstrate that a PZT-silane thin film can serve as an accurate vibration sensor [71].

5.2.1 Test Structure and Experimental Setup

Figure 5.10 shows the test structure and experimental setup. The test structure was a square plate made of aluminium alloy with a length of 120 mm and a thickness of 5.8 mm. The square plate, supported by a pillar spacer at each of the four corners, was attached to a vibration isolation table via four screws. The applied torque at each screw was the same at 4 $N \cdot m$. The spacer was aluminium with an outer diameter of 12.55 mm, an inner diameter of 10 mm, and a height of 25.28 mm.

A PZT-silane thin-film sensor was fabricated using the recipe in Section 2.1.3 with hydrothermally grown nanoparticles. It consisted a bottom electrode layer, a PZT layer, a top coat MPTS layer and a top electrode layer as shown in Fig. 5.11. It was then glued (by epoxy) to the test structure at the midpoint of one of the four sides. This PZT-silane thin film sensor will be referred to as "WD1" hereafter.

Some special treatments need to be made before measuring the charge output of the sensor, since it would be tiny. For example, all the cables need to be properly shielded and the plate structure needs to be grounded as shown in Fig. 5.12.

The experimental setup consisted of an impact hammer, a load cell, a laser Doppler vibrometer (LDV), a charge amplifier, and a spectrum analyzer. Specifications of these equipment items have already been explained in previous sections (see Tab. 7.3), therefore they will not be repeated here. In the experiments, the impact hammer stroked at the spot shown in Fig. 5.10 setting the plate into vibration. In the meantime, the load cell at the tip of the hammer recorded the applied force F. The vibration deformed the test structure and the PZT-silane sensor to generate electric charge Q, which were subsequently measured by the charge amplifier. At the same time, the LDV projected a laser beam onto the center of the gold top electrode, and measured the velocity V of the test structure at the PZT-silane sensor. The displacement D of the test structure at the sensor location can subsequently be calculated through integration of V.

The spectrum analyzer processed the measured impact force F, electric charge Q, and displacement D to obtain two frequency response functions (FRF). One is "PZT-FRF" relating the electric charge Q to the impact force F. The other is "LDV-FRF" between the displacement of the plate D and the impact force F. Since the LDV measurement point is collocated with the PZT-silane sensor, the measured "LDV-FRF" and the "PZT-FRF" should be proportional to each other if the PZT-silane sensor works properly.

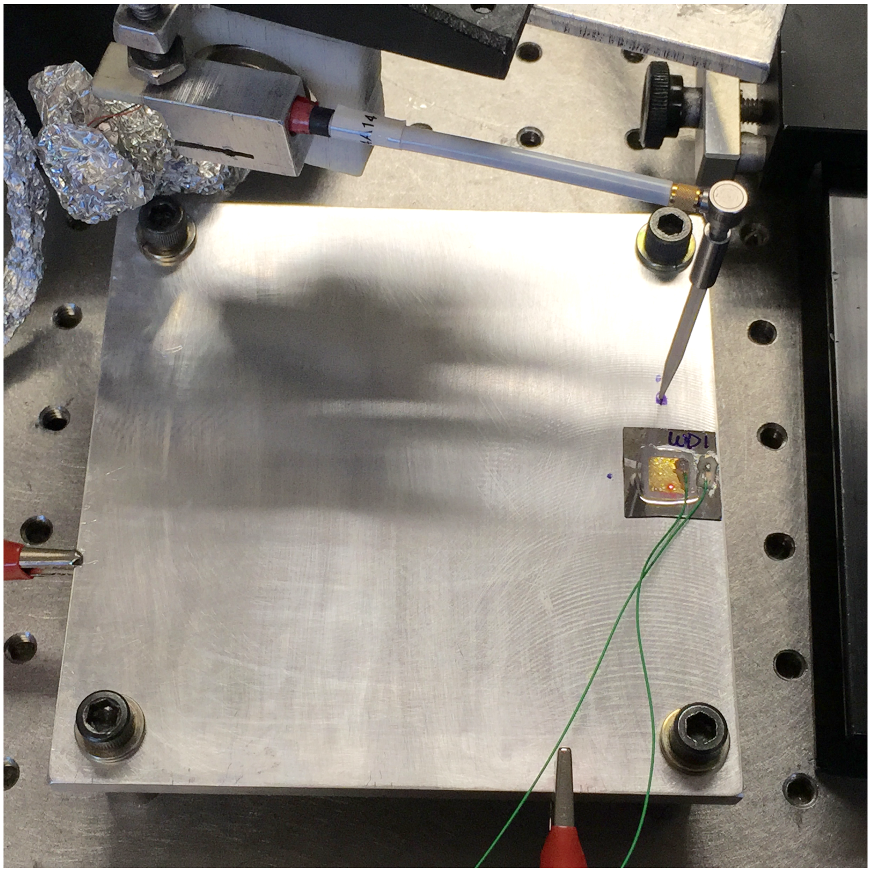

Figure 5.10: Experimental setup and test structure for sensor demonstration

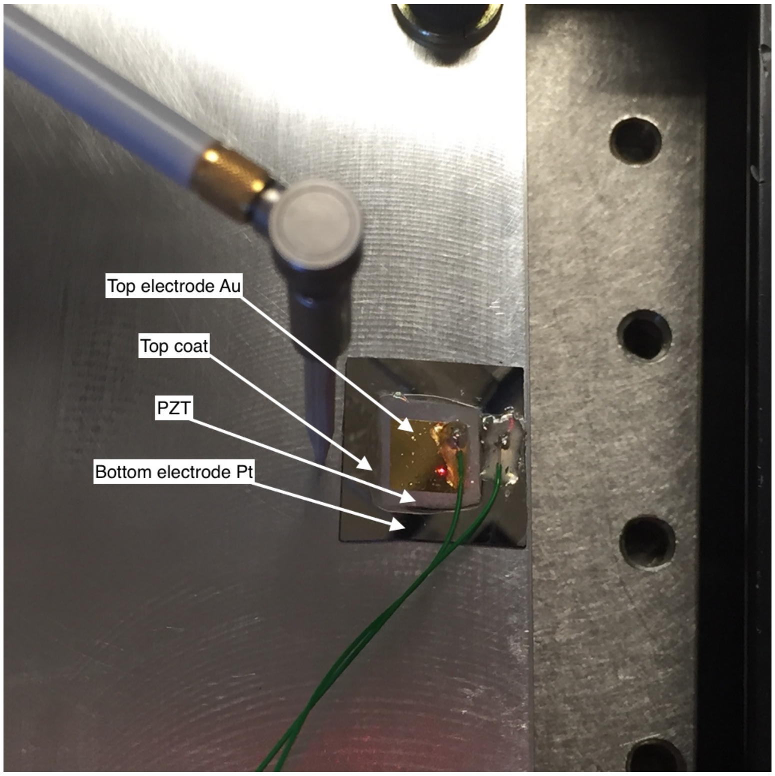

Figure 5.11: PZT-silane thin film sensor WD1

5.2.2 Dielectric Properties of WD1

PZT-silane thin film sensor WD1 had an top electrode area of $49 \times 10^{-6} m^2$ and the thickness of the film was 4.041 μm. The impedance magnitude and phase angle, capacitance and resistance values of the sensor were measured by the impedance analyzer (Agilent Model 4294A). Figure 5.13 shows the measurement results. The estimated dielectric constant and loss tangent for PZT-silane thin film sensor WD1 with PZT nanoparticles was calculated from the impedance measurements in the frequency range of 40Hz-100kHz and are shown in Fig. 5.14. Table 5.2 provides the estimated dielectric properties of WD1 at 1, 10 and 100 kHz.

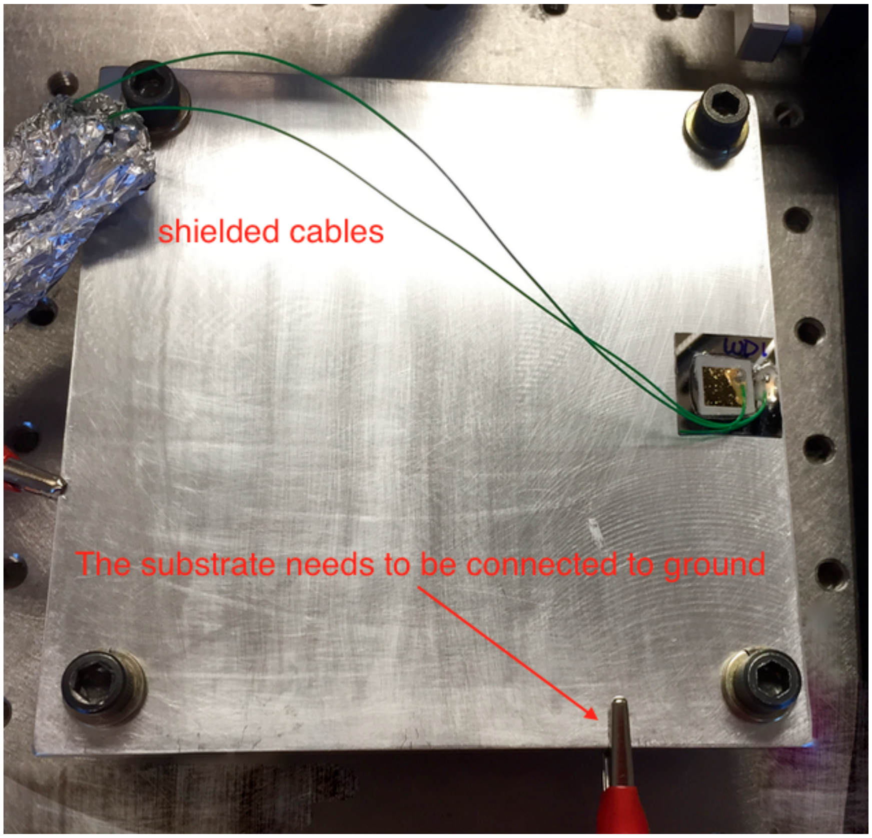

Figure 5.12: Special treatments to minimize noise in the experimental setup

5.2.3 Test Results and Discussion

Figure 5.15 compares the measured “LDV-FRF” and “PZT-FRF” in the top and bottom figures, respectively. The two FRFs are clearly proportional to each other, exhibiting identical features. They both have three resonance peaks at 1596 Hz, 276464 Hz, and 3092 Hz. There is a flat, static gain range for both FRFs. Even tiny features are accurately captured, such as the small peaks slightly above the first resonance at 1596 Hz and the unsymmetric resonance peak at 2764 Hz. The close agreement between the “PZT-FRF” and the “LDV-FRF” proves that the PZT-silane thin film is an effective and accurate sensor capable of measuring vibration of a structure.

Table 5.2: Estimated dielectric properties of WD1 at 1, 10 and 100 kHz

	Estimated dielectric constant	Estimated loss tangent
1 kHz	9.425	0.0271
10 kHz	9.047	0.0323
100 kHz	8.452	0.0539

In order to understand the physics of the three resonance peaks here, vibration of the test plate and its corresponding mode shapes were also studied. This was done by measuring the frequency responses of the displacement D over force F at 25 locations on the plate shown in Fig. 5.16 using the LDV. Figure 5.17 shows one set of the measured displacement D over force F frequency response magnitude, phase and coherence data of the plate vibration. After combining all 25 frequency response measurements, the plate vibration modes could be mapped using 3-D surface plot or 2-D contour plot.

Figure 5.18, Figure 5.19, Figure 5.20 and Figure 5.21 display the plate vibration modes 1 through 4. As a result, it can be found that the three resonance peaks correspond to a 0-nodal-line mode, a 1-nodal-line mode, and a 2-nodal-line mode, respectively, as shown in Fig. 5.22.

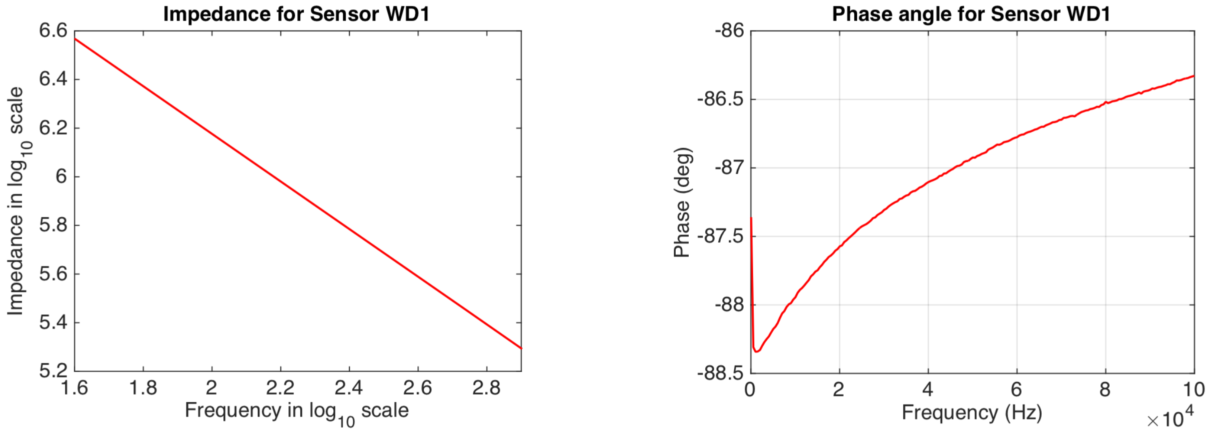

(a) WD1 impedance measurement

(b) WD1 phase measurement

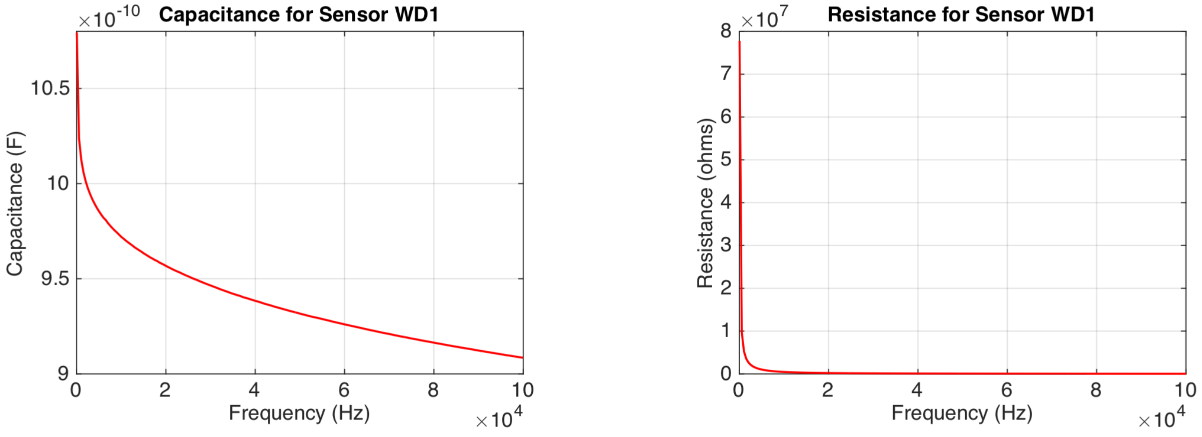

(c) WD1 capacitance measurement

(d) WD1 resistance measurement

Figure 5.13: Sensor WD1 impedance measurement data

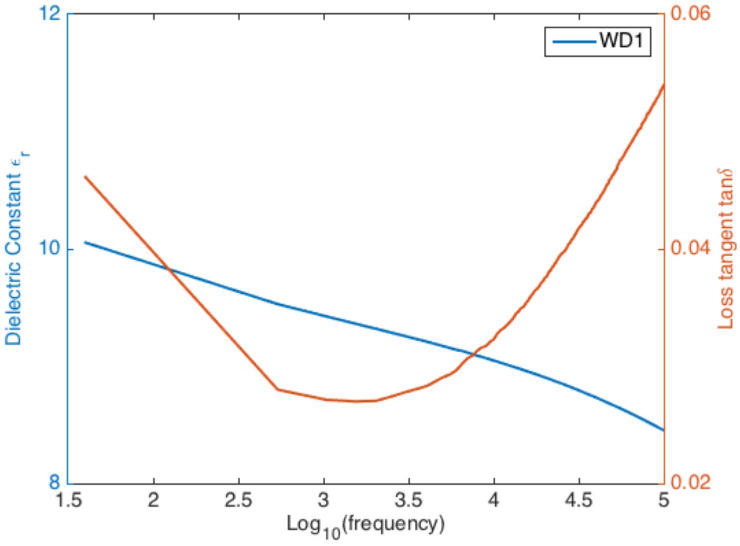

Figure 5.14: Estimated dielectric constant and loss tangent for PZT-silane thin film sensor WD1 with PZT nanoparticles in the frequency range of 40Hz-100kHz

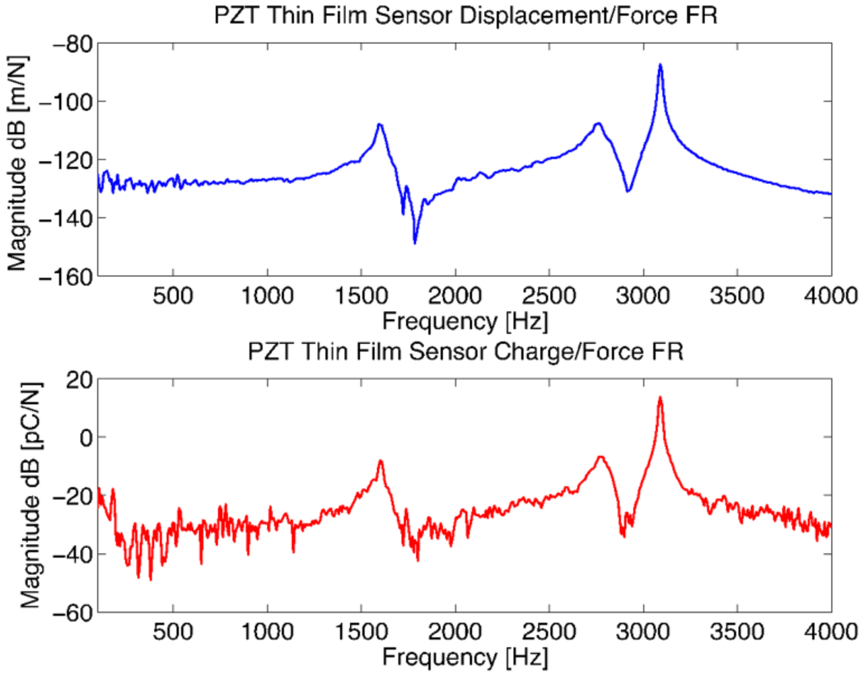

Figure 5.15: Comparison of frequency response function from the laser Doppler vibrometer (upper plot) and from the PZT-silane sensor (lower plot)

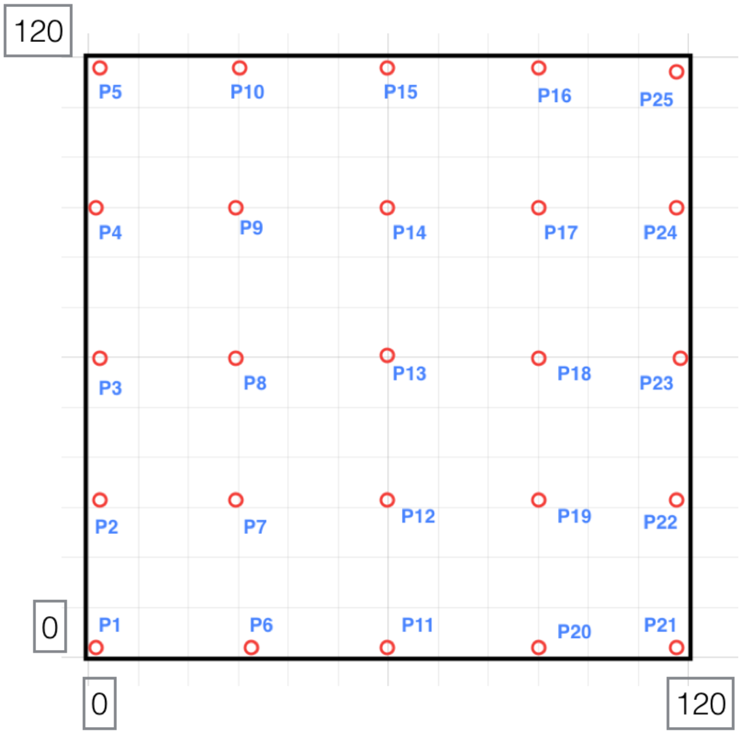

Figure 5.16: 25 measurement points on the plate

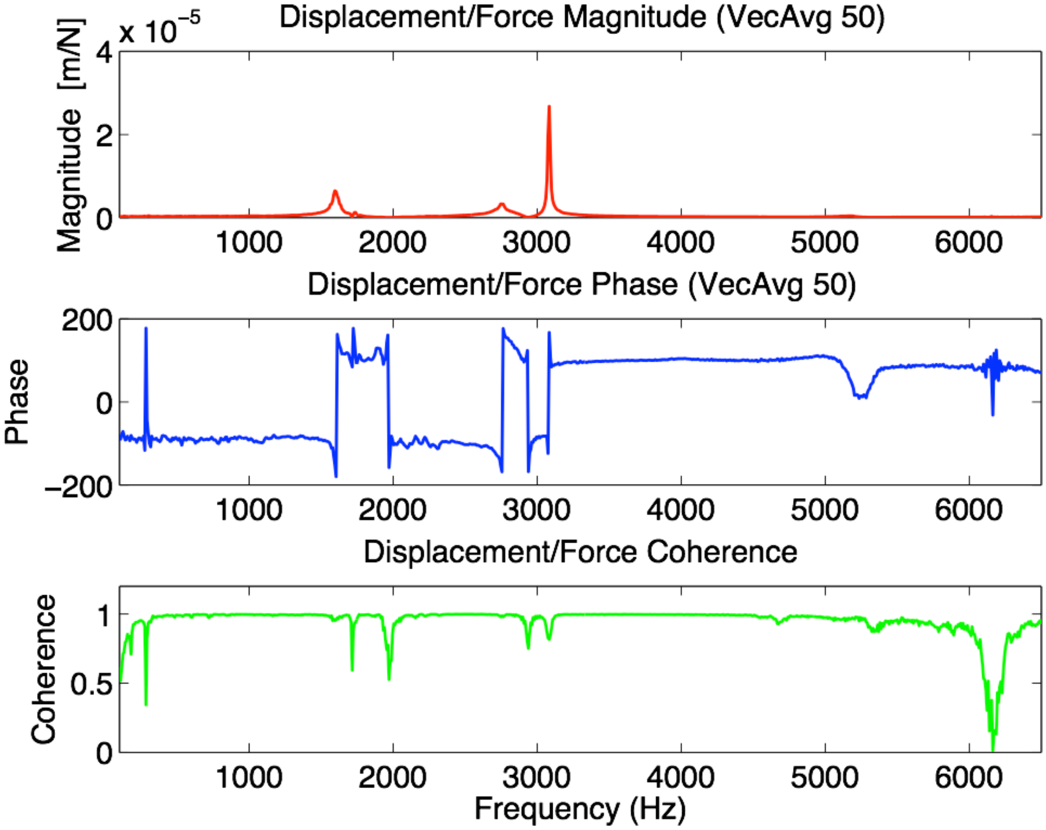

Figure 5.17: The measured displacement D over force F frequency response magnitude (top trace), phase (middle trace) and coherence (bottom trace) of the plate vibration at point P18

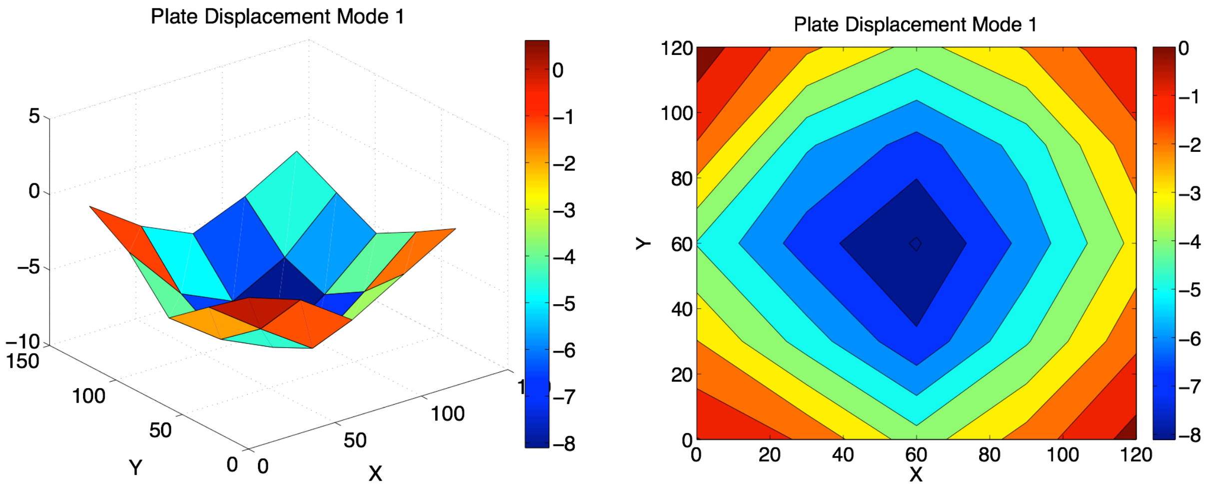

(a) 3-D surface plot

(b) 2-D contour plot

Figure 5.18: Plate vibration mode 1

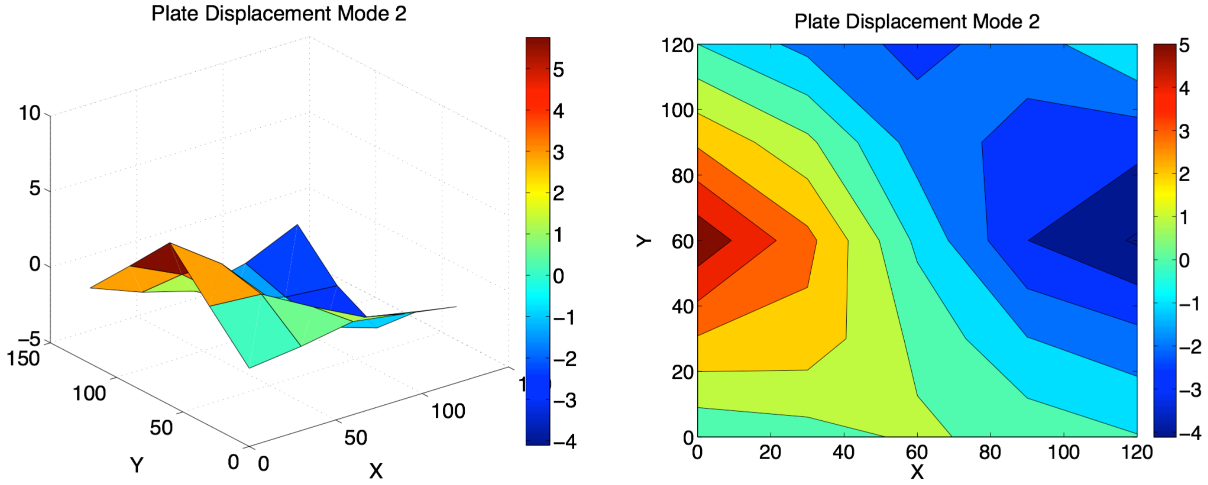

(a) 3-D surface plot

(b) 2-D contour plot

Figure 5.19: Plate vibration mode 2

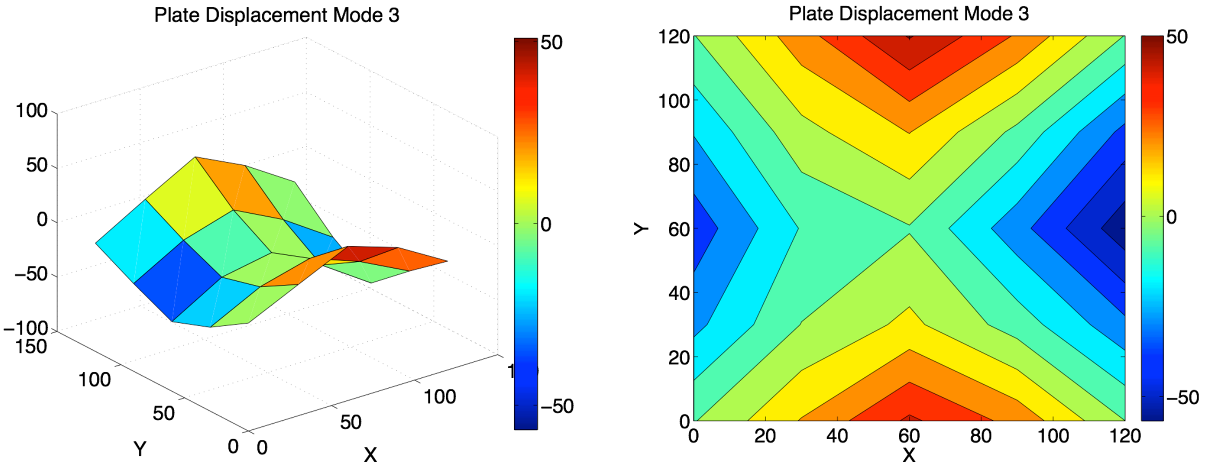

(a) 3-D surface plot

(b) 2-D contour plot

Figure 5.20: Plate vibration mode 3

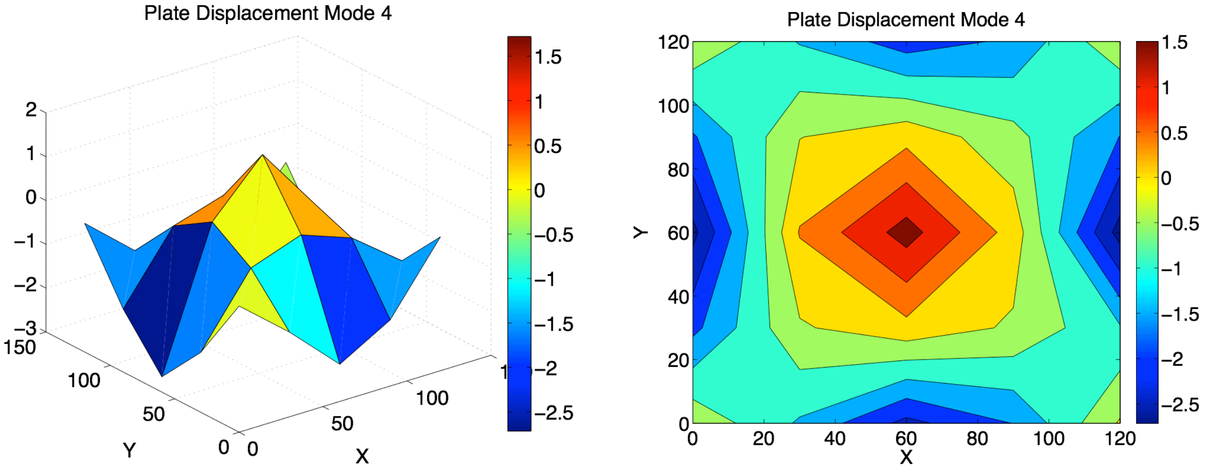

(a) 3-D surface plot

(b) 2-D contour plot

Figure 5.21: Plate vibration mode 4

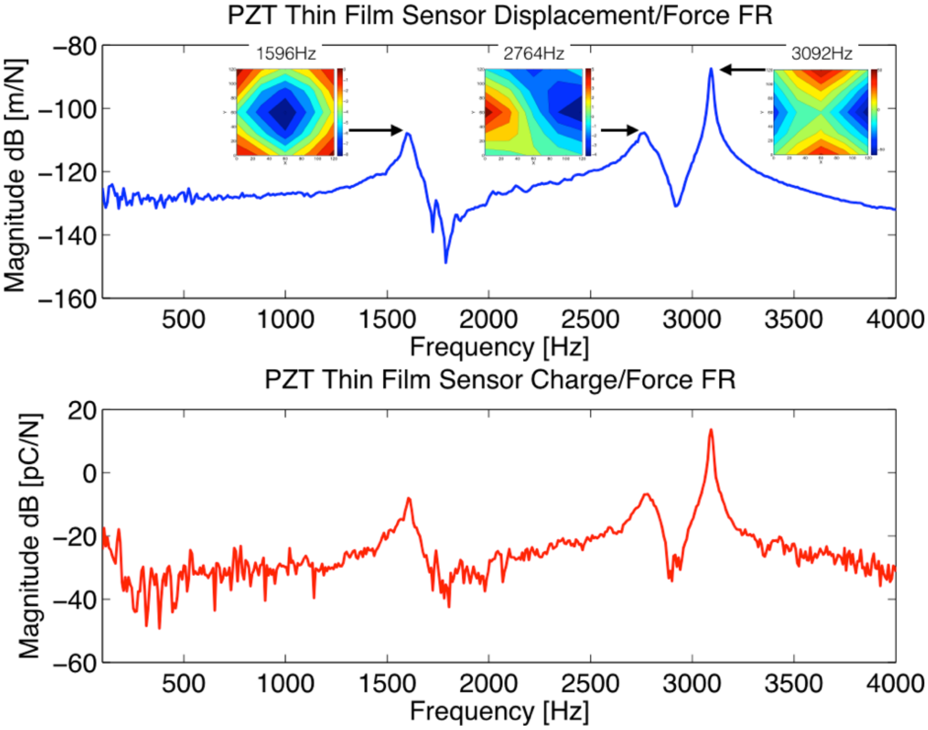

Figure 5.22: Comparison of frequency response function from the laser Doppler vibrometer (upper plot) and from the PZT-silane sensor (lower plot)

Chapter 6

PZT-SILANE THIN FILMS WITH PRINTED INTERDIGITATED ELECTRODES

6.1 Introduction

Since PZT-silane thin film has been demonstrated in Chapter 5 as an actuator and accurate vibration sensor, the main objective in this chapter is to develop a printed flexible strain sensor capable of sensing directional strain on any surface with efficient manufacturing process.

6.2 Design of PZT Strain Sensor

6.2.1 Theory and Design

There are two different sensor designs. The first is a sensor device with parallel plate electrodes in d_{31} mode in which the direction of polarization (3) is perpendicular to the direction of applied stress or strain (1). The second is a d_{33} mode sensor device with interdigitated electrodes. The polarization direction (3) of d_{33} mode is virtually parallel to the direction of applied stress or strain (3). Figure 6.1 shows a schematic drawing of these two electrode configurations with the poling direction of the d_{31} mode shown in Figure 6.1 (a) and the d_{33} mode shown in Figure 6.1 (b).

6.2.1.1 Design 1

The *stress-charge* form of the linear piezoelectric constitutive equation (4.1) can be written as Eqn. (6.1) and (6.2), where stiffness matrix $\mathbf{C}$, piezoelectric coefficient matrices $\mathbf{d}$ and $\mathbf{e}$ can be expressed as Eqn. (6.3), (6.4) and (6.5), respectively. The subscripts $i = 1, 2, 3, 4, 5, 6$, $j = 1, 2, 3, 4, 5, 6$, and $n = 1, 2, 3$ signify the direction of related physical properties. All the symbols and their units used in this chapter are listed in Tab. 4.1 and Tab. 4.2.

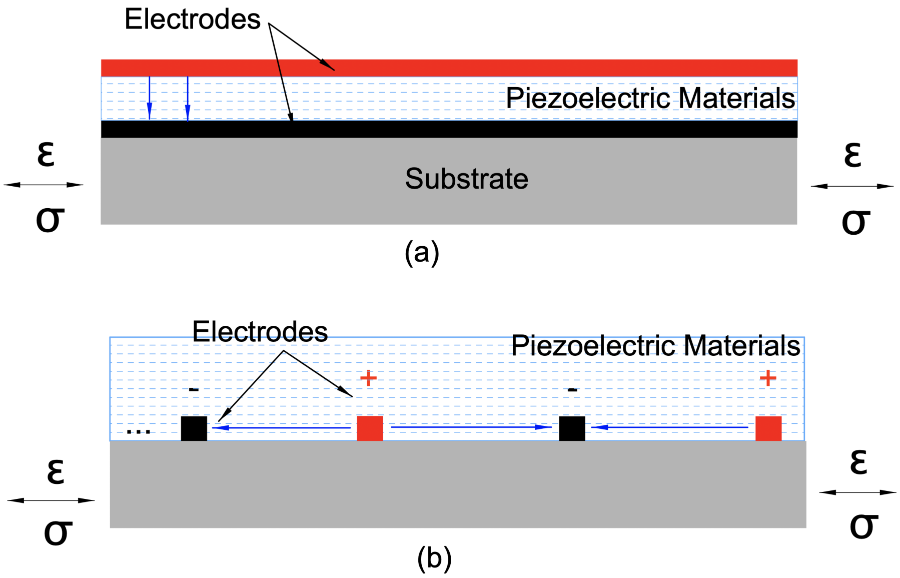

Figure 6.1: Cross section of (a) d_{31} mode and (b) d_{33} mode devices with different poling directions

$$T_i = C_{ij}^E S_j - e_{in} E_n \tag{6.1}$$

$$D_i = e_{ij}^t S_j + \varepsilon_{in}^S E_n \tag{6.2}$$

$$\mathbf{C}^E = \left[\mathbf{s}^E\right]^{-1} = \begin{bmatrix} C_{11} & C_{12} & C_{13} & 0 & 0 & 0 \\ C_{21} & C_{22} & C_{23} & 0 & 0 & 0 \\ C_{31} & C_{32} & C_{33} & 0 & 0 & 0 \\ 0 & 0 & 0 & C_{44} & 0 & 0 \\ 0 & 0 & 0 & 0 & C_{55} & 0 \\ 0 & 0 & 0 & 0 & 0 & C_{66} \end{bmatrix} \tag{6.3}$$

$$\mathbf{d_{ik}} = \begin{bmatrix} 0 & 0 & 0 & 0 & d_{15} & 0 \\ 0 & 0 & 0 & d_{15} & 0 & 0 \\ d_{31} & d_{31} & d_{33} & 0 & 0 & 0 \end{bmatrix} \tag{6.4}$$

$$\mathbf{e}^t_{ij} = \mathbf{d}_{ik}\mathbf{C}^E_{kj} = \begin{bmatrix} 0 & 0 & 0 & 0 & e_{15} & 0 \\ 0 & 0 & 0 & e_{24} & 0 & 0 \\ e_{31} & e_{32} & e_{33} & 0 & 0 & 0 \end{bmatrix} \tag{6.5}$$

The embedded PZT layer is to be modeled as a thin plate due to the fact that its thickness ($5 \sim 10\mu m$) is much smaller than its length and width dimensions ($5 \sim 10mm$). In this case, the normal stress in the thickness direction and the two corresponding transverse shear stresses can be neglected, which are:

$$T_3 = T_4 = T_5 = 0 \quad or \quad T_{33} = T_{23} = T_{13} = 0 \tag{6.6}$$

Substituting the boundary condition in Eqn. (6.6) into (6.1), and assuming $E_1 = E_2 = 0$, one can get:

$$\begin{aligned} T_3 &= C^E_{3j}S_j - e_{3n}E_n \\ &= C^E_{31}S_1 + C^E_{32}S_2 + C^E_{33}S_3 - e_{33}E_3 \\ &= 0 \end{aligned} \tag{6.7}$$

Hence S_3 can be expressed as Eqn. (6.8) by rearranging Eqn. (6.7).

$$S_3 = \frac{e_{33}E_3}{C^E_{33}} - \frac{C^E_{31}S_1}{C^E_{33}} - \frac{C^E_{32}S_2}{C^E_{33}} \tag{6.8}$$

When the PZT layer is deformed as a strain sensor, charges are displaced between the electrodes along its poling direction (3-axis). Under open circuit condition in which $D_3 = 0$, the electric field across top and bottom electrodes, E_3, is given as:

$$\begin{aligned} D_3 &= e_{3j}S_j + \varepsilon^S_{3n}E_n \\ &= e_{31}S_1 + e_{32}S_2 + e_{33}S_3 + \varepsilon^S_{33}E_3 \\ &= 0 \end{aligned} \tag{6.9}$$

$$E_3 = -\frac{e_{31}S_1}{\varepsilon^S_{33}} - \frac{e_{32}S_2}{\varepsilon^S_{33}} - \frac{e_{33}S_3}{\varepsilon^S_{33}} \tag{6.10}$$

By combining Eqn. (6.10) with (6.8), E_3 can be expressed as

$$E_3 = \frac{(\frac{e_{33}}{\varepsilon^S_{33}}\frac{C^E_{31}}{C^E_{33}} - \frac{e_{31}}{\varepsilon^S_{33}})}{(1 + \frac{e^2_{33}}{\varepsilon^S_{33}C^E_{33}})}S_1 + \frac{(\frac{e_{33}}{\varepsilon^S_{33}}\frac{C^E_{32}}{C^E_{33}} - \frac{e_{32}}{\varepsilon^S_{33}})}{(1 + \frac{e^2_{33}}{\varepsilon^S_{33}C^E_{33}})}S_2 \tag{6.11}$$

Based on the transversely isotropic properties of PZT and this sensor configuration (see Fig. 6.2), the elastic stiffness components and piezoelectric constants are symmetric about its poling direction (3-axis), yielding (6.12) and (6.13).

$$C^E_{31} = C^E_{32} \tag{6.12}$$

$$e_{31} = e_{32} \tag{6.13}$$

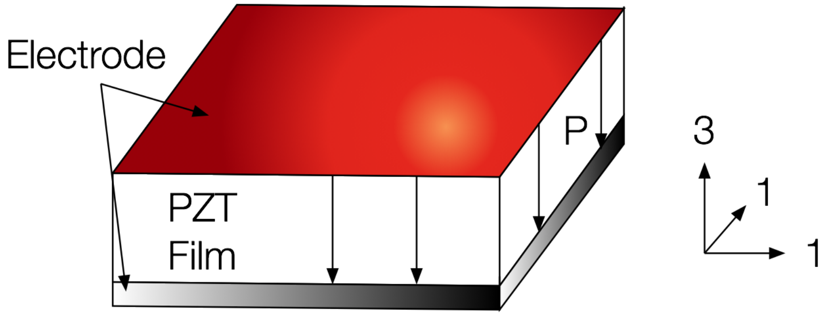

Figure 6.2: PZT strain sensor with polarized PZT film along its thickness direction (3-axis); continuous top electrode (red) and bottom electrode (black)

Therefore, the electric field intensity E_3 can be simplified to Eqn. (6.14) using Eqn. (6.12) and (6.13). The sensor output can be measured as voltage between the two electrodes or charge that is generated from the PZT thin film. Their equations are presented as Eqn. (6.15) and (6.16), where t is the thickness of PZT thin film, Q is the collected charge along the thickness direction, and A_3 is the electrode area.

$$E_3 = \frac{\left(\frac{e_{33}}{\varepsilon_{33}^S}\frac{C_{31}^E}{C_{33}^E} - \frac{e_{31}}{\varepsilon_{33}^S}\right)}{\left(1 + \frac{e_{33}^2}{\varepsilon_{33}^S C_{33}^E}\right)}(S_1 + S_2) \tag{6.14}$$

$$V_3 = \frac{\left(\frac{e_{33}}{\varepsilon_{33}^S}\frac{C_{31}^E}{C_{33}^E} - \frac{e_{31}}{\varepsilon_{33}^S}\right)}{\left(1 + \frac{e_{33}^2}{\varepsilon_{33}^S C_{33}^E}\right)}\,(S_1 + S_2)\,t \tag{6.15}$$

$$Q = \frac{\left(\frac{e_{33}}{\varepsilon_{33}^S}\frac{C_{31}^E}{C_{33}^E} - \frac{e_{31}}{\varepsilon_{33}^S}\right)}{\left(1 + \frac{e_{33}^2}{\varepsilon_{33}^S C_{33}^E}\right)}\,\varepsilon_{33}^S A_3\,(S_1 + S_2) \tag{6.16}$$

The charge and voltage equations show that the sensor's output signal is the sum of the two in-plane strains (or principal strains) times some constants, which are determined by the material properties and dimensions (thickness or electrode area) of the PZT thin film.

This shows that design A will be able to measure the principal strains but will not be able to distinguish between the two normal strains (S_1 and S_2).

6.2.1.2 Design 2

From Eqn. (6.11), one possible scheme to separate S_1 and S_2 is to make

$$\begin{aligned} C_{31}^E &\neq C_{32}^E, \\ e_{31} &\neq e_{32}. \end{aligned} \tag{6.17}$$

We can fulfill Eqn. (6.17) by changing the poling direction of PZT thin film from through-thickness direction to an in-plane direction. The d_{33} mode sensor device with interdigitated electrodes shown in Figure 6.1 (b) produces this effect. Figure 6.3 shows an in-plane polarized

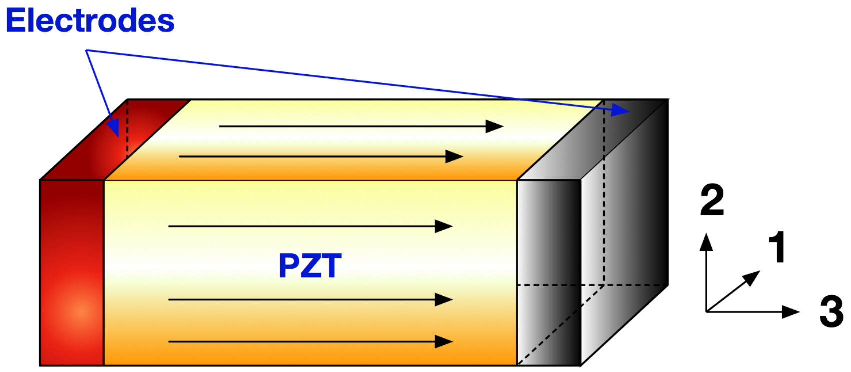

Figure 6.3: In-plane polarized PZT strain sensor with interdigitated electrodes

PZT film. The two interdigitated electrodes are indicated by red and black colors in the figure.

Voltage output of a d_{33} mode sensor device is derived using the new axis system indicated in Figure 6.3. The *stress-charge* form of the linear piezoelectric constitutive equation Eqn. (6.1) and (6.2) are used here again for the derivation.

$$T_i = C_{ij}^E S_j - e_{in}^T E_n$$

$$D_i = e_{ij} S_j + \varepsilon_{in}^S E_n$$

PZT layer is very thin (thickness is negligible compared to its length and width), so the plane stress condition can be assumed. This means that the normal and shear stresses in the direction perpendicular to the film surface are zeros or negligible ($T_2 = 0$). The direction perpendicular to the film surface is 2-axis, and the poling direction is 3-axis as shown in Fig. 6.3. After setting $T_2 = 0$, the strain in the direction perpendicular to the film surface S_2 can be solved for as shown in (6.18).

$$\begin{aligned}
T_2 &= C^E_{2j} S_j - e^T_{2n} E_n \\
&= C^E_{21} S_1 + C^E_{22} \mathbf{S_2} + C^E_{23} S_3 - e_{32} E_3 = 0 \\
\Rightarrow & \\
S_2 &= \frac{e_{32} E_3}{C^E_{22}} - \frac{C^E_{21} S_1}{C^E_{22}} - \frac{C^E_{23} S_3}{C^E_{22}}
\end{aligned} \tag{6.18}$$

When the PZT film is subjected to an in-plane strain or stress, charges will displace between the electrodes along its poling direction (3-axis). Under open circuit condition, which $D_3 = 0$, the electric field between two electrode fingers E_3 is given by (6.19).

$$\begin{aligned}
D_3 &= e_{3j} S_j + \varepsilon^S_{3n} E_n \\
&= e_{31} S_1 + e_{32} S_2 + e_{33} S_3 + \varepsilon^S_{33} \mathbf{E_3} \\
&= 0 \\
\Rightarrow & \\
E_3 &= -\frac{e_{31} S_1}{\varepsilon^S_{33}} - \frac{e_{32} S_2}{\varepsilon^S_{33}} - \frac{e_{33} S_3}{\varepsilon^S_{33}}
\end{aligned} \tag{6.19}$$

Substituting S_2 from (6.18) into (6.19) and rearrange expression for E_3 yields (6.20).

$$\begin{aligned}
E_3 &= -\frac{e_{31} S_1}{\varepsilon^S_{33}} - \frac{e_{32} S_2}{\varepsilon^S_{33}} - \frac{e_{33} S_3}{\varepsilon^S_{33}} \\
&= -\frac{e_{31} S_1}{\varepsilon^S_{33}} - \frac{e_{32}}{\varepsilon^S_{33}} \left(\frac{e_{32} E_3}{C^E_{22}} - \frac{C^E_{21} S_1}{C^E_{22}} - \frac{C^E_{23} S_3}{C^E_{22}}\right) - \frac{e_{33} S_3}{\varepsilon^S_{33}} \\
E_3 + \frac{e_{32}}{\varepsilon^S_{33}} \frac{e_{32} E_3}{C^E_{22}} &= -\frac{e_{31} S_1}{\varepsilon^S_{33}} + \frac{e_{32}}{\varepsilon^S_{33}} \frac{C^E_{21} S_1}{C^E_{22}} + \frac{e_{32}}{\varepsilon^S_{33}} \frac{C^E_{23} S_3}{C^E_{22}} - \frac{e_{33} S_3}{\varepsilon^S_{33}} \\
(1 + \frac{e_{32}}{\varepsilon^S_{33}} \frac{e_{32}}{C^E_{22}}) E_3 &= (-\frac{e_{31}}{\varepsilon^S_{33}} + \frac{e_{32}}{\varepsilon^S_{33}} \frac{C^E_{21}}{C^E_{22}}) S_1 + (\frac{e_{32}}{\varepsilon^S_{33}} \frac{C^E_{23}}{C^E_{22}} - \frac{e_{33}}{\varepsilon^S_{33}}) S_3 \\
E_3 &= \frac{(-\frac{e_{31}}{\varepsilon^S_{33}} + \frac{e_{32}}{\varepsilon^S_{33}} \frac{C^E_{21}}{C^E_{22}})}{(1 + \frac{e_{32}}{\varepsilon^S_{33}} \frac{e_{32}}{C^E_{22}})} S_1 + \frac{(\frac{e_{32}}{\varepsilon^S_{33}} \frac{C^E_{23}}{C^E_{22}} - \frac{e_{33}}{\varepsilon^S_{33}})}{(1 + \frac{e_{32}}{\varepsilon^S_{33}} \frac{e_{32}}{C^E_{22}})} S_3
\end{aligned} \tag{6.20}$$

Since $\frac{(-\frac{e_{31}}{\varepsilon^S_{33}} + \frac{e_{32}}{\varepsilon^S_{33}} \frac{C^E_{21}}{C^E_{22}})}{(1 + \frac{e_{32}}{\varepsilon^S_{33}} \frac{e_{32}}{C^E_{22}})} \neq \frac{(\frac{e_{32}}{\varepsilon^S_{33}} \frac{C^E_{23}}{C^E_{22}} - \frac{e_{33}}{\varepsilon^S_{33}})}{(1 + \frac{e_{32}}{\varepsilon^S_{33}} \frac{e_{32}}{C^E_{22}})}$ (coefficients before S_1 and S_3), with multiple sensors oriented in different directions, one can distinguish and separate two normal strains (S_1 and S_3) from charges or voltages measured from the sensors.

Following the design guideline in Section 6.2.1.2, a feasibility test of PZT thin films with interdigitated electrodes is performed. A prototype of PZT strain sensor (shown in Fig. 6.4) with interdigitated electrodes is first fabricated by drop-casting PZT ink onto a rectangular die from a silicon wafer and curing PZT thin film on the substrate using UV light and a furnace. The interdigitated electrodes are cut from conductive tape and pasted onto the PZT thin film. A DC voltage is applied between the two electrodes and pole the film in the in-plane (X) direction indicated in Fig. 6.4.

After the prototype sensor is prepared, it is glued onto an aluminium block for testing. An impact hammer is used to excite the block, and the charge output from the sensor is measured with a charge amplifier. This test is used to confirm the existence of piezoelectricity in PZT-silane thin films in this polarization direction.

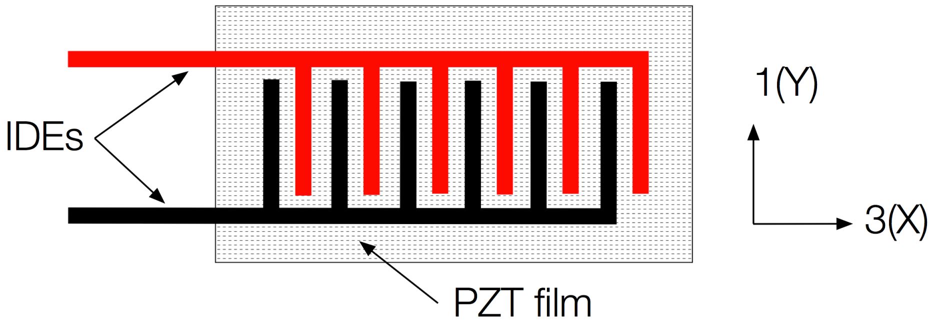

Figure 6.4: PZT strain sensor with interdigitated electrodes

6.2.2 Design 1: Experimental Validation of Strain Invariants

The theoretical conclusion of strain invariants for Design 1 is experimentally validated using the same impact hammer test setup described in Section 5.2.1.

Three PZT thin film sensors are placed together with each sensor oriented in a different direction (e.g. 0°, 45°, and 90°). Locate three sensors as close together as possible in order to accurately approximate the strain measurement at a single point. Figure 6.5 shows the sensor configuration of this design with top view (see Fig. 6.5 (a)) and cross-sectional view (see Fig. 6.5 (b)) of the PZT strain sensor having continuous top and bottom electrodes. PZT thin films are then poled between the two electrodes. Note that in this configuration only normal strains can be detected by the sensors with through-thickness polarized PZT film and the sensor cannot separate out the two normal strains ($\epsilon_x + \epsilon_y$). The theoretical explanation is given in Section 6.2.1.1.

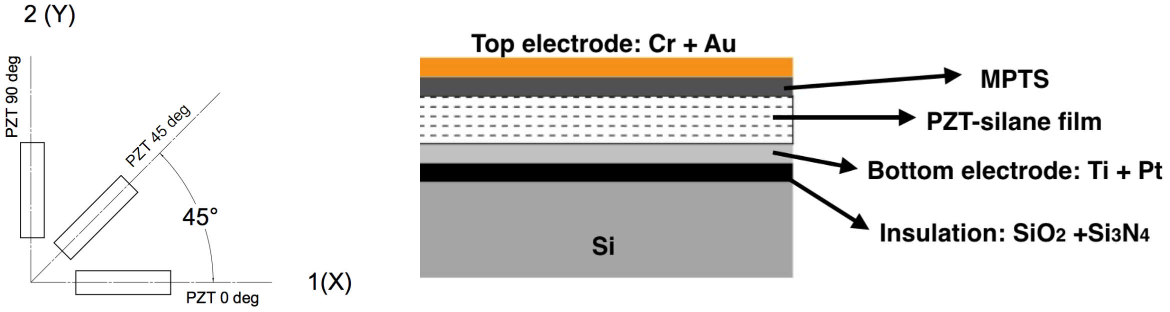

(a) Top view

(b) Cross-sectional view

Figure 6.5: PZT strain rosette with continuous top and bottom electrodes

The sensors oriented in 0°, 45°, and 90°directions are referred to hereafter as sensor A, B and C respectively as indicated in Fig. 6.6. During the tests, an impact hammer with a load cell hits at a location next to the senors causing the plate into vibration. A laser Doppler vibrometer (LDV) measures the velocity V on the top of sensors A, B and C. The displacement D at the sensor locations can be derived through integration of V. All measurements are recorded by the spectrum analyzer.

Two plots of frequency response functions (FRF) are obtained. Figure 6.7 shows “LDV-FRF” relating the displacement of three sensors A, B and C (D_A, D_B, D_C) to the impact force F. These three “LDV-FRF” are referred to as “LDV A” “LDV B” and “LDV C” hereafter. Figure 6.8 is “PZT-FRF” between the electric charge Q and the impact force F. The charge/force FRF of three sensors are referred to as “Sensor A” “Sensor B” and “Sensor C” hereafter.

Test results indicate that “LDV A” “LDV B” and “LDV C” are almost identical because three sensors are relatively small and placed very close together. Their charge output FRFs “Sensor A” “Sensor B” and “Sensor C” are also extremely close, and vary by only 0.23%, which means placing sensors on different orientations does not affect their charge output and the sensor cannot distinguish between the two normal strains (ϵ_x, ϵ_y), as predicted by theory.

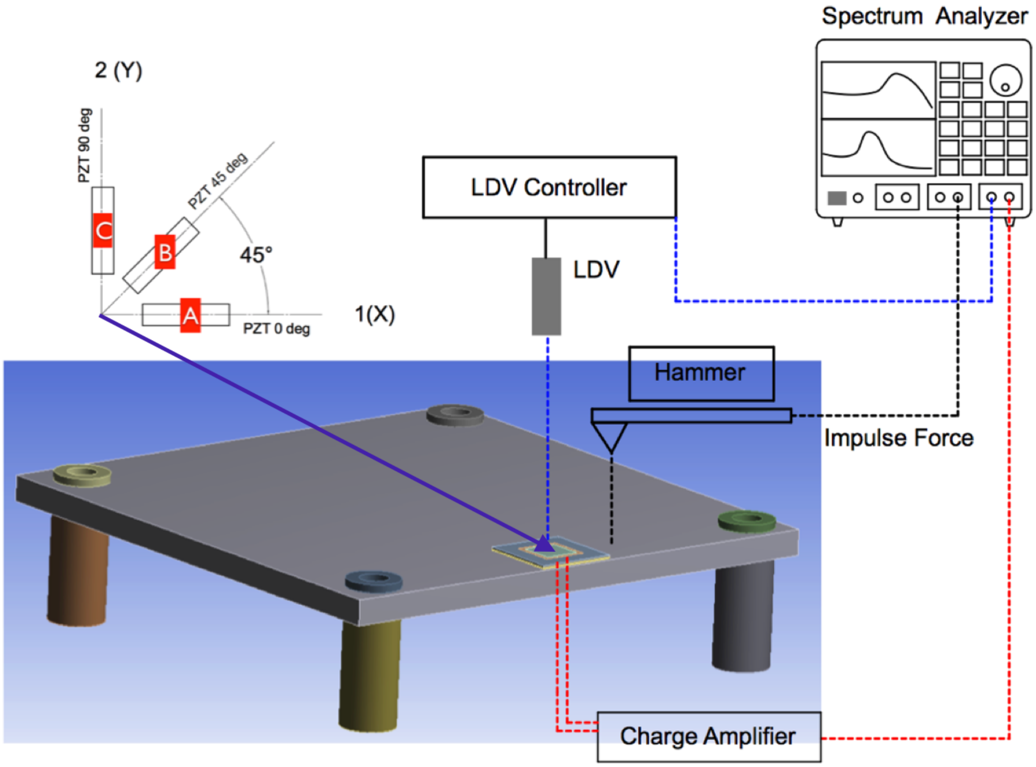

Figure 6.6: Experimental setup for sensor measurement of strain invariants

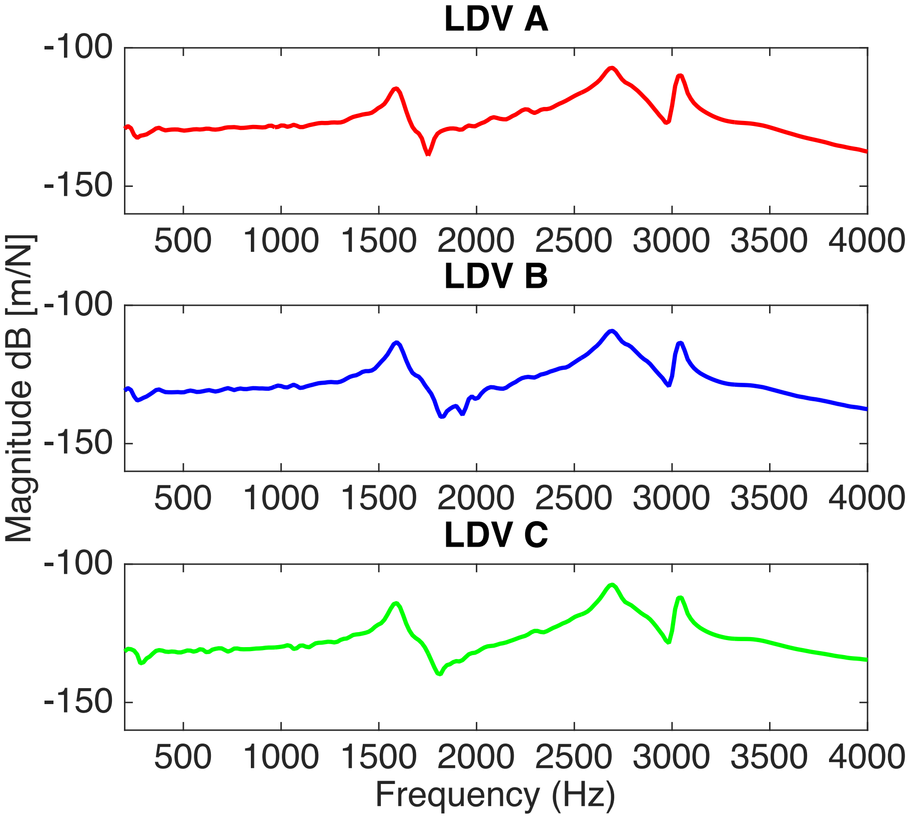

Figure 6.7: Frequency response function from LDV: displacement/force FRF

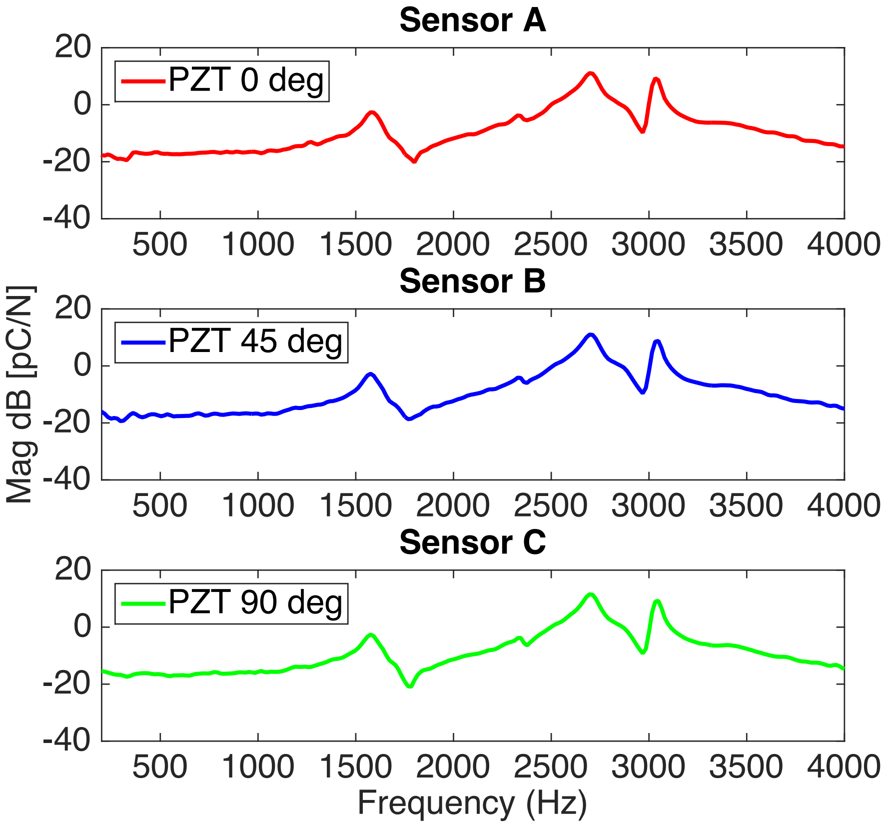

Figure 6.8: Frequency response function from charge amplifier: charge/force FRF

6.2.3 Design 2: Feasibility Study for Interdigitated Electrodes

A feasibility study is carried out to test the idea of PZT-silane thin films with interdigitated electrodes design as sensors. In this study, a prototype sensor having PZT composite thin film with interdigitated copper tape electrodes is fabricated following the procedures below:

1. Drop-cast PZT ink onto a silicon substrate to form a thin fluid layer. Cure the deposited layer under UV light for 2.5 hours and in a furnace at 120 °C for 12 hours.
2. Tape thin copper strips as interdigitated electrodes onto the PZT-silane film as shown in Fig. 6.9.

This prototype is attached to the edge of an aluminum alloy square plate with dimensions $222 \times 222 \times 5mm$; see Fig. 6.10. The square plate is supported by four pillar spacers at its corners and screwed onto the vibration isolation table. These spacers are aluminum with an outer diameter of 12.55 mm, an inner diameter of 10 mm, and a height of 25.28 mm. The experimental setup (impact hammer with a load cell, a laser Doppler vibrometer (LDV), a charge amplifier, and a spectrum analyzer) and specifications are the same as in Section 5.2.1.

The prototype sensor is first poled at 80V for 12 hours and then tested for film's piezoelectricity. The sensor is non-responsive during impact hammer test under this poling condition. Since the gap between electrode fingers is around 300 - 500 μm, the electric field applied is too weak to align the internal dipole moments of the material. A larger poling voltage is required for this prototype. Therefore the sensor is poled at 1500V for 12 hours. Figure 6.11 shows impedance magnitude, phase angle, capacitance and resistance values for the sensor measured by the impedance analyzer (Agilent Model 4294A) under two different poling voltages.

After poling, the impact hammer test is performed as shown in Fig. 6.12. While the load cell at the tip of hammer records the applied force F, charge amplifier measures the electric charge Q generated by PZT-silane film. Figure 6.13 shows the laser location of LDV

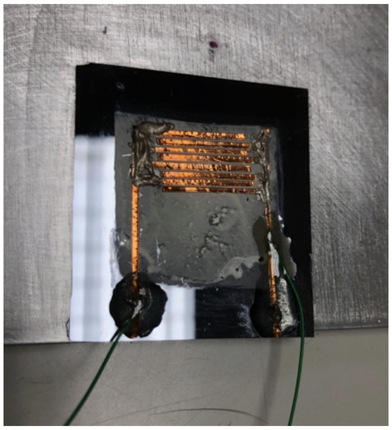

Figure 6.9: Interdigitated copper tape as electrodes on the PZT-silane film

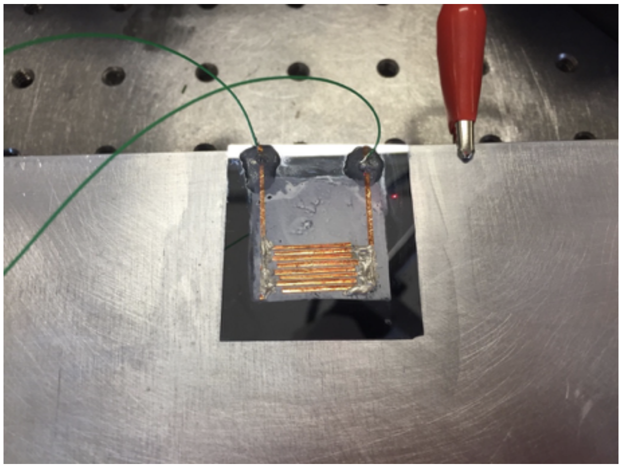

Figure 6.10: Sensor placement

projected on the silicon substrate. Velocity V and displacement D of the test structure are measured by the LDV controller. Again spectrum analyzer processes the measured impact force F, electric charge Q, and displacement D. From this data, two frequency response functions (FRF) are generated. Figure 6.14 shows the measured "Charge/Force FRF" and "Displacement/Force FRF" in the top and bottom figures, respectively. The charge FRF captures first three resonance peaks of the square plate at 348 Hz, 620 Hz, and 714 Hz as indicated in the displacement of the plate D and the impact force F (D/F) FRF. There is some electrical noise in electric charge Q and impact force F FRF because the sensor is just a prototype with copper tape electrodes that are not shielded properly. For example, the first peak of 180Hz in "Charge/Force FRF" comes from the third harmonic of line noise (60Hz).

The comparison between two FRFs proves that the idea of PZT-silane thin film with interdigitated electrodes would work as sensors. The next step is to use additive manufacturing methods to print electrodes for better dimensional control and accuracy.

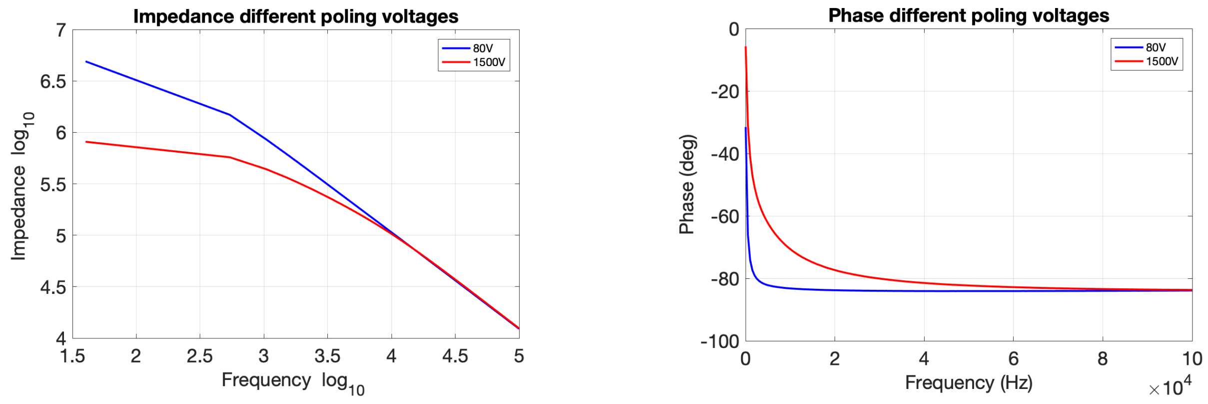

(a) Impedance magnitude (b) Phase angle

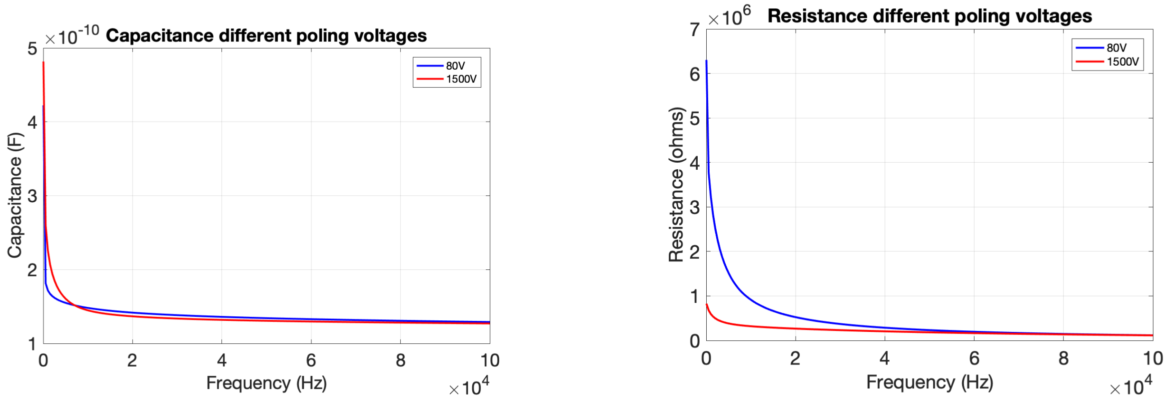

(c) Capacitance (d) Resistance

Figure 6.11: Prototype impedance measurement under two different poling voltages 80V vs 1500V

6.3 Fabrication of PZT Strain Sensor with Printed Electrodes

PZT composite thin films have been realized via drop casting on rigid silicon substrate as an actuator and accurate vibration sensor using the sandwich electrode configuration in Fig. 1.18. The fabrication process (listed below) uses a cleanroom environment.

1. Prepare silicon wafers with layers of silicon oxide, silicon nitride, titanium, and platinum to form the substrate and bottom electrode (in cleanroom).

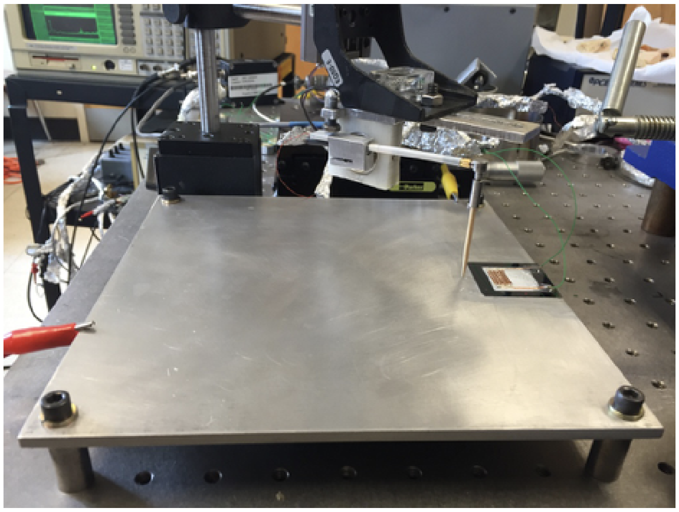

Figure 6.12: Experimental setup

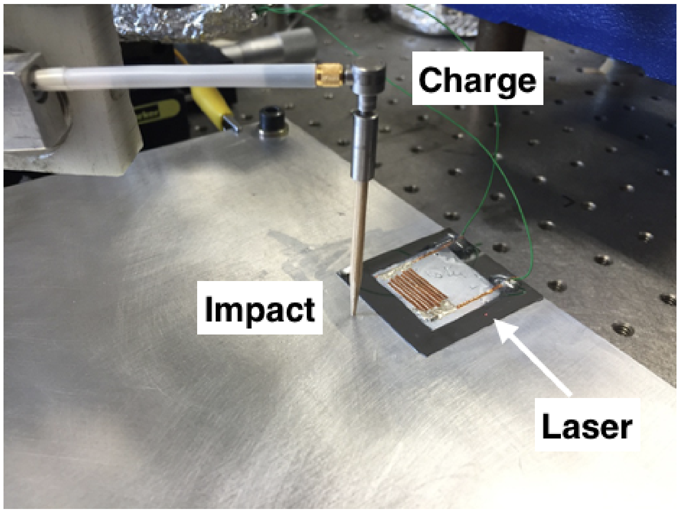

Figure 6.13: Experimental setup and laser location

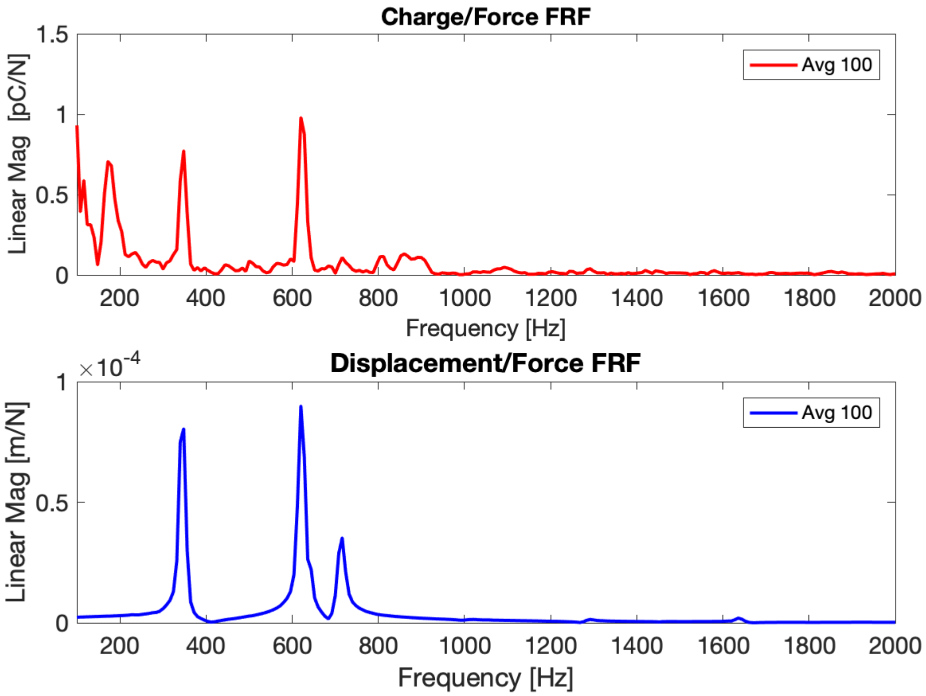

Figure 6.14: Charge/force and displacement/force frequency response functions

2. Drop-cast the PZT ink onto the silicon substrate to form a thin fluid layer (or printing via aerosol jets). Cure the newly deposited layer under UV light for 2.5 hours and in a furnace at 120 °C for 12 hours. As the ethanol evaporates, the PZT ink is reduced to a thin film with numerous PZT NPs embedded in a silane polymeric matrix. Thickness of the PZT-silane film is on the order of 5-10 μm.

3. An MPTS binder topcoat is subsequently deposited to protect the PZT-silane film.

4. A top electrode (gold on chromium) is deposited on the PZT-silane film via e-beam evaporation (in cleanroom).

The next step is to simplify the manufacturing process and fabricate sensors and actuators with printed electrodes.

6.3.1 Printing of Sandwich Electrodes Design

Printed electrodes have been studied extensively. Many 3D printed electrodes are stand-alone electrodes fabricated via extrusion or selective laser welding [76–80]. 3D printed thin-film electrodes on flexible substrate, also known as stretchable conductors [81], are often used as a sensor via piezoresistive effects. For these printed electrodes, high conductivity is required [81]. Also, a main challenge is to overcome weak interfacial bonding between the electrodes and the flexible substrate [81].

Realization of the sandwich design via inkjet printing involves three steps.

1. Print the bottom electrode on a flexible substrate, such as Kapton or PET tapes. This is a well-known technology, so it is not repeated here.

2. Deposit PZT-silane film onto the bottom electrode additively. This step is illustrated in previous chapters via drop casting and aerosol jet; therefore, it is not addressed in this section either.

3. The third step is to print the top electrode onto the PZT-silane film. Since its feasibility has not been studied before, printing a silver top electrode directly on the PZT-silane film is studied in this chapter to realize the sandwich electrode design.

6.3.1.1 Print Top Electrode onto the PZT-silane Film

- Prepare PZT-silane films on silicon wafers following the recipe stated in Chapter 2.

- Print NP ink (silver ink: Silverjet DGP-40LT-15C, Ag nanoparticle 30 wt% in triethylene glycol monomethyl ether, resistivity 11 $\mu\Omega - cm$, for printing on plastic films) via a Dimatix inkjet printer onto the PZT-silane films. Ag curing temperature is 100-150°C.

The inkjet printer used is a Dimatix DMP-2800 shown in Fig. 6.15, and the key printing parameters are:

- Cartridge type:10 pL

- Cartridge temperature: 30°C

- Substrate temperature: 60°C

- Jetting frequency: 5 kHz

- Applied voltage to the piezoelectric inkjet head: 24 V

- The size of the printed electrode traces is 0.12 mm in width and 4.84 mm in length.

- Drop spacing (spacing between two dots) was set to 60 μm. Line spacing was set to 240 μm for 1 layer of Ag ink and 960 μm for multiple layers.

- Features
  - Piezoelectric
  - 16 nozzles
  - 1 or 10 pL droplets
- Ink requirements
  - Viscosity: 8 – 12 cP
  - Particle size < 1 µm
  - Stable
  - pH from 3 to 10

Figure 6.15: Dimatix DMP-2800 with features and ink requirements

6.3.1.2 Resistance of the Printed Top Electrode

For a single silver electrode layer, there is no resistance readings when curing at 120°C for 10 minutes. The first approach is to increase curing time for better binding of Ag nanoparticles in the film. The curing time is increased from 10 minutes → 2 hours → 12 hours. However, the printed electrode remained non-conductive providing no resistance reading even curing up to 12 hours. The electrical resistance was probably around or beyond $G\Omega$.

The second approach is to print silver electrodes with multiple layers as shown in Fig. 6.16. The photos indicate that the width of electrodes starts to smear and significantly lose their dimension accuracy as more than two layers of electrodes are printed. The distortion of the electrode dimensions adversely affects spatial resolutions. As shown in Fig. 6.17, two printed electrodes with a line spacing of 480 μm will be in contact with each other shorting the electrodes. Although the two printed electrodes are not in contact as the line spacing is increased to 960 μm, the gap between the two electrodes is no longer uniform because of the dimension distortion.

Table 6.1 lists measured electrical resistance of these layered electrodes. The measurement is performed in a Signatone probe station (Fig. 6.18) using two test probes shown in Fig. 6.19. Although the electrical resistance drops significantly as the number of layer increases, the electrode has become so distorted in dimensions rendering the electrode totally useless.

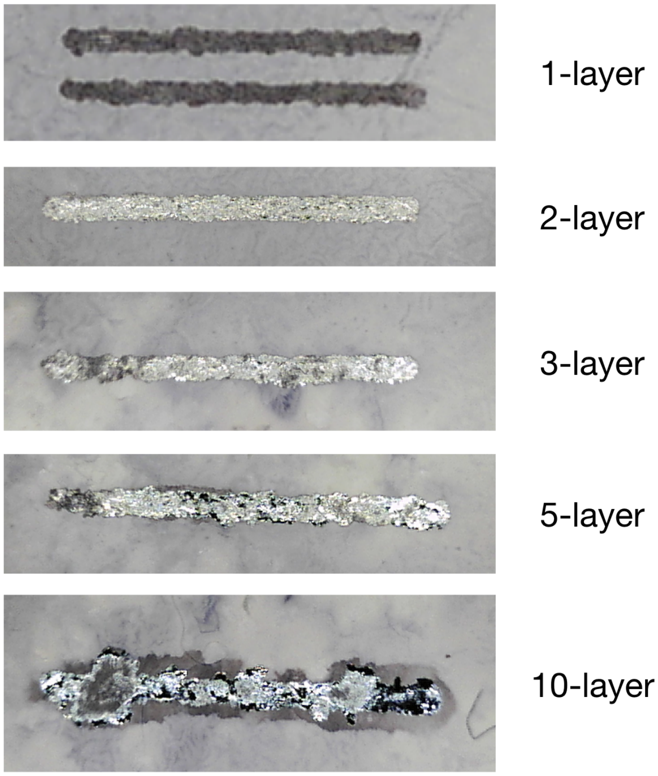

Figure 6.16: Photos of inkjet electrodes with multiple layers

The third approach is to deposit an MPTS layer on top of the PZT-silane layer, hoping that the silver electrode will perform better when printed on the MPTS layer. Figure 6.20 shows the printing results of silver electrodes on top of MPTS protective layer. The wettability of MPTS layer, however, is so poor that the silver electrode simply does not wet properly.

All things considered, the top electrode does not print properly on the PZT-silane film with an acceptable electrical resistance. The sandwich electrode design is difficult to realize. Therefore, a better design to achieve additive manufacturing of PZT-silane film must be sought.

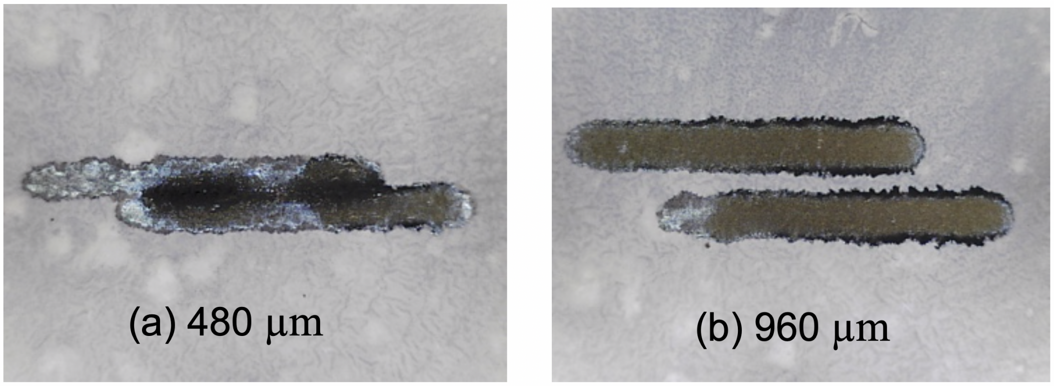

Figure 6.17: Electrode traces with two different line spacings

Table 6.1: Electrical Resistance of Layered Electrodes

No. of Electrode Layers	**Electrical Resistance**
1 layer	N/A
2 layers	20-30 $M\Omega$
3 layers	12-16 $k\Omega$
5 layers	13.6 Ω

6.3.1.3 Challenges and Solution

Migration of the manufacturing platform from a rigid substrate to a flexible substrate with full additive manufacturing capabilities, however, faces many arduous challenges. The first challenge is printing functional electrodes with high conductivity. A inkjet printed electrode may seem fine under an optical microscope but actually has electrical resistance in the $G\Omega$ range rendering the electrode entirely non-functional. The conductivity of the printed electrodes depends on many factors, such as surface roughness and wettability of the previous layer. Also, it takes a long time to identify optimal process parameters (e.g., printing con-

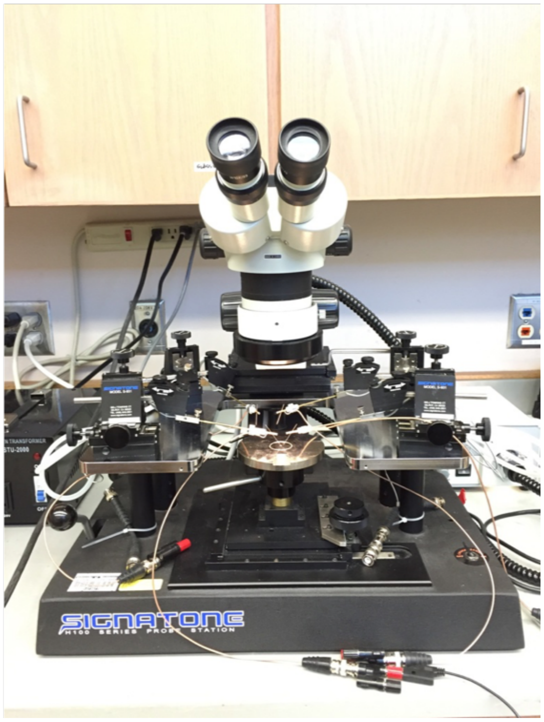

Figure 6.18: Signatone Probe Station

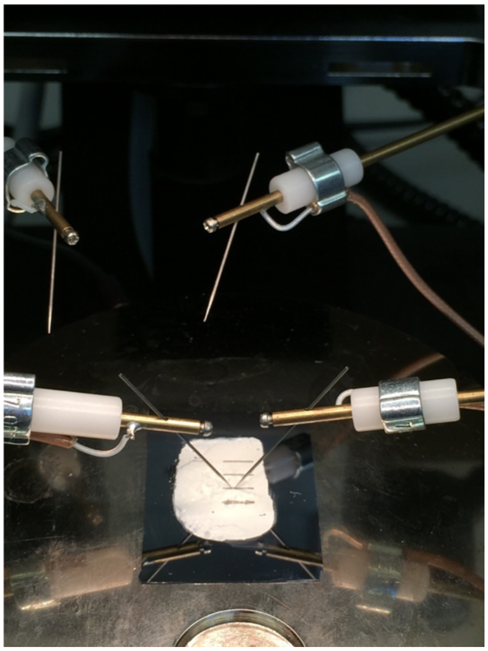

Figure 6.19: Measure resistance through two test probes

dition and drop spacing) to print a highly conductive electrode on a polymeric material. In view of this challenge, the sandwich electrodes are not desirable, because the electrodes need to be printed twice on two different materials (i.e., one on the substrate material and one on the PZT-silane film or MPTS top coat).

The second challenge is thickness uniformity of the PZT-silane films. After the solvent in the PZT ink evaporates, the top surface of the PZT film presents hills and valleys with PZT NPs randomly stacked on top of one another. Note that the PZT-silane film is very thin (e.g., 5 μm) and the NPs have a size distribution from 300-800 nm. As a result, random stacking of PZT NPs implies that the PZT-silane film thickness is not very uniform percentagewise. In terms of the film thickness, the sandwich electrodes in Fig. 1.18 are not desirable. As a result of the non-uniform PZT-silane film thickness, voltage applied to the sandwich electrodes leads to non-uniform electrical fields in the PZT-silane film. The

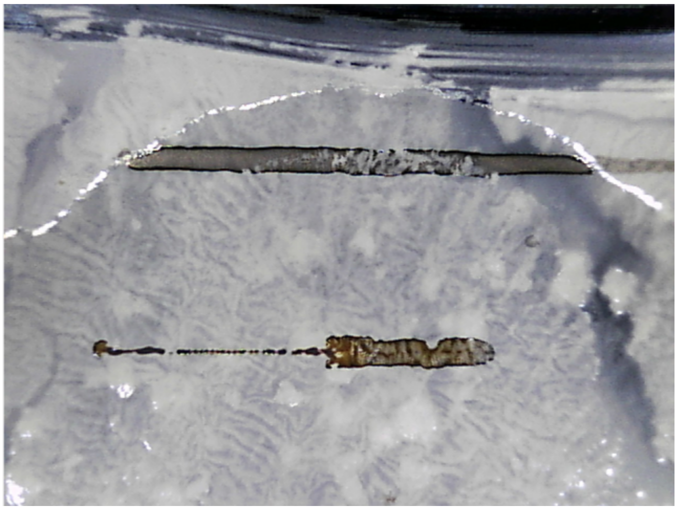

Figure 6.20: Print silver electrodes on top of MPTS protective layer

electrical field may become much more intense at the valleys, causing the PZT-silane film to electrically break down.

Motivated by the need to shift the manufacturing platform and the challenges it faces, a new design that adopts interdigitated electrodes (IDEs) is presented in next section to enables additive manufacturing of PZT thin-film sensors and actuators on flexible substrate.

6.3.2 Printing of Interdigitated Electrodes Design

Since it is a mature technology to inkjet printing silver electrodes on flat and smooth flexible substrate such as Kapton and PET films, it makes more sense to print both electrodes on the flexible substrate in the form of interdigitated electrodes (IDEs). In view of additive manufacturing, the use of IDEs offers many advantages. First, it reduces the number of layers to be printed. Second, both electrodes will be printed on the same material, significantly reducing manufacturing uncertainties.

Figure 6.21 shows silver IDEs inkjet printed on a PET film (as substrate). The width of the IDE fingers is 50 μm, while the gap between two neighboring fingers is 150 μm. PZT-silane ink can be deposited additively (e.g., via aerosol jet or drop-casting) over the IDEs to form an actuator or a sensor device. This two-step fabrication process can be viewed in Fig. 6.22. Figure 6.23 shows a magnified photo of the printed silver IDEs and its features. The width and separation can be as small as 10 μm. The IDEs layout is quite versatile and can be printed on both rigid or flexible substrates.

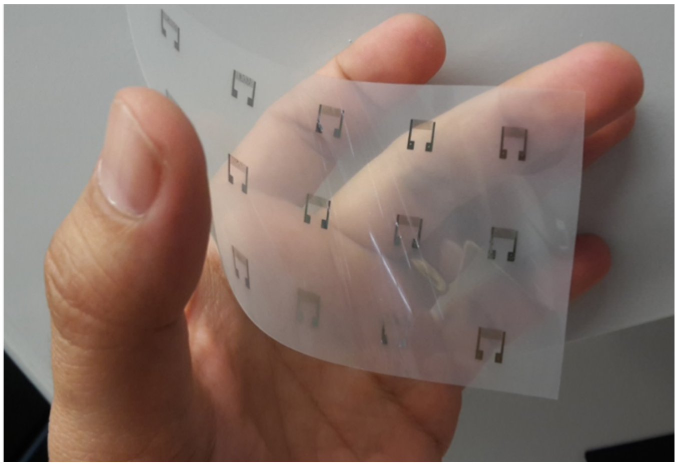

Figure 6.21: IDEs on PET film via inkjet printing

6.3.3 *Fabrication of PZT Devices with Printed Interdigitated Electrodes*

The fabrication process for PZT strain sensor with printed interdigitated electrodes is simple and straightforward. The electrode pattern can be changed easily and dimensions can be well controlled. Figure 6.24 shows a functional device with a PZT-silane film drop-cast on the IDEs with a PET substrate. Its fabrication process is listed as follows.

1. Interdigitated electrodes (e.g., silver) pattern is printed directly on PET or Kapton film with a Dimatix inkjet printer at 60 °C substrate temperature.
    (a) IDE geometry: electrode pattern is shown in Fig. 6.23.
        i. Width of fingers: 50 μm

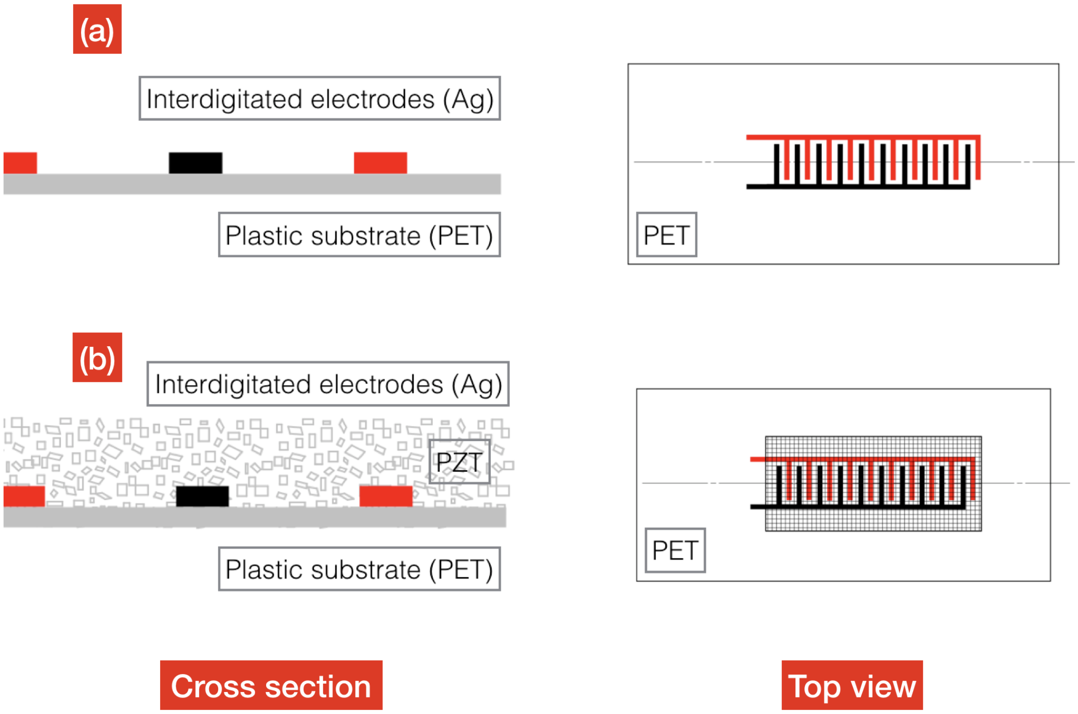

Figure 6.22: IDEs on PET film fabrication process

   ii. Gap between fingers: 150 μm
   iii. Number of fingers: 6

(b) Silver electrodes sintering condition: 120 °C for 10 minutes

(c) Number of printing passes: 1 pass

(d) Silver ink used: Silverjet DGP-40LT-15C, Ag nanoparticle 30 wt% in triethylene glycol monomethyl ether, resistivity 11 $\mu\Omega - cm$, for printing on plastic films

(e) Cartridge type: 10 pL

(f) Drop spacing: 40 μm

(g) Applied voltage range to piezoelectric inkjet head: 18-26 V

2. PZT thin films are drop-casted or printed on PET substrate with IDEs; see Fig. 6.22.

Subsequently, the films are cured under UV light for 2.5 hours first and then in a furnace with 5°C/min ramping rate till 120°C and held at 120°C for 12 hours.

3. Finally, lead wires are attached to the IDEs soldering pads via silver epoxy (conductive) and the wire connections are reinforced via epoxy.

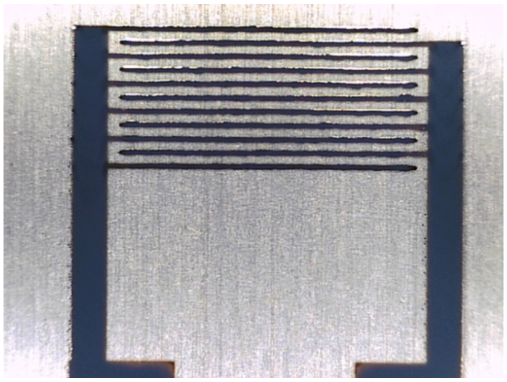

- Features
  - Width = 50 to 100 µm (maybe ~ 10 µm)
  - Separation = 50 µm (maybe ~ 10 µm)
  - Rigid or flexible
  - Versatile layout
  - Conductivity around 10-50% of pure metal
  - Ag, Au and Cu

Figure 6.23: IDEs with features

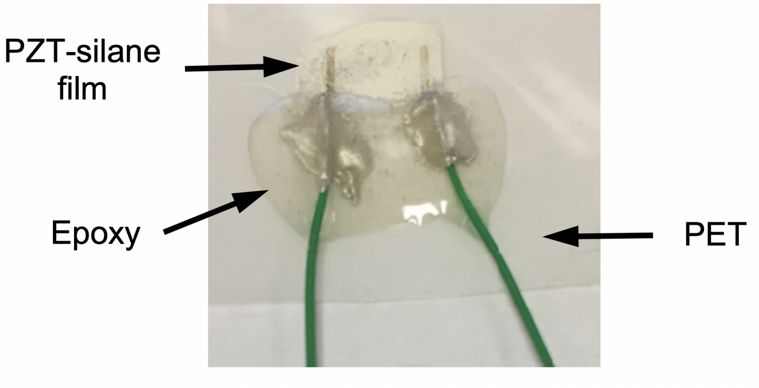

Figure 6.24: Magnification of PZT-silane sensor/actuator on PET

Chapter 7

PZT-SILANE THIN FILMS WITH PRINTED INTERDIGITATED ELECTRODES AS ACTUATOR, VIBRATION AND STRAIN SENSORS

7.1 Actuator Application

The fabricated PZT-silane thin film with IDEs is tested as an actuator in this section. Finite element analysis of the PZT/IDEs/PET actuator is conducted to simulate its response in experiment and also to showcase its performance of an alternative actuator design with enhanced piezoelectric properties on this PET film.

7.1.1 Experiment Setup and Test Result

First, the PET film is cantilevered with its right end constrained as shown in Fig. 7.1. The PZT-silane thin film with IDEs is printed near this fixed end in order to produce largest actuation for the PET beam. A copper tape is then attached to the free end of the PET film to create a reflective surface for a laser Doppler vibrometer (LDV) to measure its velocity. Next, the PZT-silane film is driven using function generator and power amplifier shown in Fig. 7.2 with a swept sine. First natural frequency of the PET beam is identified by analyzing the LDV measurements. Finally, the PZT-silane thin film is driven at its first natural frequency to induce resonance and the velocity response via LDV recorded on a digital oscilloscope as shown in Fig. 7.2.

Figure 7.3 shows one such responses recorded for the PZT/IDEs/PET structure at its first resonance. The top trace shows the driving voltage of 10V peak-to-peak around 90.5 Hz, and the bottom trace is the velocity measured via the LDV. With an LDV sensitivity of 5 mm/s/V, the measured velocity amplitude of the film is around 7.55 $\mu m/s$. This

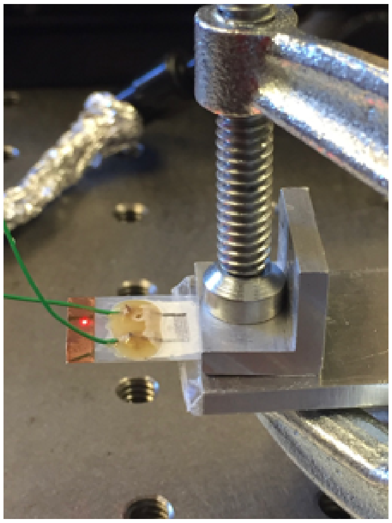

Figure 7.1: Photo of the test setup

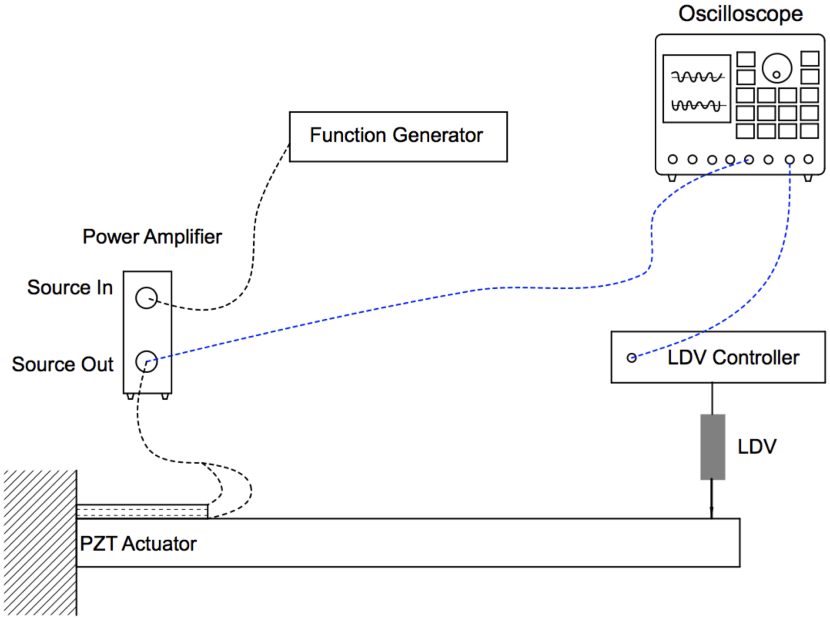

Figure 7.2: Experimental setup for actuator testing of PZT-silane film with IDEs

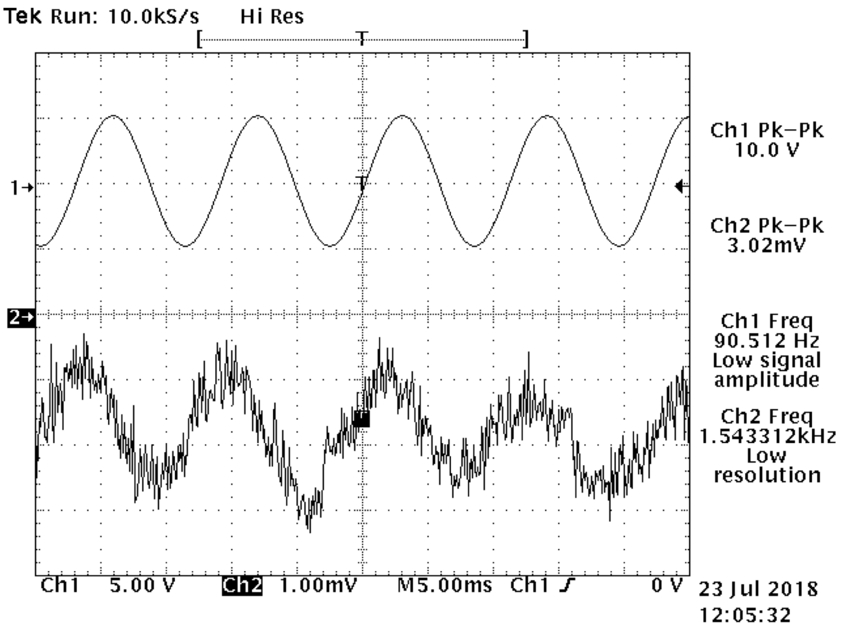

Figure 7.3: Resonant response at the first mode

measurement demonstrates the feasibility of printed PZT-silane films as an actuator.

7.1.2 Finite Element Analysis

Although the PZT/IDEs/PET structure shows an appreciable resonant response as an actuator, the measured velocity is somewhat noisy. Also, the non-resonant response is not obvious. These observations imply that the actuation is not strong enough. Based on past experimental and finite element analysis results, we estimate that the piezoelectric constant of the PZT film is about 0.6% of that of bulk PZT-4. The poor performance might result from presence of lead oxide (PbO) in the PZT nanoparticles, because significant excess lead (50-80 wt%) was used to prevent agglomeration. PbO is not piezoelectric and its presence degrades piezoelectric properties of the PZT nanoparticles. The piezoelectric properties of PZT nanoparticles should be enhanced significantly to make PZT-silane films more feasible for actuator applications.

Figure 7.4 shows a finite element (FE) model of the test setup in Fig. 7.1. The PZT/IDEs/PET tape is fixed at the top boundary and the PZT/IDEs actuator is placed 3 mm below this fixed boundary and 3.25 mm away from the left edge to simulate the experimental conditions. A FE figure of PZT with interdigitated electrodes is shown in Fig. 7.5. From this figure, we can see that the PZT/IDEs actuator consists of six sets of electrodes and eleven PZT strips. The PZT strips (5000 μm x 150 μm with 10 μm in thickness) are modeled using piezoelectric elements. Moreover, electrical boundary conditions are set as follows. The voltage of the PZT surface nodes near the positive electrodes (red portions in Fig. 7.6) is 5V, and the voltage of the nodes near the negative electrodes (black portions in Fig. 7.6) are -5V, thus creating the 10V peak to peak actuating voltage used in the experiment.

As a reference, bulk material PZT-4 has a density of $\rho = 7500kg/m^3$, $\varepsilon_{\mathbf{o}} = 8.854 \times 10^{-12}\,\frac{F}{m}$, and the following stiffness matrix C, piezoelectric matric d, and dielectric matric.

$$\mathbf{C}^E = \begin{bmatrix} 139.00 & 77.84 & 74.28 & 0 & 0 & 0 \\ 77.84 & 139.00 & 74.28 & 0 & 0 & 0 \\ 74.28 & 74.28 & 115.41 & 0 & 0 & 0 \\ 0 & 0 & 0 & 30.58 & 0 & 0 \\ 0 & 0 & 0 & 0 & 25.64 & 0 \\ 0 & 0 & 0 & 0 & 0 & 25.64 \end{bmatrix} GPa \tag{7.1}$$

$$\mathbf{d} = \begin{bmatrix} 0 & 0 & 0 & 0 & 496 & 0 \\ 0 & 0 & 0 & 496 & 0 & 0 \\ -123 & -123 & 289 & 0 & 0 & 0 \end{bmatrix} pC/N \tag{7.2}$$

$$\frac{\varepsilon_{\mathbf{T}}}{\varepsilon_{\mathbf{o}}} = \begin{bmatrix} 762 & 0 & 0 \\ 0 & 762 & 0 \\ 0 & 0 & 663 \end{bmatrix} \tag{7.3}$$

Since the PZT-silane film is not entirely PZT, the material properties must be modified in this simulation to reflect the presence of silane. For the density and stiffness matrix C,

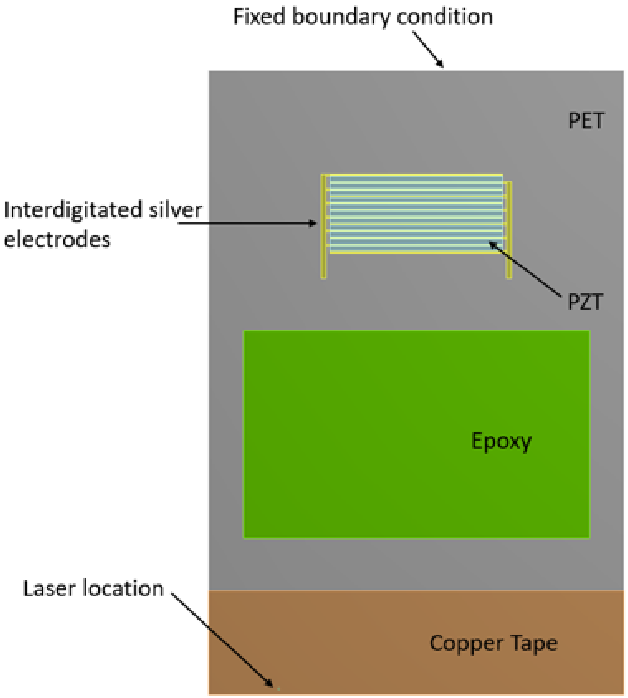

Figure 7.4: Finite element model of the PZT/IDEs/PET actuator

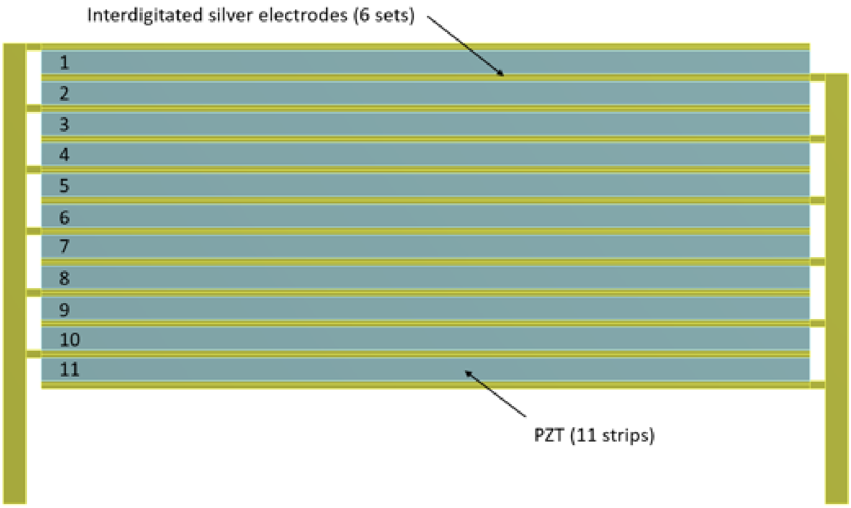

Figure 7.5: Finite element model of PZT with IDEs

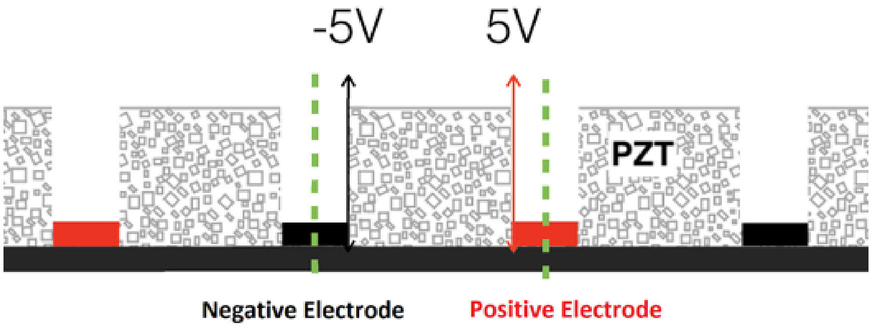

Figure 7.6: Cross section schematic for electrical boundary conditions (not to scale)

we used 0.1% of the standard values for PZT-4, because the polymer content reduces the density and stiffness of the PZT-silane films.

The rest of the actuator is modeled using solid elements. The components' dimensions and material properties are shown in Tab. 7.1. For the PET layer, its size is 18 mm x 12 mm, thickness is 130 μm, density is 1300 kg/m^3, Young's modulus is 2.55 GPa, and Poisson's ratio is 0.39. For the epoxy block, its size is 10 mm x 6 mm, thickness is 500 μm, its density is 1250 kg/m^3, Young's modulus is 3.5 GPa, and Poisson's ratio is 0.33. The size of copper tape is 12 mm x 3 mm, thickness is 20 μm, density is 8960 kg/m^3, Young's modulus is 110 GPa, and Poisson's ratio is 0.34. For the silver electrodes, their size is 5 mm x 50 μm, thickness is 300 nm, density is 10,500 kg/m^3, Young's modulus is 84 GPa, and Poisson's ratio is 0.365.

When the PZT-silane layer is subjected to a sinusoidal driving voltage, it will expand and contract, causing the PET layer to deform and vibrate. The first natural frequency and its mode shape is predicted via modal analysis. The calculated mode shape is shown in Fig. 7.7. The frequency of this first bending mode is 90.512 Hz, which agrees with the experimental results.

Harmonic analysis is also conducted to simulate the actuators frequency response with the following parameters and conditions:

Table 7.1: Finite element model properties of the PZT/IDEs/PET actuator

	PET	**Epoxy block**	**Copper tape**	**Silver electrode**
Length (mm)	18	10	12	5
Width (mm)	12	6	3	$50\mu m$
Thickness (μm)	130	500	20	300nm
Density (kg/m^3)	1300	1250	8960	10,500
Young's Modulus (GPa)	2.55	3.5	110	84
Poisson's Ratio	0.39	0.33	0.34	0.365

- Structural damping coefficient is 0.05%.
- For the PZT-silane layer properties, 0.1% of the density value and stiffness matrix, 0.6% of the piezoelectric and dielectric matrices of PZT-4 are used.
- A sinusoidal driving voltage of 10V peak-to-peak is applied to the PZT actuator.
- The velocity at the laser location (cf. Fig. 7.4) is simulated between 90-91 Hz and plotted in log scale as shown in Fig. 7.8.

Figure 7.8 indicates that the velocity amplitude at the laser location when driving PZT thin films at the first natural frequency (90.51Hz) is 7.64 $\mu m/s$, which is very close to the experimental results shown in Fig. 7.3. Therefore, the modal analysis and harmonic analysis confirm that the finite element model is accurate and can be relied on for future prediction. This design and test configuration will be referred to hereafter as "original design".

The displacement frequency response at the laser location of this design is simulated and plotted in log scale; see Fig. 7.9. The actuator has a constant gain ($\sim 3.4 \times 10^{-11}$ m) in the low frequency range, and a peak displacement amplitude of 7.98×10^{-8} m at resonance.

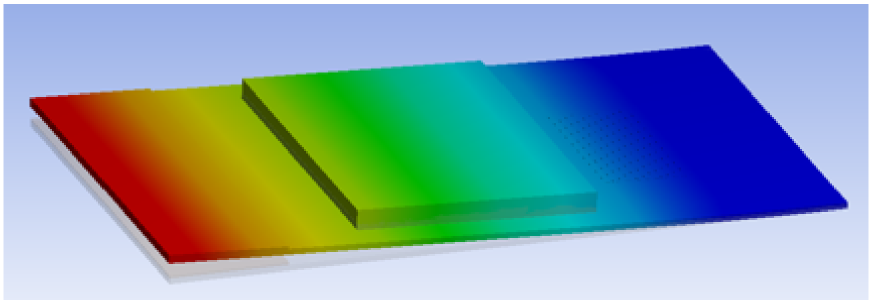

Figure 7.7: The first mode shape of the actuator obtained from finite element modal analysis with first natural frequency at 90.512 Hz

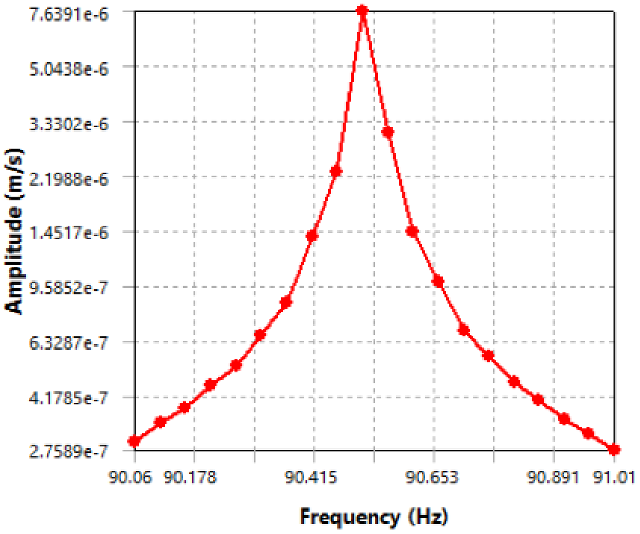

Figure 7.8: Velocity frequency response (90-91Hz) for actuator original design

To find out the potential performance for an actuator with a better electrode design and enhanced piezoelectric properties for the PZT layer, a second harmonic analysis is conducted with the following configurations.

- For the PZT-silane films properties, 50% of piezoelectric and dielectric matrices of PZT-4 are adopted.
- All of the other parts of the model except for the PZT with IDEs remain the same, which means the same PET film, epoxy, and copper tape are used in their original locations.
- The harmonic analysis is performed with the same structural damping coefficient of 0.05%.
- The new PZT/IDEs actuator design consists of sixteen sets of electrodes and thirty-one PZT strips. The dimensions for a PZT strip are 11000 x 150 μm with 10 μm in thickness. The PZT/IDEs actuator is placed 0.5 mm below the fixed boundary and 0.25 mm away from the left edge as depicted in Fig. 7.10.
- For the electrical boundary conditions, a sinusoidal driving voltage of 300V peak-to-peak is used. The voltage of the PZT surface nodes near the positive electrodes are set to 300V, and the voltage of the nodes near the negative are set to 0 (electric field $\sim 2V/\mu m$). This electrical field has been tested on PZT thin-film actuators before and its well below the PZT thin film dielectric breakdown strength ($\sim 20V/\mu m$ [82]).

The second design and test configuration will be referred to hereafter as "new design". The PZT/IDEs/PET actuator with the new design has a resonance frequency around 91.34 Hz, a constant gain of 5.9×10^{-7} m in the low frequency range, and a peak displacement amplitude of 1.452×10^{-3} m at resonance. A performance comparison between these two designs is summarized in Tab. 7.2. It reveals that with a better electrode design, enhanced

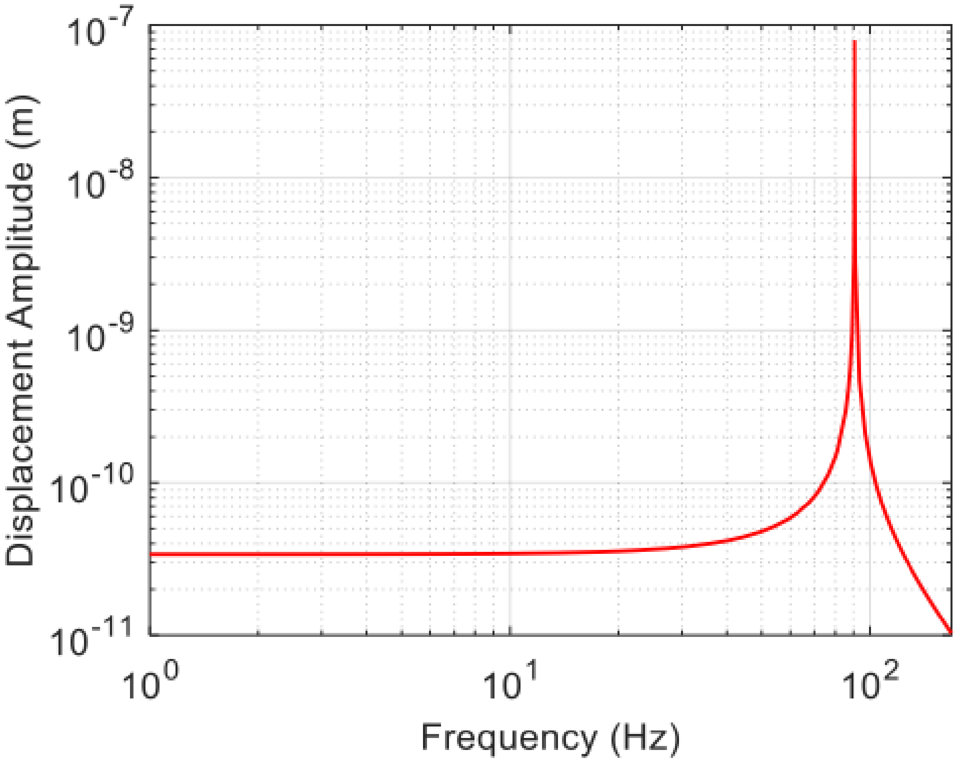

Figure 7.9: Displacement frequency response for actuator original design

piezoelectric properties and an elevated actuation voltage, the actuators static gain could be improved 1.7353×10^4 times and the peak displacement amplitude could be roughly 1.8197×10^4 times higher.

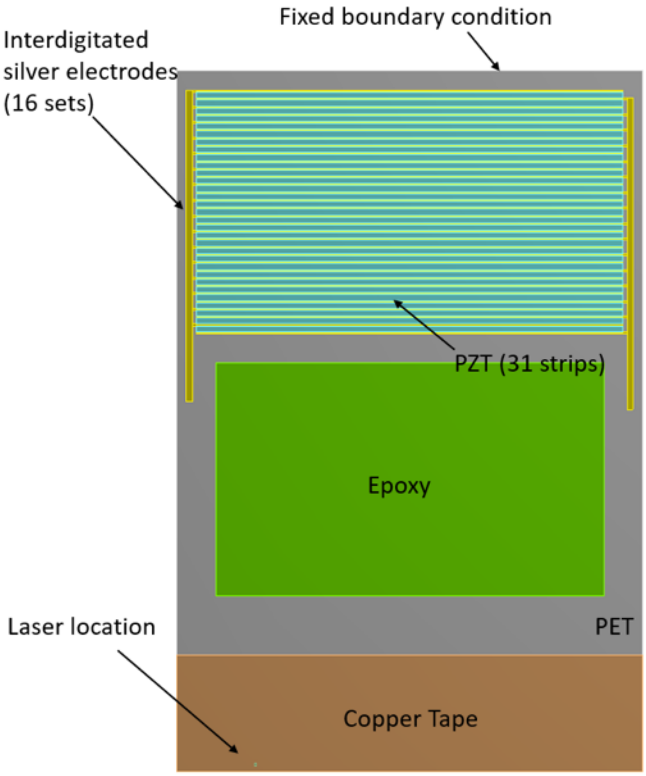

Figure 7.10: FEA model of the PZT/IDEs/PET actuator new design

Table 7.2: Actuator Performance Comparison

	Static Gain	Peak Displacement Amplitude at Resonance
Original Design	$3.4 \times 10^{-11}\ m$	$7.98 \times 10^{-8}\ m$
New Design	$5.9 \times 10^{-7}\ m$	$1.452 \times 10^{-3}\ m$

7.2 Sensor Applications

The fabricated PZT-silane films with IDEs are tested as

1. A vibration sensor on a beam structure

2. A vibration and strain sensor on a rotating wing structure

3. A strain sensor with direction sensing capability

7.2.1 Vibration Sensor on a Beam

Figure 7.11 is a schematic diagram for a vibration impact test setup to demonstrate the vibration sensing capability of a PZT-silane thin film with printed IDEs. The test is performed on a beam structure made of aluminum alloy with a length of 223 mm, a width of 25 mm and a thickness of 5 mm. This test beam is supported by a pillar spacer at one end that is screwed onto a vibration isolation table to create a cantilever beam structure. The spacer is made of aluminum with an outer diameter of 12.55 mm, an inner diameter of 10 mm, and a height of 25.28 mm. The sensor is poled at 72V for 12 hours and placed near the fixed end of the cantilever beam as indicated in Fig. 7.11.

The experimental setup consists of impact hammer with a load cell, laser Doppler vibrometer (LDV), charge amplifier, and spectrum analyzer for data processing same as in Section 5.2.1. Figure 7.12 shows the results of impact hammer test performed. The upper plot is a frequency response function collected by the laser Doppler vibrometer (LDV) and processed in spectrum analyzer. It shows a relationship of D/F: ratio of the displacement D of the cantilever beam to the impact hammer force F. From the graph, we can see the most prominent peaks at 92 Hz, 568 Hz, 1340Hz, 1684Hz and 1836 Hz.

The lower plot is a frequency response function collected by charge amplifier and processed in the spectrum analyzer. The “Charge/Force FRF” shows the electric charge Q generated by the PZT-silane film under impact force F. The sensor can capture the most prominent peaks of the beam at frequencies indicated in “Displacement/Force FRF”. However there are some electrical noise signals appear in the electric charge Q and impact force F FRF because the poling electrical field strength might not be big enough. Considering the gap between electrode fingers is around 100 - 150 μm, an applied electric field of $0.48 - 0.72 V/\mu m$ may be too weak. Furthermore, vibration generated by impact hammer under current loading conditions may be too small for sensor to pick up. As shown in the second plot, the first peak of 60 Hz in “Charge/Force FRF” comes from electrical line noise. Improvements to the test setup could be made to create a larger strain condition for sensor measurements and demonstrations, which will be elaborated in the next section.

Overall, the agreement between two FRFs proves that PZT-silane thin films with printed interdigitated electrodes on PET work as a vibration sensor. The next step is to build a test structure that could generate a larger strain or vibration signal for sensor demonstration.

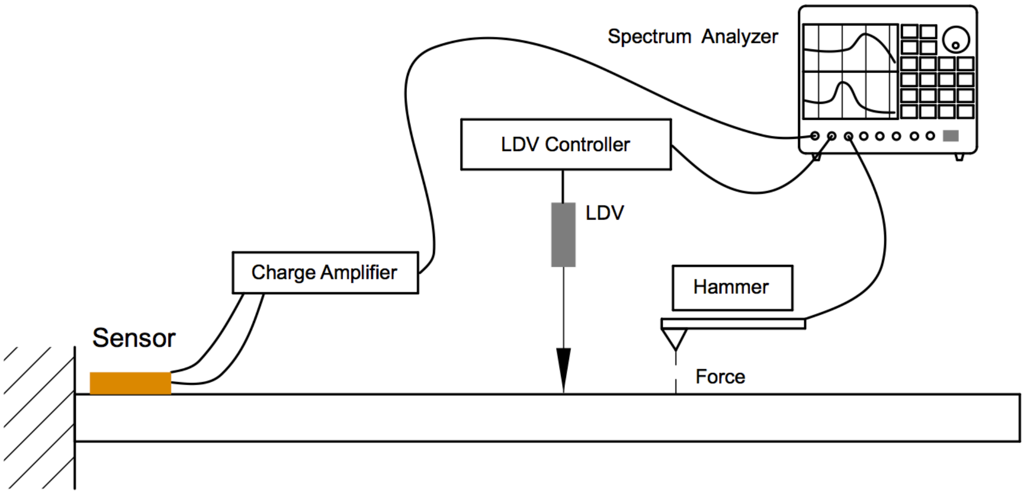

Figure 7.11: Schematic diagram of vibration impact test setup

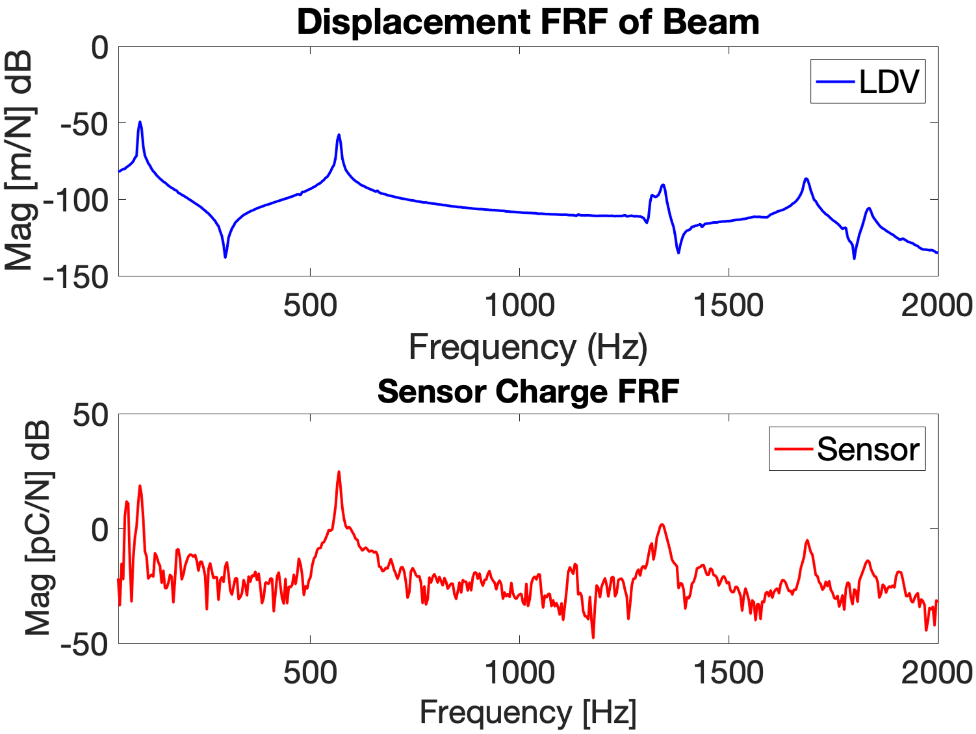

Figure 7.12: Comparison of frequency response functions from the laser Doppler vibrometer (upper plot) and from the PZT-silane sensor (lower plot)

7.2.2 Vibration and Strain Sensor on Rotating Wing Structures

7.2.2.1 Experimental Setup

Figure 7.13 shows a single-axis rotation stage controlled by a 60W motor and a clamping mechanism fixed to the stage providing a clamped boundary condition for the test wing. This rotational stage was build by Mark Jankauski [83]. The DC motor (Maxon Motors with part. no. 310007) uses a 24 VDC power supply and it has a nominal speed of 8050 rpm, torque of 85.6 mNm and a resolution of 2000 qc/revolution. The motor controller for communicating is an EPOS2 24/5 (part. no. 367676) shown in Fig. 7.13. It needs a power supply of 24 VDC with 5A regulated current. LabVIEW virtual instruments (VIs) is used for controlling the motor. The LabVIEW front panel is shown in Fig. 7.14. Combined with a data acquisition module [1] (NI myDAQ), LabVIEW is also used for recording outputs.

The 60W rotation motor used in this experiment is named 'Motor 1' in the labVIEW VI (see Fig. 7.15). There are only three parameters required: Frequency (Motor 1), scaling and offset. (There is no need to use a second motor in this case.) The "frequency" [2] input controls oscillation frequency in Hz for the motor. The "scaling" and "offset" tabs are both used to configure the rotation amplitude of the test structure. The "scaling" tab has a sensitivity setting of $\frac{20}{9}\ qc/V$ per rotation amplitude of 1°and the "offset" tab has a sensitivity setting of $\frac{2000}{360}\ qc$ per rotation amplitude of 1°. For one revolution, 2000 qc = 360°. The "offset" tab is used to set motor's initial position by linking it to zero voltage and should correspond to the negative farthest position of the motor. Let us consider a rotation amplitude of 5°, the total range of rotation is 10°. The scaling tab should be set to 11.1 qc/V and the "offset" [3] tab in this case should be set to $-27.7778 \approx -28qc$.

Strain gauges and their measurement components are purchased from Omega Engineering. Uniaxial, two-lead, 350Ω strain gauges (part. no. SGD-2/350-LY13) are used in the demonstration. Figure 7.16 shows a picture of a 1-axis linear gauge for static and dynamic applications. It can detect strain in the direction indicated in the figure. Figure 7.17 shows a bridge completion module with part. no. BCM-1. It is used for the quarter-bridge Wheatstone bridge circuit. The "ZERO" knob on the center of module is used to balance the bridge and define the zero strain condition. The voltage output of Wheatstone bridge circuit ('VOUT' on the right) is connected to the input of a strain gauge amplifier (pins 10 and 11) shown in Fig. 7.18 to amplify the strain signal. After the bridge circuit is balanced for the zero strain condition, the gauge amplifier output needs to be set to zero again for balancing the circuit.

---

[1] The data acquisition module (NI myDAQ) analog input voltage to motor controller varies between $0-5V$.

[2] The default frequency is set to 0 Hz when opening LabVIEW, and must be set to desired frequency before each experiment.

[3] "Offset" links 0 V input voltage to -5°, 2.5 V input voltage to 0°and 5 V input voltage to 5°.

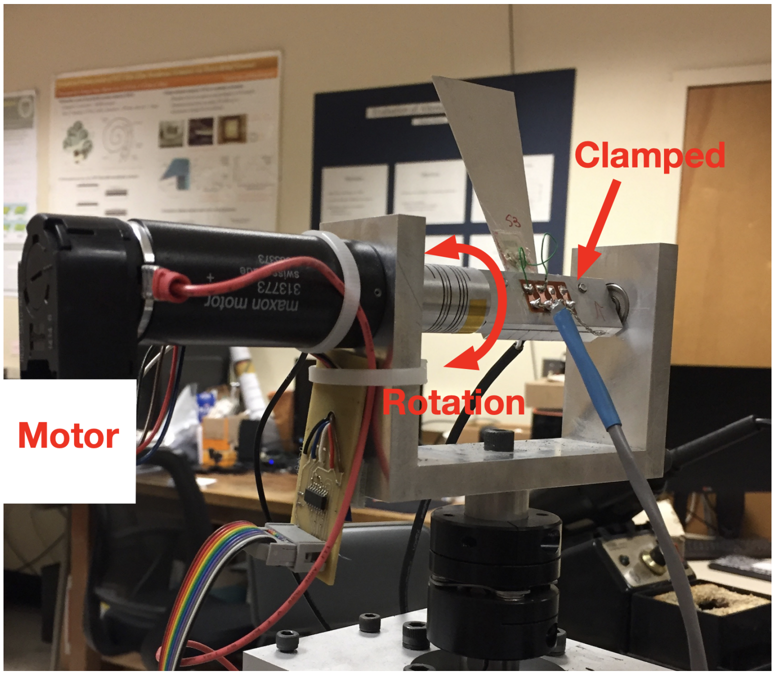

Figure 7.13: Rotation stage setup photo

Strain data can be interpreted through the amplifier output V_{out} using Eqn. (7.4),

$$\varepsilon = \frac{4V_{out}}{(BV)(GF)(AG)} \tag{7.4}$$

where BV stands for bridge excitation voltage, which is set to 5V, GF stands for gauge factor, which is set to 2.14, and AG is amplifier gain, which is set to 175 during strain gauge measurements.

7.2.2.2 Vibration Sensor Demonstration

An aluminum triangular wing with 0.42 mm thickness is prepare as test structure (see Fig. 7.19 (a) for detail wing geometry). The material's Youngs modulus is 68.9 GPa, Poisson's ratio is 0.33, and density is 2700 kg/m^3. A PZT-silane thin film with IDEs sensor (Fig. 6.24) is attached to one side of wing surface (see Fig. 7.19 (b) for PZT sensor location). The PZT sensor is 12mm wide and 17mm long. On the side of wing surface, a linear, two-lead, 350Ω

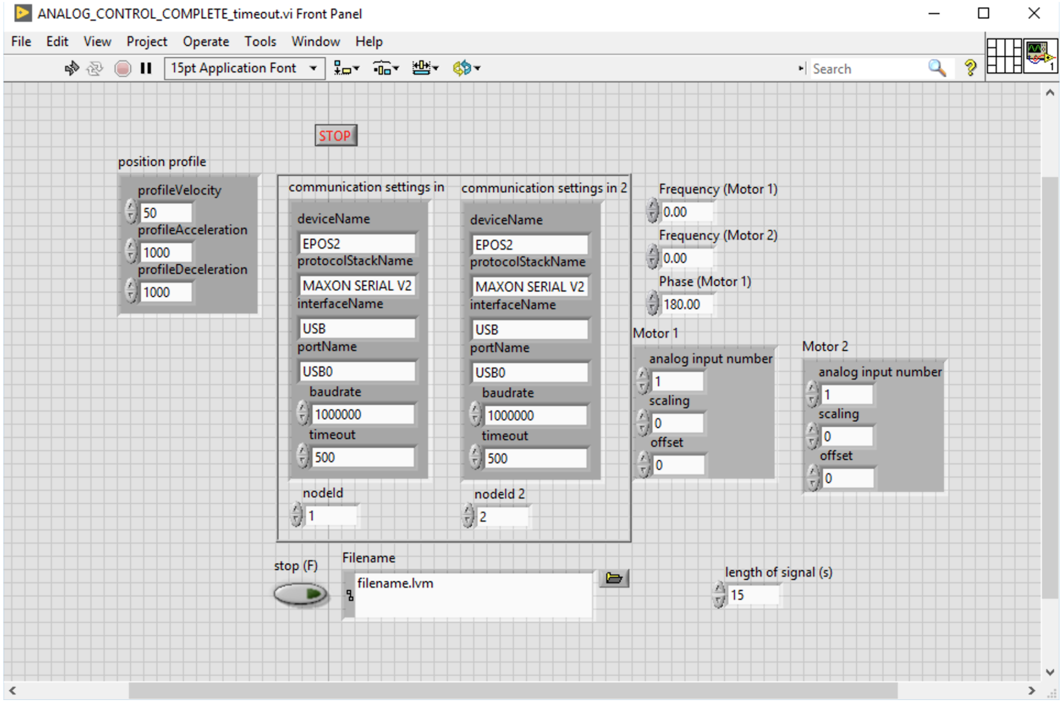

position profile
profileVelocity
50
profileAcceleration
1000
profileDeceleration
1000

communication settings in
deviceName
EPOS2
protocolStackName
MAXON SERIAL V2
interfaceName
USB
portName
USB0
baudrate
1000000
timeout
500
nodeId
1

communication settings in 2
deviceName
EPOS2
protocolStackName
MAXON SERIAL V2
interfaceName
USB
portName
USB0
baudrate
1000000
timeout
500
nodeId 2
2

Frequency (Motor 1)
0.00
Frequency (Motor 2)
0.00
Phase (Motor 1)
180.00

Motor 1
analog input number
1
scaling
0
offset
0

Motor 2
analog input number
1
scaling
0
offset
0

stop (F)

Filename
filename.lvm

length of signal (s)
15

Figure 7.14: Front panel of the experimental LabVIEW software

strain gauge with part. no. SGD-2/350-LY13 is attached. This strain gauge's dimension and placement can be found in Fig. 7.19 (c).

Stage rotation is controlled by LabVIEW VI [4] through the motor controller. Stage rotates sinusoidally with a driving frequency of 18Hz and rotation amplitude of 5 degrees. The "Frequency" is set to 18Hz, "scaling" parameter is set to 11.1 qc/V and "offset" tab is set to $-28qc$ during this vibration sensor demonstration on the wing structure. Figure 7.20 shows a schematic diagram of the rotation wing test setup. First a laser Doppler vibrometer (LDV) is used to measure velocity of the test wing. The laser location can be seen in Fig. 7.21. Second, a charge amplifier is used to capture the response of the PZT- IDEs sensor. Third, a strain gauge amplifier and bridge completer are used to measure the strain of the test wing through commercial strain gauge. A digital oscilloscope is used to record all

---

[4] LabVIEW VI → Function Generator (NI my DAQ) → Motor Controller → DC Motor (60W)

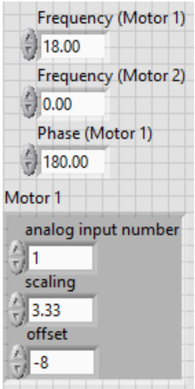

Frequency (Motor 1)
18.00
Frequency (Motor 2)
0.00
Phase (Motor 1)
180.00
Motor 1
analog input number
1
scaling
3.33
offset
-8

Figure 7.15: LabVIEW VIs Zoom

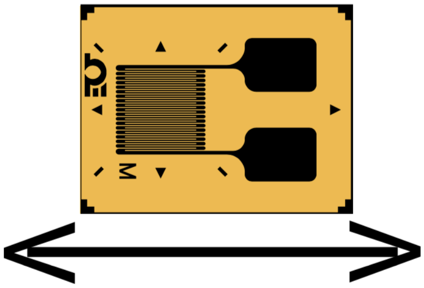

Figure 7.16: Strain gauge with part. no. SGD-2/350-LY13 (7.6mm)

three measurements.

Figure 7.22 shows one of the time-domain measurements as viewed through the oscilloscope during the experiment. The top trace (Ch 1) is the velocity V through LDV, middle trace (Ch 2) is the electric charge generated Q from the PZT thin film with IDEs sensor, and the bottom trace (Ch 3) is the strain gauge reading ϵ. These results confirm that PZT sensor can be used as a vibration sensor because the charge output has the same frequency as both the velocity and the strain of the test wing.

7.2.2.3 Strain Sensor Demonstration

A second aluminum triangular wing with a 0.42 mm thickness is selected as test structure for demonstration of PZT-silane thin film with printed IDEs sensor as strain sensor. The aluminum wing has a Youngs modulus of 68.9 GPa, a Poisson's ratio of 0.33, and a density of 2700 kg/m^3. Figure 7.23 shows a detail drawing of wing geometry. A PZT-IDEs sensor with dimension 12×16 mm is attached to front side of the wing; see Fig. 7.23 (a) for PZT sensor location. On the back side (see Fig. 7.19 (b)), a linear 350Ω strain gauge with same specifications as in the last section is attached. Strain gauge has a dimension of 6×7.6 mm and placement details can be found in Fig. 7.19 (b).

Figure 7.17: Bridge completion module with part. no. BCM-1

Figure 7.24 shows a schematic diagram of the second wing rotation test setup [5]. LabVIEW VI is used to input desired parameters to control stage rotation. During this test, stage rotates sinusoidally with a driving frequency of 18Hz and sweep angle amplitude of 1 to 4 degrees. The“scaling” and “offset” tabs are set according to Tab. 7.3 during strain sensor demonstration on the wing structure.

Table 7.3: Sweep angle control for rotation Motor 1

Sweep Angle	**0.5°**	**1°**	**1.5°**	**2°**	**3°**	**4°**
Scaling	1.11	2.22	3.33	4.44	6.66	8.88
Offset	-3	-6	-8	-11	-17	-22

In the second part of the tests, both a digital oscilloscope (Tektronix, TDS540A) and a spectrum analyzer (Stanford Research Systems Model SR785 SR785 Two-Channel Dynamic

---

[5] Rotation stage is powered by a 60W DC motor, controlled by a function generator in NI myDAQ and a motor controller.

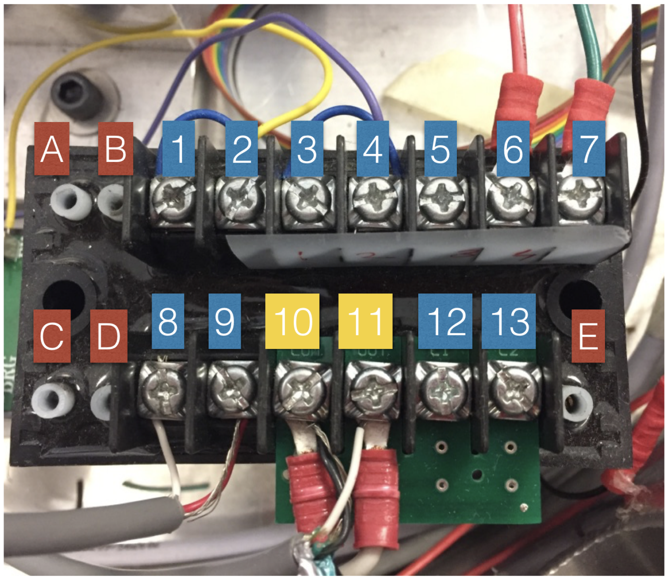

Figure 7.18: Strain gauge amplifier with part. no. DMD-465WB

Signal Analyzer) are used for recording and processing data. Time and frequency domain signals from the voltage output coming from strain gauge amplifier and the response from the charge amplifier are collected and analyzed below.

Figure 7.25 (a) shows the time domain outputs when the wing vibrates at 18 Hz with angular amplitude of 1°. Channel 1 is the strain gauge output (upper waveform) and channel 2 is the PZT-IDEs sensor charge output (lower waveform). Fast Fourier transforms (FFT) of the strain and charge signals are also recorded by the spectrum analyzer. Figure 7.25 (b) shows the frequency domain measurements when wing vibrates at 18 Hz with an amplitude of 1°. Upper plot is the strain FFT magnitude measurement from strain gauge and the lower plot is charge FFT magnitude measurement from the PZT-silane thin film with IDEs. Each FFT data represents the vector average value of 100 trials. Repeating this procedure, time and frequency domain measurements are also taken when the wing vibrates at 18 Hz with angular amplitude at 2, 3 and 4 degrees (see Fig. 7.26, Fig. 7.27 and Fig. 7.28). The strain signal in time and frequency domains at 1° are pretty noisy due to small strain state present.

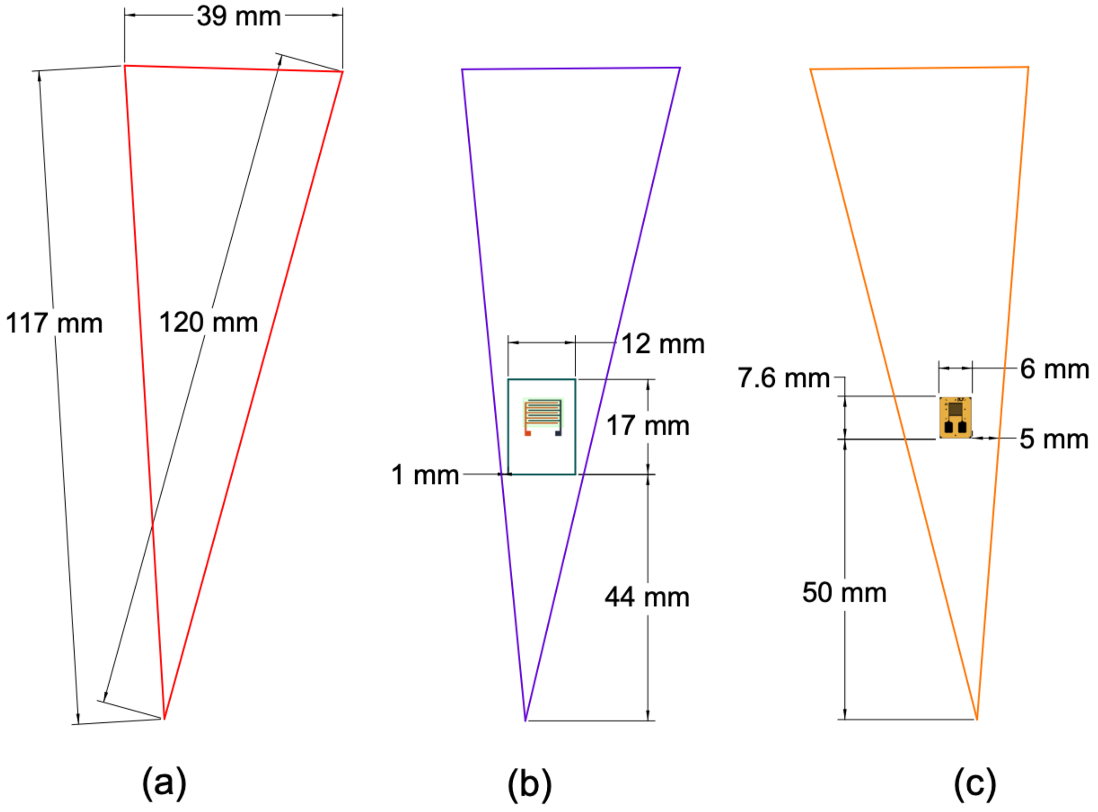

Figure 7.19: (a) Aluminum wing geometry 0.42mm thin; (b) PZT-silane thin film with IDEs (S4) on one side and (c) strain gauge (G4) on the other side

Strain data can be interpreted through the strain amplifier output V_{out} using Eqn. (7.5) provided below. The strain signals look much cleaner when the driving angular amplitude at 2 to 4 degrees.

$$\varepsilon = \frac{4V_{out}}{(5)(2.14)(175)} = 0.0021V_{out} \tag{7.5}$$

There are higher-order harmonic vibrations present in the data (see Fig. 7.26). They are induced by the motor and/or the coupling between the rotation stage and shaft [83]. The angular acceleration of the motor is found to cause higher order harmonic vibrations [84]. The motor input is not purely sinusoidal but periodic. The higher-order harmonic vibrations

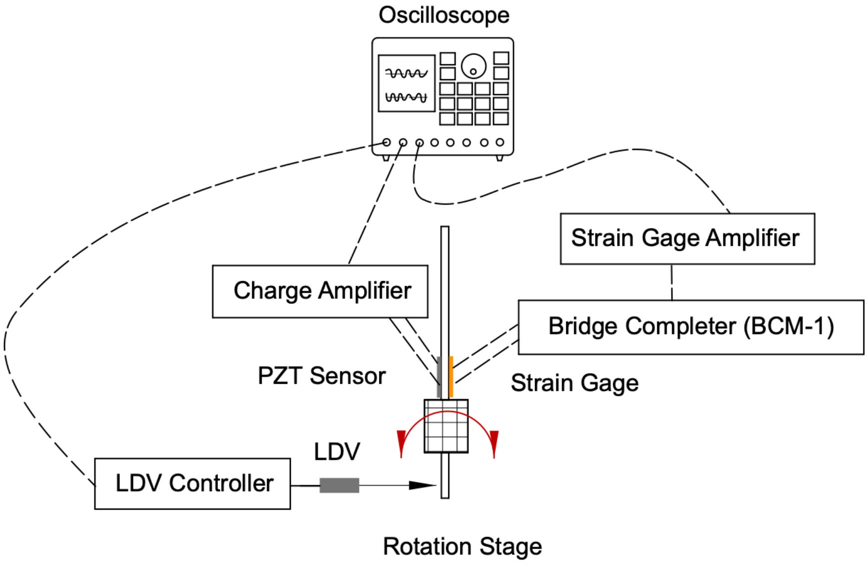

Figure 7.20: Schematic diagram of the first wing rotation test setup

will occur at integer multiples of the driving frequency, such as 36Hz, 54Hz, 72Hz in this case.

At a driving frequency of 18Hz, strain ϵ and charge Q measurements are taken and plotted from 1° to 4° as shown in Fig. 7.29. Upper plot is the strain data from strain gauge and the lower plot is the charge data from the PZT-silane thin film with IDEs sensor. From the graph, we can see charge output is increased when the vibration amplitude increases and also PZT-IDEs sensor responses are approximately proportional to strain gauge outputs as vibration amplitude increases from 2° to 4°. Figure 7.30 shows ratios between PZT-IDEs sensor charge output and strain gauge strain outputs measured at 18 Hz taken from Fig. 7.29 as sweep angle amplitude increases from 2° to 4°. The strain signals in time and frequency domains are pretty noisy for vibration amplitude of 1°, so the ratio for this case is not included. All three ratios are all around 0.2 $pC/\mu\epsilon$. This finding indicates that PZT-silane thin film with printed IDEs can also be used as a strain sensor.

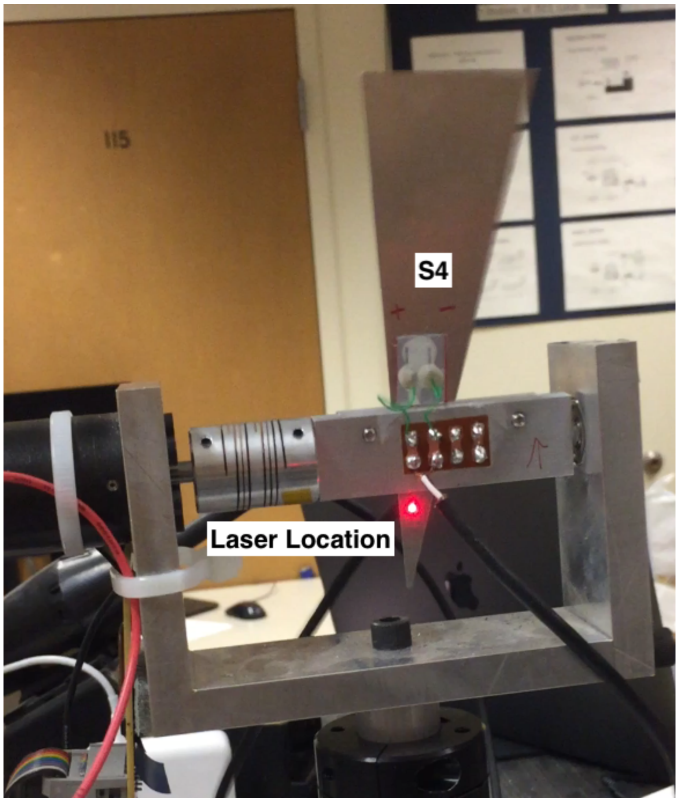

Figure 7.21: Vibration test setup photo

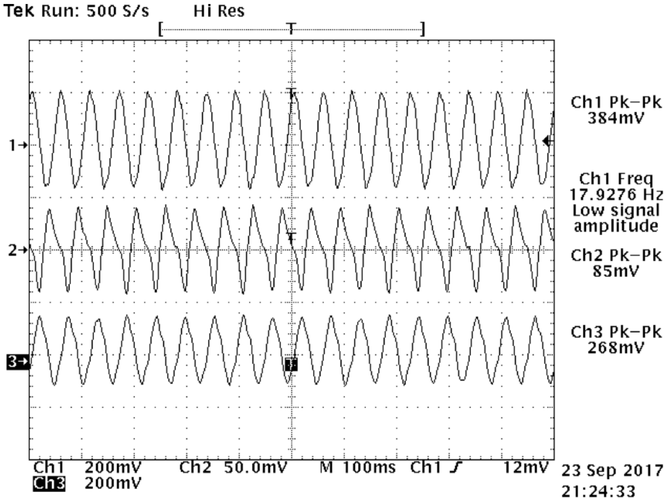

Figure 7.22: Time domain oscilloscope data when the wing vibrates at 18 Hz: Channel 1 Velocity by LDV; Channel 2 Charge by PZT-IDEs sensor; Channel 3 Strain by strain gauge

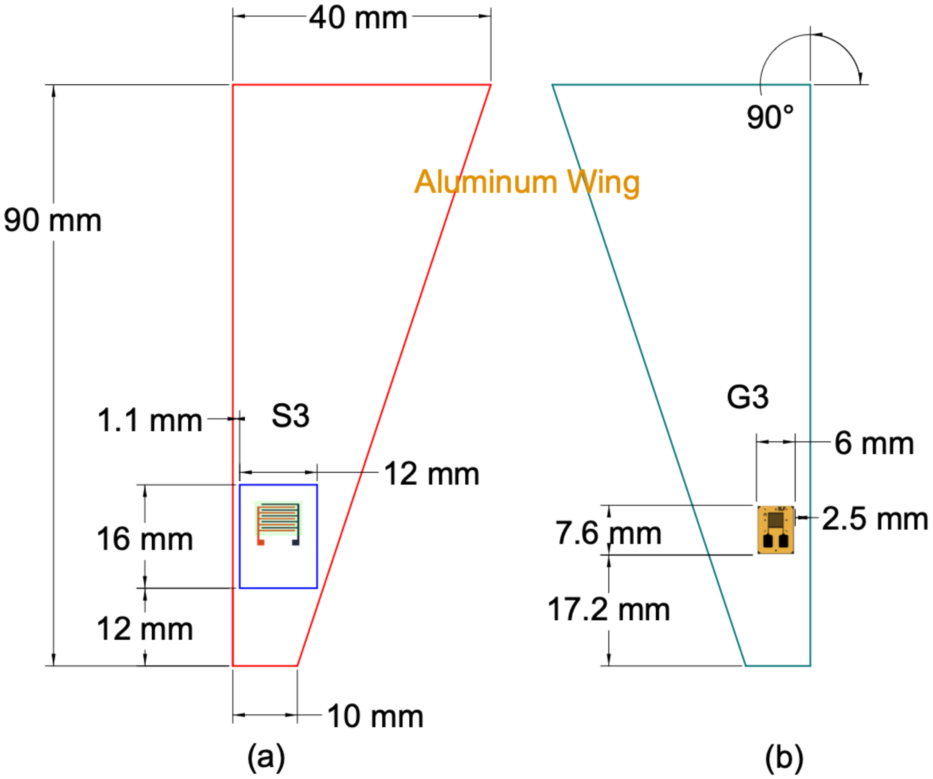

Figure 7.23: Aluminum wing with (a) PZT-silane thin film sensor with IDEs (S3) on one side and (b) strain gauge (G3) on the other side

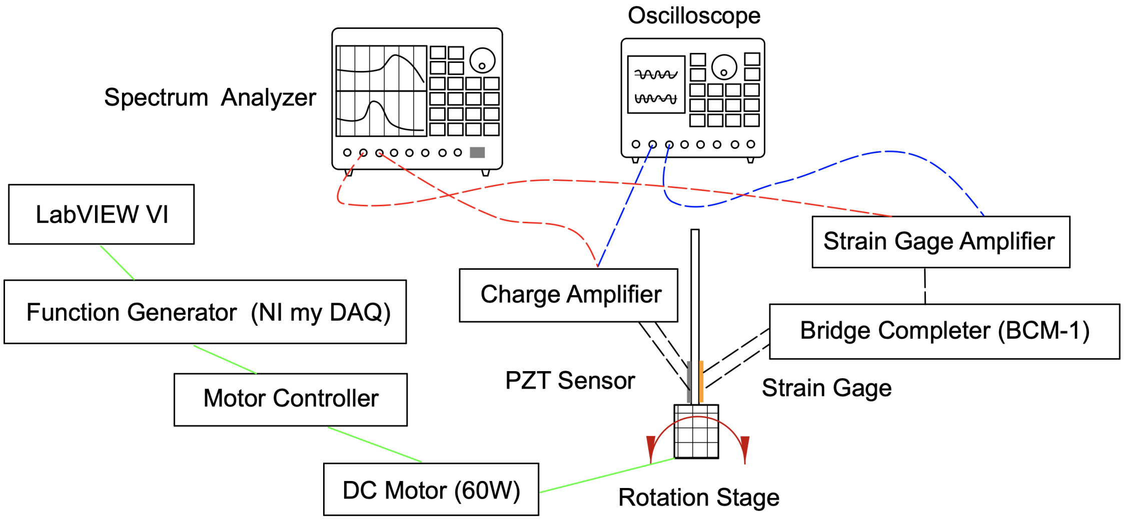

Figure 7.24: Schematic diagram of the second wing rotation test setup

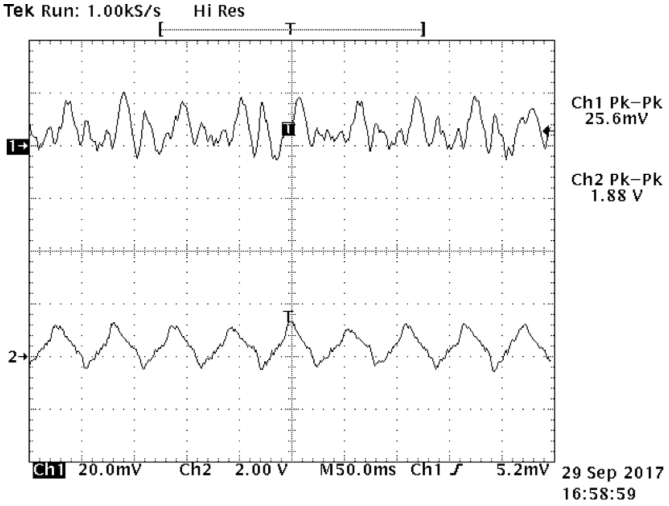

(a) Time Domain

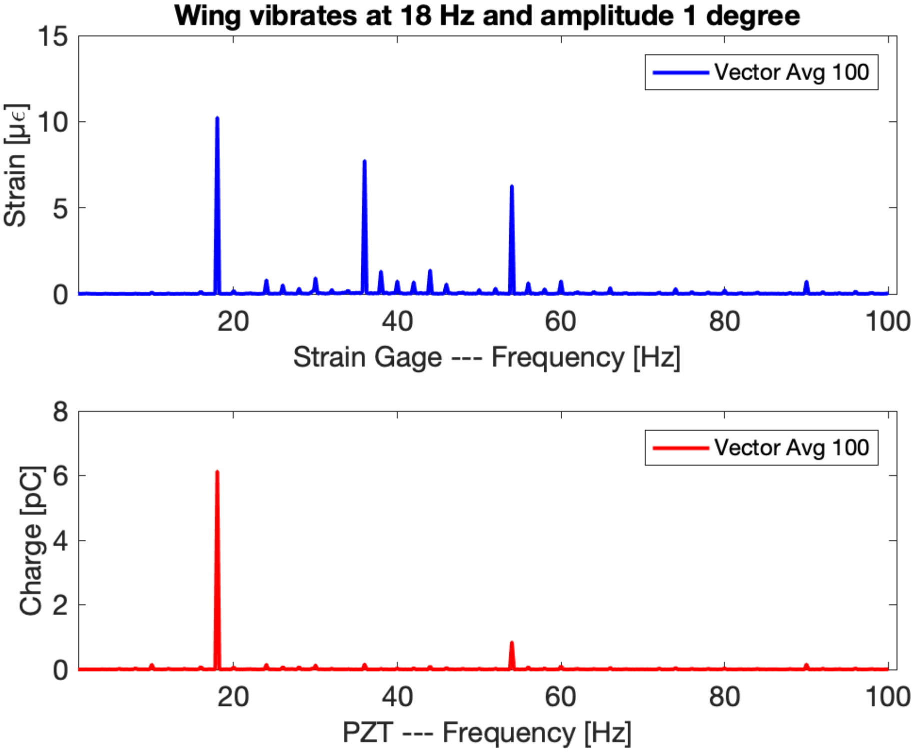

(b) Frequency Domain

Figure 7.25: Wing vibrates at 18 Hz with amplitude 1°: (a) Time domain outputs: Channel 1 is strain gauge output (upper waveform) and Channel 2 is sensor charge output (lower waveform); (b) Frequency domain measurements: upper plot is strain measurement from strain gauge and lower plot is charge measurement from PZT-silane thin film with IDEs

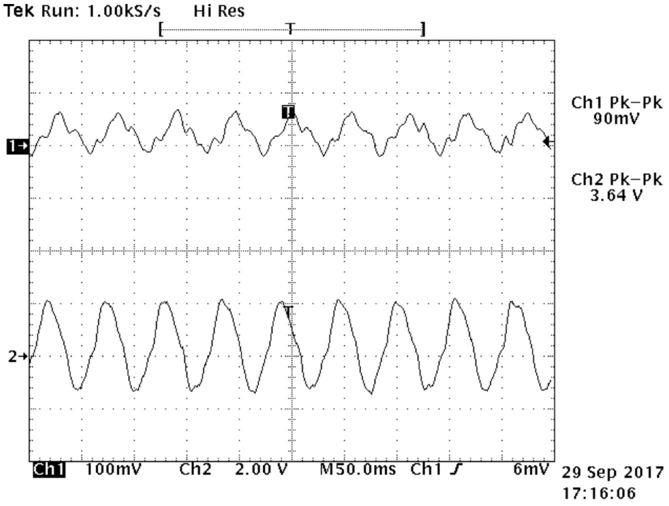

(a) Time Domain

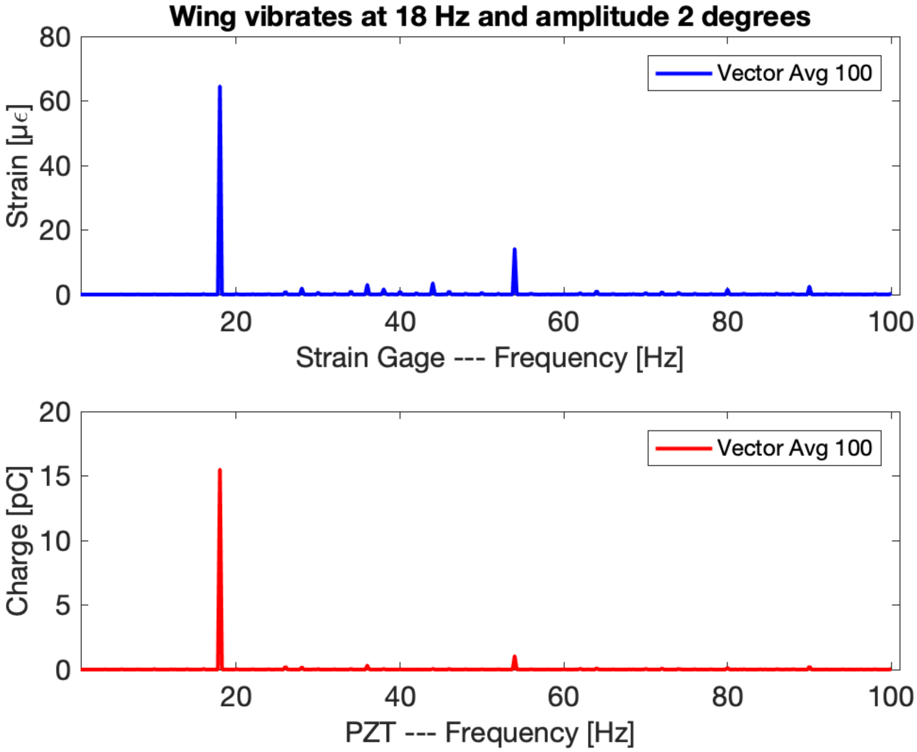

(b) Frequency Domain

Figure 7.26: Wing vibrates at 18 Hz with amplitude 2°: (a) Time domain outputs: Channel 1 is strain gauge output (upper waveform) and Channel 2 is sensor charge output (lower waveform); (b) Frequency domain measurements: upper plot is strain measurement from strain gauge and lower plot is charge measurement from PZT-silane thin film with IDEs

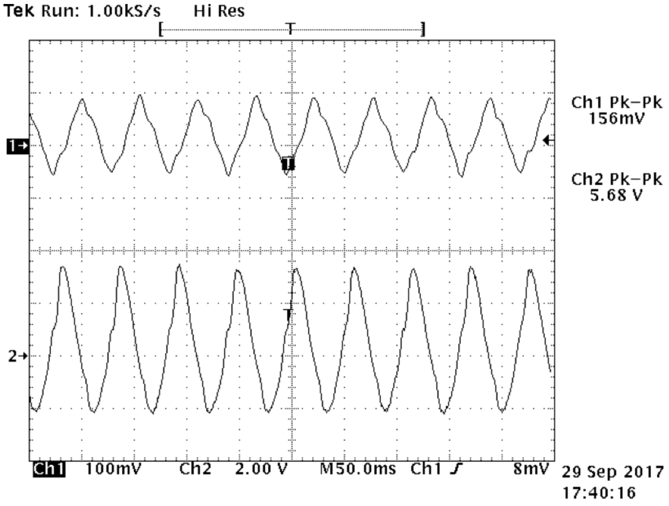

(a) Time Domain

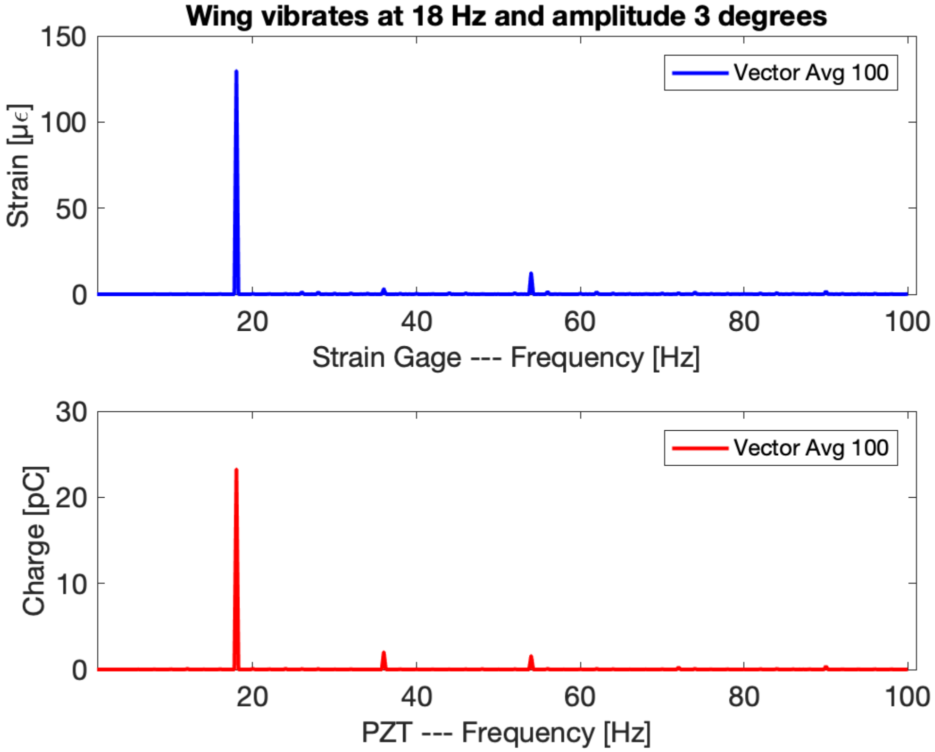

(b) Frequency Domain

Figure 7.27: Wing vibrates at 18 Hz with amplitude 3°: (a) Time domain outputs: Channel 1 is strain gauge output (upper waveform) and Channel 2 is sensor charge output (lower waveform); (b) Frequency domain measurements: upper plot is strain measurement from strain gauge and lower plot is charge measurement from PZT-silane thin film with IDEs

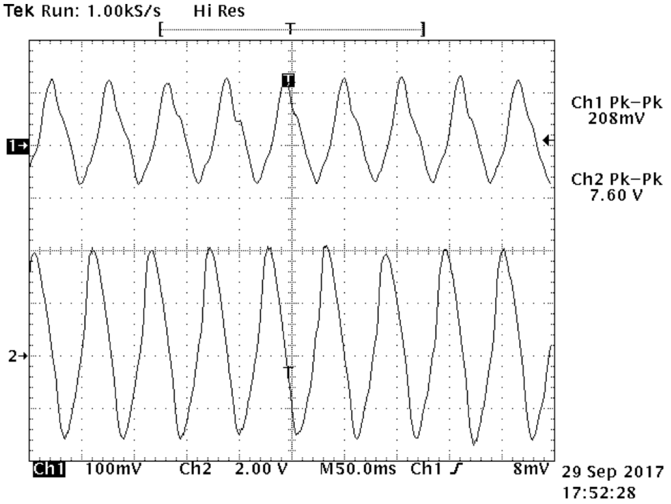

(a) Time Domain

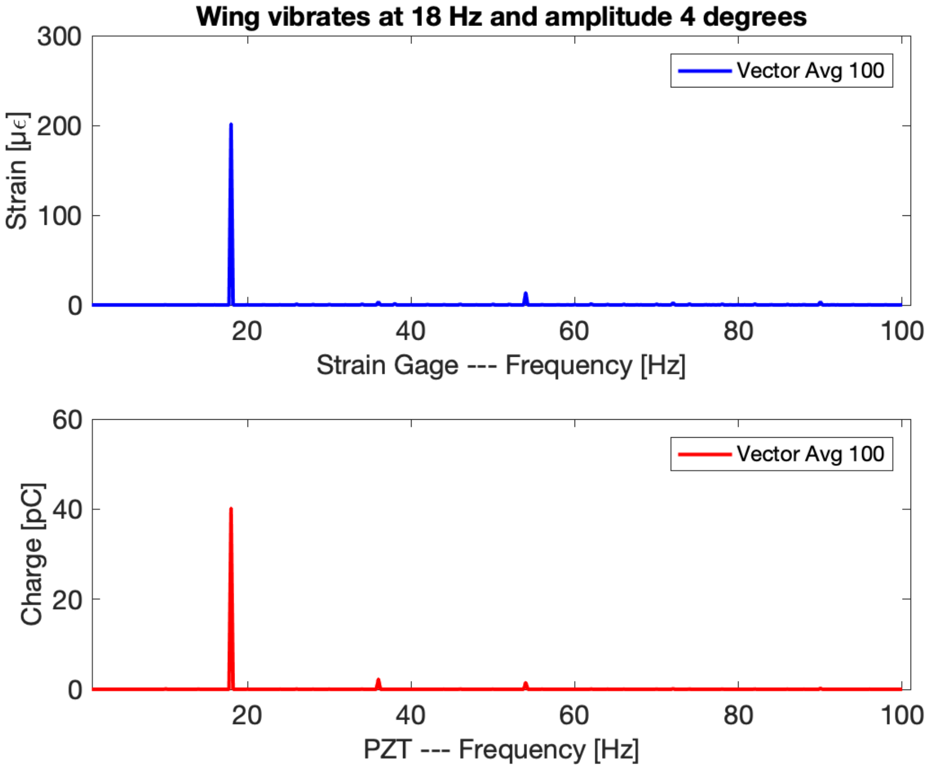

(b) Frequency Domain

Figure 7.28: Wing vibrates at 18 Hz with amplitude 4°: (a) Time domain outputs: Channel 1 is strain gauge output (upper waveform) and Channel 2 is sensor charge output (lower waveform); (b) Frequency domain measurements: upper plot is strain measurement from strain gauge and lower plot is charge measurement from PZT-silane thin film with IDEs

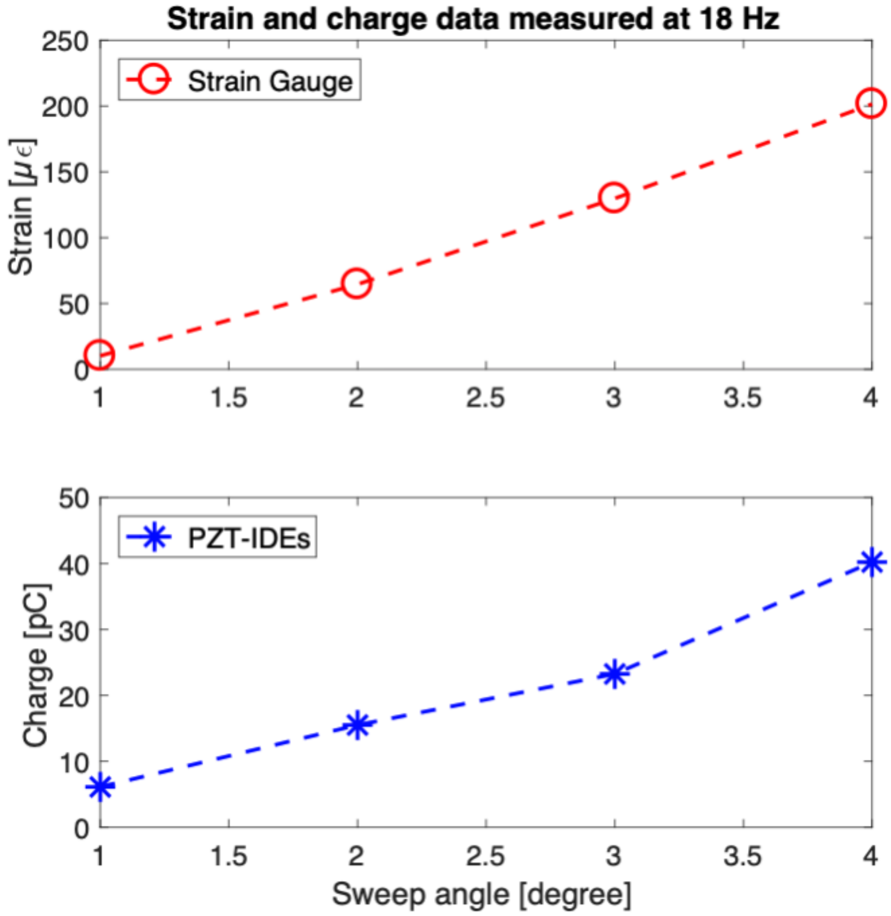

Figure 7.29: Frequency response measurement summary when wing vibrates at 18 Hz with sweep from 1°to 4°: Upper plot is strain data from strain gauge and lower plot is charge data from PZT-silane thin film with IDEs measured at 18Hz

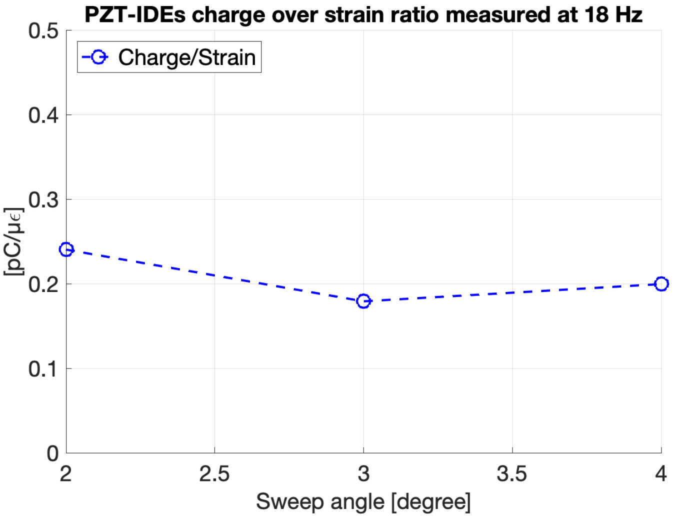

Figure 7.30: PZT-IDEs sensor charge output over strain gauge strain output ratios measured at 18 Hz when wing vibrates at 18 Hz with sweep angle from 2°to 4°

7.2.3 Strain Sensor with Direction Sensing Capability

7.2.3.1 Theoretical Prediction

Based on the geometrical and loading conditions of test specimen and experiment setup, small angle rotations about points on the neutral axis of test beam can be approximately simplified as pure bending of the beam. The shear stresses induced in test beam will be negligible in comparison with the normal stresses, because the length-to-height ratio is big in this case.

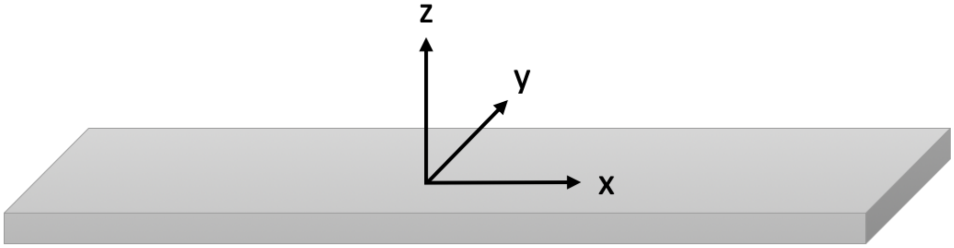

Figure 7.31: Beam and its coordinate system (x, y, z)

Under pure bending condition, the only stress is σ_x ($\sigma_x \neq 0$, along beam length direction), and all other stresses are zero: $\sigma_y = \sigma_z = \tau_{xy} = \tau_{xz} = \tau_{yz} = 0$; see Fig. 7.31 for beam coordinate system. In this theoretical model, only bending moments are applied and there are no additional transverse or longitudinal forces. Due to the Poisson effect, strains $\epsilon_x, \epsilon_y, \epsilon_z$ would all present. However there are no shear strains $\gamma_{xy} = \gamma_{xz} = \gamma_{yz} = 0$. ϵ_x can be obtained directly from Hooke's law, and ϵ_y and ϵ_z from Poisson effect as shown in Eqn. (7.6), where E and υ are Young's modulus and Poisson ratio of the material respectively.

$$\begin{aligned} \epsilon_x &= \frac{\sigma_x}{E} \\ \epsilon_y &= -\upsilon\,\frac{\sigma_x}{E} \\ \epsilon_z &= -\upsilon\,\frac{\sigma_x}{E} \end{aligned} \tag{7.6}$$

From the derivation in Section 6.2.1.2, the electrical field between two in-plane electrodes E_3 is repeated below. By plugging in material properties for Lead Zirconate Titanate (PZT-4) listed in Tab. 7.4 into the equation, we can evaluate E_3 using Eqn. (7.7). For an in-plane polarized PZT (Fig. 7.32) with a length L, the voltage output V_3 is given by Eqn. (7.8).

$$\begin{aligned} E_3 &= \frac{\left(-\frac{e_{31}}{\varepsilon^S_{33}} + \frac{e_{32}}{\varepsilon^S_{33}}\frac{C^E_{21}}{C^E_{22}}\right)}{\left(1 + \frac{e_{32}}{\varepsilon^S_{33}}\frac{e_{32}}{C^E_{22}}\right)} S_1 + \frac{\left(\frac{e_{32}}{\varepsilon^S_{33}}\frac{C^E_{23}}{C^E_{22}} - \frac{e_{33}}{\varepsilon^S_{33}}\right)}{\left(1 + \frac{e_{32}}{\varepsilon^S_{33}}\frac{e_{32}}{C^E_{22}}\right)} S_3 \\ &= (3.7734 \times 10^8)\ S_1 + (-2.9440 \times 10^9)\ S_3 \end{aligned} \tag{7.7}$$

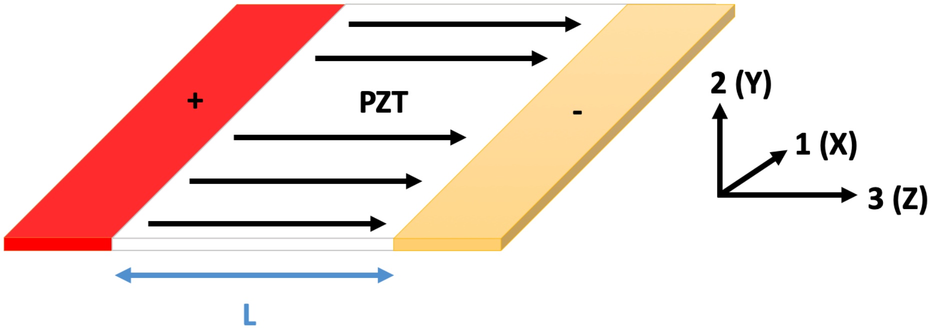

Figure 7.32: In-plane polarized PZT with positive (red), negative (yellow) electrodes and its coordinate system $(1, 2, 3$ or $X, Y, Z)$

$$V_3 = E_3 \times L \tag{7.8}$$

For example, if an aluminum beam is under pure bending condition, the only stress is σ_x and three strains are Eqn. (7.9). There are two in-plane polarized PZT sensors with different poling directions that are perpendicular with each other. 'PZT1' is polarized along beam x-axis and 'PZT2' is polarized along beam y-axis as indicated in Fig. 7.33 . Their local coordinate systems $(1, 2, 3)$ are also shown in the figure below.

Table 7.4: Material Properties for Lead Zirconate Titanate (PZT-4)

Constants	PZT-4
Stiffness constants C_{ij}	$C_{21}^E = 7.78 \times 10^{10} N/m^2$ $C_{22}^E = 1.39 \times 10^{11} N/m^2$ $C_{23}^E = 7.43 \times 10^{10} N/m^2$
Piezoelectric constants e_{ij}	$e_{31} = -5.2028\ C/m^2$ $e_{32} = -5.2028\ C/m^2$ $e_{33} = 15.0804\ C/m^2$
Dielectric constants $\varepsilon_o = 8.854{\times}10^{-12}\ F/m$	$\varepsilon_{11}^S = 762\ \varepsilon_o = 6.7467 \times 10^{-9}\ F/m$ $\varepsilon_{22}^S = 762\ \varepsilon_o = 6.7467 \times 10^{-9}\ F/m$ $\varepsilon_{33}^S = 663\ \varepsilon_o = 5.8702 \times 10^{-9}\ F/m$

$$\begin{aligned}\epsilon_x &= \frac{\sigma_x}{E} = 1 \times 10^{-5} \\ \epsilon_y &= -\upsilon\,\frac{\sigma_x}{E} = -0.33 \times 10^{-5} \\ \epsilon_z &= -\upsilon\,\frac{\sigma_x}{E} = -0.33 \times 10^{-5}\end{aligned} \tag{7.9}$$

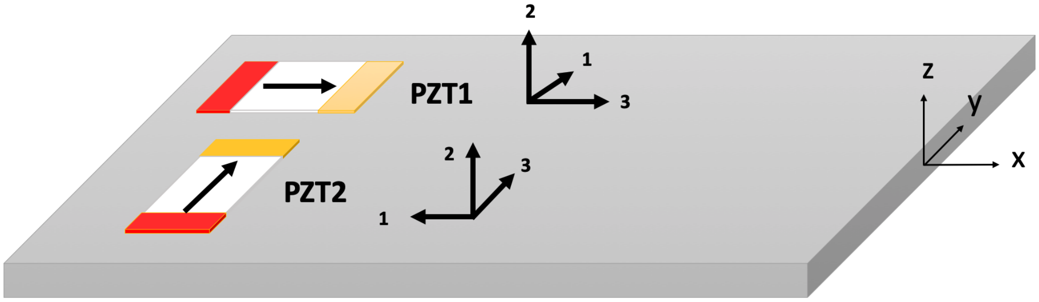

Figure 7.33: Beam under pure bending condition with two in-plane polarized PZT sensors orientated 90°apart

For PZT1 with $L = 5mm$:

$$\begin{aligned}S_3 &= \epsilon_x = 1 \times 10^{-5} \\ S_1 &= \epsilon_y = -0.33 \times 10^{-5} \\ E_3 &= -3.07 \times 10^4 \ V/m \\ V_3 &= -153.4746 \ V\end{aligned} \tag{7.10}$$

For PZT2 with $L = 5mm$:

$$\begin{aligned}S_1 &= \epsilon_x = 1 \times 10^{-5} \\ S_3 &= \epsilon_y = -0.33 \times 10^{-5} \\ E_3 &= 1.35 \times 10^4 \ V/m \\ V_3 &= 67.4640 \ V\end{aligned} \tag{7.11}$$

The voltage ratio between PZT1 and PZT2 is calculated to be Eqn. (7.12).

$$Ratio_{theory} = \frac{V_{PZT1}}{V_{PZT2}} = |\frac{-153.4746}{67.4640}| = 2.275 \tag{7.12}$$

7.2.3.2 Finite Element Verification

Finite element analysis is used to verify the theoretical prediction in Section 7.2.3.1 and also to predict future scenarios with different geometry and boundary conditions.

A finite element model of a PZT thin film with length $5mm$, width $5mm$ and $0.01mm$ in the thickness direction is created to fit plane stress situation in the theory; see Fig. 7.34. Figure 7.35 shows a mesh for this model. The element size is $0.5mm$ and number of divisions is 2 in the thickness direction. Coordinate system used is shown in Fig. 7.34, where polarization axis is set to Z-axis. Z-axis in the model is the same as 3-axis in Fig. 7.33 for PZT1 and PZT2.

To simulate situation with PZT1, nodal displacements in X, Y and Z directions are set to be (1) all nodal displacements expend 1 unit at Z-direction (3-axis), (2) all nodal displacements shrink 0.33 at X-direction (1-axis), and (3) free nodal displacement for Y-direction (2-axis), except for at Y=0, nodal displacement for Y component is 0. The (X,Y,Z) or (1,2,3) used is for PZT film local coordinate and will continue hereafter.

To simulate situation with PZT2, nodal displacements in X, Y and Z directions are set to be (1) all nodal displacements shrink 0.33 at Z-direction (3-axis), (2) all nodal displacements expend 1 unit at X-direction (1-axis), and (3) free nodal displacement for Y-direction (2-axis), except for at Y=0, nodal displacement for Y component is 0.

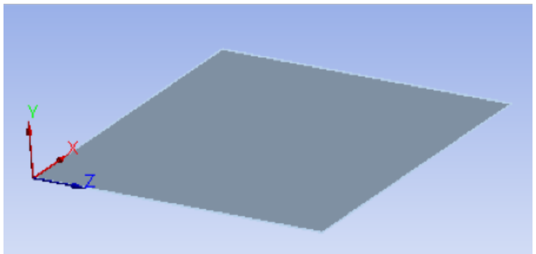

Figure 7.34: PZT thin film $5\times5\times0.01mm$

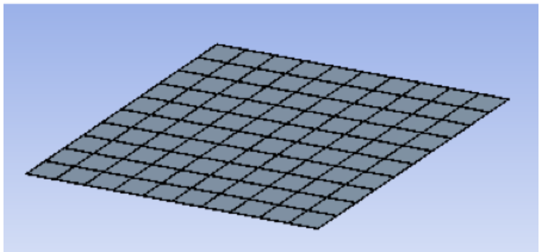

Figure 7.35: Mesh for PZT thin film

Figure 7.36 shows both total and directional deformations in X, Y Z axes for PZT1 and PZT2 after prescribed nodal displacements. From Fig. 7.36 (a) and (b) total deformation plots, we can tell that PZT1 is controlled to expend in its Z-axis, meanwhile PZT2 in its X-axis. Directional deformations in X and Z axes confirms the prescribed motion and there is relatively small deformation in Y-axis (about three orders of magnitude lower).

X, Y and Z- axis normal elastic strains for PZT thin films PZT1 and PZT2 are shown in Fig. 7.37. The normal strain values are controlled to be identical with the theoretical prediction examples for comparison. The normal stresses (Pa; newtons per square meter) in X, Y and Z- axis is simulated for both cases and are shown in Fig. 7.38. The electric field strength (V/m) in Z- direction for PZT1 and PZT2 is simulated to be $PZT1_{E3} = 3.0695 \times 10^4\ V/m$ and $PZT2_{E3} = 1.3493 \times 10^4\ V/m$. And voltage across to be $PZT1_{V3} = -153.47V$ and $PZT2_{V3} = 67.464V$, respectively. The simulation results for E_3, V_3 can be found in Fig. 7.39.

In summary,

1. PZT1 $5 \times 5 \times 0.01mm$ expands in its Z-Axis:

$$\begin{aligned}
&\epsilon_z = 1 \times 10^{-5},\ \epsilon_x = -0.33 \times 10^{-5},\ \epsilon_y = -0.2347 \times 10^{-5} \\
&\sigma_z = 1.1975 \times 10^{6},\ \sigma_x = -0.58287 \times 10^{5},\ \sigma_y = -8 \sim 3 \times 10^{-6} \\
&E_3 = -3.0695 \times 10^{4}\ V/m \\
&V_3 = -153.47\ V
\end{aligned} \tag{7.13}$$

2. PZT2 $5 \times 5 \times 0.01mm$ expands in its X-Axis:

$$\begin{aligned}
&\epsilon_x = 1 \times 10^{-5},\ \epsilon_z = -0.33 \times 10^{-5},\ \epsilon_y = -0.43416 \times 10^{-5} \\
&\sigma_x = 8.7713 \times 10^{5},\ \sigma_z = -1.6402 \times 10^{5},\ \sigma_y = -1.18 \sim 3.6486 \times 10^{-6} \\
&E_3 = 1.3493 \times 10^{4}\ V/m \\
&V_3 = 67.464\ V
\end{aligned} \tag{7.14}$$

3. The voltage ratio between PZT1 and PZT2 in finite element simulation is Eqn. (7.15) and the same as predicted in the theory:

$$Ratio_{FEA} = \frac{V_{PZT1}}{V_{PZT2}} = |\frac{-153.47}{67.464}| = 2.2748 \qquad (7.15)$$

Second ANSYS model is created to study effect of added substrate on voltage ratio between PZT1 and PZT2. A finite element model of a PZT thin film with length 5 mm, width 5 mm and thickness 0.01 mm placed on the center of a PET layer 50 × 50 × 1 mm is created; see Fig. 7.40. Figure 7.41 shows a mesh for the second model. The element sizes are 5 mm for PET and 0.1 mm for PZT. Numbers of divisions are both 2 in the thickness direction fo PET and PZT.

There are three coordinate systems used for PET-PZT1 and PET-PZT2 simulation: local coordinates for PET-PZT1, local coordinates for PET-PZT2, and global coordinates (X,Y,Z). Figure 7.42 (a) shows local coordinates for PET-PZT1 is the same as global coordinates (X,Y,Z). Figure 7.42 (b) indicates that local coordinates for PET-PZT2 and global coordinates (X,Y,Z) are not the same; their X and Z-axis are flipped. Polarization axis is set to local coordinate Z-axis for both PET-PZT1 and PET-PZT2. To simulate situation with PET-PZT1, nodal displacements for PET layer in local X, Y and Z directions are set to be (1) all nodal displacements expend 1 unit at local Z-direction (global Z-axis), (2) all nodal displacements shrink 0.33 at local X-direction (global X-axis), and (3) free nodal displacement for local Y-direction (global Y-axis), except for at Y=0, nodal displacement for Y component is 0. To simulate situation with PET-PZT2, nodal displacements for PET layer in local X, Y and Z directions are set to be (1) all nodal displacements shrink 0.33 at local Z-direction (global X-axis), (2) all nodal displacements expend 1 unit at local X-direction (global Z-axis), and (3) free nodal displacement for Y-direction (global Y-axis), except for at Y=0, nodal displacement for Y component is 0.

Normal elastic strains in global coordinates X, Y and Z-axis for PET with PZT thin films PZT1 and PET with PZT2 are shown in Fig. 7.43 and Fig. 7.44. The normal elastic strain in global coordinates Z and X-axis are controlled to be the same for PET-PZT1 and PET-PZT2 cases. The normal stresses (Pa; newtons per square meter) in global X, Y and

Z-axis are provided for both cases for reference and are shown in Fig. 7.45 and Fig. 7.46. Figure 7.47 (a) and (c) show electric field strength (V/m) in their local Z- direction for PET-PZT1 and PET-PZT2. And voltage across simulated be $PET - PZT1_{V3} = -147.52\ V$ and $PET - PZT2_{V3} = -65.978\ V$, respectively. The simulation results for E_3, V_3 can be found in Fig. 7.47. The voltage ratio between PET-PZT1 and PET-PZT2 in finite element simulation is Eqn. (7.18).

1. PET-PZT1 case: PET expands in global Z-Axis:

$$\begin{aligned} PET - \epsilon_{global-Z} &= 1 \times 10^{-5} \\ PET - \epsilon_{global-X} &= -0.33 \times 10^{-5} \\ PET - \epsilon_{global-Y} &= -0.42836 \times 10^{-5} \\ PZT1 - E_{3-ave} &= -2.9181 \times 10^{4}\ V/m \\ PZT1 - V_3 &= -147.52\ V \end{aligned} \tag{7.16}$$

2. PET-PZT2 case: PET expands in global Z-Axis:

$$\begin{aligned} PET - \epsilon_{global-Z} &= 1 \times 10^{-5} \\ PET - \epsilon_{global-X} &= -0.33 \times 10^{-5} \\ PET - \epsilon_{global-Y} &= -0.42836 \times 10^{-5} \\ PZT2 - E_{3-ave} &= 1.3148 \times 10^{4}\ V/m \\ PZT2 - V_3 &= -65.978\ V \end{aligned} \tag{7.17}$$

3. The voltage ratio between PET-PZT1 and PET-PZT1 under identical substrate (PET) strain state in second finite element simulation is Eqn. (7.18) and a little bit smaller than the one predicted in the theory:

$$Ratio_{FEA} = \frac{V_{PET-PZT1}}{V_{PET-PZT2}} = |\frac{-147.52}{-65.978}| = 2.2359 \tag{7.18}$$

Table 7.5 shows the strain sensor with direction sensing capability summary for the theoretical prediction and the two finite element analysis. The ratio of 2.2359 for PZT thin films with PET in two different poling directions is smaller than 2.2748 for PZT thin film alone during FE simulation. This suggests that with added substrate layers, the ratio between PZT1 and PZT2 would decease and the number will be lower than theoretical prediction ratio of 2.2748.

Table 7.5: Strain sensor with direction sensing capability summary for the theoretical prediction and the finite element verification

		PZT1 Voltage	**PZT2 Voltage**	**Ratio**
Theory	PZT alone	153.4746V	67.4640V	2.275
FE simulation	PZT alone	153.47V	67.4640V	2.2748
	PZT with PET	147.52V	65.978V	2.2359

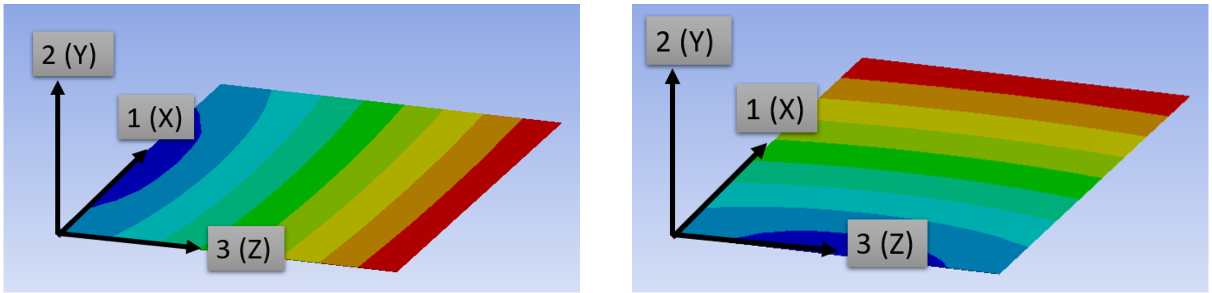

(a) PZT1 Total deformation

(b) PZT2 Total deformation

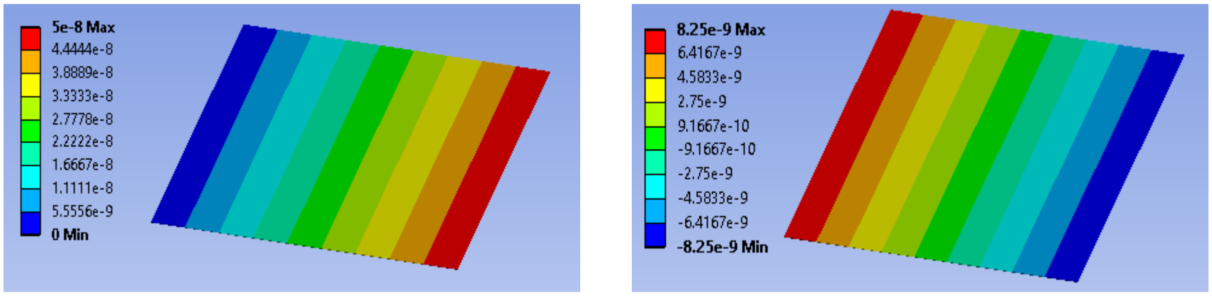

(c) PZT1 Z-Axis directional deformation

(d) PZT2 Z-Axis directional deformation

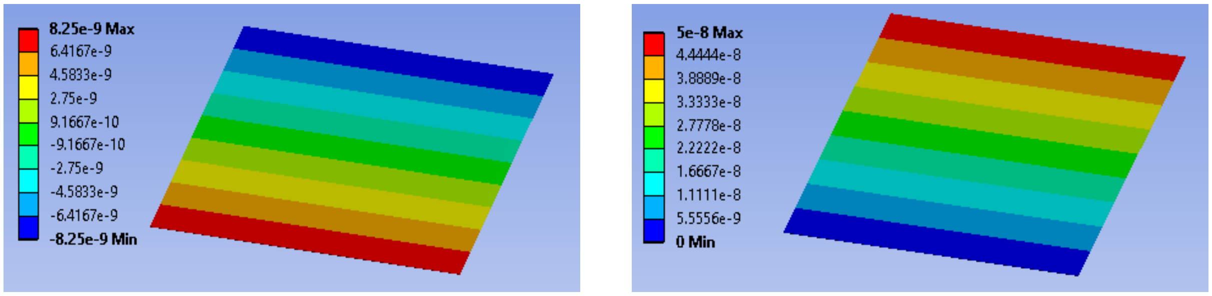

(e) PZT1 X-Axis directional deformation

(f) PZT2 X-Axis directional deformation

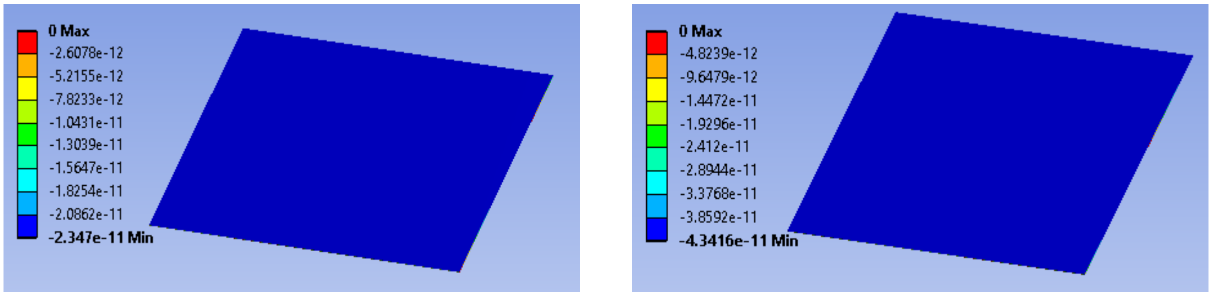

(g) PZT1 Y-Axis directional deformation

(h) PZT2 Y-Axis directional deformation

Figure 7.36: Total and directional deformation for PZT thin films

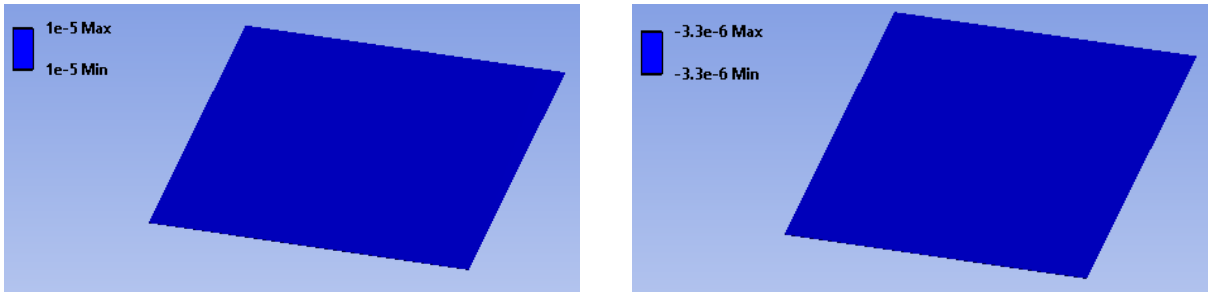

(a) PZT1 Z-Axis

(b) PZT2 Z-Axis

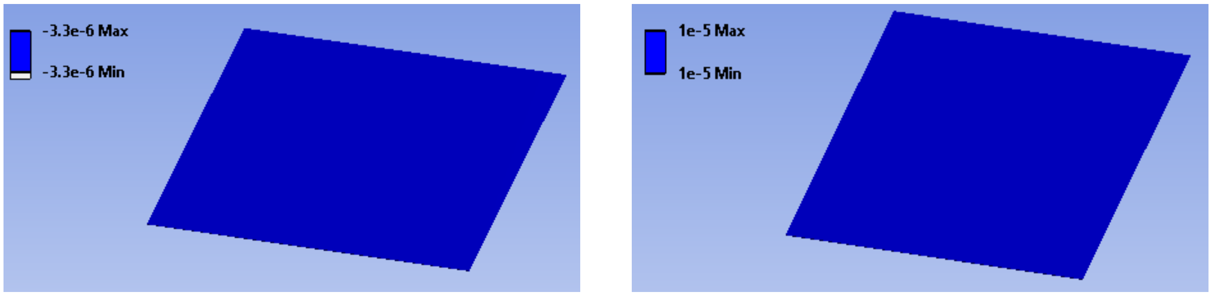

(c) PZT1 X-Axis

(d) PZT2 X-Axis

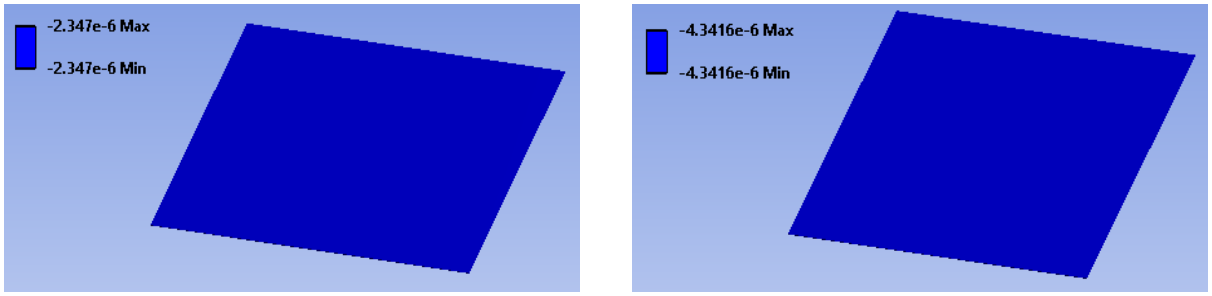

(e) PZT1 Y-Axis

(f) PZT2 Y-Axis

Figure 7.37: Normal elastic strain for PZT thin films

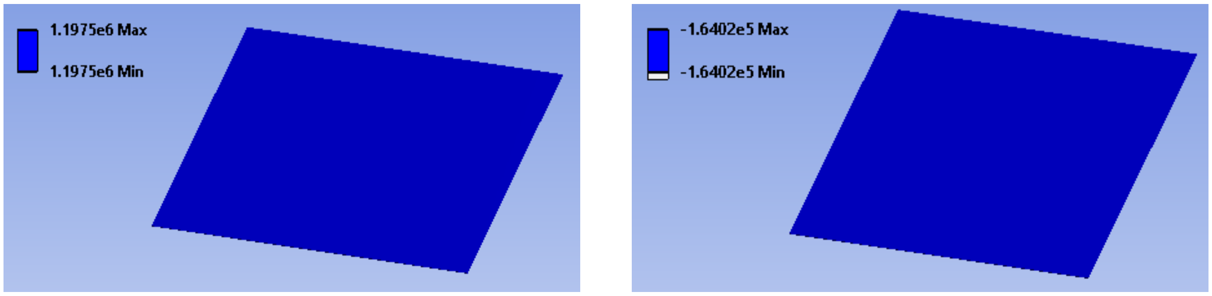

(a) PZT1 Z-Axis (b) PZT2 Z-Axis

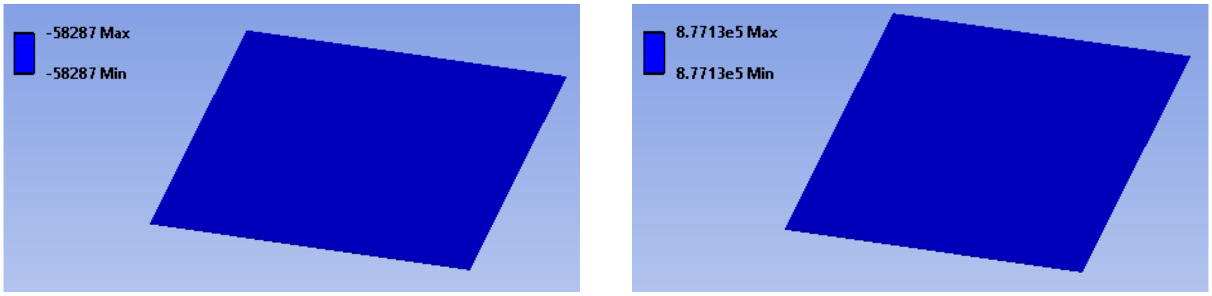

(c) PZT1 X-Axis (d) PZT2 X-Axis

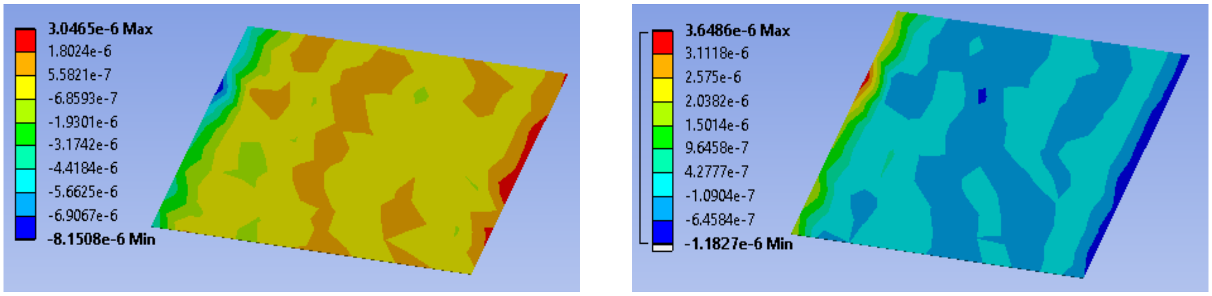

(e) PZT1 Y-Axis (f) PZT2 Y-Axis

Figure 7.38: Normal stress for PZT thin films

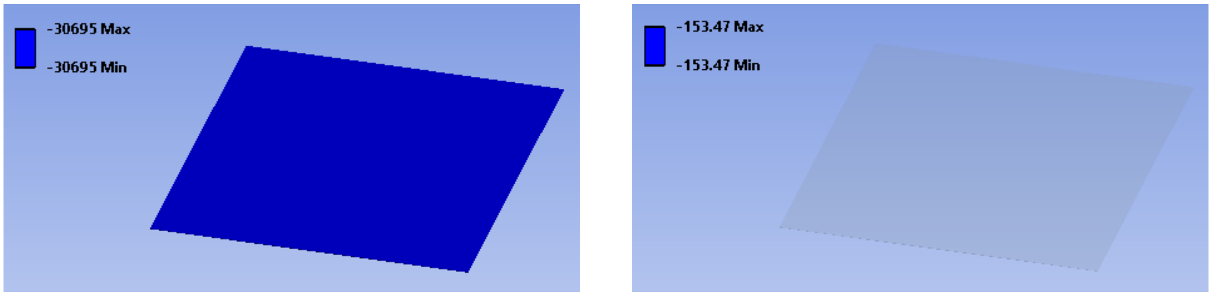

(a) PZT1 E_3 (b) PZT1 V_3

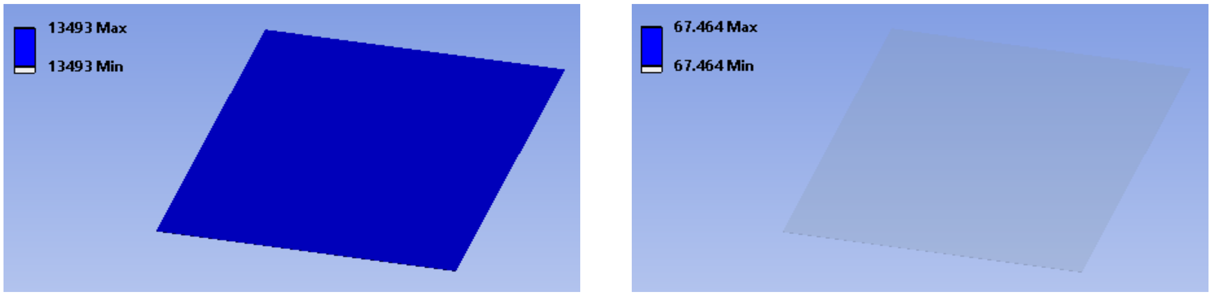

(c) PZT2 E_3 (d) PZT2 V_3

Figure 7.39: Electric field and voltage across two electrodes for PZT1 and PZT2

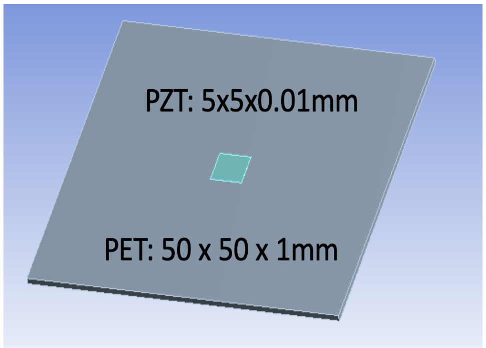

Figure 7.40: PET with PZT geometry

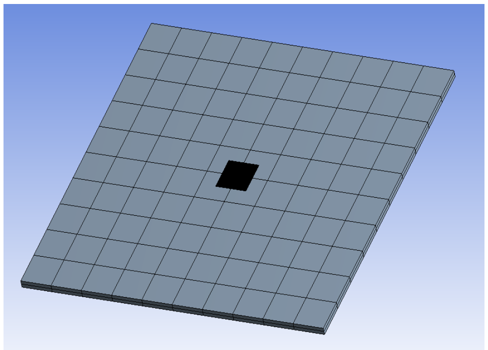

Figure 7.41: Mesh for PET with PZT

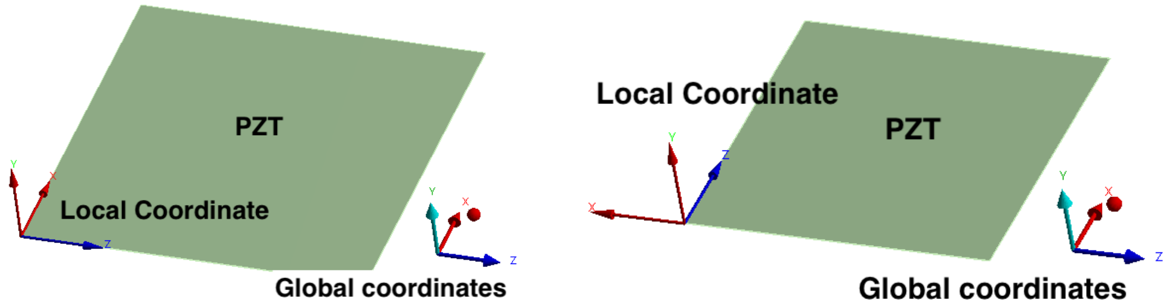

(a) PET-PZT1

(b) PET-PZT2

Figure 7.42: Global and local coordinate systems used for PET with PZT thin films

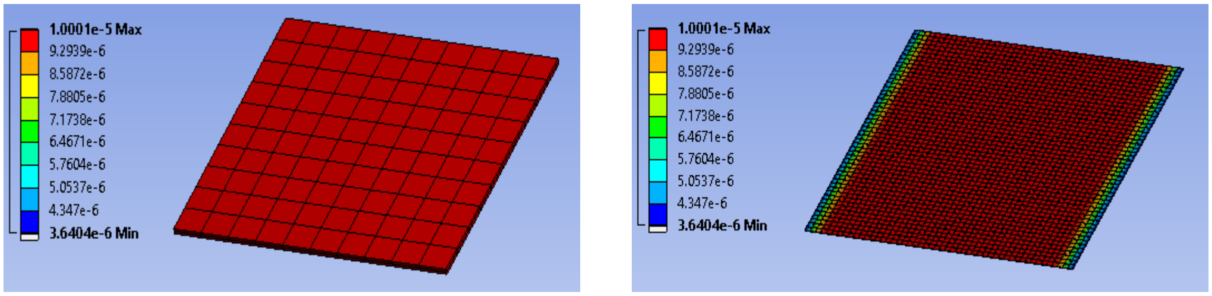

(a) PET Global Z-Axis (b) PZT1 Global Z-Axis

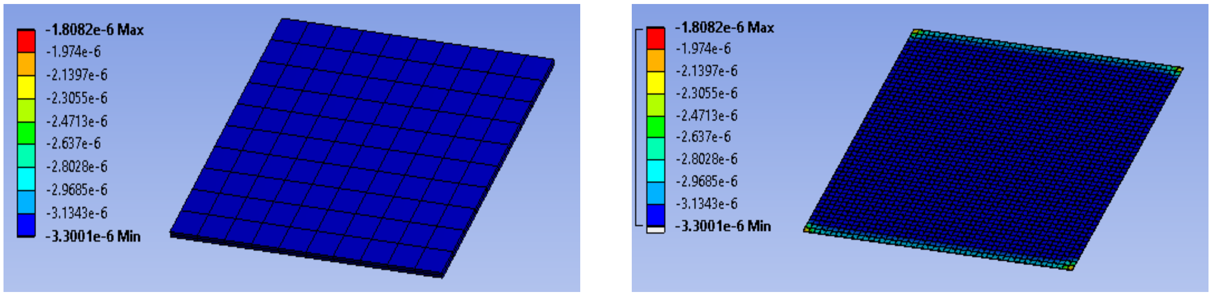

(c) PET Global X-Axis (d) PZT1 Global X-Axis

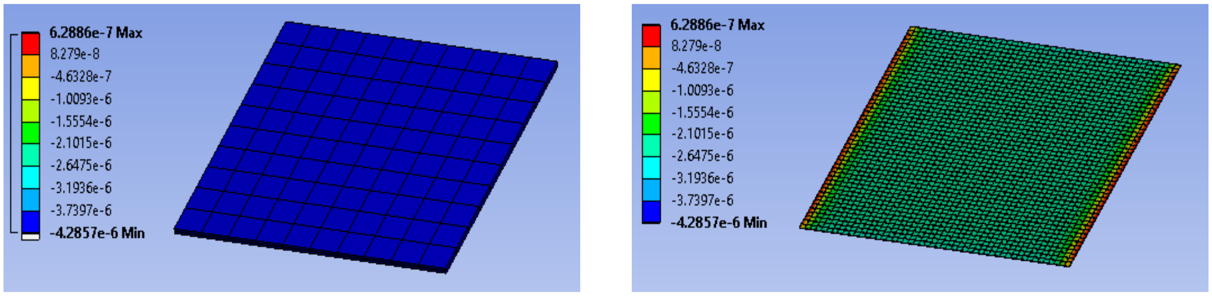

(e) PET Global Y-Axis (f) PZT1 Global Y-Axis

Figure 7.43: Normal elastic strain for PET-PZT1

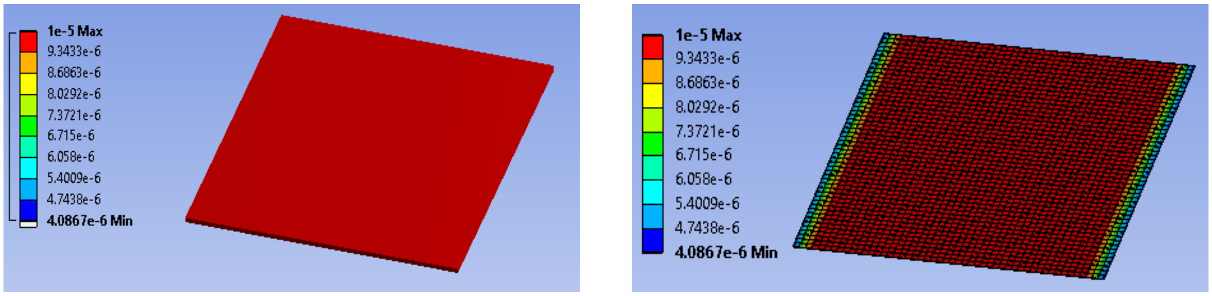

(a) PET Global Z-Axis

(b) PZT2 Global Z-Axis

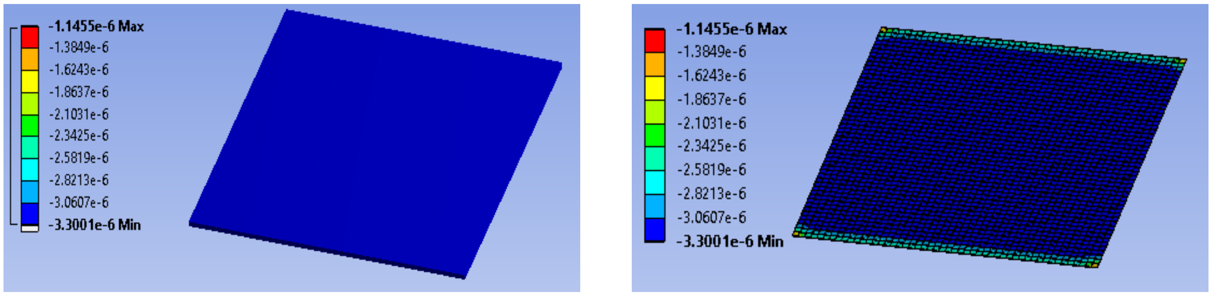

(c) PET Global X-Axis

(d) PZT2 Global X-Axis

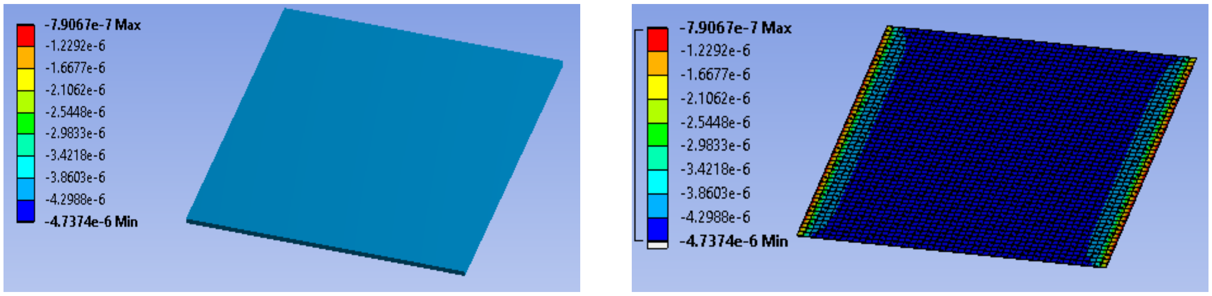

(e) PET Global Y-Axis

(f) PZT2 Global Y-Axis

Figure 7.44: Normal elastic strain for PET-PZT2

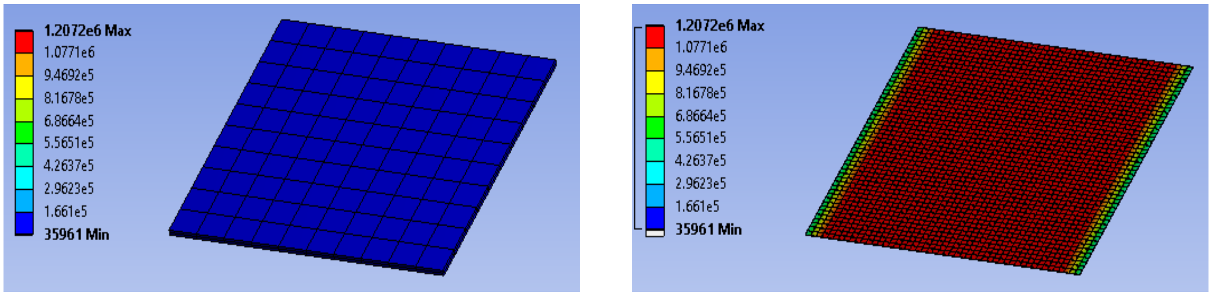

(a) PET Global Z-Axis

(b) PZT1 Global Z-Axis

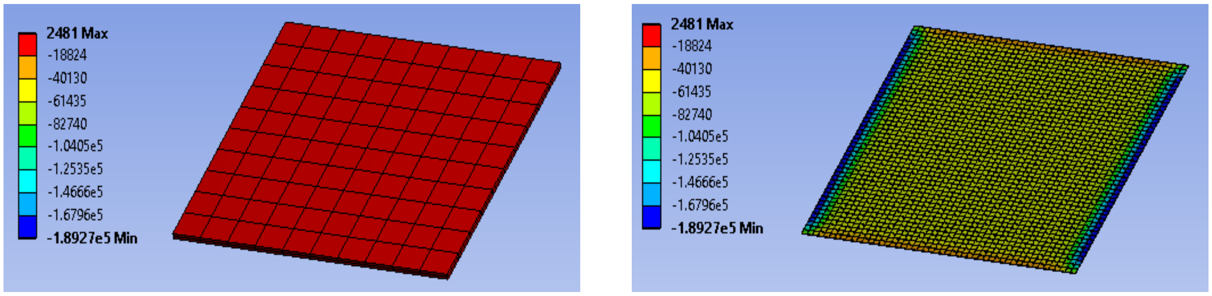

(c) PET Global X-Axis

(d) PZT1 Global X-Axis

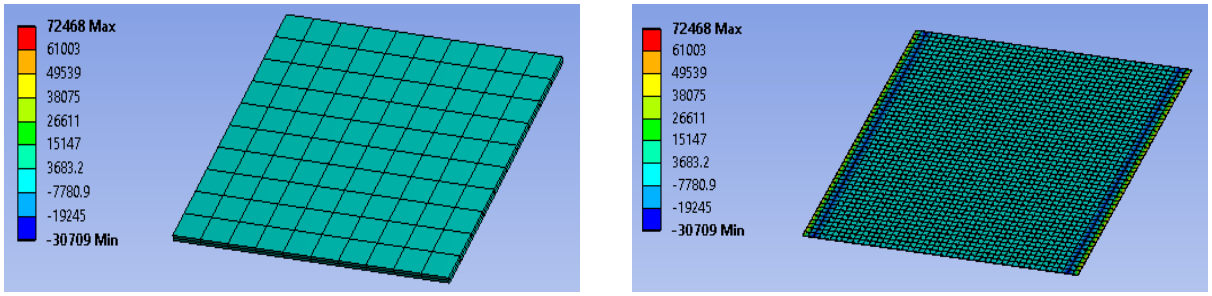

(e) PET Global Y-Axis

(f) PZT1 Global Y-Axis

Figure 7.45: Normal stress for PET-PZT1

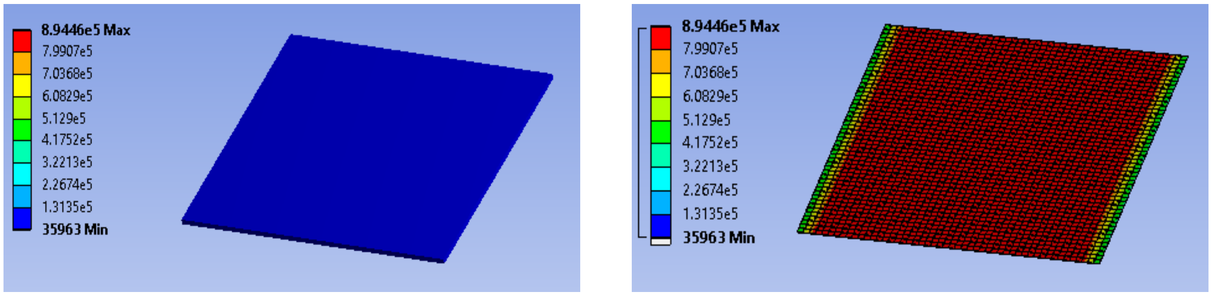

(a) PET Global Z-Axis (b) PZT2 Global Z-Axis

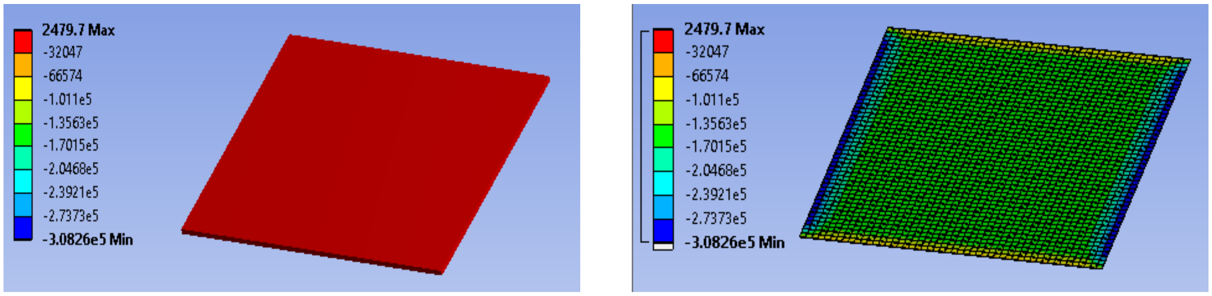

(c) PET Global X-Axis (d) PZT2 Global X-Axis

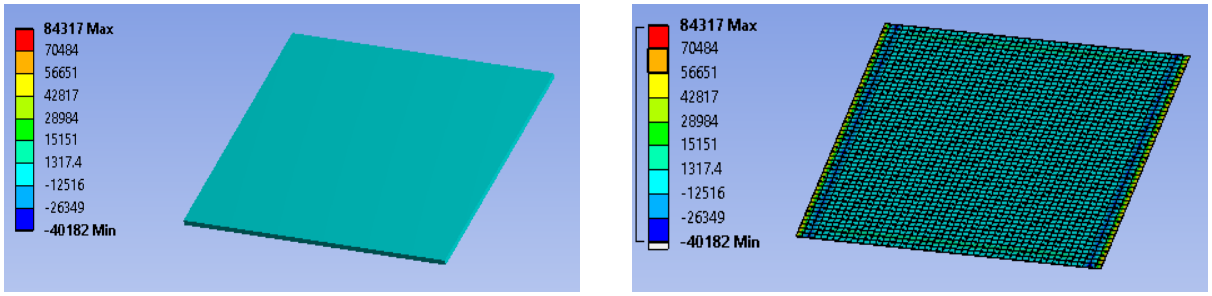

(e) PET Global Y-Axis (f) PZT2 Global Y-Axis

Figure 7.46: Normal stress for PET-PZT2

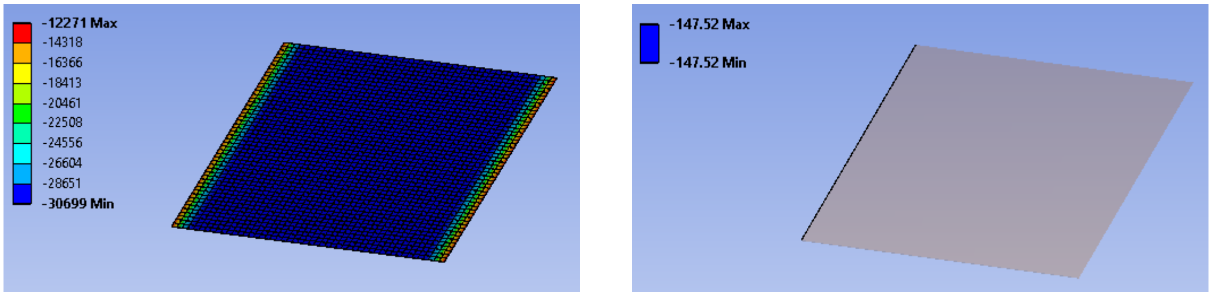

(a) PZT1 E_3

(b) PZT1 V_3

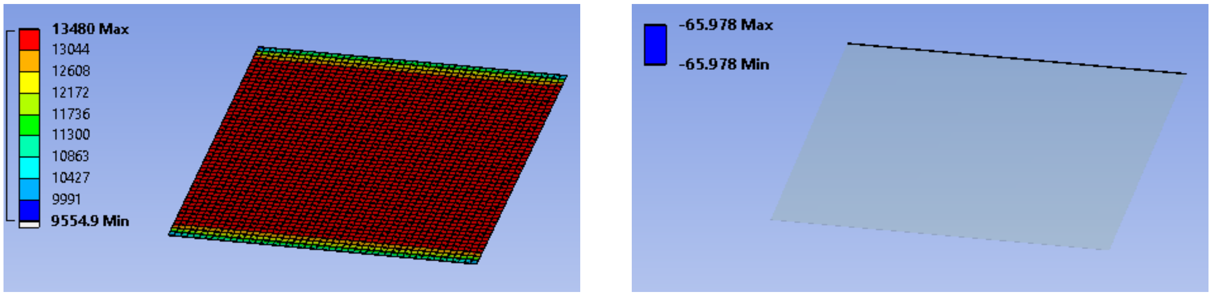

(c) PZT2 E_3

(d) PZT2 V_3

Figure 7.47: Electric field and voltage across two electrodes for PET-PZT1 and PET-PZT2

7.2.3.3 *Experimental Demonstration*

An aluminum beam with length 101 mm, width 26 mm, and thickness 0.4 mm is prepared as test structure for demonstration of the sensors directional sensitivity. Figure 7.48 shows a detail drawing of the beam structure with four sensors attached. The aluminum beam has a Youngs modulus of 68.9 GPa, a Poisson's ratio of 0.33, and a density of 2700 kg/m^3. PZT-silane thin film with printed IDEs uses polyethylene terephthalate (PET) as substrate layer. PET has a density of 1300 kg/m^3, Young's modulus of 2.55 GPa, and Poisson's ratio of 0.39.

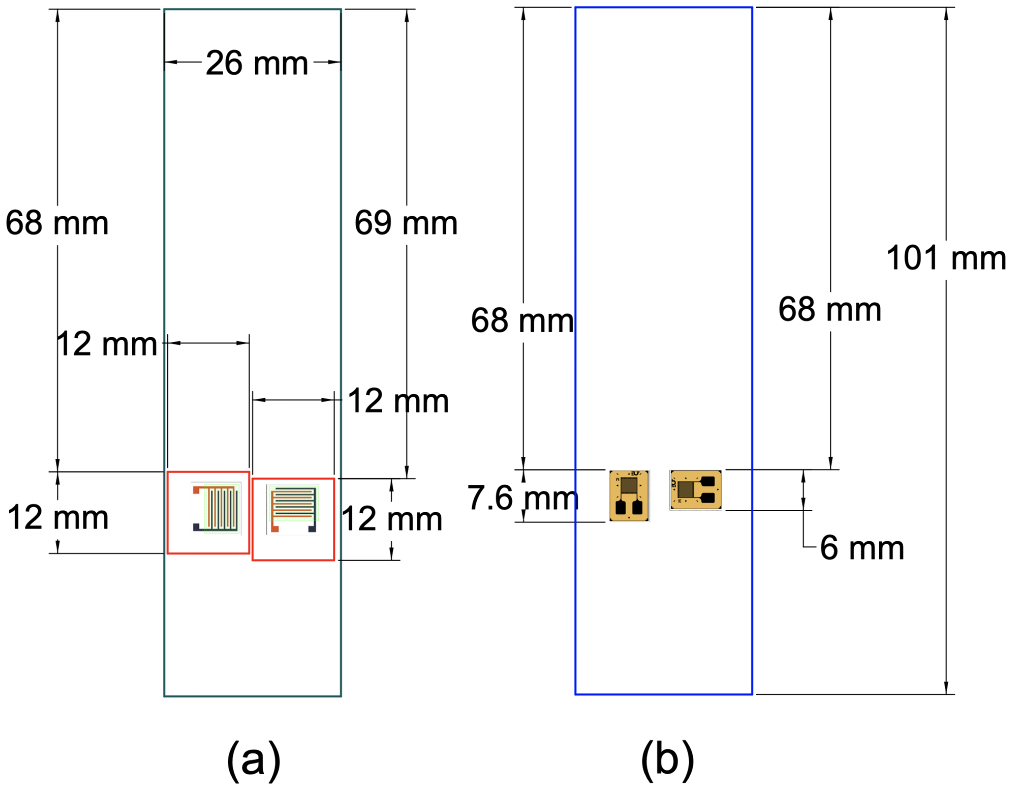

Figure 7.48: Thin aluminum beam with (a) PZT-silane thin films with IDEs on one side and (b) strain gauges on the other side

There are two PZT-IDEs sensors S1 & S2 attached to the front side of the beam (see

Fig. 7.49 (a)). The one on the left is S1, PET layer dimension is 12 × 12 mm. One on the right is S2, PET layer dimension is 12 × 12 mm. Notice that they are oriented 90 degrees apart. Based on theoretical and finite element analyses done earlier, we predict that S2 would be more sensitive to y-axis and S1 would be more sensitive to x-axis for beam deformation. Figure 7.48 (a) shows dimensions and locations for the two PZT-IDEs sensors.

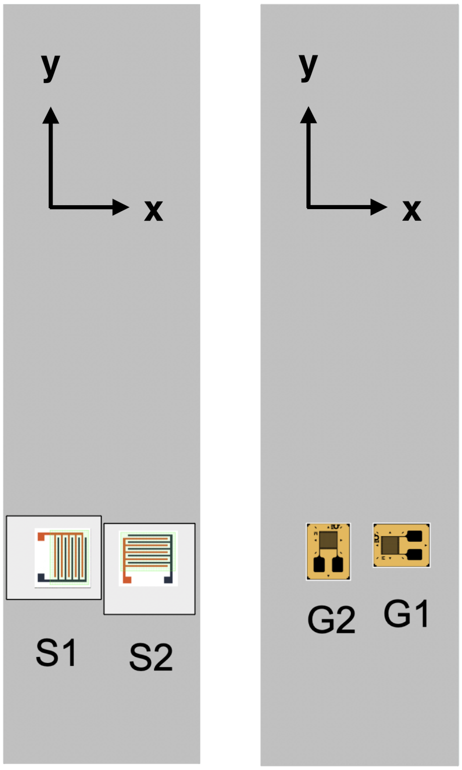

(a) Front (b) Back

Figure 7.49: Aluminum beam front side (a) PZT-silane thin films with IDEs (S1 and S2); back side (b) strain gauges (G2 and G1) with beam coordinates

On the back side of the beam, two linear, one-axis, 350Ω strain gauge with part. no. SGD-2/350-LY13 are attached. One on the left is G2 and one on the right is G1 as indicated in Fig. 7.49 (b). Notice that they are oriented 90 degrees apart and are only sensitive to strain in one direction. Gage G2 can only measure strain in y-direction and G1 can only measure strain in x-direction during beam deformation. Strain gauges (G1 and G2) have the same dimensions: $6 \times 7.6\ mm$. Their placements detail can be found in Fig. 7.48 (b).

The test plan for direction sensing capability demonstration consists of two steps.

1. Identify strains in two different directions ϵ_x, ϵ_y of the beam under vibration testing (18 Hz with angular amplitude of 1.5°). Check ϵ_x/ϵ_y ratio.
2. Demonstrate that two PZT-silane thin films with IDEs (S1 and S2) can distinguish strains in two different directions. Check the Q_{S1}/Q_{S2} ratio under the same strain state.

Figure 7.50 shows an experimental photo of the demonstration first step. Rotation of the stage is set by LabVIEW VI [6]. Stage rotates sinusoidally with a driving frequency of 18Hz and rotation amplitude of 1.5°. The "Frequency" is set to 18Hz, "scaling" parameter is set to 3.33 qc/V and "offset" tab is set to $-8qc$ during testing.

A spectrum analyzer (Model SR785 SR785 two-channel dynamic signal analyzer) is used during the tests. Strain voltage output from two strain gauges G1 and G2 through strain amplifier are collected and analyzed below. Noted that G2 can only measure strain ϵ_y and G1 can only measure ϵ_x during beam deformation. Figure 7.51 shows frequency domain measurements when wing vibrates at 18 Hz with amplitude of 1.5°. Upper plot is strain FFT magnitude measurement from strain gauge G1 and lower plot is strain FFT magnitude measurement from strain gauge G2. Each FFT data represents the vector average value of 50 trials.

At driving frequency of 18Hz, strain ϵ_x from G1 is 8.746 $\mu\epsilon$ and ϵ_y from G2 is 26.32 $\mu\epsilon$. ϵ_x/ϵ_y ratio is calculated to be 0.3323, which is very close to Poisson's ratio of aluminum (0.33). This shows that beam pure bending model can be used for analyzing experimental loading condition.

---

[6] LabVIEW VI → Function Generator (NI myDAQ) → Motor Controller → DC Motor (60W)

Next the spectrum analyzer is used to measure charge outputs coming from two PZT-IDEs sensors S1 and S2 through charge amplifier to see if they can distinguish strains in two different directions (see Fig. 7.52 for setup photo). Figure 7.53 and Figure 7.54 are test results in the frequency domain measurements when beam vibrates at 18 Hz with amplitude of 1.5°. Figure 7.53 shows the charge output of PZT-IDEs sensor S1 in upper plot and strain output from strain gauge G2 in lower plot for measuring strain ϵ_y during test. Similarly, Figure 7.54 shows the charge output of PZT-IDEs sensor S2 in upper plot and the strain output from strain gauge G2 in lower plot for correlating to the strain ϵ_y during test. Each FFT data represents the vector average value of 50 trials.

At a driving frequency of 18Hz, S1 outputs a charge of 0.2175 pC and strain gauge G2 outputs a ϵ_y of 18.63 $\mu\epsilon$ simultaneously. Repeating this process, S2 outputs a charge of 0.4866 pC and strain gauge G2 outputs a ϵ_y of 21.85 $\mu\epsilon$. Table 7.6 shows the experimental result summary for strain sensors directional sensitivity demonstration. The charge per strain ϵ_y for S1 is $Q_{S1}/\epsilon_y = 0.01167\ pC/\mu\epsilon$, and for S2 is $Q_{S2}/\epsilon_y = 0.02227\ pC/\mu\epsilon$. The ratio of 1.9075 (Eqn. (7.19)) shows that two PZT-silane thin films with IDEs (S1 and S2) oriented 90 degrees apart have different sensitivities towards ϵ_y and PZT thin films with interdigitated electrode design can distinguish strains in two different directions.

$$\frac{Q_{S2}/\epsilon_y}{Q_{S1}/\epsilon_y} = 1.9075 \tag{7.19}$$

Table 7.6: Strain sensor with direction sensing capability summary for experimental demonstration

Strain gauges	**G1**	**G2**	**G2/G1**
	$8.746\mu\epsilon$	$26.32\mu\epsilon$	3.0093
PZT-IDEs sensors	Q_{S1}/ϵ_y	Q_{S2}/ϵ_y	Q_{S2}/Q_{S1}
	0.01167	0.02227	1.9075

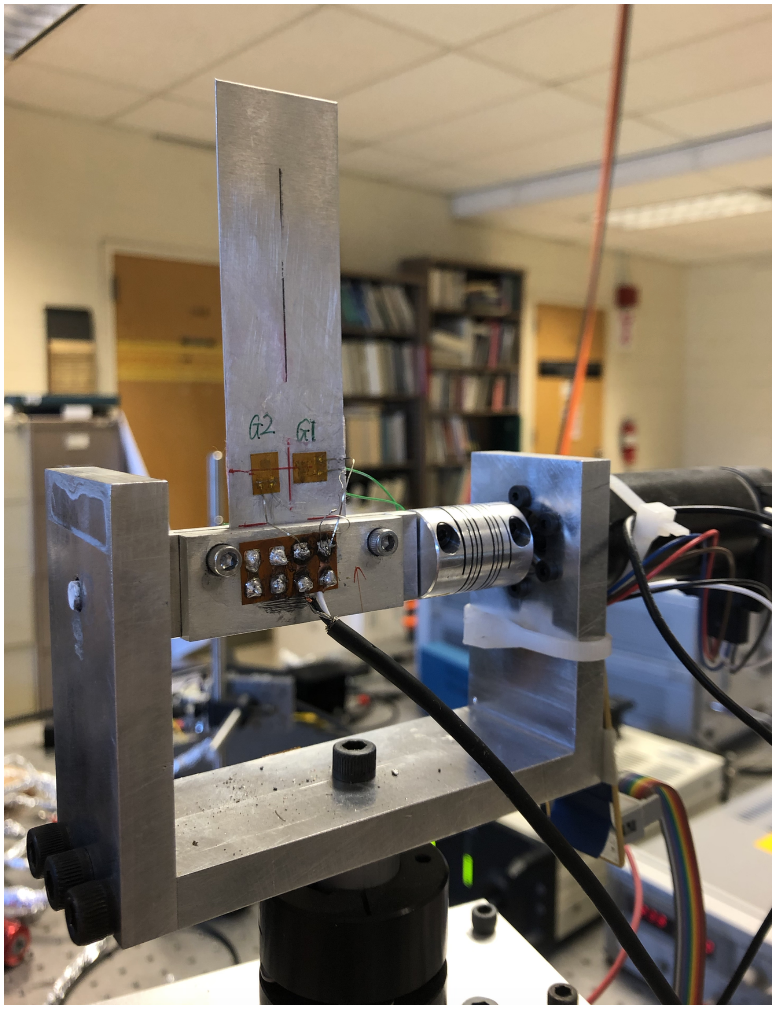

Figure 7.50: Experiment setup photo for strain gauges G1 & G2 measurements when beam vibrates at 18 Hz with sweep angle of 1.5°

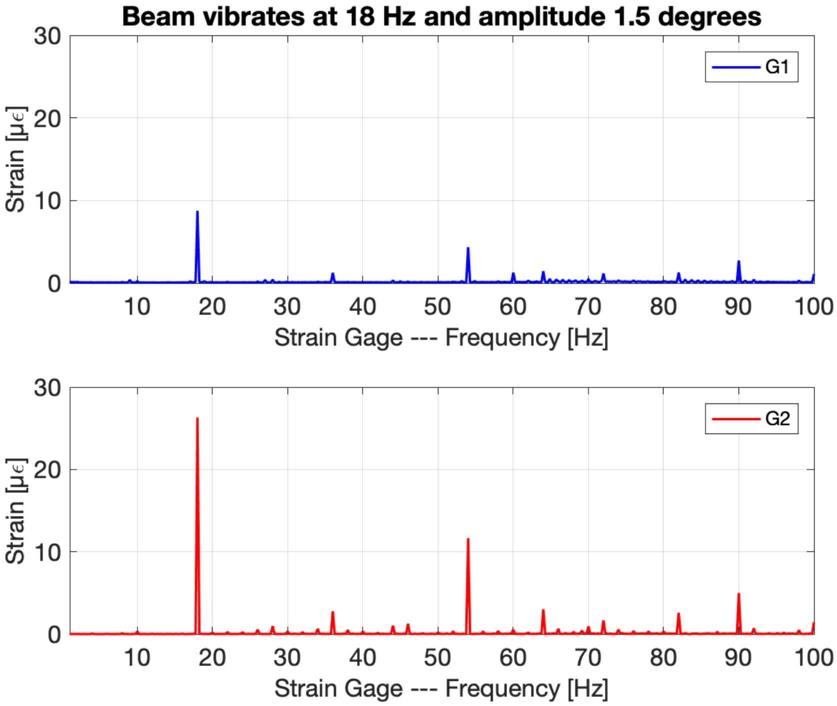

Figure 7.51: Frequency response measurement when wing vibrates at 18 Hz with sweep angle of 1.5°: Upper plot is strain data from strain gauge G1 and lower plot is strain data from strain gauge G2

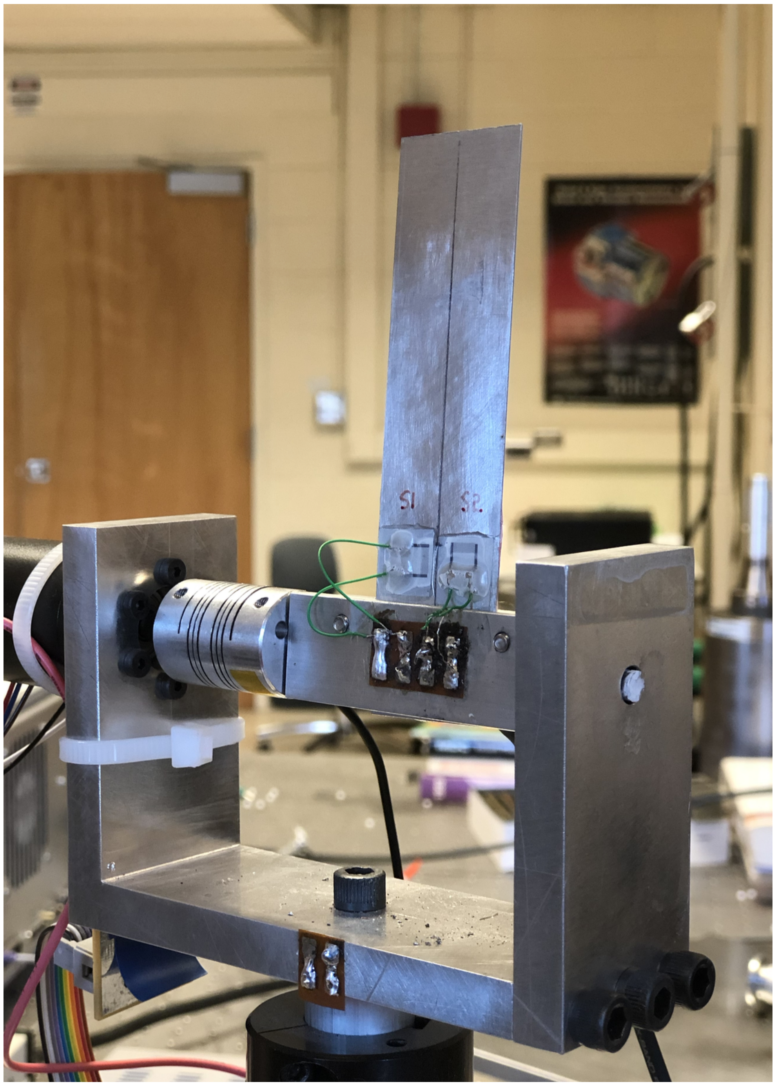

Figure 7.52: Experiment setup photo for PZT-IDEs sensor S1 & S2 measurements when beam vibrates at 18 Hz with sweep angle of 1.5°

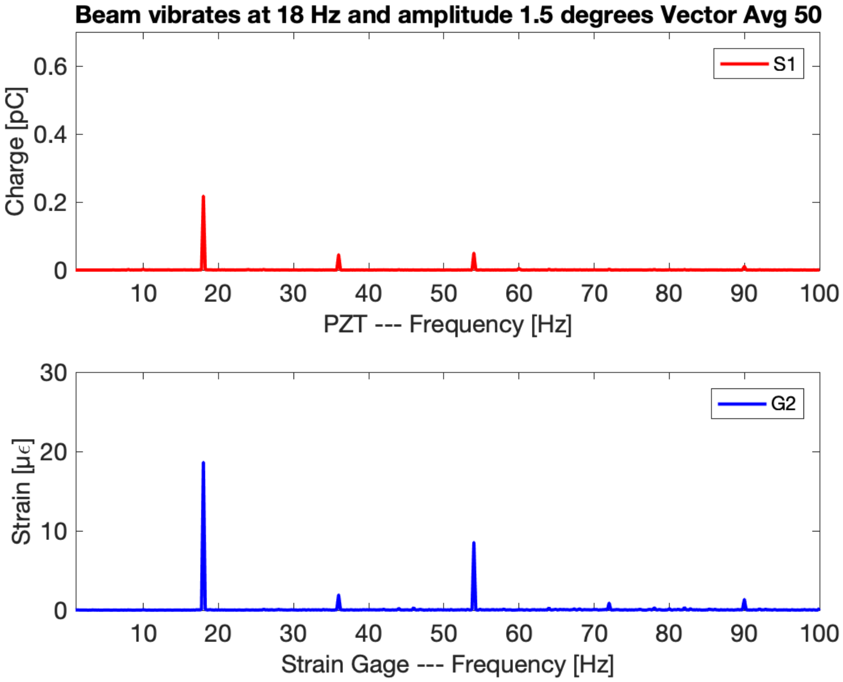

Figure 7.53: FFT measurements when beam vibrates at 18 Hz with sweep angle of 1.5°: Upper plot is charge output of PZT-IDEs sensor S1 and lower plot is strain output from strain gauge G2 during test

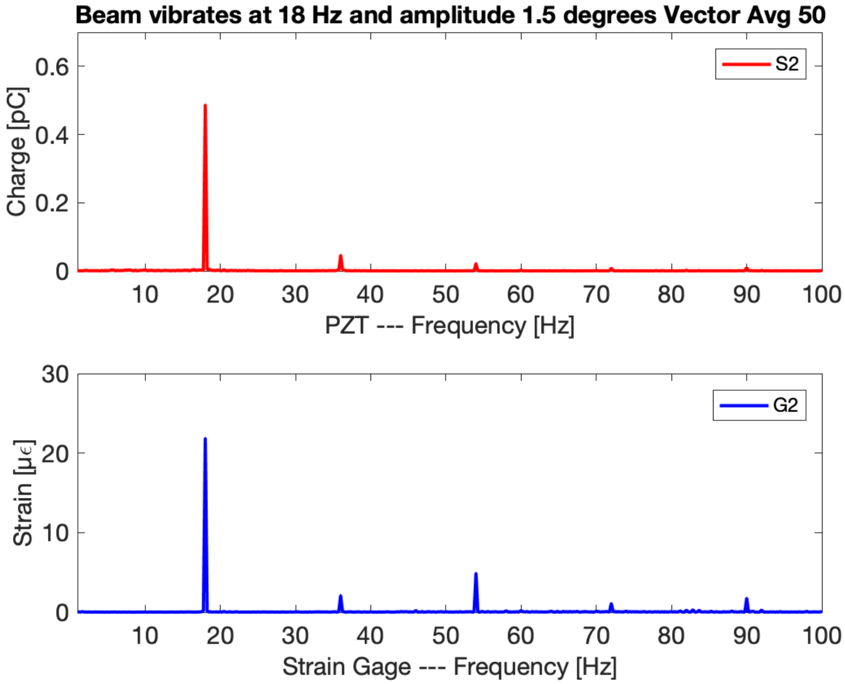

Figure 7.54: FFT measurements when beam vibrates at 18 Hz with sweep angle of 1.5°: Upper plot is charge output of PZT-IDEs sensor S2 and lower plot is strain output from strain gauge G2 during test

7.2.3.4 Finite Element Simulation of Experiment

The experimental results show that two PZT-silane thin films with IDEs oriented 90 degrees apart have different sensitivities towards same directional strain and PZT thin films with an interdigitated electrode design can use to distinguish strains from two different directions. Figure 7.55 shows a finite element model of S1 and S2 sensors on test beam. Aluminum beam model has a length of 82 mm [7], width of 26 mm and thickness of 0.4 mm.

The PZT-IDEs sensors are attached near the clamped bottom edge and locations are set as shown in Fig. 7.48 to simulate the experimental conditions. PZT sensor S1 with interdigitated electrodes is shown in Fig. 7.56, and sensor S2 has an identical structure but offset 90 degrees. Figure 7.56 (a) shows the top view of PZT-IDEs sensor S1 and Fig. 7.56 (b) shows the cross-sectional view across the dashed line in (a). A magnified illustration is also provided for the PZT with IDEs region as shown in Fig. 7.57. One PZT-IDEs sensor consists of six sets of electrodes and eleven PZT strips. The PZT strips (5000 m x 150 μm with 10 μm in thickness) are modeled using piezoelectric elements.

Since the PZT-silane thin film is not entirely PZT, the material properties must be modified to reflect the presence of polymer. For density and stiffness matrix C, a 0.1% modification factor is applied to the values in PZT-4 because the polymer content will reduce the density and stiffness of the PZT-silane films. Bulk PZT-4 has a density of $\rho = 7500 kg/m^3$, and its stiffness matrix $\mathbf{C}$, piezoelectric matrix $\mathbf{d}$, and dielectric matrix can be found in Eqn. (7.1), Eqn. (7.2) and Eqn. (7.3).

The rest of the setup is modeled using solid elements. The aluminum beam has a Youngs modulus of 68.9 GPa, a Poisson's ratio of 0.33, and a density of 2700 kg/m^3. For the PET layer, its size is 12 mm x 12 mm, thickness is 130 μm, density is 1300 kg/m^3, Young's modulus is 2.55 GPa, and Poisson's ratio is 0.39. For the epoxy block, its size is 10 mm x 6 mm, thickness is 500 μm, its density is 1250 kg/m^3, Young's modulus is 3.5 GPa, and Poisson's ratio is 0.33. For the silver electrodes, their size is 5 mm x 50 μm, thickness is 300

---

[7] Beam length is shorter than the one used in experiment, because beam is clamped 82 mm away from the top boundary as shown in Fig. 7.52

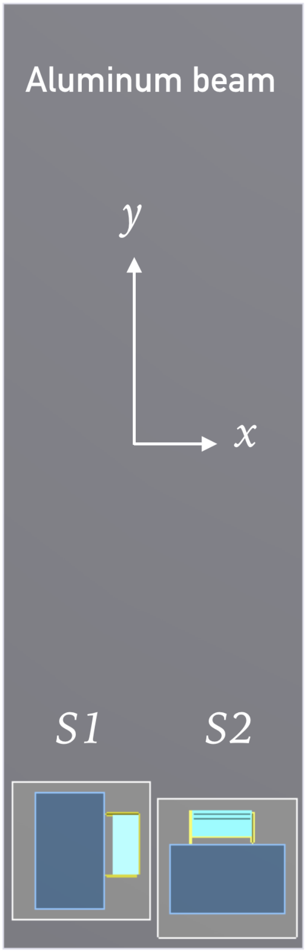

Figure 7.55: Finite element model of S1 and S2 sensors on test beam

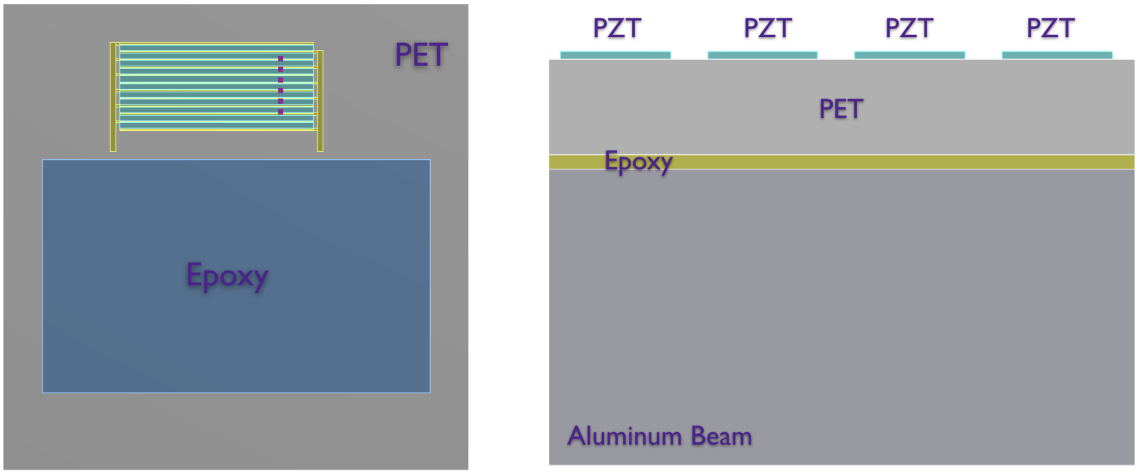

(a) Top view (b) Cross-sectional view

Figure 7.56: Finite element model of a PZT-IDEs sensor: (a) top view (b) cross-sectional view

nm, density is 10,500 kg/m^3, Young's modulus is 84 GPa, and Poisson's ratio is 0.365.

Static structural analysis is conducted to simulate sensor voltage outputs with the following parameters and conditions:

- For the PZT-silane layer properties, 0.1% of the density value and stiffness matrix values, 50% of the piezoelectric and dielectric matrix values of PZT-4 are used.

- The lectrical boundary conditions are set for reading out voltage outputs. The voltage of the PZT surface nodes near the positive electrodes (red portions in Fig. 7.58) are all coupled, and the voltage of the nodes near the negative electrodes (black portions in Fig. 7.58) are 0 V. The sensor provides a single voltage value by reading out voltage information at the positive electrodes.

- A force of 1N is used to pull the beam along its y-axis to simulate stress σ_y only along beam length direction as shown in Fig. 7.59.

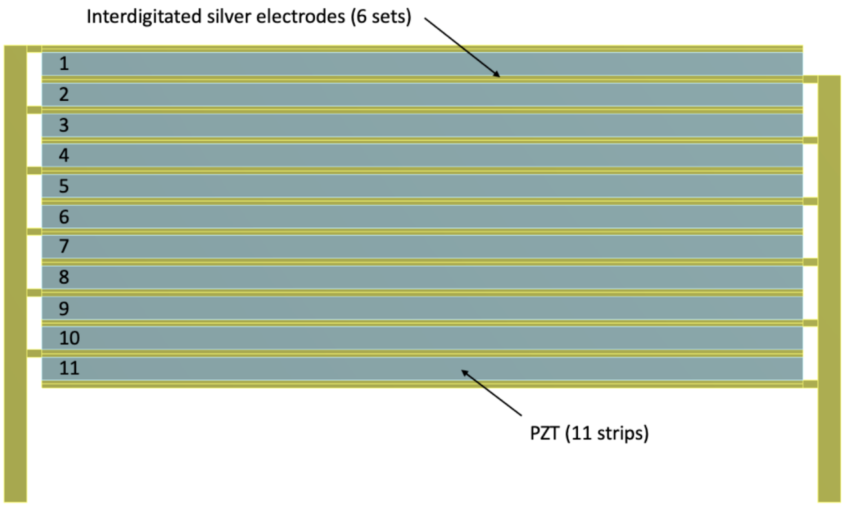

Figure 7.57: Finite element model of PZT with IDEs

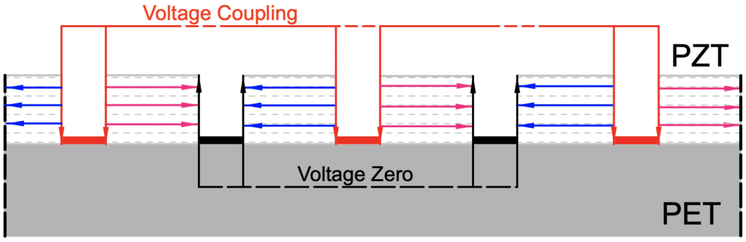

Figure 7.58: Cross section schematic for electrical boundary conditions

Figure 7.59: Loading condition for simulation

Figure 7.60 shows the beam's normal elastic strains in x and y-axis on the opposite side of PZT-IDEs sensors (approximately the same locations as G1 and G2). The strain state in those two axis are pretty uniform. From Figure 7.60 (a) we get an average strain $\epsilon_x \approx -0.44\ \mu\epsilon$ and from (b) we get an average strain $\epsilon_y \approx 1.4\ \mu\epsilon$. ϵ_x/ϵ_y ratio is calculated to be 0.314, and it's close to Poisson's ratio of aluminum (0.33). This shows the model is accurate enough to represent experimental loading condition.

During FE simulation, S1 outputs voltage amplitude $2.6254 \times 10^{-4}\ V$ and S2 outputs voltage amplitude $5.1894 \times 10^{-4}\ V$ as displayed in Fig. 7.61. The ratio of 1.9766 (Eqn. (7.20)) is very close to the ratio obtained in experiment.

$$\frac{V_{S2}}{V_{S1}} = 1.9766 \tag{7.20}$$

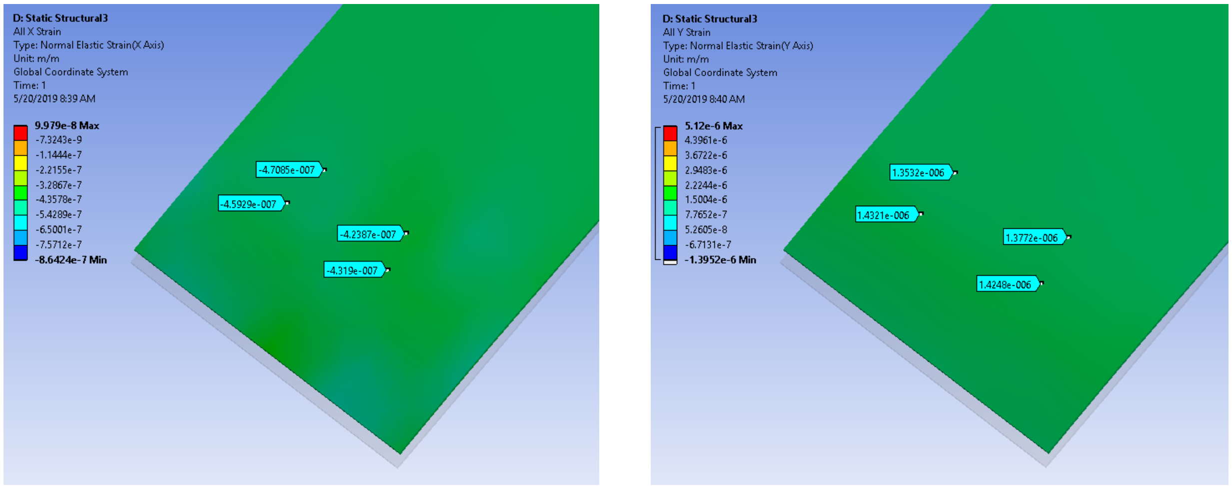

(a) x-axis

(b) y-axis

Figure 7.60: Aluminum beam back side (a) normal elastic strain in x-axis (b) normal elastic strain in y-axis

Table 7.7 summarized the finite element simulation results in this section for strain sensor directional sensitivity demonstration. The simulation finding proves PZT thin films with

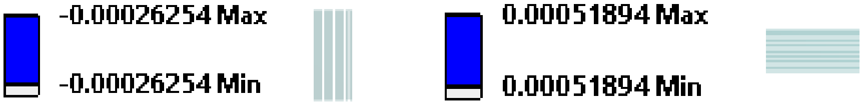

(a) S1 (b) S2

Figure 7.61: Voltage outputs for PZT-IDEs sensors S1 and S2

interdigitated electrode design can distinguish strains in two different directions and the ratio 1.9766 is very close to the ratio 1.9075 obtained in experiment.

Table 7.7: Strain sensor with direction sensing capability summary for finite element simulation on experimentation

Normal strains of the beam	ϵ_x	ϵ_y	ϵ_y/ϵ_x
	0.44 $\mu\epsilon$	1.4 $\mu\epsilon$	3.1818
PZT-IDEs sensors	V_{S1}	V_{S2}	V_{S2}/V_{S1}
	0.26254 mV	0.51894 mV	1.9766

Chapter 8

CONCLUSIONS

This dissertation has illustrated the need for a flexible, printable sensor with a low curing temperature for structural health monitoring (SHM). In line with our research goal and objectives, this study is summarized below:

1. PZT nanoparticles in this study are fabricated through expedited hydrothermal processing (EHP) with fast ramping and cooling rates and particle size distribution primarily in the range of 300 nm to 800 nm.

2. PZT ink contains hydrothermally grown PZT nanoparticles, a UV-sensitive silane-based binder, and ethanol. The use of the UV-sensitive binder can reduce the curing temperature of the film (less than 120 °C). The use of PZT nanoparticles allows PZT ink to

    - have a higher solid content compared to crushed PZT particles,
    - use a low-viscosity solvent, such as ethanol,
    - be less likely to precipitate, clog print heads and feed catheters,
    - be considerably more suitable for printing.

3. PZT-silane films have thicknesses around 5-10 micrometers. Dielectric characterization of PZT-silane thin films with top and bottom electrodes shows they have very small loss tangents.

4. Piezoelectric characterization is performed by applying a calibrated force directly onto the film while an accurate charge amplifier records the induced charges. Finite element

models of PZT-silane thin films with parallel-plate electrodes are created to estimate the piezoelectric d_{33} from the measured charge-to-force ratios. The estimated d_{33} is about 0.6% that of bulk PZT-4.

5. PZT-silane films with rigid and flexible substrates, e-beam evaporated and inkjet-printed electrodes, and parallel-plate and interdigitated electrodes designs are demonstrated as functional piezoelectric actuators and sensors.

6. PZT-silane thin film with parallel-plate electrodes is attached near the fixed end of a cantilevered Kapton beam. Vibration of the beam is synchronized with actuation voltages provided when driving the film near the beam's natural frequencies, indicating PZT films can served as actuators.

7. Validity of PZT-silane thin films with parallel-plate electrodes as an accurate and effective vibration sensor has been established. Frequency response functions of a square plate using a PZT-silane thin film and a laser Doppler vibrometer are measured simultaneously. Close agreement between the two measurements demonstrates the viability of the PZT-silane thin-film sensor.

8. Additive manufacturing of PZT-silane thin films on a flexible substrate is not feasible using parallel-plate electrodes. Silver electrodes inkjet printed onto the PZT-silane films do not have enough conductivity unless many layers are used, which in turn causes inaccurate electrode dimensions. Interdigitated electrodes printed directly on PET substrate followed by an additively manufactured PZT-silane film offer a much simpler and reliable manufacturing platform for such piezoelectric devices. Vibration tests indicate that PZT/IDEs/PET actuator present appreciable resonant response. To obtain the non-resonant response, the PZT NPs must be improved to have larger piezoelectric constant and the electrode design must be optimized, as supported by finite element simulations.

9. PZT-silane thin films with printed interdigitated electrodes (IDEs) are demonstrated as vibration and strain sensors on cantilever beam, oscillating wing and beam structures. The agreement between displacement and charge frequency domain measurements proves that PZT-IDEs sensors work as vibration sensors. PZT-IDEs sensors are secured on one side of test structure and strain gauges on the other side for comparison and characterization. PZT-IDEs outputs increase when oscillating angle gets larger and charge responses are approximately proportional to strain gauge outputs as oscillation increases. This indicates PZT-silane thin film with printed IDEs can be used as strain sensors.

10. PZT-silane thin films with printed IDEs have directional strain sensing capability as demonstrated in theory, finite element analysis and experimentally. Two PZT-silane thin films with printed IDEs oriented 90 degrees apart are adhered on a oscillating beam. Strain and charge FFT measurements show different sensitivities towards single-axis strain and experiment proves the PZT thin films with interdigitated electrode design can distinguish strains in two different directions.

    The fabricated PZT-IDEs strain sensor has the following advantages.

    - PZT-silane strain sensors can distinguish strains in two different directions.
    - Such sensors may conform to any complex or 2-D flexible surfaces.
    - The strain sensors are lightweight and extremely thin. They are printed directly on the target surface with 5-10 μm in thickness.
    - PZT-silane strain sensors will not inflict any sort of physical change to the surface because no machining is required and the curing temperature of the functional films is low (80-120°C).
    - PZT-silane strain sensors are self-powered. This is a big advantage over the conventional strain sensors, which require electric energy sources to work, especially when the sensor location is a long distance away from any available power supply.

- The strain sensors preserve the surfaces' structural integrity, and have minimal impact on the aerodynamic characteristics of the monitored surface (e.g., airfoils and wings).
- The manufacturing of strain sensor, wiring and packaging can be easily integrated into the 3-D printing process.
- PZT-silane strain sensors have very little weight penalty. The thin film has negligible mass to the surface structures. Furthermore, the wiring, circuit board and interconnects can also be printed to lower the weight penalty.

BIBLIOGRAPHY

[1] Daniel Balageas, Claus-Peter Fritzen, and Alfredo Güemes. *Structural health monitoring*, volume 493. Wiley Online Library, 2006.

[2] Victor Giurgiutiu. *Structural health monitoring: with piezoelectric wafer active sensors.* Academic Press, 2007.

[3] Vistasp M Karbhari and Farhad Ansari. *Structural health monitoring of civil infrastructure systems.* Elsevier, 2009.

[4] Fu-Kuo Chang. *Structural health monitoring: current status and perspectives.* CRC Press, 1998.

[5] Hoon Sohn, Charles R Farrar, Francois M Hemez, Devin D Shunk, Daniel W Stinemates, Brett R Nadler, and Jerry J Czarnecki. A review of structural health monitoring literature: 1996-2001, 2004.

[6] T Harms, B Banks, S Sedigh Sarvestani, and Filippo Bastianini. Design and testing of a low-power wireless sensor network for structural health monitoring of bridges. In *SPIE Smart Structures and Materials+ Nondestructive Evaluation and Health Monitoring*, pages 72920U–72920U. International Society for Optics and Photonics, 2009.

[7] Jeong-Beom Ihn and Fu-Kuo Chang. Pitch-catch active sensing methods in structural health monitoring for aircraft structures. *Structural Health Monitoring*, 7(1):5–19, 2008.

[8] Victor Giurgiutiu and Adrian Cuc. Embedded non-destructive evaluation for structural health monitoring, damage detection, and failure prevention. *Shock and Vibration Digest*, 37(2):83, 2005.

[9] Ajay Raghavan and Carlos ES Cesnik. Review of guided-wave structural health monitoring. *Shock and Vibration Digest*, 39(2):91–116, 2007.

[10] Petia Dineva, Dietmar Gross, Ralf Müller, and Tsviatko Rangelov. Dynamic fracture of piezoelectric materials. *AMC*, 10:12, 2014.

[11] Jeong-Beom Ihn and Fu-Kuo Chang. Multicrack growth monitoring at riveted lap joints using piezoelectric patches. In *NDE For Health Monitoring and Diagnostics*, pages 29–40. International Society for Optics and Photonics, 2002.

[12] Jeong-Beom Ihn and Fu-Kuo Chang. Detection and monitoring of hidden fatigue crack growth using a built-in piezoelectric sensor/actuator network: I. diagnostics. *Smart materials and structures*, 13(3):609, 2004.

[13] Jeong-Beom Ihn and Fu-Kuo Chang. Detection and monitoring of hidden fatigue crack growth using a built-in piezoelectric sensor/actuator network: Ii. validation using riveted joints and repair patches. *Smart materials and structures*, 13(3):621, 2004.

[14] Victor Giurgiutiu. *Structural health monitoring: with piezoelectric wafer active sensors.* Academic Press, 2007.

[15] Zhigang Sun, Bruno Rocha, Kuo-Ting Wu, and Nezih Mrad. A methodological review of piezoelectric based acoustic wave generation and detection techniques for structural health monitoring. *International Journal of Aerospace Engineering*, 2013, 2013.

[16] Victor Giurgiutiu, Andrei Zagrai, and Jing Jing Bao. Piezoelectric wafer embedded active sensors for aging aircraft structural health monitoring. *Structural Health Monitoring*, 1(1):41–61, 2002.

[17] Inpil Kang, Mark J Schulz, Jay H Kim, Vesselin Shanov, and Donglu Shi. A carbon nanotube strain sensor for structural health monitoring. *Smart materials and structures*, 15(3):737, 2006.

[18] Chia Chen Ciang, Jung-Ryul Lee, and Hyung-Joon Bang. Structural health monitoring for a wind turbine system: a review of damage detection methods. *Measurement Science and Technology*, 19(12):122001, 2008.

[19] PJ Schubel, RJ Crossley, EKG Boateng, and JR Hutchinson. Review of structural health and cure monitoring techniques for large wind turbine blades. *Renewable Energy*, 51:113–123, 2013.

[20] Joseph Yan, Robert J Wood, Srinath Avadhanula, Metin Sitti, and Ronald S Fearing. Towards flapping wing control for a micromechanical flying insect. In *Robotics and Automation, 2001. Proceedings 2001 ICRA. IEEE International Conference on*, volume 4, pages 3901–3908. IEEE, 2001.

[21] Valery Pylypchuk, Shih-Ken Chen, and Nikolai Moshchuk. Tire force estimation with strain gauge measurement. In *ASME 2014 International Mechanical Engineering Congress and Exposition*, pages V012T15A007–V012T15A007. American Society of Mechanical Engineers, 2014.

[22] E Peiner, A Tibrewala, R Bandorf, S Biehl, H Lüthje, and L Doering. Micro force sensor with piezoresistive amorphous carbon strain gauge. *Sensors and Actuators A: Physical*, 130:75–82, 2006.

[23] Gaizka Durana, Marlene Kirchhof, Michael Luber, Idurre Sáez de Ocáriz, Hans Poisel, Joseba Zubia, and Carmen Vázquez. Use of a novel fiber optical strain sensor for monitoring the vertical deflection of an aircraft flap. *IEEE sensors journal*, 9(10):1219–1225, 2009.

[24] YL Park, S Elayaperumal, BL Daniel, E Kaye, KB Pauly, RJ Black, and MR Cutkosky. Mri-compatible haptics: Feasibility of using optical fiber bragg grating strain-sensors to detect deflection of needles in an mri environment. *International Society for Magnetic Resonance in Medicine (ISMRM) 2008*, 2008.

[25] Byoungho Lee. Review of the present status of optical fiber sensors. *Optical fiber technology*, 9(2):57–79, 2003.

[26] Lae-Hyong Kang, Dae-Kwan Kim, and Jae-Hung Han. Estimation of dynamic structural displacements using fiber bragg grating strain sensors. *Journal of sound and vibration*, 305(3):534–542, 2007.

[27] GC Foss and ED Haugse. Using modal test results to develop strain to displacement transformations. In *Proceedings of the 13th international modal analysis conference*, volume 2460, page 112, 1995.

[28] Philip B Bogert, Eric Haugse, and Ralph E Gehrki. Structural shape identification from experimental strains using a modal transformation technique. In *Proceedings of 44th AIAA/ASME/ASCE/AHS Structures, Structural Dynamics and Materials Conference, Norfolk, Virginia*, 2003.

[29] Mayuko Nishio, T Mizutani, and N Takeda. Structural shape reconstruction with consideration of the reliability of distributed strain data from a brillouin-scattering-based optical fiber sensor. *Smart Materials and Structures*, 19(3):035011, 2010.

[30] Wikipedia. Strain gauge — wikipedia, the free encyclopedia, 2016. [Online; accessed 2-July-2016].

[31] Marcelo M Werneck, RCSB Allil, Bessie A Ribeiro, and Fábio VB de Nazaré. A guide to fiber bragg grating sensors. *Current Trends in Shortand Long-period Fiber Gratings, ed. C. Cuadrado-Laborde*, 2013.

[32] Manfred Kreuzer. Strain measurement with fiber bragg grating sensors. *HBM: Darmstadt, Germany*, 2006.

[33] $http://www.fbgs.com/technology/fbgprinciple/$.

[34] Iker Garca, Joseba Zubia, Gaizka Durana, Gotzon Aldabaldetreku, Mara Asuncin Illarramendi, and Joel Villatoro. Optical fiber sensors for aircraft structural health monitoring. *Sensors*, 15(7):15494, 2015.

[35] Gayan C Kahandawa, Jayantha Epaarachchi, Hao Wang, and KT Lau. Use of fbg sensors for shm in aerospace structures. *Photonic Sensors*, 2(3):203–214, 2012.

[36] Donald G Krantz, John H Belk, Paul J Biermann, Joel Dubow, Lee W Gause, Ramesh Harjani, Susan C Mantell, Dennis L Polla, and Philip R Troyk. Project update: applied research on remotely queried embedded microsensors. In *1999 Symposium on Smart Structures and Materials*, pages 157–164. International Society for Optics and Photonics, 1999.

[37] MS Vijaya. *Piezoelectric Materials and Devices: Applications in Engineering and Medical Sciences*. CRC Press, 2012.

[38] Kenji Uchino. *Advanced piezoelectric materials: Science and technology*. Elsevier, 2010.

[39] Wesley G Nelson. *Piezoelectric Materials: Structure, Properties, and Applications*. Nova Science Publishers, 2010.

[40] Wikipedia. Piezoelectricity — wikipedia, the free encyclopedia, 2016.

[41] Bernard Jaffe. *Piezoelectric ceramics*, volume 3. Elsevier, 2012.

[42] Jiashi Yang. *An introduction to the theory of piezoelectricity*, volume 9. Springer Science & Business Media, 2004.

[43] $https://www.comsol.com/blogs/piezoelectric - materials - crystal - orientation - polingdirection/$.

[44] Heiji Kawai. The piezoelectricity of poly (vinylidene fluoride). *Japanese Journal of Applied Physics*, 8(7):975, 1969.

[45] SAS Piezotech. Piezotech piezoelectric films leaflet, 2015. *URL http://www. piezotech. fr/image/documents/22-31-32-33-piezotech-piezoelectric-films-leaflet. pdf.*

[46] Daniel Mason Esterly. Manufacturing of poly (vinylidene fluoride) and evaluation of its mechanical properties. 2002.

[47] Ye Lu, Lin Ye, and Zhongqing Su. Crack identification in aluminium plates using lamb wave signals of a pzt sensor network. *Smart Materials and Structures*, 15(3):839, 2006.

[48] G Song, PZ Qiao, WK Binienda, and GP Zou. Active vibration damping of composite beam using smart sensors and actuators. *Journal of aerospace engineering*, 15(3):97–103, 2002.

[49] Khaled S Ramadan, D Sameoto, and S Evoy. A review of piezoelectric polymers as functional materials for electromechanical transducers. *Smart Materials and Structures*, 23(3):033001, 2014.

[50] E Koray Akdogan, Mehdi Allahverdi, and Ahmad Safari. Piezoelectric composites for sensor and actuator applications. *Ultrasonics, Ferroelectrics, and Frequency Control, IEEE Transactions on*, 52(5):746–775, 2005.

[51] TR Gururaja. Piezoelectrics for medical ultrasonic imaging. *American Ceramic Society Bulletin*, 73(5):50–55, 1994.

[52] Jeffrey Lynn Duce, Scott Robert Johnston, I-Yeu Shen, Guozhong Cao, and Hsien-Lin Huang. Method and system of fabricating pzt nanoparticle ink based piezoelectric sensor, December 24 2013. US Patent 8,614,724.

[53] AR Bhatti, M Mott, JRG Evans, and MJ Edirisinghe. Pzt pillars for 1-3 composites prepared by ink-jet printing. *Journal of materials science letters*, 20(13):1245–1248, 2001.

[54] Francesca Bortolani and Robert A Dorey. Molten salt synthesis of pzt powder for direct write inks. *Journal of the European Ceramic Society*, 30(10):2073–2079, 2010.

[55] Tianming Wang and Brian Derby. Ink-jet printing and sintering of pzt. *Journal of the American Ceramic Society*, 88(8):2053–2058, 2005.

[56] J Windle and B Derby. Ink jet printing of pzt aqueous ceramic suspensions. *Journal of materials science letters*, 18(2):87–90, 1999.

[57] K Sivanandan, Asha T Achuthan, V Kumar, and Isaku Kanno. Fabrication and transverse piezoelectric characteristics of pzt thick-film actuators on alumina substrates. *Sensors and Actuators A: Physical*, 148(1):134–137, 2008.

[58] Soichiro Okamura, Rie Takeuchi, and Tadashi Shiosaki. Fabrication of ferroelectric pb (zr, ti) o3 thin films with various zr/ti ratios by ink-jet printing. *Japanese journal of applied physics*, 41(11S):6714, 2002.

[59] JM Hale and J Tuck. A novel thick-film strain transducer using piezoelectric paint. *Proceedings of the Institution of Mechanical Engineers, Part C: Journal of Mechanical Engineering Science*, 213(6):613–622, 1999.

[60] JM Hale, JR White, R Stephenson, and F Liu. Development of piezoelectric paint thick-film vibration sensors. *Proceedings of the Institution of Mechanical Engineers, Part C: Journal of Mechanical Engineering Science*, 219(1):1–9, 2005.

[61] Shigenori Egusa and Naozumi Iwasawa. Piezoelectric paints as one approach to smart structural materials with health-monitoring capabilities. *Smart Materials and Structures*, 7(4):438, 1998.

[62] Yunfeng Zhang. In situ fatigue crack detection using piezoelectric paint sensor. *Journal of Intelligent Material Systems and Structures*, 17(10):843–852, 2006.

[63] X Li and Y Zhang. Analytical study of piezoelectric paint sensor for acoustic emission-based fracture monitoring. *Fatigue & Fracture of Engineering Materials & Structures*, 31(8):684–694, 2008.

[64] Chun-Hung Hsueh and Chia-Che Wu. Fabrication of lead zirconium titanium and silica composite films on copper/polyimide flexible substrates. *Smart Materials and Structures*, 19(12):124005, 2010.

[65] JR White, B De Poumeyrol, JM Hale, and R Stephenson. Piezoelectric paint: Ceramic-polymer composites for vibration sensors. *Journal of Materials Science*, 39(9):3105–3114, 2004.

[66] Oleksandr Noshchenko, Danjela Kuscer, Oana Cătălina Mocioiu, Maria Zaharescu, Marian Bele, and Barbara Malič. Effect of milling time and ph on the dispersibility of lead zirconate titanate in aqueous media for inkjet printing. *Journal of the European Ceramic Society*, 34(2):297–305, 2014.

[67] Hsien-Lin Huang, GZ Cao, and IY Shen. Hydrothermal synthesis of lead zirconate titanate ($pztorpb(zr_{0.52}ti_{0.48})o_3$) nano-particles using controlled ramping and cooling rates. *Sensors and Actuators A: Physical*, 214:111–119, 2014.

[68] Oral Büyüköztürk, Tzu-Yang Yu, and Jose Alberto Ortega. A methodology for determining complex permittivity of construction materials based on transmission-only coherent, wide-bandwidth free-space measurements. *Cement and Concrete Composites*, 28(4):349–359, 2006.

[69] Hiroshi Haruta. *The Impedance Measurement Handbook: A Guide to Measurement Technology and Techniques*. Agilent Technologies, 2000.

[70] Agilent Application Note. Agilent basics of measuring the dielectric properties of materials. *Agilent Literature Number*, 2006.

[71] Weiwei Xu, Hsien-Lin Huang, Yifeng Liu, Chuan Luo, GZ Cao, and IY Shen. Fabrication and characterization of pzt-silane nano-composite thin-film sensors. *Sensors and Actuators A: Physical*, 246:102–113, 2016.

[72] AH Meitzler et al. Ieee standard on piezoelectricity: An american national standard. std 176, 66 p. *IEEE-ANSI, New York, USA*, 1987.

[73] *http://www.piusa.us/tutorial/4_16.html*.

[74] Qing Guo, GZ Cao, and IY Shen. Measurements of piezoelectric coefficient d33 of lead zirconate titanate thin films using a mini force hammer. *Journal of Vibration and Acoustics*, 135(1):011003, 2013.

[75] Qing Guo. *Development of Thin-Film Based Microdevices and Process Enhancement for Making the Same*. PhD thesis, University of Washington, 2012.

[76] I-Yeu Shen, Guozhong Cao, and Hsien-Lin Huang. Methods for forming lead zirconate titanate nanoparticles, April 14 2015. US Patent 9,005,465.

[77] Wei Yu, Ben Q Li, Shujiang Ding, and Hongzhong Liu. 3d printing of interdigitated electrode for all-solid-state microsupercapacitors. *Journal of Micromechanics and Microengineering*, 28(10):105014, 2018.

[78] Bella Rosa Liyarita, Adriano Ambrosi, and Martin Pumera. 3d-printed electrodes for sensing of biologically active molecules. *Electroanalysis*, 30(7):1319–1326, 2018.

[79] C Lorena Manzanares Palenzuela, Filip Novotny, Petr Krupicka, Zdenek Sofer, and Martin Pumera. 3d-printed graphene/polylactic acid electrodes promise high sensitivity in electroanalysis. *Analytical chemistry*, 90(9):5753–5757, 2018.

[80] Ke Sun, Teng-Sing Wei, Bok Yeop Ahn, Jung Yoon Seo, Shen J Dillon, and Jennifer A Lewis. 3d printing of interdigitated li-ion microbattery architectures. *Advanced materials*, 25(33):4539–4543, 2013.

[81] Jonas Lölsberg, Ottokar Starck, Serafin Stiefel, Jonas Hereijgers, Tom Breugelmans, and Matthias Wessling. 3d-printed electrodes with improved mass transport properties. *ChemElectroChem*, 4(12):3309–3313, 2017.

[82] Kwok Siong Teh. Additive direct-write microfabrication for mems: A review. *Frontiers of Mechanical Engineering*, 12(4):490–509, 2017.

[83] Mark Andrew Jankauski et al. *Dynamic Modeling of Insect Flight Mechanisms*. PhD thesis, 2017.

[84] Pranay Seshadri, Moble Benedict, and Inderjit Chopra. Understanding micro air vehicle flapping-wing aerodynamics using force and flowfield measurements. *Journal of Aircraft*, 50(4):1070–1087, 2013.

[85] Nava Setter and EL Colla. *Ferroelectric ceramics: Tutorial reviews, theory, processing, and applications*. Birkhauser, 1993.

[86] Takeo Yamada, Yuhei Hayamizu, Yuki Yamamoto, Yoshiki Yomogida, Ali Izadi-Najafabadi, Don N Futaba, and Kenji Hata. A stretchable carbon nanotube strain sensor for human-motion detection. *Nature nanotechnology*, 6(5):296–301, 2011.

[87] Ning Hu, Hisao Fukunaga, Satoshi Atobe, Yaolu Liu, Jinhua Li, et al. Piezoresistive strain sensors made from carbon nanotubes based polymer nanocomposites. *Sensors*, 11(11):10691–10723, 2011.

[88] Rüdiger G Ballas. *Piezoelectric multilayer beam bending actuators: static and dynamic behavior and aspects of sensor integration*. Springer Science & Business Media, 2007.

Appendix A

SYNTHESIS OF PZT NANOPARTICLES

The following procedures for synthesis of PZT nanoparticles was developed by Hsien-Lin Huang [67]

1. Note: Lead is a hazardous material, please search MSDS of lead and PZT or contact EH&S at UW for proper personal protection equipment requirements and proper disposal methods

    - The chemical usage in this procedure should have enough PZT feedstock for 4-5 runs of hydrothermal.
    - Autoclave should be placed at the center of furnace, keep in mind that never put more than one autoclave in the furnace.
    - Make sure all glassware and necessary equipment are clean.
    - Please respect other peoples experiments. Dont move others chemicals or setups without notifying them or Professor Cao from MSE lab.

The main chemicals used in this process is
Tetra Iso Propyltitanate (denoted as TIPT)

1. TIPT (2.86 mL)+ AcAc (1.96 mL), stir 4 hours under room temperature

    - When adding AcAc into TIPT, add it slowly
    - The mixture should first be darker yellow and then turn into orange

2. ZrO(OAc)2 (4.66 mL) slowly added into mixture from (1) and stir for 15 mins under room temperature
    - After adding Zr, the mixture should turn into light yellow
3. Adding mixture from (2) into 1M KOH solution while stirring, drop wise
    - 150mL DI water + 8.5475 g KOH = 1M KOH
    - White precipitation formed during this process
    - If adding mixture from (2) too fast, incomplete reaction may occur and result in poor quality PZT powder
4. Let the precipitation stir under room temperature for 2-3 days
    - It is to ensure all chemical reaction occurs in (3) are complete
    - From experience, wait for 2-3 days before next step will have more stable product quality
5. Wash precipitation with DI water by centrifuge till pH appears to be weak base
    - pH test paper should appear to be lighter green (pH 8-9)
6. Add DI (40 mL) water into the washed precipitation and stir for 15 mins under room temperature
    - It is to ensure the precipitation is well disperse in the DI water rather than clustered in DI water
7. Add Pb 8.526 g and stir for 15 mins under room temperature

  - It is to ensure that Pb is completely dissolved and well mixed with the precipitation
  - The mixture should appear more like solution than gel after Pb is added
  - Up to this point, the mixture should be white

8. Add KOH (5.61056g)slowly and stir for 5 mins under room temperature
    - Solution should be white, very light orange-pink
    - Adding KOH to fast will result in promoting formation of lead oxides, solution may be light green, light latte color, dark orange-pink (sign of poor quality final product)
9. Put 10 mL PZT feedstock into the Teflon container
10. Seal autoclave
    - Make sure the autoclave is sealed well, losing vacuum inside of autoclave means the pressure wont be able to reach the necessary level for PZT formation
11. Hydrothermal process for 2 hours
    - We have tolerance up to plus half hour
12. Remove autoclave from furnace and cool under room temperature
    - Safety: Make sure not to tile the autoclave when removing it from the furnace since the pressure inside of the autoclave is still high at this point
13. After cooling down, washing PZT powder with DI water by centrifuge 3 times

- When you open the Teflon container, liquid layer should be larger volume compared to solid
- Resulting PZT powder should appear to be white powder
- From experience, yellow or pink powder usually means larger particles and more agglomeration
- If the resulting particles settle down very fast after you transfer them into a plastic tube and DI water, then you most likely have good PZT NPs

14. Wash PZT powder with 10% vol. acetic acid 3-5 times (till the upper layer of the solution appears to be clear, not cloudy)
    - Prepare 10% vol acetic acid: 10mL acetic acid + 90mL DI water
    - Usually, first time using diluted acetic acid Washington PZT powder, the liquid will be clear and it will be more cloudy second time of washing. Then, slowly the liquid will be clear again
15. Wash PZT powder with DI water till pH neutral
16. Oven dry PZT powder under 80C for 24 hours

Appendix B

IMPEDANCE DATA

Table B.1: Impedance measurement data for sensor NS1

Frequency (Hz)	**Impedance**	**Phase**	C_p	R_p
40	1.41E+06	-79.72	2.78E-09	7.96E+06
540	1.26E+05	-84.99	2.34E-09	1.44E+06
1040	6.73E+04	-85.72	2.27E-09	9.02E+05
1539	4.62E+04	-86.05	2.23E-09	6.71E+05
2039	3.53E+04	-86.25	2.21E-09	5.39E+05
2539	2.85E+04	-86.38	2.19E-09	4.52E+05
3039	2.40E+04	-86.46	2.18E-09	3.88E+05
3539	2.07E+04	-86.53	2.17E-09	3.42E+05
4038	1.82E+04	-86.58	2.16E-09	3.06E+05
4538	1.63E+04	-86.62	2.15E-09	2.77E+05
5038	1.47E+04	-86.65	2.14E-09	2.53E+05
5538	1.34E+04	-86.68	2.13E-09	2.32E+05
6038	1.24E+04	-86.70	2.13E-09	2.15E+05
6537	1.15E+04	-86.72	2.12E-09	2.00E+05
7037	1.07E+04	-86.73	2.12E-09	1.87E+05
7537	9.98E+03	-86.74	2.11E-09	1.75E+05
8037	9.38E+03	-86.75	2.11E-09	1.66E+05

Continued on next page

Table B.1 – *Continued from previous page*

Frequency (Hz)	**Impedance**	**Phase**	C_p	R_p
8537	8.85E+03	-86.75	2.10E-09	1.56E+05
9036	8.38E+03	-86.77	2.10E-09	1.49E+05
9536	7.95E+03	-86.77	2.10E-09	1.41E+05
10036	7.57E+03	-86.78	2.09E-09	1.35E+05
10536	7.22E+03	-86.77	2.09E-09	1.28E+05
11036	6.90E+03	-86.77	2.09E-09	1.23E+05
11535	6.61E+03	-86.77	2.08E-09	1.18E+05
12035	6.35E+03	-86.77	2.08E-09	1.13E+05
12535	6.10E+03	-86.77	2.08E-09	1.08E+05
13035	5.88E+03	-86.76	2.07E-09	1.04E+05
13535	5.67E+03	-86.76	2.07E-09	1.00E+05
14034	5.47E+03	-86.75	2.07E-09	9.67E+04
14534	5.29E+03	-86.75	2.07E-09	9.36E+04
15034	5.12E+03	-86.75	2.06E-09	9.03E+04
15534	4.96E+03	-86.74	2.06E-09	8.76E+04
16034	4.81E+03	-86.73	2.06E-09	8.47E+04
16533	4.67E+03	-86.74	2.06E-09	8.20E+04
17033	4.54E+03	-86.73	2.06E-09	7.95E+04
17533	4.41E+03	-86.73	2.05E-09	7.74E+04
18033	4.29E+03	-86.72	2.05E-09	7.51E+04
18533	4.18E+03	-86.72	2.05E-09	7.32E+04
19032	4.08E+03	-86.71	2.05E-09	7.11E+04
19532	3.97E+03	-86.71	2.05E-09	6.91E+04

Continued on next page

Table B.1 – *Continued from previous page*

Frequency (Hz)	**Impedance**	**Phase**	C_p	R_p
20032	3.88E+03	-86.70	2.04E-09	6.74E+04
20532	3.79E+03	-86.69	2.04E-09	6.57E+04
21032	3.70E+03	-86.69	2.04E-09	6.41E+04
21531	3.62E+03	-86.68	2.04E-09	6.26E+04
22031	3.54E+03	-86.67	2.04E-09	6.11E+04
22531	3.46E+03	-86.67	2.04E-09	5.97E+04
23031	3.39E+03	-86.66	2.04E-09	5.83E+04
23531	3.32E+03	-86.65	2.03E-09	5.69E+04
24030	3.25E+03	-86.65	2.03E-09	5.57E+04
24530	3.19E+03	-86.62	2.03E-09	5.42E+04
25030	3.13E+03	-86.62	2.03E-09	5.31E+04
25530	3.07E+03	-86.62	2.03E-09	5.20E+04
26030	3.01E+03	-86.61	2.03E-09	5.10E+04
26529	2.96E+03	-86.60	2.03E-09	5.00E+04
27029	2.90E+03	-86.60	2.02E-09	4.90E+04
27529	2.85E+03	-86.60	2.02E-09	4.80E+04
28029	2.80E+03	-86.59	2.02E-09	4.71E+04
28529	2.76E+03	-86.58	2.02E-09	4.63E+04
29028	2.71E+03	-86.57	2.02E-09	4.54E+04
29528	2.67E+03	-86.57	2.02E-09	4.45E+04
30028	2.62E+03	-86.56	2.02E-09	4.37E+04
30528	2.58E+03	-86.55	2.02E-09	4.29E+04
31028	2.54E+03	-86.55	2.01E-09	4.23E+04

Continued on next page

Table B.1 – *Continued from previous page*

Frequency (Hz)	**Impedance**	**Phase**	C_p	R_p
31527	2.50E+03	-86.54	2.01E-09	4.15E+04
32027	2.46E+03	-86.53	2.01E-09	4.08E+04
32527	2.43E+03	-86.53	2.01E-09	4.01E+04
33027	2.39E+03	-86.52	2.01E-09	3.95E+04
33527	2.36E+03	-86.52	2.01E-09	3.88E+04
34026	2.32E+03	-86.51	2.01E-09	3.83E+04
34526	2.29E+03	-86.50	2.01E-09	3.77E+04
35026	2.26E+03	-86.50	2.01E-09	3.71E+04
35526	2.23E+03	-86.49	2.00E-09	3.65E+04
36026	2.20E+03	-86.49	2.00E-09	3.59E+04
36525	2.17E+03	-86.48	2.00E-09	3.54E+04
37025	2.14E+03	-86.47	2.00E-09	3.49E+04
37525	2.12E+03	-86.47	2.00E-09	3.44E+04
38025	2.09E+03	-86.46	2.00E-09	3.39E+04
38525	2.06E+03	-86.46	2.00E-09	3.34E+04
39024	2.04E+03	-86.45	2.00E-09	3.29E+04
39524	2.01E+03	-86.45	2.00E-09	3.25E+04
40024	1.99E+03	-86.44	2.00E-09	3.21E+04
40524	1.96E+03	-86.43	2.00E-09	3.15E+04
41024	1.94E+03	-86.43	1.99E-09	3.11E+04
41523	1.92E+03	-86.42	1.99E-09	3.07E+04
42023	1.90E+03	-86.41	1.99E-09	3.03E+04
42523	1.87E+03	-86.41	1.99E-09	2.99E+04

Continued on next page

Table B.1 – *Continued from previous page*

Frequency (Hz)	**Impedance**	**Phase**	C_p	R_p
43023	1.85E+03	-86.40	1.99E-09	2.95E+04
43523	1.83E+03	-86.40	1.99E-09	2.92E+04
44022	1.81E+03	-86.40	1.99E-09	2.89E+04
44522	1.79E+03	-86.38	1.99E-09	2.84E+04
45022	1.77E+03	-86.37	1.99E-09	2.81E+04
45522	1.76E+03	-86.37	1.99E-09	2.78E+04
46022	1.74E+03	-86.37	1.99E-09	2.74E+04
46521	1.72E+03	-86.36	1.99E-09	2.71E+04
47021	1.70E+03	-86.35	1.98E-09	2.68E+04
47521	1.68E+03	-86.35	1.98E-09	2.64E+04
48021	1.67E+03	-86.33	1.98E-09	2.61E+04
48521	1.65E+03	-86.33	1.98E-09	2.58E+04
49020	1.63E+03	-86.32	1.98E-09	2.55E+04
49520	1.62E+03	-86.31	1.98E-09	2.52E+04
50020	1.60E+03	-86.31	1.98E-09	2.49E+04
50520	1.59E+03	-86.31	1.98E-09	2.46E+04
51020	1.57E+03	-86.31	1.98E-09	2.44E+04
51519	1.56E+03	-86.30	1.98E-09	2.41E+04
52019	1.54E+03	-86.29	1.98E-09	2.39E+04
52519	1.53E+03	-86.28	1.98E-09	2.36E+04
53019	1.52E+03	-86.28	1.98E-09	2.34E+04
53519	1.50E+03	-86.26	1.98E-09	2.31E+04
54018	1.49E+03	-86.27	1.97E-09	2.29E+04

Continued on next page

Table B.1 – *Continued from previous page*

Frequency (Hz)	**Impedance**	**Phase**	C_p	R_p
54518	1.48E+03	-86.26	1.97E-09	2.26E+04
55018	1.46E+03	-86.26	1.97E-09	2.24E+04
55518	1.45E+03	-86.25	1.97E-09	2.22E+04
56018	1.44E+03	-86.25	1.97E-09	2.19E+04
56517	1.43E+03	-86.24	1.97E-09	2.17E+04
57017	1.41E+03	-86.23	1.97E-09	2.15E+04
57517	1.40E+03	-86.23	1.97E-09	2.13E+04
58017	1.39E+03	-86.22	1.97E-09	2.11E+04
58517	1.38E+03	-86.21	1.97E-09	2.09E+04
59016	1.37E+03	-86.21	1.97E-09	2.07E+04
59516	1.36E+03	-86.21	1.97E-09	2.05E+04
60016	1.35E+03	-86.20	1.97E-09	2.03E+04
60516	1.33E+03	-86.19	1.97E-09	2.01E+04
61016	1.32E+03	-86.19	1.97E-09	1.99E+04
61515	1.31E+03	-86.18	1.97E-09	1.97E+04
62015	1.30E+03	-86.17	1.96E-09	1.96E+04
62515	1.29E+03	-86.17	1.96E-09	1.94E+04
63015	1.28E+03	-86.17	1.96E-09	1.92E+04
63515	1.27E+03	-86.16	1.96E-09	1.90E+04
64014	1.26E+03	-86.15	1.96E-09	1.89E+04
64514	1.25E+03	-86.15	1.96E-09	1.87E+04
65014	1.25E+03	-86.14	1.96E-09	1.85E+04
65514	1.24E+03	-86.14	1.96E-09	1.84E+04

Continued on next page

Table B.1 – *Continued from previous page*

Frequency (Hz)	**Impedance**	**Phase**	C_p	R_p
66014	1.23E+03	-86.13	1.96E-09	1.82E+04
66513	1.22E+03	-86.13	1.96E-09	1.80E+04
67013	1.21E+03	-86.12	1.96E-09	1.79E+04
67513	1.20E+03	-86.12	1.96E-09	1.77E+04
68013	1.19E+03	-86.11	1.96E-09	1.76E+04
68513	1.18E+03	-86.10	1.96E-09	1.75E+04
69012	1.18E+03	-86.10	1.96E-09	1.73E+04
69512	1.17E+03	-86.09	1.96E-09	1.72E+04
70012	1.16E+03	-86.09	1.96E-09	1.70E+04
70512	1.15E+03	-86.08	1.95E-09	1.69E+04
71012	1.14E+03	-86.08	1.95E-09	1.67E+04
71511	1.14E+03	-86.07	1.95E-09	1.66E+04
72011	1.13E+03	-86.07	1.95E-09	1.65E+04
72511	1.12E+03	-86.06	1.95E-09	1.63E+04
73011	1.11E+03	-86.07	1.95E-09	1.62E+04
73511	1.11E+03	-86.05	1.95E-09	1.61E+04
74010	1.10E+03	-86.05	1.95E-09	1.60E+04
74510	1.09E+03	-86.04	1.95E-09	1.58E+04
75010	1.09E+03	-86.04	1.95E-09	1.57E+04
75510	1.08E+03	-86.03	1.95E-09	1.56E+04
76010	1.07E+03	-86.03	1.95E-09	1.55E+04
76509	1.06E+03	-86.02	1.95E-09	1.54E+04
77009	1.06E+03	-86.02	1.95E-09	1.52E+04

Continued on next page

Table B.1 – *Continued from previous page*

Frequency (Hz)	**Impedance**	**Phase**	C_p	R_p
77509	1.05E+03	-86.01	1.95E-09	1.51E+04
78009	1.05E+03	-86.00	1.95E-09	1.50E+04
78509	1.04E+03	-86.00	1.95E-09	1.49E+04
79008	1.03E+03	-85.99	1.95E-09	1.48E+04
79508	1.03E+03	-85.99	1.95E-09	1.47E+04
80008	1.02E+03	-85.97	1.95E-09	1.45E+04
80508	1.01E+03	-85.98	1.94E-09	1.45E+04
81008	1.01E+03	-85.97	1.94E-09	1.43E+04
81507	1.00E+03	-85.97	1.94E-09	1.43E+04
82007	9.96E+02	-85.95	1.94E-09	1.42E+04
82507	9.90E+02	-85.96	1.94E-09	1.41E+04
83007	9.85E+02	-85.95	1.94E-09	1.40E+04
83507	9.79E+02	-85.95	1.94E-09	1.39E+04
84006	9.73E+02	-85.94	1.94E-09	1.38E+04
84506	9.68E+02	-85.94	1.94E-09	1.37E+04
85006	9.62E+02	-85.93	1.94E-09	1.36E+04
85506	9.57E+02	-85.93	1.94E-09	1.35E+04
86006	9.52E+02	-85.92	1.94E-09	1.34E+04
86505	9.46E+02	-85.92	1.94E-09	1.33E+04
87005	9.41E+02	-85.91	1.94E-09	1.32E+04
87505	9.36E+02	-85.90	1.94E-09	1.31E+04
88005	9.31E+02	-85.91	1.94E-09	1.31E+04
88505	9.26E+02	-85.89	1.94E-09	1.30E+04

Continued on next page

Table B.1 – *Continued from previous page*

Frequency (Hz)	**Impedance**	**Phase**	C_p	R_p
89004	9.21E+02	-85.89	1.94E-09	1.29E+04
89504	9.16E+02	-85.89	1.94E-09	1.28E+04
90004	9.11E+02	-85.88	1.94E-09	1.27E+04
90504	9.06E+02	-85.88	1.94E-09	1.26E+04
91004	9.01E+02	-85.87	1.94E-09	1.25E+04
91503	8.97E+02	-85.87	1.93E-09	1.24E+04
92003	8.92E+02	-85.86	1.93E-09	1.24E+04
92503	8.87E+02	-85.86	1.93E-09	1.23E+04
93003	8.83E+02	-85.85	1.93E-09	1.22E+04
93503	8.78E+02	-85.85	1.93E-09	1.21E+04
94002	8.74E+02	-85.84	1.93E-09	1.20E+04
94502	8.69E+02	-85.84	1.93E-09	1.20E+04
95002	8.65E+02	-85.83	1.93E-09	1.19E+04
95502	8.60E+02	-85.83	1.93E-09	1.18E+04
96002	8.56E+02	-85.81	1.93E-09	1.17E+04
96501	8.52E+02	-85.81	1.93E-09	1.17E+04
97001	8.48E+02	-85.81	1.93E-09	1.16E+04
97501	8.43E+02	-85.80	1.93E-09	1.15E+04
98001	8.39E+02	-85.80	1.93E-09	1.15E+04
98501	8.35E+02	-85.80	1.93E-09	1.14E+04
99000	8.31E+02	-85.79	1.93E-09	1.13E+04
99500	8.27E+02	-85.78	1.93E-09	1.13E+04
100000	8.23E+02	-85.78	1.93E-09	1.12E+04

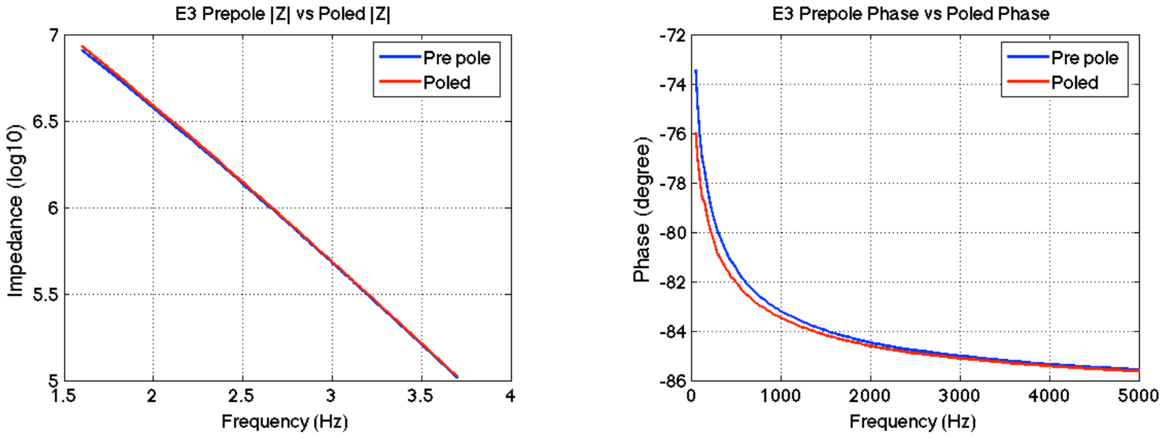

(a) Impedance magnitude

(b) Impedance phase angle

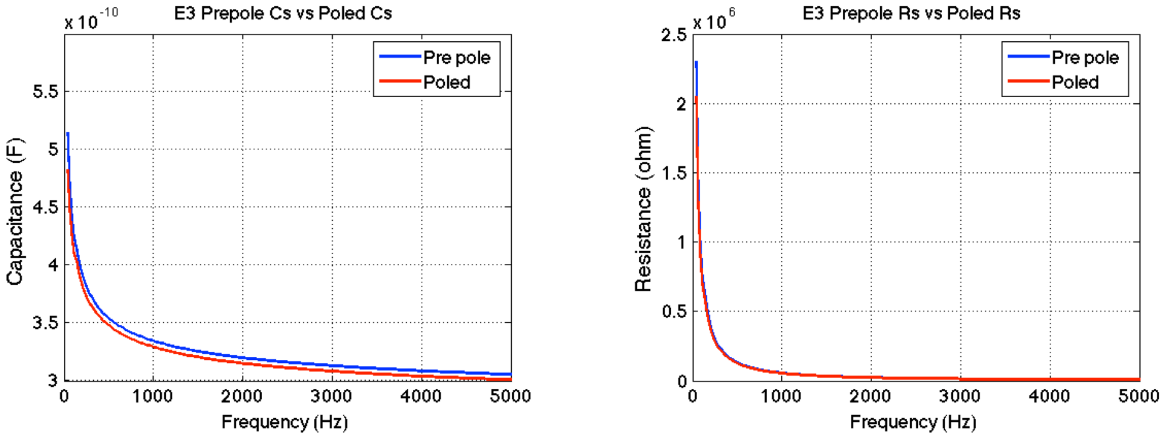

(c) Capacitance C_p

(d) Resistance R_p

Figure B.1: PZT thin film actuator E3 impedance analysis data: pre-pole versus poled

Appendix C

SCANNING ELECTRON MICROSCOPE IMAGES

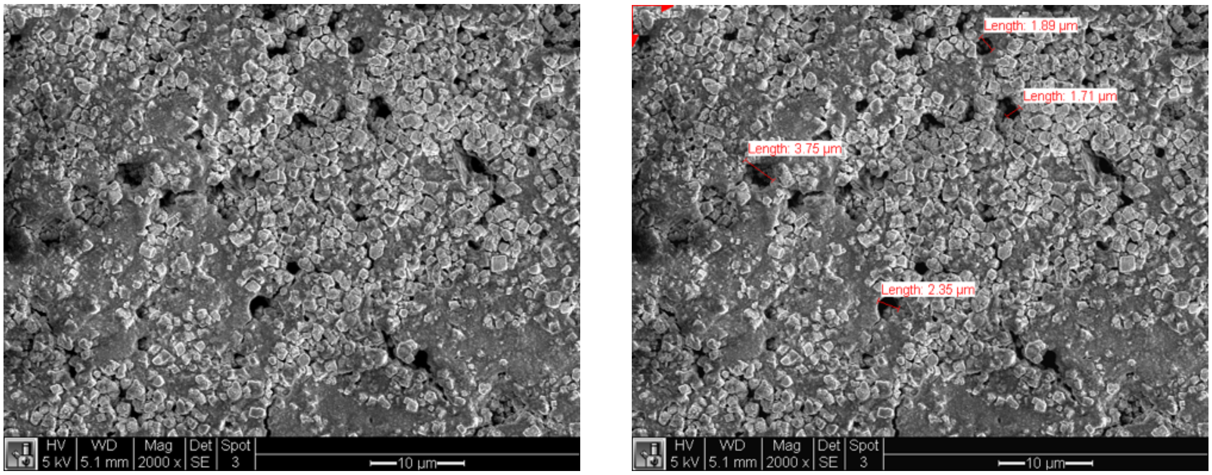

(a) Voids in the thin film (b) Measurement of holes

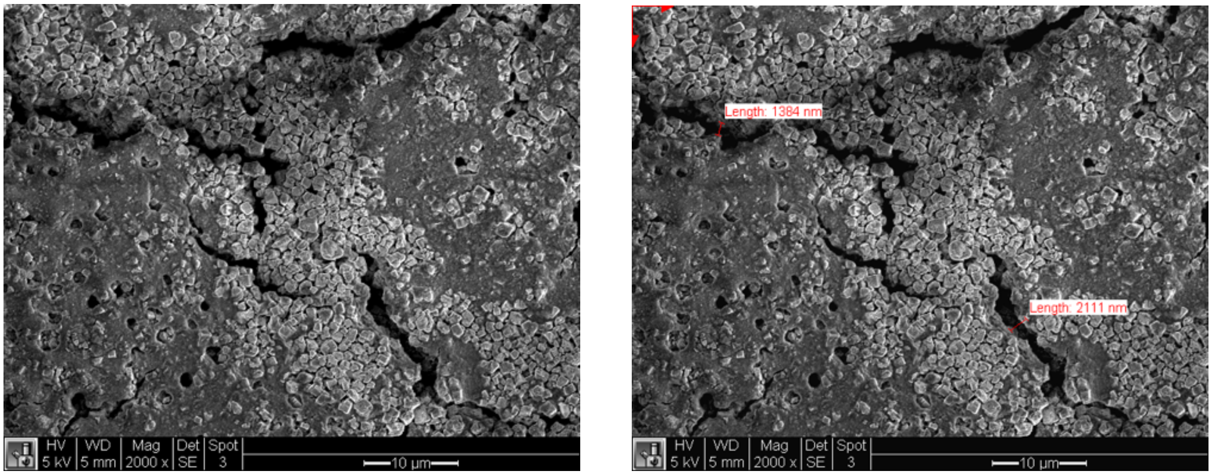

(c) Cracks in the thin film (d) Measurement of cracks

Figure C.1: Top view SEM images of hydrothermal grown PZT nanoparticles thin films with defects at 2000X magnification

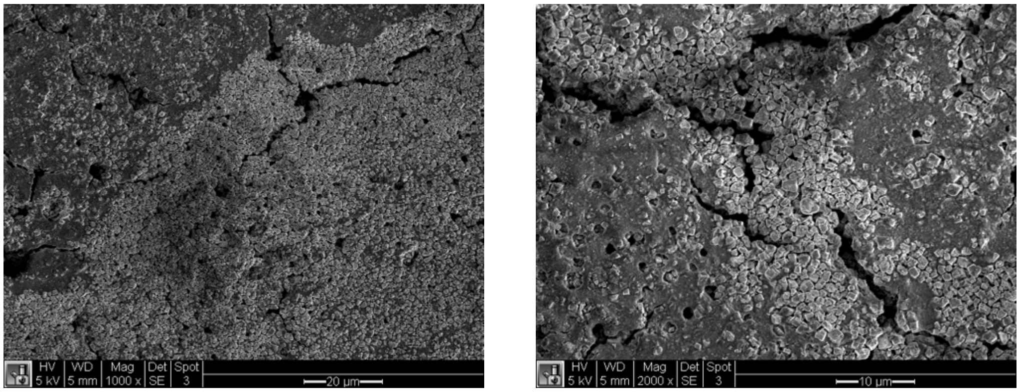

(a) Magnification: 1,000X

(b) Magnification: 40,000X

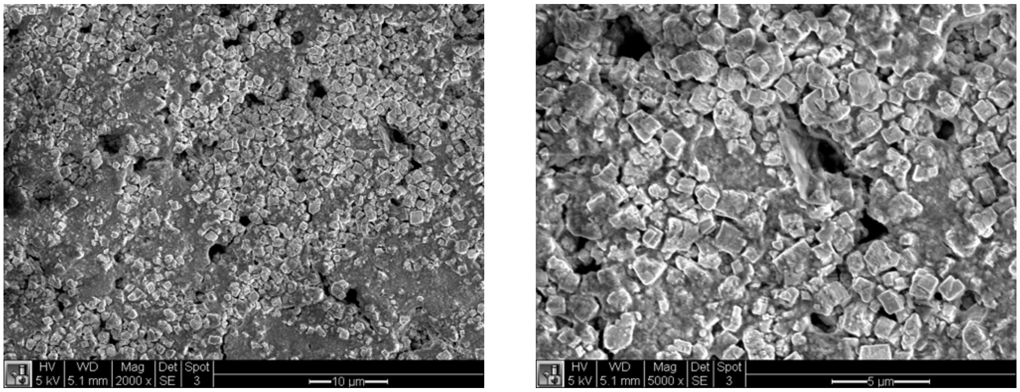

(c) Magnification: 2,000X

(d) Magnification: 5,000X

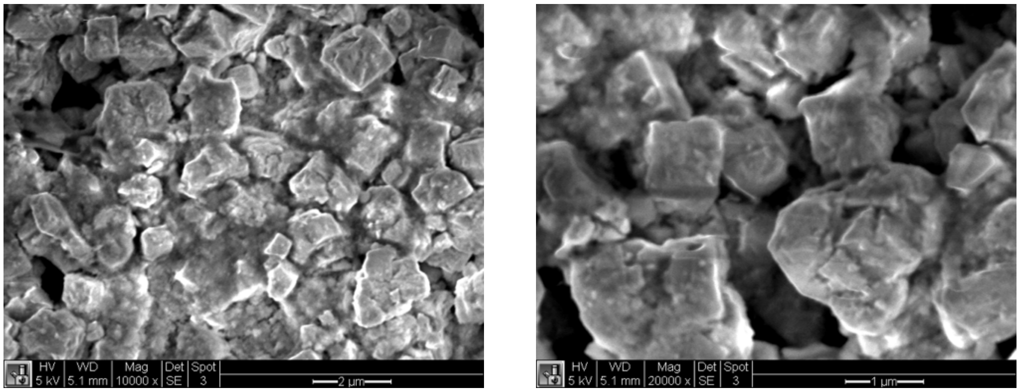

(e) Magnification: 10,000X

(f) Magnification: 20,000X

Figure C.2: SEM of hydrothermal grown PZT nanoparticles in different magnifications

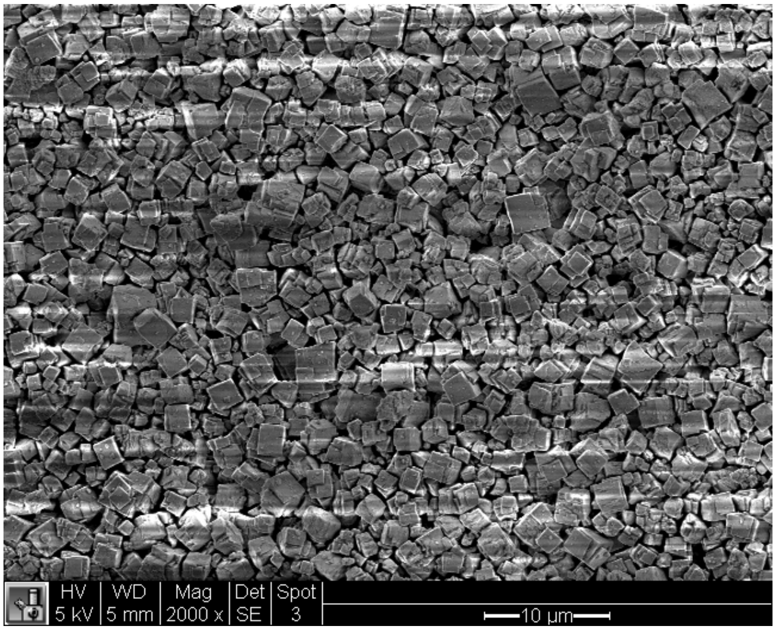

Figure C.3: PZT nanoparticles in power form

Appendix D

THEORY

$$\mathbf{s^E} = \begin{bmatrix} \mathbf{s}^E_{1111} & \mathbf{s}^E_{1122} & \mathbf{s}^E_{1133} & \mathbf{s}^E_{1123} & \mathbf{s}^E_{1113} & \mathbf{s}^E_{1112} \\ \mathbf{s}^E_{1122} & \mathbf{s}^E_{2222} & \mathbf{s}^E_{2233} & \mathbf{s}^E_{2223} & \mathbf{s}^E_{2213} & \mathbf{s}^E_{2212} \\ \mathbf{s}^E_{1133} & \mathbf{s}^E_{2233} & \mathbf{s}^E_{3333} & \mathbf{s}^E_{3323} & \mathbf{s}^E_{3313} & \mathbf{s}^E_{3312} \\ \mathbf{s}^E_{1123} & \mathbf{s}^E_{2223} & \mathbf{s}^E_{3323} & \mathbf{s}^E_{2323} & \mathbf{s}^E_{2313} & \mathbf{s}^E_{2312} \\ \mathbf{s}^E_{1113} & \mathbf{s}^E_{2213} & \mathbf{s}^E_{3313} & \mathbf{s}^E_{2313} & \mathbf{s}^E_{1313} & \mathbf{s}^E_{1312} \\ \mathbf{s}^E_{1112} & \mathbf{s}^E_{2212} & \mathbf{s}^E_{3312} & \mathbf{s}^E_{2312} & \mathbf{s}^E_{1312} & \mathbf{s}^E_{1212} \end{bmatrix} \tag{D.1}$$

$$[\mathbf{s}]_{6\times 6} = \begin{bmatrix} s_{1111} & s_{1122} & s_{1133} & s_{1123} & s_{1113} & s_{1112} \\ s_{1122} & s_{2222} & s_{2233} & s_{2223} & s_{2213} & s_{2212} \\ s_{1133} & s_{2233} & s_{3333} & s_{3323} & s_{3313} & s_{3312} \\ s_{1123} & s_{2223} & s_{3323} & s_{2323} & s_{2313} & s_{2312} \\ s_{1113} & s_{2213} & s_{3313} & s_{2313} & s_{1313} & s_{1312} \\ s_{1112} & s_{2212} & s_{3312} & s_{2312} & s_{1312} & s_{1212} \end{bmatrix} \tag{D.2}$$

Piezoelectric constitutive equations:

$$\begin{bmatrix} \{\mathbf{S}\}_{\mathbf{6\times 1}} \\ \{\mathbf{D}\}_{\mathbf{3\times 1}} \end{bmatrix} = \begin{bmatrix} [\mathbf{s}^E]_{6\times 6} & [\mathbf{d}]_{6\times 3} \\ [\mathbf{d}^t]_{3\times 6} & [\varepsilon^T]_{3\times 3} \end{bmatrix} \begin{bmatrix} \{\mathbf{T}\}_{6\times 1} \\ \{\mathbf{E}\}_{3\times 1} \end{bmatrix} \tag{D.3}$$

$$S_{ij} = s^E_{ijkl} T_{kl} + d_{kij} E_k \tag{D.4}$$

$$D_i = d_{ikl} T_{kl} + \varepsilon^T_{ik} E_k \tag{D.5}$$

Poled piezoceramics (such as PZT-5A and PZT-4) are transversely isotropic materials. Voigt's notation is used for presenting symmetric tensors here, so the double subscripts can be replaced with a single notation following: 11 → 1, 22 → 2, 33 → 3, 23/32 → 4, 13/31 → 5, 12/21 → 6. For piezoelectric transversely isotropic materials:

$$\mathbf{s^E} = \begin{bmatrix} \mathbf{s}_{11}^E & \mathbf{s}_{12}^E & \mathbf{s}_{13}^E & 0 & 0 & 0 \\ \mathbf{s}_{12}^E & \mathbf{s}_{11}^E & \mathbf{s}_{13}^E & 0 & 0 & 0 \\ \mathbf{s}_{13}^E & \mathbf{s}_{13}^E & \mathbf{s}_{33}^E & 0 & 0 & 0 \\ 0 & 0 & 0 & \mathbf{s}_{55}^E & 0 & 0 \\ 0 & 0 & 0 & 0 & \mathbf{s}_{55}^E & 0 \\ 0 & 0 & 0 & 0 & 0 & \mathbf{s}_{66}^E \end{bmatrix} \tag{D.6}$$

$$\mathbf{d} = \begin{bmatrix} 0 & 0 & d_{31} \\ 0 & 0 & d_{31} \\ 0 & 0 & d_{33} \\ 0 & d_{15} & 0 \\ d_{15} & 0 & 0 \\ 0 & 0 & 0 \end{bmatrix} \tag{D.7}$$

$$\varepsilon^{\mathbf{T}} = \begin{bmatrix} \varepsilon_{11}^T & 0 & 0 \\ 0 & \varepsilon_{11}^T & 0 \\ 0 & 0 & \varepsilon_{33}^T \end{bmatrix} \tag{D.8}$$

Substitute Eqn. (D.6), (D.7) and (D.8) into Eqn. (D.4):

$$\begin{bmatrix} S_1 \\ S_2 \\ S_3 \\ S_4 \\ S_5 \\ S_6 \end{bmatrix} = \begin{bmatrix} \mathbf{s}_{11}^E & \mathbf{s}_{12}^E & \mathbf{s}_{13}^E & 0 & 0 & 0 \\ \mathbf{s}_{12}^E & \mathbf{s}_{11}^E & \mathbf{s}_{13}^E & 0 & 0 & 0 \\ \mathbf{s}_{13}^E & \mathbf{s}_{13}^E & \mathbf{s}_{33}^E & 0 & 0 & 0 \\ 0 & 0 & 0 & \mathbf{s}_{55}^E & 0 & 0 \\ 0 & 0 & 0 & 0 & \mathbf{s}_{55}^E & 0 \\ 0 & 0 & 0 & 0 & 0 & \mathbf{s}_{66}^E \end{bmatrix} \begin{bmatrix} T_1 \\ T_2 \\ T_3 \\ T_4 \\ T_5 \\ T_6 \end{bmatrix} + \begin{bmatrix} 0 & 0 & d_{31} \\ 0 & 0 & d_{31} \\ 0 & 0 & d_{33} \\ 0 & d_{15} & 0 \\ d_{15} & 0 & 0 \\ 0 & 0 & 0 \end{bmatrix} \begin{bmatrix} E_1 \\ E_2 \\ E_3 \end{bmatrix} \tag{D.9}$$

For isotropic materials, the compliance matrix is:

$$\mathbf{s_{isotropic}} = (\frac{1}{E}) \begin{bmatrix} 1 & -\nu & -\nu & 0 & 0 & 0 \\ -\nu & 1 & -\nu & 0 & 0 & 0 \\ -\nu & -\nu & 1 & 0 & 0 & 0 \\ 0 & 0 & 0 & 1+\nu & 0 & 0 \\ 0 & 0 & 0 & 0 & 1+\nu & 0 \\ 0 & 0 & 0 & 0 & 0 & 1+\nu \end{bmatrix} \tag{D.10}$$

For PZT-4:

$$\mathbf{s^E} = \begin{bmatrix} 12.3 & -4.05 & -5.31 & 0 & 0 & 0 \\ -4.05 & 12.3 & -5.31 & 0 & 0 & 0 \\ -5.31 & -5.31 & 15.5 & 0 & 0 & 0 \\ 0 & 0 & 0 & 39 & 0 & 0 \\ 0 & 0 & 0 & 0 & 39 & 0 \\ 0 & 0 & 0 & 0 & 0 & 32.7 \end{bmatrix} \times 10^{-12}\ \frac{m^2}{N} \tag{D.11}$$

$$\mathbf{d} = \begin{bmatrix} 0 & 0 & -123 \\ 0 & 0 & -123 \\ 0 & 0 & 289 \\ 0 & 496 & 0 \\ 496 & 0 & 0 \\ 0 & 0 & 0 \end{bmatrix} \times 10^{-12}\ \frac{C}{N} \tag{D.12}$$

$$\frac{\varepsilon^{\mathbf{T}}}{\varepsilon_{\mathbf{o}}} = \begin{bmatrix} 1475 & 0 & 0 \\ 0 & 1475 & 0 \\ 0 & 0 & 1300 \end{bmatrix},\ \varepsilon_{\mathbf{o}} = 8.854 \times 10^{-12}\ \frac{F}{m} \tag{D.13}$$

$$\mathbf{s^E} = \begin{bmatrix} \mathbf{s}^E_{1111} & \mathbf{s}^E_{1122} & \mathbf{s}^E_{1133} & \mathbf{s}^E_{1123} & \mathbf{s}^E_{1113} & \mathbf{s}^E_{1112} \\ \mathbf{s}^E_{1122} & \mathbf{s}^E_{2222} & \mathbf{s}^E_{2233} & \mathbf{s}^E_{2223} & \mathbf{s}^E_{2213} & \mathbf{s}^E_{2212} \\ \mathbf{s}^E_{1133} & \mathbf{s}^E_{2233} & \mathbf{s}^E_{3333} & \mathbf{s}^E_{3323} & \mathbf{s}^E_{3313} & \mathbf{s}^E_{3312} \\ \mathbf{s}^E_{1123} & \mathbf{s}^E_{2223} & \mathbf{s}^E_{3323} & \mathbf{s}^E_{2323} & \mathbf{s}^E_{2313} & \mathbf{s}^E_{2312} \\ \mathbf{s}^E_{1113} & \mathbf{s}^E_{2213} & \mathbf{s}^E_{3313} & \mathbf{s}^E_{2313} & \mathbf{s}^E_{1313} & \mathbf{s}^E_{1312} \\ \mathbf{s}^E_{1112} & \mathbf{s}^E_{2212} & \mathbf{s}^E_{3312} & \mathbf{s}^E_{2312} & \mathbf{s}^E_{1312} & \mathbf{s}^E_{1212} \end{bmatrix} \tag{D.14}$$

$$[\mathbf{s}]_{6\times 6} = \begin{bmatrix} s_{1111} & s_{1122} & s_{1133} & s_{1123} & s_{1113} & s_{1112} \\ s_{1122} & s_{2222} & s_{2233} & s_{2223} & s_{2213} & s_{2212} \\ s_{1133} & s_{2233} & s_{3333} & s_{3323} & s_{3313} & s_{3312} \\ s_{1123} & s_{2223} & s_{3323} & s_{2323} & s_{2313} & s_{2312} \\ s_{1113} & s_{2213} & s_{3313} & s_{2313} & s_{1313} & s_{1312} \\ s_{1112} & s_{2212} & s_{3312} & s_{2312} & s_{1312} & s_{1212} \end{bmatrix} \tag{D.15}$$

Appendix E

ACTUATOR SETUP WITH A BINDER CLIP AND TEST RESULTS

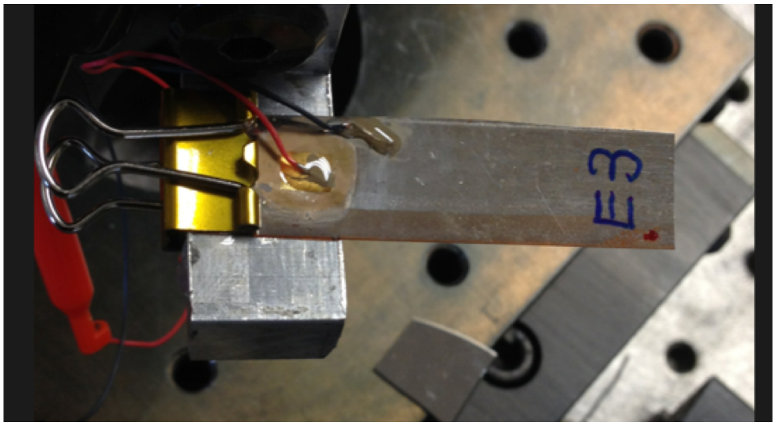

Figure E.1: The photo of the experimental set up for actuator demonstration

Figure E.2 shows the measured swept sine FRF of beam tip velocity over driving voltage for the Poled PZT thin film actuator E3. It can be observed that the first three resonance frequencies of the test structure were (1) 273 Hz, (2) 690 Hz and (3) 1.195 kHz.

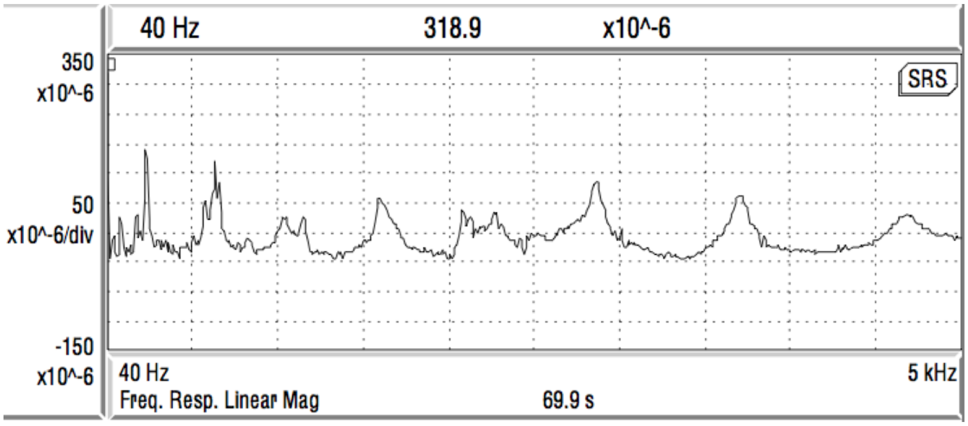

(a) Pre-pole E3

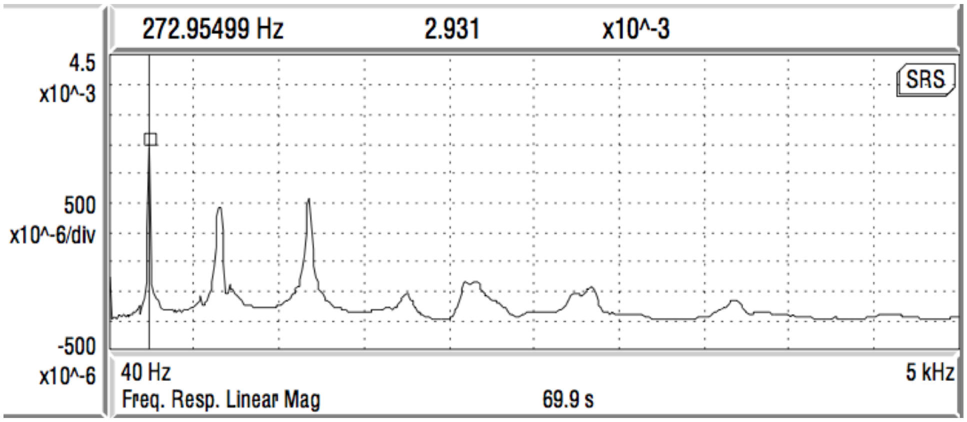

(b) Poled E3

Figure E.2: Swept sine frequency responses of beam tip velocity over input voltage

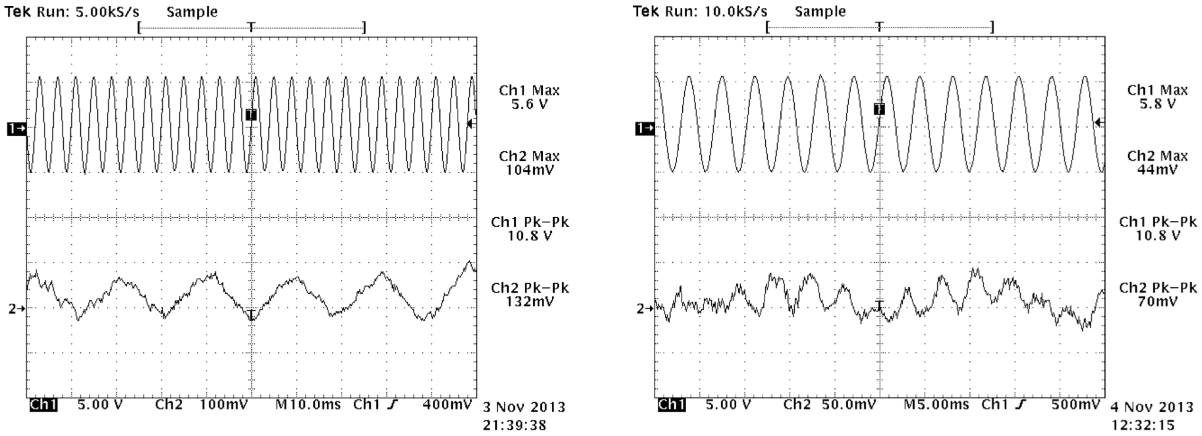

(a) Pre-pole E3

(b) Poled E3

Figure E.3: PZT thin film actuator E3 response to a sinusoidal voltage of 270 Hz

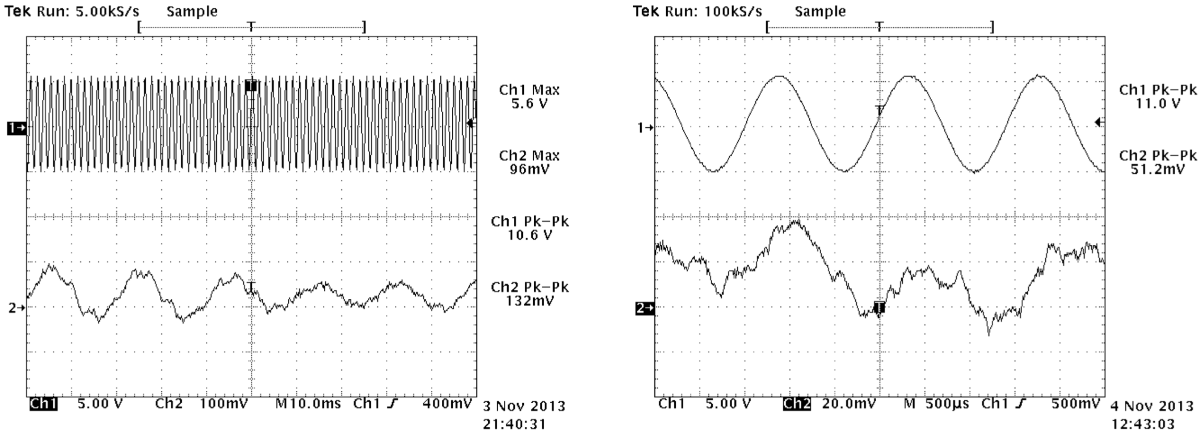

(a) Pre-pole E3

(b) Poled E3

Figure E.4: PZT thin film actuator E3 response to a sinusoidal voltage of 690 Hz

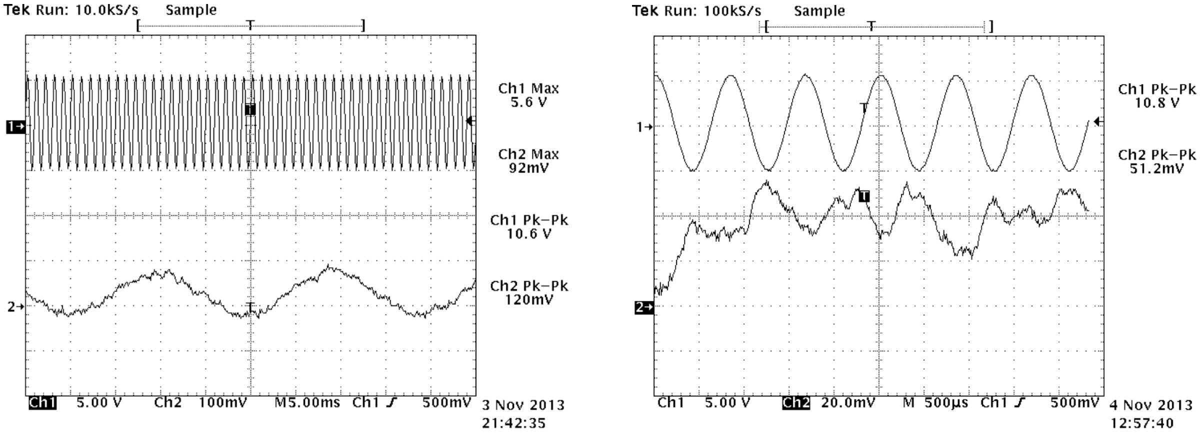

(a) Pre-pole E3

(b) Poled E3

Figure E.5: PZT thin film actuator E3 response to a sinusoidal voltage of 1.95 kHz

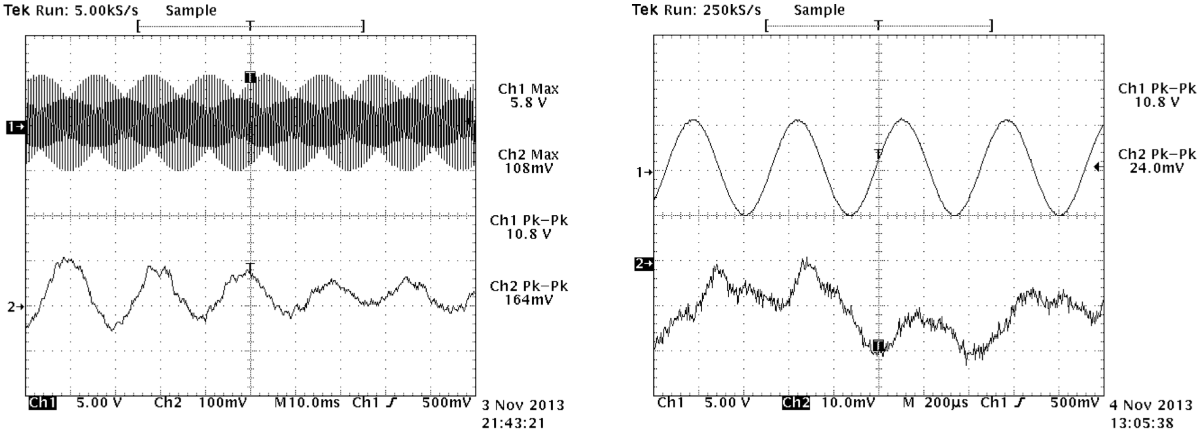

(a) Pre-pole E3

(b) Poled E3

Figure E.6: PZT thin film actuator E3 response to a sinusoidal voltage of 2.15 kHz

Appendix F

AEROSOL-JET MICRO-ADDITIVE PRINTING RESULTS OF PZT INKS

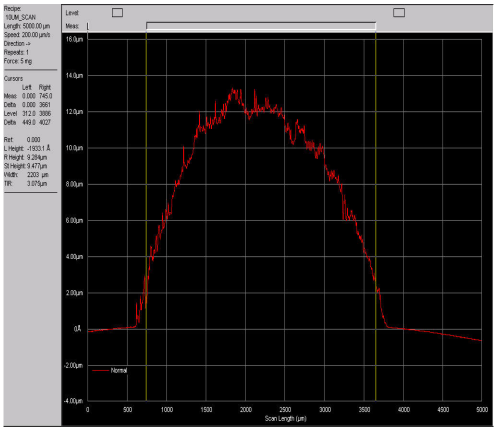

```
Recipe:
 10UM_SCAN
Length: 5000.00 µm
Speed: 200.00 µm/s
Direction ->
Repeats: 1
Force: 5 mg

Cursors
        Left   Right
Meas    0.000  745.0
Delta   0.000  3661
Level   312.0  3886
Delta   449.0  4027

Ref:       0.000
L Height:  -1933.1 Å
R Height:  9.284µm
St Height: 9.477µm
Width:     2203  µm
TIR:       3.075µm
```

```
Recipe:
 10UM_SCAN
Length: 5000.00 µm
Speed: 200.00 µm/s
Direction ->
Repeats: 1
Force: 5 mg

Cursors
        Left   Right
Meas    191.0  648.0
Delta   191.0  3723
Level   312.0  3886
Delta   449.0  4027

Ref:       0.000
L Height:  -829.9 Å
R Height:  10.61µm
St Height: 10.69µm
Width:     1995  µm
TIR:       2.615µm
```

(a) H-1 (b) H-2

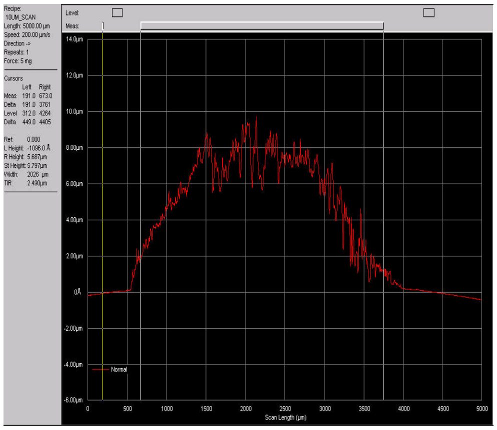

```
Recipe:
 10UM_SCAN
Length: 5000.00 µm
Speed: 200.00 µm/s
Direction ->
Repeats: 1
Force: 5 mg

Cursors
        Left   Right
Meas    191.0  673.0
Delta   191.0  3761
Level   312.0  4264
Delta   449.0  4405

Ref:       0.000
L Height:  -1096.0 Å
R Height:  5.687µm
St Height: 5.797µm
Width:     2026  µm
TIR:       2.490µm
```

```
Recipe:
 10UM_SCAN
Length: 5000.00 µm
Speed: 200.00 µm/s
Direction ->
Repeats: 1
Force: 5 mg

Cursors
        Left   Right
Meas    191.0  784.0
Delta   191.0  3872
Level   337.0  4379
Delta   347.0  4398

Ref:       0.000
L Height:  -541.9 Å
R Height:  7.368µm
St Height: 7.423µm
Width:     2137  µm
TIR:       2.013µm
```

(c) H-3 (d) V-1

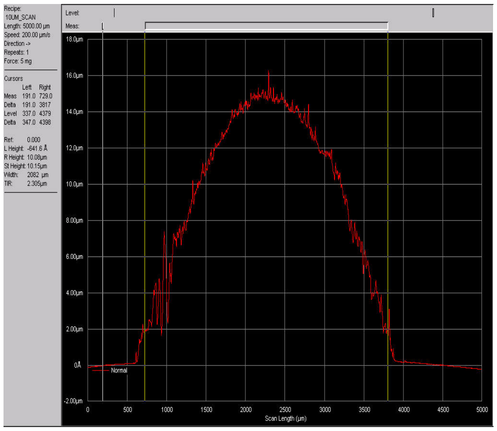

```
Recipe:
 10UM_SCAN
Length: 5000.00 µm
Speed: 200.00 µm/s
Direction ->
Repeats: 1
Force: 5 mg

Cursors
        Left   Right
Meas    191.0  729.0
Delta   191.0  3817
Level   337.0  4379
Delta   347.0  4398

Ref:       0.000
L Height:  -641.6 Å
R Height:  10.08µm
St Height: 10.15µm
Width:     2082  µm
TIR:       2.305µm
```

```
Recipe:
 10UM_SCAN
Length: 5000.00 µm
Speed: 200.00 µm/s
Direction ->
Repeats: 1
Force: 5 mg

Cursors
        Left   Right
Meas    191.0  729.0
Delta   191.0  3817
Level   337.0  4379
Delta   347.0  4398

Ref:       0.000
L Height:  -641.6 Å
R Height:  10.08µm
St Height: 10.15µm
Width:     2082  µm
TIR:       2.305µm
```

(e) V-2 (f) V-3

Figure F.1: Surface profilometry of printed crushed PZT particles ink

Appendix G

THE EFFECT OF REPETITIVE POLING ON PZT THIN FILM SENSORS PERFORMANCE

The purpose of this section is for estimating the uncertainty of the impact test results for determine the charge-to-force ratios. NW1, NW2 and NW5 are hydrothermally grown PZT nanoparticles sensors[1] and NB3, NB4 and NB5 are PZT crushed particles sensors

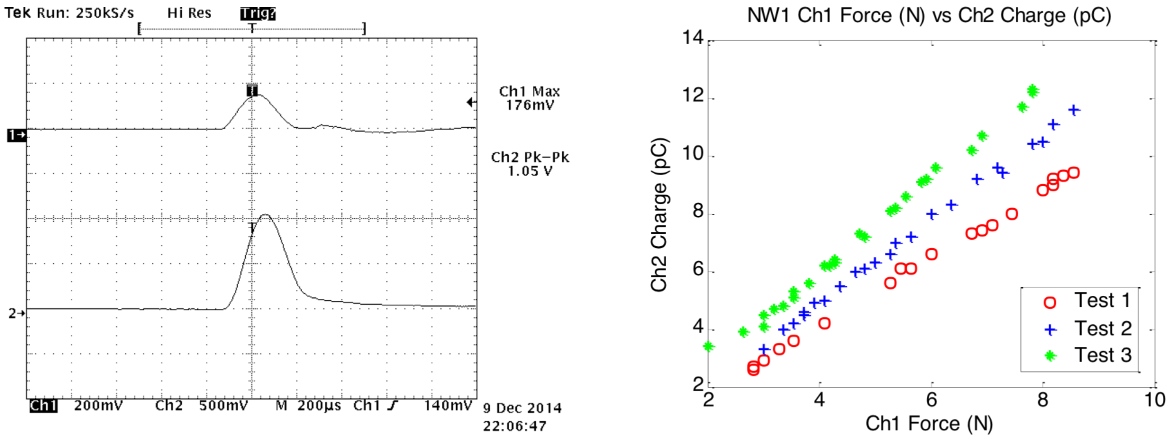

(a) Oscilloscope time-domain measurement

(b) Measured Q/F curve

Figure G.1: Specimen NW1 time domain measurements from three repeatability tests

---

[1] Both PZT nanoparticles and ink were made by Weiwei Xu

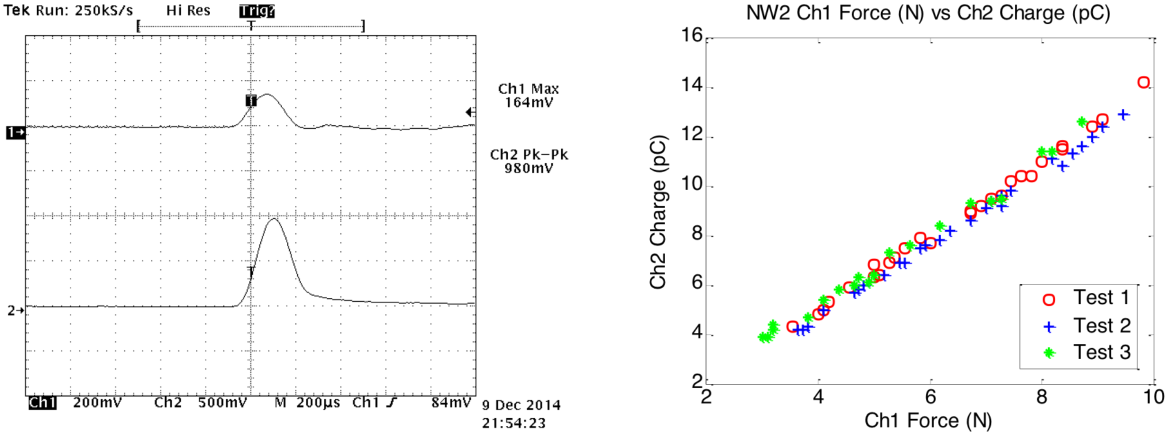

(a) Oscilloscope time-domain measurement

(b) Measured Q/F curve

Figure G.2: Specimen NW2 time domain measurements from three repeatability tests

Table G.1: Repeatability study of Q/F ratios for expedited hydrothermal grown PZT nanoparticles thin films

Specimen	**Test 1**	**Test 2**	**Test 3**	**Mean**	**Sta. Dev.**
NW1	1.18	1.45	1.63	1.42	0.18
NW2	1.52	1.48	1.46	1.49	0.02
NW5	0.4	0.93	1.05	0.79	0.28

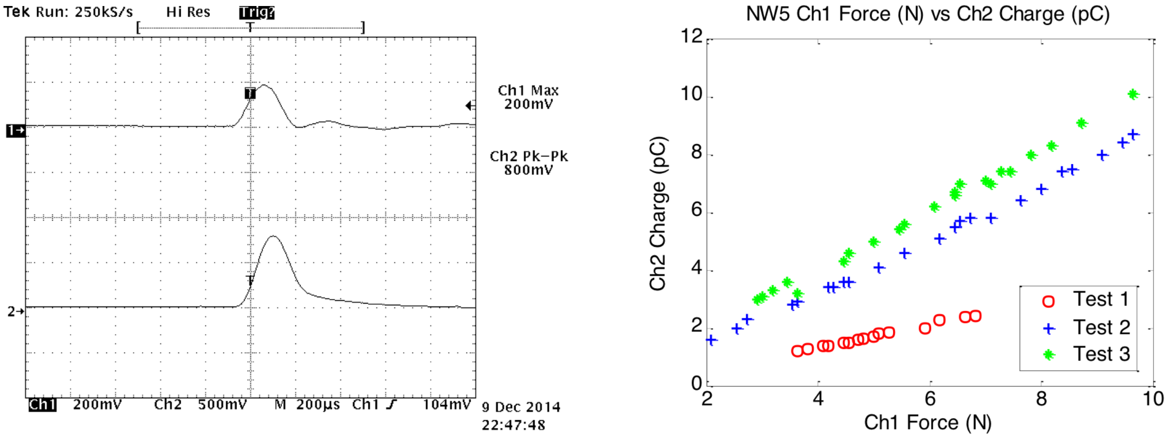

(a) Oscilloscope time-domain measurement

(b) Measured Q/F curve

Figure G.3: Specimen NW5 time domain measurements from three repeatability tests

Table G.2: Measured Q/F ratios for hydrothermal grown PZT nanoparticles thin films

Specimen	**Top Electrode Area** (mm^2)	**Thickness** (μm)	**Poling Electric Field** ($V/\mu m$)	Q/F **Mean [SD]** (pC/N)
NW1	42	14.2	1.69	1.42 [0.18]
NW2	56	16	1.5	1.49 [0.02]
NW5	52.5	17.6	1.36	0.79 [0.28]

Table G.3: Repeatability study of Q/F ratios for crushed PZT particles thin films

Specimen	**Test 1**	**Test 2**	**Test 3**	**Mean**	**Sta. Dev.**
NB3	4.86	4.41	5.36	4.88	0.39
NB4	8.41	7.15	6.25	7.27	0.89
NB5	3.67	4.08	4.24	4	0.24

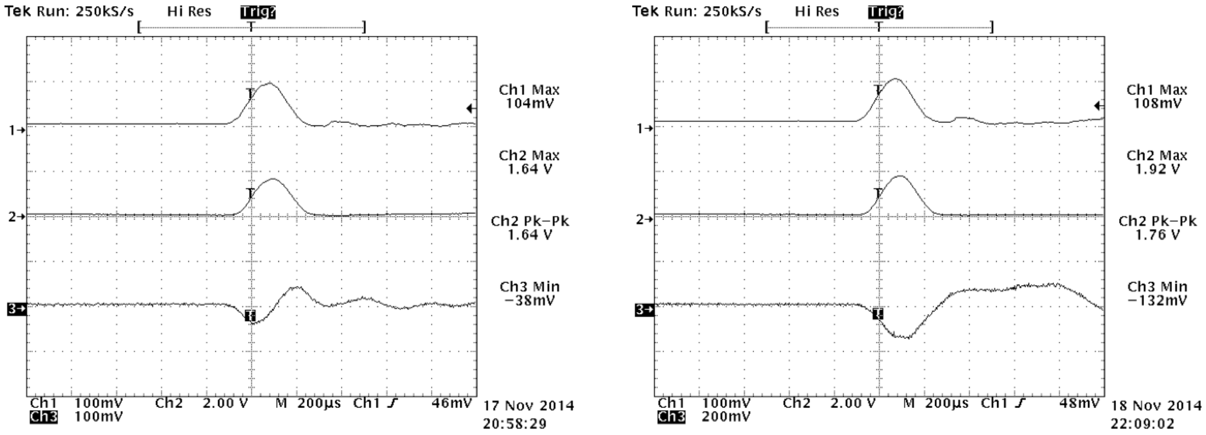

(a) Specimen NB5 Test 1

(b) Specimen NB5 Test 2

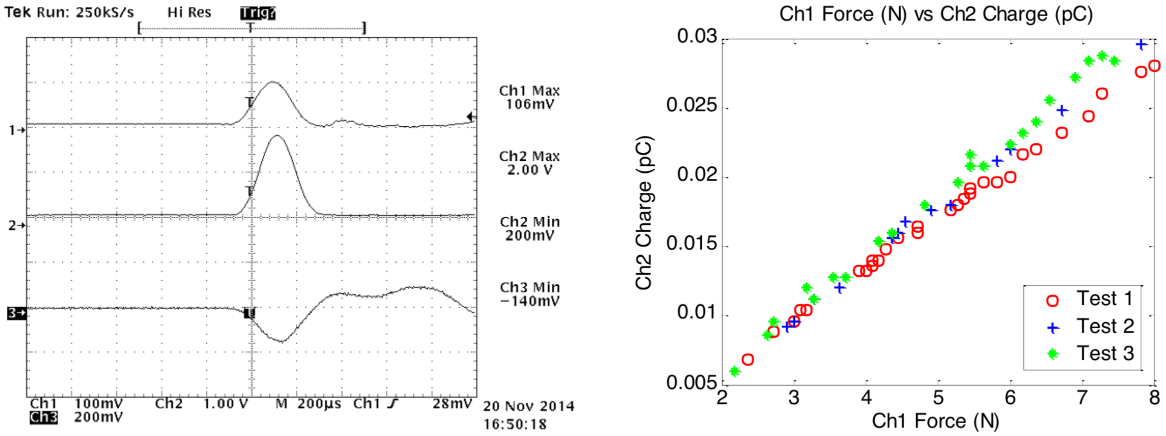

(c) Specimen NB5 Test 3

(d) Measured Q/F curves for three tests

Figure G.4: Specimen NB5 time domain measurements from three repeatability tests

Table G.4: Measured Q/F ratios for crushed PZT particles thin films

Specimen	**Top Electrode Area** (mm^2)	**Thickness** (μm)	**Poling Electric Field** ($V/\mu m$)	Q/F **Mean [SD]** (pC/N)
NB3	64	4.76	5.04	4.88 [0.39]
NB4	36	3.41	7.03	7.27 [0.89]
NB5	36	3.97	6.05	4.00 [0.24]